Call: NFRP-2019-2020

Topic: NFRP-2019-2020-02 Safety assessments for Long Term Operation (LTO) upgrades of Generation II and III reactors

Funding Scheme: Research and Innovation Action (RIA)

Deliverable No. 3.5

Public Summary Report of WP3

Grant Agreement no.:	945253
Project Title:	**Advanced PTS Analysis for LTO**
Contractual Submission Date:	30/06/2023
Actual Submission Date:	06/09/2024
Responsible partner:	P2: Framatome GmbH (FRA-G)

APAL has received funding from the Euratom research and training programme 2019-2020 under grant agreement No 945253.

Grant agreement no.	945253
Project full title	Advanced PTS Analysis for LTO

Deliverable number	**D3.5**
Deliverable title	**Public Summary WP3**
Type[1]	R
Dissemination level[2]	PU
Work package number	WP3
Work package leader	FRA-G
Author(s)	Ralf Tiete, Katharina Angermeier, Polina Baranova, Sébastien Blasset, Thomas Nicak (FRA-G), Bernadett Pusztai-Spisák (BZN), Klaus Heckmann, Christoph Bläsius, Jürgen Sievers (GRS), Yaroslav Dubyk, Vitalii Antonchenko (IPP), Minh-Bao Le (IRSN), Oriol Costa-Garrido (JSI), Petter von Unge, Andrey Shipsha, Peter Dillström (KIWA), Diego F. Mora (PSI), Oleksii Shugailo, Volodymyr Diemienkov (SSTC), Susana Flores, David Florez, Carlos Cueto (Tecnatom), Katarina Siskova, Miroslav Posta, Dana Lauerova, Vladislav Pistora (UJV), Piotr Darnowski, Piotr Mazgaj (WUT), Richard Bass (OCI), Hisashi Takamizawa (JAEA)
Keywords	APAL, PTS, Fracture mechanics, benchmark, LTO improvements, TH uncertainties, structural assessment, margin assessment

The research leading to these results has received funding from the Euratom research and training programme 2019-2020 under grant agreement No 945253.

The author is solely responsible for its content, it does not represent the opinion of the European Commission and the Commission is not responsible for any use that might be made of data appearing therein.

[1] **Type**: Use one of the following codes (in consistence with the Description of the Action):
- R: Document, report (excluding the periodic and final reports)
- DEM: Demonstrator, pilot, prototype, plan designs
- DEC: Websites, patents filing, press & media actions, videos, etc.
- OTHER: Software, technical diagram, etc.

[2] **Dissemination level**: Use one of the following codes (in consistence with the Description of the Action)
- PU: Public, fully open, e.g. web
- CO: Confidential, restricted under conditions set out in the Model Grant Agreement
- CI: Classified, information as referred to in Commission Decision 2001/844/EC

Table of Contents

1 Introduction 8
1.1 Definition of terms used in the assessments 9
1.2 Alignment/interface between WP3 and WP4 10
2 Structural assessment (Task 3.1 + Task 4.1) 12
2.1 Input data 12
2.1.1 RPV geometry 12
2.1.2 Material Properties 13
2.1.3 Boundary conditions 14
2.2 Sensitivity analyses 14
2.2.1 TH input from RELAP 14
2.2.2 Comparison between the partners' results 18
2.2.3 3D Simulations 19
2.2.4 Other locations 20
2.2.5 Mesh refinement 22
2.2.6 Time steps 23
2.3 LTO improvements 24
2.3.1 Results from 1D FE 25
2.3.2 Results from 3D FE 31
2.4 TH uncertainties 37
2.4.1 Uncertainties in TH data analyses for Wilks 37
2.4.2 Typical Wilks TH input data for structural analyses 37
2.4.3 Results for stress and temperature distributions through the RPV wall thickness 39
2.5 Conclusions from structural assessment 47
2.5.1 General conclusions on structural assessment 47
2.5.2 Assessment of LTO improvements 48
2.5.3 Structural Assessment for TH uncertainties 49
3 Benchmark Definition 53
3.1 Basic data for RPV fracture mechanics safety assessment 53
3.1.1 RPV Geometry 54
3.1.2 Material properties (mechanical and physical) 55
3.1.3 Brittle fracture, crack initiation fracture toughness K_{IC} and crack arrest fracture toughness K_{IA} 56
3.1.4 Upper shelf limit, ductile fracture toughness J / ductile tearing 59
3.1.5 Crack types 60
3.1.6 Flaw orientation 62
3.1.7 Transient load 62

3.1.8 Other loads (residual stresses) 63
3.1.9 Stress intensity factors 64
3.1.10 Fracture mechanics RPV safety assessment and limit conditions 65
3.2 Description of first benchmark performance: Pre-Requisite deterministic analyses (PR-Det) 69
3.2.1 PR-DET 1.1: Determination of SIF with provided temperature, stresses and pressure profiles 70
3.2.2 PR-DET 1.2: Determination of max. all. ART considering crack initiation 71
3.2.3 PR-Det 1.3: Determination of max. all. ART considering crack arrest (non-mandatory) 73
3.2.4 PR-DET 1.4: Crack arrest analysis (non-mandatory) 73
3.2.5 PR-DET 2: Evaluation of max. all. ART based on different TH calculations and individual SA and methods 73
3.3 Margin Assessment 74
3.3.1 Benchmark for tasks 3.4 considering LTOs improvement 74
3.3.2 Benchmark for task 3.5 considering TH uncertainties 75
4 First Benchmark Performance 76
4.1 First benchmark performance part 1 results: Calculations based on provided temperature and stress distributions (PR-Det-1) 76
4.1.1 Description of the task 76
4.1.2 Results for part 1.1: Determination of SIF 77
4.1.3 Results for part 1.2: Determination of max. allowable ART considering crack initiation 83
4.1.4 Results for part 1.3: Determination of max. allowable ART considering crack arrest (non-mandatory) 89
4.1.5 Observations and recommendations 90
4.2 First benchmark performance part 2 results: Calculations based on several TH calculations and individual structural and FM methods (PR-Det-2) 95
4.2.1 Results for part 2.1: Determination of SIF 96
4.2.2 Observations and recommendations 106
4.3 Results for part 2.2: Determination of max. allowable ART 106
4.3.1 Tangent approach 107
4.3.2 Simple WPS-max. approach 118
4.3.3 Sophisticated WPS approaches 129
4.3.4 FW Locations 137
4.3.5 Observations and recommendations 146
5 Safety margins related to LTO improvements and TH uncertainties 147
5.1 Safety margins related to LTO improvements 148
5.1.1 Short description of LTO improvements 148
5.1.2 Summary evaluation of LTOs for TCC 149

5.1.3 Summary evaluation of LTOs for UCC 157
5.1.4 Summary of evaluation of LTOs for embedded crack 159
5.2 Safety margins related to TH uncertainties 162
5.2.1 Comparison of temperature vs. time curves (based on Wilks data sets) 162
5.2.2 Comparison of empirical CDFs (based on Wilks data sets) 166
5.2.3 Comparison of 95%/95% lower limit values of max. all. RT_{NDT} (based on Wilks data sets) and selected margins 171
5.2.4 Comparison of the behaviour of the tangent and WPS-max approach 175
6 Conclusions 177
6.1 Conclusions from structural assessment 177
6.1.1 General Conclusions on structural assessment 177
6.1.2 Assessment of LTO improvements 177
6.1.3 Structural Assessment for TH uncertainties 178
6.2 Conclusions from first benchmark performance 181
6.3 Conclusions for chapter “Safety margins related to LTO improvements” 182
6.4 Conclusions for chapter “Safety margins related to TH uncertainties” 185
7 References 188
8 Annexes 190
8.1 Stress and temperature plots from 3D FE with input from RELAP in combination with mixing code (KWU-MIX) – base case transient 190
8.1.1 Stress and temperature fields for base case transient at core weld position P0 191
8.1.2 Stress and temperature fields for base case transient at flange weld position P1 192
8.1.3 Stress and temperature fields for base case transient at core weld position – outside plume P3 193
8.1.4 Stress and temperature fields for base case transient at nozzle corner P2 194

List of Abbreviations

1dSA	one-dimensional calculation performed within structural assessment
3dSA	three-dimensional calculation performed within structural assessment
ACC	accumulator
ALT	Average Liquid Temperature
APAL	Advanced PTS Analysis for LTO
ARS	APAL residual stress profile
ART	Adjusted reference temperature
BC	base case (transient), in some context also boundary conditions
BE	best-estimate (transient)
BM	base metal
CC	conservative-case (transient)
CDF	cumulative distribution function
CL	centre line (in other context, cold leg)
CW	core weld
DC	downcomer of reactor pressure vessel
EC	embedded crack
ECDF	empirical cumulative distribution function
FAVOR	Fracture Analysis of Vessels – Oak Ridge (software)
FE	Finite Element
FEA	Finite Element Analysis
FEM	Finite Element Method
FL	fusion line (interface between cladding and base metal)
FM	fracture mechanics
FRS	FAVOR residual stress profile
FW	flange weld
HAZ	heat affected zone
HL	hot leg
HPSI	high-pressure safety injection
HTC	heat transfer coefficient
ICAS	International Comparative Assessment Study (OECD NEA project)
IMP	in merging plumes
IP	in plume
KWU	Kraftwerk Union AG
LOCA	Loss of Coolant Accident
LPSI	low-pressure safety injection
LT	liquid temperature
LTO	long term operation
LTO 1	LTO improvement No. 1; similarly for other LTOs (No. 2, …, 9)
OP	Outside of Plume
NA	Not available
noRS	calculation performed without residual stress due to weld (only residual stress due to stress-free temperature is considered)
PTS	pressurized thermal shock
PWR	pressurized-water reactor
RELAP	Reactor Excursion and Leak Analysis Program (software)
RPV	reactor pressure vessel
RS	residual stress
SA	structural analysis (calculation of temperature and stress fields in RPV)
SB LOCA	Small Break LOCA
SIF	Stress Intensity Factor

TCC through-clad crack
TH thermal-hydraulic
T3.4 Task 3.4
T3.5 Task 3.5
UCC underclad crack
WPS warm pre-stressing
WPS-max maximum approach within WPS
WRS weld residual stress

1 Introduction

APAL (Advanced PTS Analysis for LTO) is a project funded by the EU within HORIZON 2020 programme. One of the most limiting safety assessments for the long-term operation (LTO) of nuclear power plants (NPPs) is the reactor pressure vessel (RPV) integrity assessment for pressurized thermal shock (PTS). The main objectives of APAL project are following:

- development of advanced deterministic and probabilistic PTS assessment methods,
- quantification of deterministic and probabilistic safety margins,
- development of best-practice guidance.

The APAL project consists of 7 work packages (WP):

- WP1 – State-of-the-art for LTO improvements relevant for PTS event
- WP2 - Improvement of TH analysis
- **WP3 - Deterministic margin assessment**
- WP4 - Probabilistic margin assessment
- WP5 - Definition of best-practice for advanced PTS analysis
- WP6 - Training, Communication, Dissemination and Exploitation
- WP7 - Scientific coordination and project management

The interaction between these 7 WPs is shown in Figure 1.1.

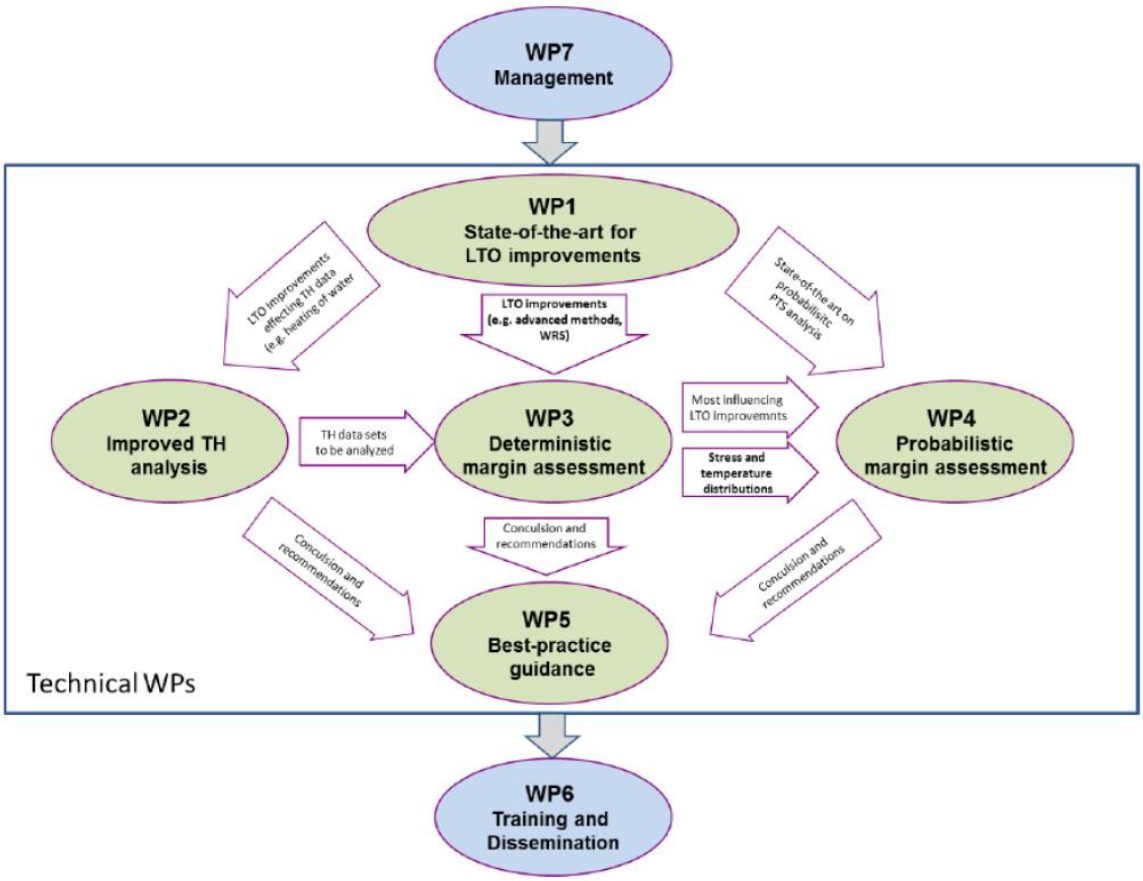

Figure 1.1: Structure of WPs within APAL

This report summarises the work, main results, conclusions and lessons learned of WP3 "Deterministic margin assessment". The main objective of the WP3 was to perform benchmarks to harmonize calculation tools and avoid errors as well as to determine the impact of LTO improvements and

uncertainties in thermal hydraulic (TH) data on the results of PTS analysis using deterministic assessment.

The WP3 (Deterministic margin assessment) consists of five tasks:

- Task 3.1: Structural assessment
- Task 3.2: Definition of deterministic benchmark
- Task 3.3: Baseline deterministic benchmark
- Task 3.4: Margin assessment related to LTO improvements
- Task 3.5: Margin assessment related to TH uncertainties

In Task3.1 "*Structural assessment"* the structural calculations for the determination of strains, stresses and temperatures in the RPV wall were carried out for a selected ICAS transient APAL-ICAS T2 (base case), and for the selected LTO improvements. The TH data were obtained from WP2. To have a better understanding of the results, sensitivity cases were also generated.

In Task 3.2 "Definition of deterministic benchmark" a benchmark for the deterministic fracture mechanics assessment was defined, which also was the basis for the benchmark for the probabilistic PTS analysis carried out in WP4. The benchmark definition is based on a sound technical basis and allows verification of results. The benchmark has mandatory (determination of crack initiation) and non-mandatory parts (e.g. determination of RPV failure including crack arrest analysis, investigations of statistical data set to identify the most conservative loading conditions).

In Task 3.3 "Baseline deterministic benchmark" a first deterministic fracture mechanics benchmark performance was carried out based on the base case TH data set. The first benchmark performance was done stepwise, starting with input data and methods given to identify critical steps within the defined benchmark. The results from the first deterministic benchmark performance were compared and analysed. Secondly, participants may have used their own calculation methods and input data.

In Tasks 3.4 *"Margin assessment related to LTO improvements"* and 3.5 *"Margin assessment related to TH uncertainties"* the impact of selected LTO improvements and TH uncertainties on deterministic margin assessment was evaluated, as illustrated in Table 1.1.

Table 1.1: Quantification of impact of LTO improvements and TH uncertainties on margin assessment

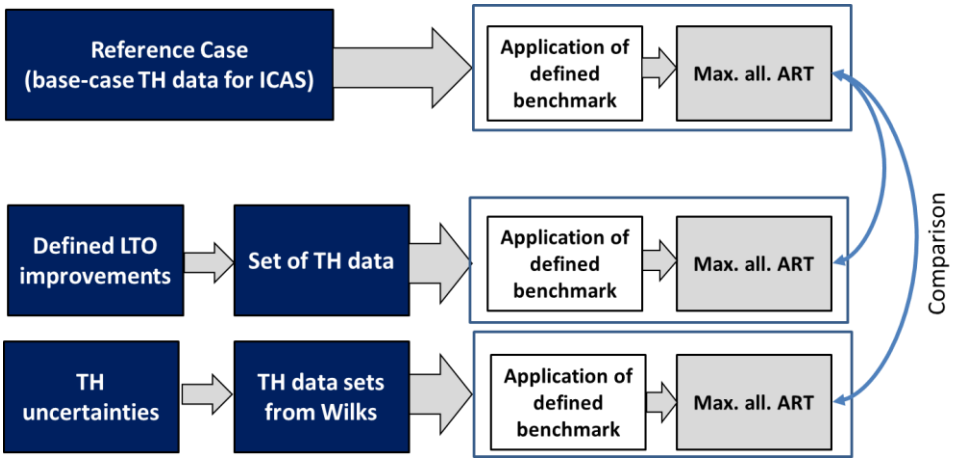

1.1 Definition of terms used in the assessments

This Section provides definitions that were used for the assessments within the APAL project:

- **Baseline case** = benchmark case with methods, models and set of parameters to be investigated by all partners (mandatory)

- **Base case TH data set** = new conservative transient (in the meaning to be conservative for the safety assessment) for transient T2 from the ICAS project (among others, accumulator tank was newly included into the TH model), named now APAL-ICAS T2, this is the reference transient
- **Best estimate TH data set** = transient results from Task 2.3 **"**best estimate solution**"** is a solution of TH calculations for the APAL transient with all input parameters (both plant parameters and model parameters, as well as human-factor parameters) set to their best estimate values if they are available. (Otherwise, the conservative value is applied.)
- **Base line assessment** = basic assessment considering base case TH loading for structural assessment, RPV location of interest at core weld below cold leg with safety injection
- **Statistical TH data sets** = set of all transients with randomly sampled input TH parameters (i.e., coming from Wilks method) resulting from task 2.3. They were evaluated in Task 3.5 (margin assessment related to TH uncertainties)
- **Long term operation (LTO) improvements** = set of transients concerning NPP improvements (potentially beneficial for PTS) for long term operation resulting from Task 2.1, which were assessed in Tasks 3.4 and 4.4 (margin assessment related to LTO improvement)
- **ART** = adjusted reference temperature (from indirect or direct measurement), this is the name chosen for the index of the K_{Ic} curve (RT_{NDT} concept, indirect) as well as for the index from the Master Curve (direct measurement of T_0 + margin = RT_0).
- **max. all. ART =** This is the (calculated from PTS fracture mechanics safety assessment) value being shifted in order to find the highest index fulfilling the limit condition (tangent or WPS). The max. all. ART can be either max. all. RT_{NDT} or max. all. T_0, depending on the adopted concept (RT_{NDT} or Master Curve)
- **margin** (in…against … between … and …due to ...) = the term "margin" alone does not mean anything, the relation leading to a margin must be always specified. Specifically, in the APAL project the definition of the margin is given by: margin in maximum allowable reference temperature (max. all. ART) against RPV failure (situation leading to crack initiation or non-arresting crack), this is given by the comparison (difference) of maximum allowable ARTs between situation A and situation B due to the change of a given parameter.
- **Inherent margin** = Unquantifiable positive bias in results of some method, calculation, assessment, measurement, etc.
- **RPV failure** = within the APAL project, this is the name of the situation obtained if a postulated crack could initiate under given combination of loading and aging (mandatory task, penalizing) and if the propagating crack cannot stop or growths up to some given proportion of RPV thickness (e.g. 75%) under given combination of loading and aging (aging is non-mandatory task), i.e. RPV failure = crack initiation and growth up to 75% of the RPV wall thickness
- **Limit condition** (or limit state): WPS or tangent approach; initiation or unstable (non-arresting) crack growth (or too deep crack, i.e., plastic collapse).

1.2 Alignment/interface between WP3 and WP4

Within APAL, WP3 and WP4 have a strong interaction as the deterministic and probabilistic benchmark definition are both based on the same technical basis and inputs from structural assessment (i.e. stress and temperature fields) are identical.

Both benchmarks have common input data that are treated deterministically and use the same methods, like

- RPV geometry
- Material properties (mechanical and physical)
- Residual stresses
- Stresses from PTS transient
- SIF solution

- Limit conditions (tangent approach, WPS)

Another common approach is the location of postulated flaw. In both benchmarks a single flaw is assessed located at a position of interest (e.g. core weld elevation inside cold plume).

Within the probabilistic fracture mechanics benchmark some input data were treated as distributed parameters. Starting from sampling exercises, and beginning with only fracture toughness as distributed parameter, the level of complexity of the probabilistic assessment was increased during the benchmark performance and due to type of probabilistic margin assessment (see [5]). Concerning the determination of max. all. ART within the probabilistic margin assessment, a connection to the deterministic assessment was ensured, as the appropriate quantiles (i.e. pre-defined lower bounds) of the fracture toughness (and crack arrest curves) distribution were used in the deterministic assessment:

- Fracture toughness:
  - RT_{NDT} concept: Use ASME K_{IC} curve as Mean – 2x Standard deviation (i.e. 2.5% lower bound) for the deterministic benchmark
  - Master Curve (T_0) concept: Use 5% lower bound of crack initiation distribution for the deterministic benchmark
- Crack Arrest:
  - RT_{NDT} concept: Use ASME crack arrest curve as Mean – 2x Standard deviation (i.e. 2.5% lower bound) for the deterministic benchmark
  - Master Curve (T_0) concept: Use 5% lower bound of crack arrest distribution for the deterministic benchmark

In addition, the quantification of impact of TH uncertainties was done based on both approaches, although it is more related to a full probabilistic assessment. The impact of the TH uncertainties on stress and temperature fields was determined by assessing all of the Wilks data sets (see [5]). As the goal of APAL was to determine the impact of TH uncertainties on a margin, it was out of scope to derive a stress and temperature uncertainty due to TH input data variation. The APAL approach within WP2 was to determine lower bound TH data sets by Wilks analysis and compare it with base case TH data set. But it turned out, that the identification of the most conservative TH data set requires the full chain of PTS analysis up to final fracture mechanics for margin assessment. Therefore, the assessment of all TH data sets from Wilks analysis was required in both, deterministic and probabilistic margin assessment.

As the structural assessment is a common basis for both, deterministic and probabilistic benchmark, the corresponding chapter will be part of both public summary reports.

2 Structural assessment (Task 3.1 + Task 4.1)

In Tasks 3.1 and 4.1 "*Structural assessment*" [1], [5] the structural calculations for the determination of temperature, strains and stresses in the RPV wall are carried out for the selected transient (base case), for the selected LTO improvements (task 3.1), and for TH uncertainties (task 4.1). As the structural assessment is a common basis for both, deterministic and probabilistic benchmark, the corresponding chapter is part of both public summary reports.

To have a better understanding of the results, sensitivity cases were also generated. To have more knowledge not only about the TH data influence but also about the geometric effects, the 1D, 2D and 3D models were created. One of the most sensitive parts of the RPV from the point of the PTS integrity assessment are the welds. The chosen reactor pressure vessel contains two circumferential welds in the beltline region, namely the core weld and the flange weld. The core weld is relatively far away from the conical part of the RPV, close to the RPV nozzles, so it is not notably affected by the difference in the geometry, however the conical part can have a significant effect on the flange weld stress. Thus, the comparison of the two welds is also important. In these calculations cold leg and ambient (outside plume) positions were investigated as the circumferential angle. The effect of the cladding thickness was also investigated as it can vary during the manufacturing of the RPV. Another investigated case was related to the used size of time steps of the TH data. The results of the TH calculations were available up to 10 000 s of the transient, where the time step was 1 s or 4 s depending on the partner. For 1D simulations, a small-time step does not cause a major problem, but it greatly increases the run time of a 3D simulation, so the effect of the time step size and simplification of the data was also checked. Other effects investigated were the uniformity of the TH data and the mesh density.

The following work was performed:

- Numerical (e.g., Finite Elements) calculations to determine the temperature and stress distributions in the RPV wall for the subsequent fracture-mechanics assessment
- Evaluation of temperature and stress distributions through the RPV wall, in the location(s) of the postulated flaws as specified in the benchmark definition
- Determination of temperature and stress distributions for the sensitivity cases.

2.1 Input data

2.1.1 RPV geometry

The investigated reactor was a four-loop, 1300 MWe PWR of the type built by Siemens/KWU, such as the PWR at Grafenrheinfeld. In the near-core region, the proposed four-loop RPV has the following dimensions:

- internal diameter of 4870 mm in the downcomer,
- wall thickness of 243 mm in the base/weld material and
- 6 mm cladding thickness.

Details of the relevant RPV geometry (core region and nozzles) are shown in Figure 2.1.

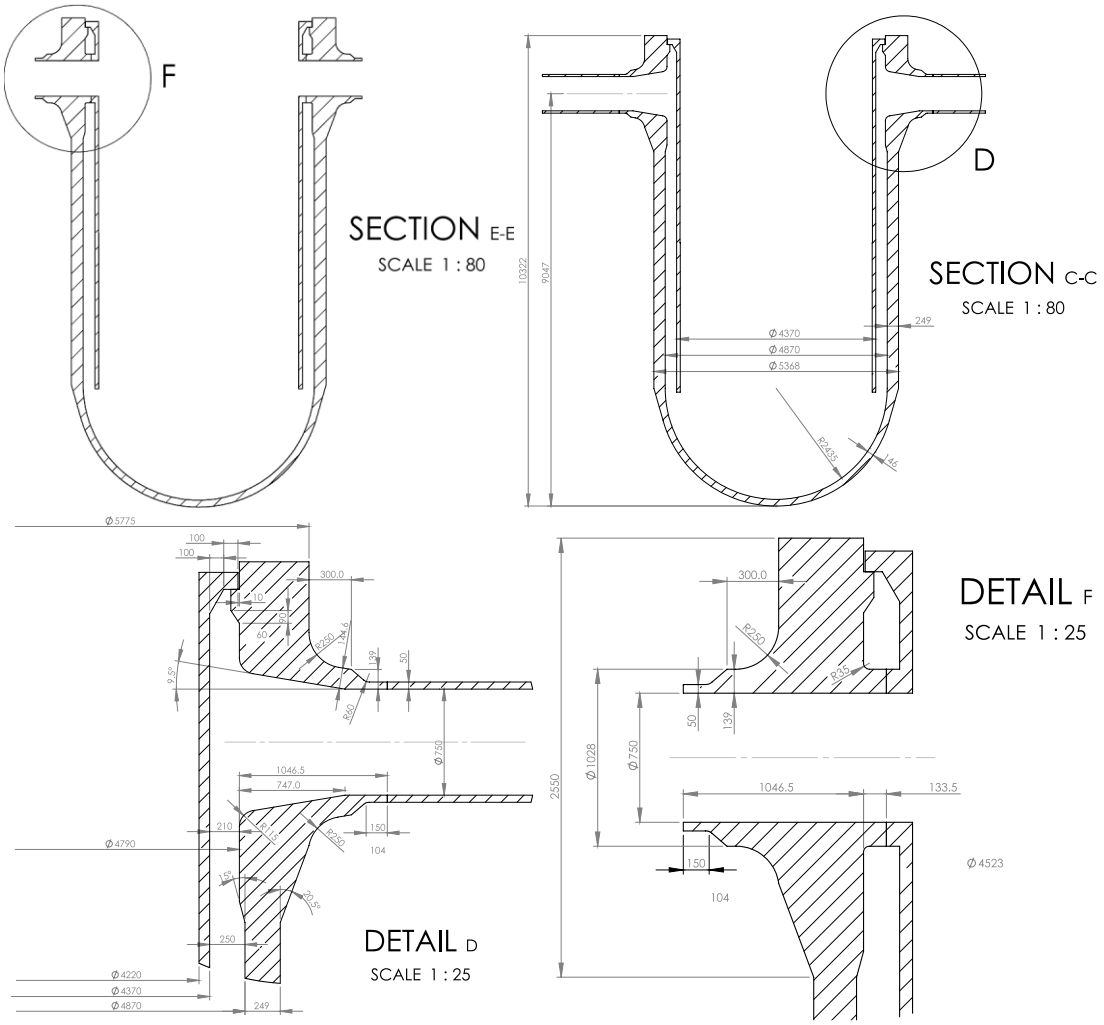

Figure 2.1: Geometry of the KWU reactor pressure vessel and its nozzles

2.1.2 Material Properties

The base material is assumed to be ferritic steel 22NiMoCr37, and the material number of the austenitic stainless steel cladding is 1.4551. For the simulations the linear-elastic material model was applied. In this case for the mechanical properties the knowledge of the Young's modulus and the Poisson's ratio is sufficient. The density of the base/weld metal and the cladding was set as 7800 kg/m^3.

Furthermore, the relevant temperature dependent material properties of the RPV are presented in Table 2.1 and

Table 2.2.

Table 2.1: Material properties of the base metal (22NiMoCr37) and the weld metal

T [°C]	20 (T_m)	100	200	300	350
E [MPa]	206000	199000	190000	181000	172000
ν [-]	0.3	0.3	0.3	0.3	0.3
λ [W/(m·K)]	44.4	44.4	43.2	41.8	39.4
C_p [J/(g·K)]	0.45	0.49	0.52	0.56	0.61
α [10^{-6}/K]	10.3	11.1	12.1	12.9	13.5

Table 2.2: Material properties of the austenitic cladding

T [°C]	20 (T_m)	100	200	300	400
E [MPa]	200000	194000	186000	179000	172000
ν [-]	0.3	0.3	0.3	0.3	0.3
λ [W/(m·K)]	16	16	17	17	18
C_p [J/(g·K)]	0.5	0.5	0.54	0.54	0.59
α [10^{-6}/K]	15	16	17	19	21

In the tables, the reference temperature for thermal expansion T_m is 20°C (the temperature, from which is defined the thermal expansion for establishing the mean thermal expansion coefficient α), however for the consideration of stress-free state in cladding with initial transient temperature (291.042°C), the temperature has to be changed in some cases as the thermal expansion coefficient depends on it.

2.1.3 Boundary conditions

The following boundary conditions were applied for the simulations:

- Thermal inside:
  - Liquid temperature (from TH analysis)
  - HTC (from TH analysis)
- Thermal outside:
  - Adiabatic or
  - $HTC = 1$ W/m^2 K and $T_{outside} = 40$°C
- Mechanical:
  - Inner pressure at the cladding wet surface (from TH analysis)
  - Outer pressure: $p_{outside} = 0$ MPa
  - End cap pressure for axial stress applied to end cross-section of a RPV model
  - Fixed displacement at the other side of the RPV

The stress-free state in RPV is set at initial transient temperature (291.042°C). For the consideration of stress-free state in RPV at initial transient temperature (291.042°C), a conversion of thermal expansion coefficient α could be required depending on the used code.

2.2 Sensitivity analyses

2.2.1 TH input from RELAP

The input data for the benchmark task were received from WP2, where for the generation of thermal hydraulic (TH) data the RELAP5 code was applied. However, due to the geometric limitation of a 1D FEM structural analysis it had to be simplified. Therefore, so called 0D/1D/2D simulation TH data were generated. Here the denotation 0D/1D/2D is related to the TH data simplification and has no relationship to the 1D/2D/3D symbols related to the FEM model for structural analyses. Table 2.3 contains the RELAP5 data cases with their explanations.

Table 2.3: RELAP5 TH data variations

Number of Case	Description of the Case	Evaluation of RELAP5 data	
		Elevation (height)	Azimuth (circumference)
Case 1	0D – average	average	average
Case 2	1D – core weld	2638 mm (V05)	average
Case 3	2D – core weld/cold plume	2638 mm (V05)	202.5° (A-095 below HP injection)
Case 4	2D – core weld/ambient	2638 mm (V05)	337.5° (A-098 ambient)
Case 5	1D – flange weld	1130 mm* (V03)	Average
Case 6	2D – flange weld/cold plume	1130 mm* (V03)	202.5° (A-095 below HP injection)
Case 7	2D – flange weld/ambient	1130 mm* (V03)	337.5° (A-098 ambient)

* the flange weld elevation is 1350 mm, however, the RELAP5 nodalisation has only evaluated 1130mm

The elevation and azimuth values in the RPV give the position in the downcomer from where the TH data were obtained for the structural analysis. As it can be seen from Figure 2.3, RELAP5 "divides" the downcomer height into 11 parts (named as V01 to V11 as stated in Table 2.5, where the elevations are given in the middle of these volumes). Along the circumference the downcomer is divided into 8 parts (named as DC channels 091-098), where the azimuthal angle (as it is shown in Table 2.4) is given in the middle of these parts. For every cell (in total 11x8 cells), temperature and HTC distributions were generated which are time dependent. Therefore, the 0D/1D/2D cases mean the following:

- 0D simulation: In the whole geometry the TH inputs were averaged and are time dependent.
- 1D simulations: at the given elevation (2638 mm or 1130 mm) the TH input data were averaged along the circumference and are time dependent.
- 2D simulations: the TH inputs were from a specific position of the downcomer (V05 and DC channel 095; V05 and DC channel 098; V03 and DC channel 095; V03 and DC channel 098)

Table 2.4: Azimuthal positions of inlet/outlet nozzles

Nozzle	No of DC channel in R5 model	Azimuthal angle
CL1	A-091	22.5°
HL1	A-092	67.5°
HL2	A-093	112.5°
CL2	A-094	157.5°
CL3	A-095	202.5°
HL3	A-096	247.5°
HL4	A-097	292.5°
CL4	A-098	337.5°

Table 2.5: Elevation of DC volumes

Volume	Elevation [m]
V01	+0.5725
V02	0.0
V03	-1.13
V04	-2.083
V05	-2.638
V06	-3.3215
V07	-3.9745
V08	-4.6275
V09	-5.2809
V10	-5.9335
V11	-6.5155

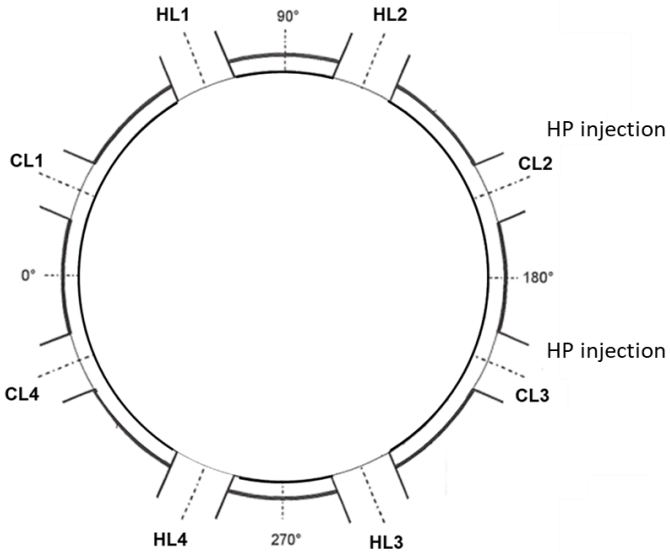

Figure 2.2: Azimuthal position of hot and cold legs

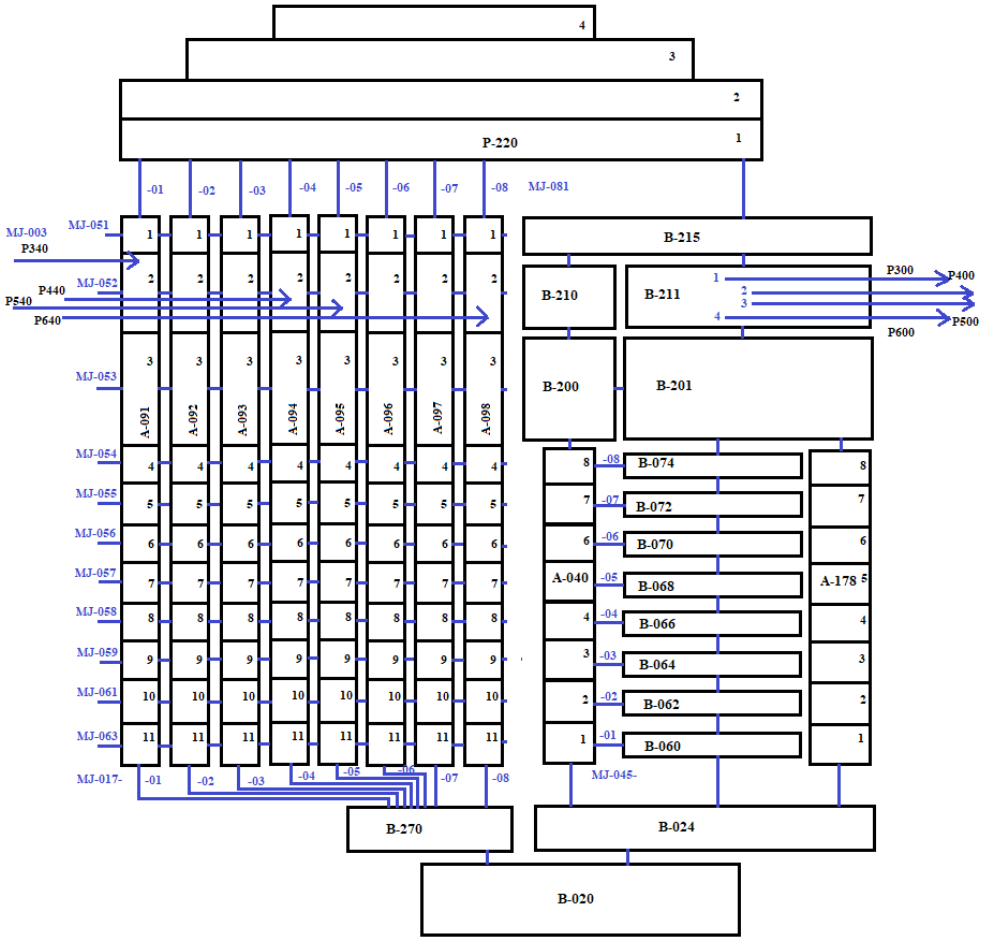

Figure 2.3: RELAP5 Nodalization of reactor

The aim was to compare the averaging effects and to select the appropriate TH data for flange and core welds. The seven cases were therefore compared where the values were generated from the averaging of the results of all the partners. The most relevant position for comparing the results is the position of the crack tip, this was chosen to be in the depth of 16 mm from the inner surface, therefore

Figure 2.4 shows the temperature distribution as a function of time, while Figure 2.5 illustrates the stress profiles at this value for the 7 cases.

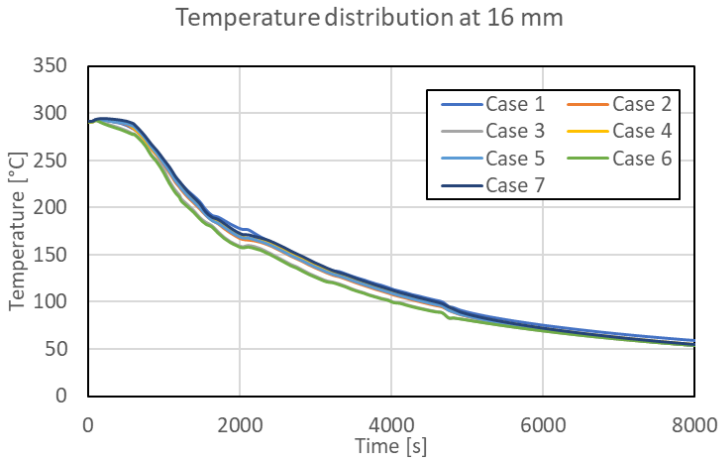

Figure 2.4: Comparison of temperature time evolution for the 7 cases

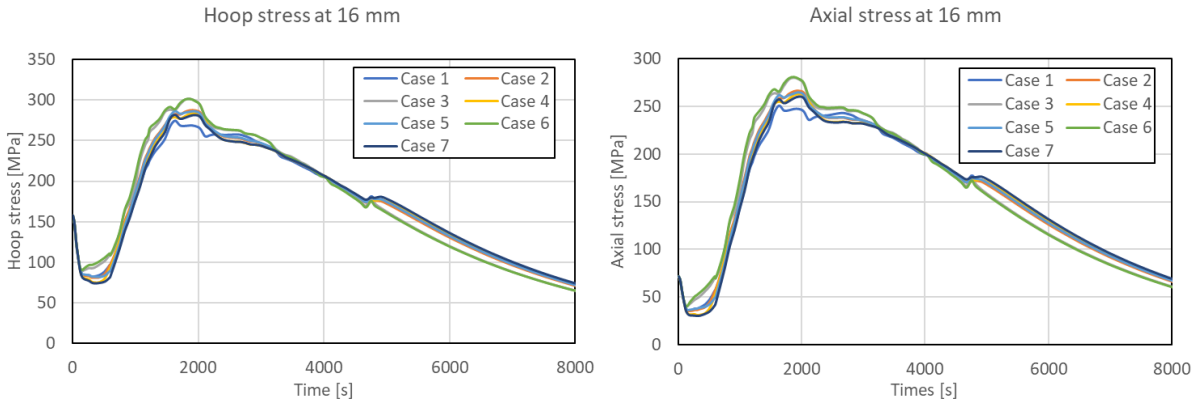

Figure 2.5: Comparison of stress profiles for the 7 cases

From these curves, it is difficult to determine which case gives the most conservative results, so the differences at the predefined time steps were also compared, which are shown in MPa and in percentages in Figure 2.6, where the comparison was based on Case 3 and therefore its values are zero.

16 mm (crack tip)	T [°C] t=6 s	T [°C] t=30 s	T [°C] t=300 s	T [°C] t=600 s	T [°C] t=1200 s	T [°C] t=2400 s	T [°C] t=3600 s	T [°C] t=4800 s	T [°C] t= 6000 s	T t=6 s	T t=30 s	T t=300 s	T t=600 s	T t=1200 s	T t=2400 s	T t=3600 s	T t=4800 s	T t= 6000 s
Case1	291.0246	290.9865	291.0717	283.0639	227.4962	163.4227	124.0889	94.29672	75.30929	0.00%	0.00%	1.24%	1.66%	6.34%	7.67%	11.90%	13.69%	8.09%
Case2	291.0243	290.9927	291.4319	283.1341	221.5777	159.2739	118.3109	89.47096	70.61129	0.00%	0.00%	1.36%	1.68%	3.58%	4.94%	6.69%	7.87%	1.35%
Case3	291.0361	290.9845	287.5198	278.4552	213.9295	151.7742	110.8964	82.9418	69.67016	0.00%	0.00%	0.00%	0.00%	0.00%	0.00%	0.00%	0.00%	0.00%
Case4	291.0249	291.0525	293.2582	284.9182	224.9799	162.678	121.2822	92.4583	71.75906	0.00%	0.02%	2.00%	2.32%	5.17%	7.18%	9.37%	11.47%	3.00%
Case5	291.0192	290.9871	291.0518	285.6972	222.9435	159.9724	119.2041	89.65766	70.58362	-0.01%	0.00%	1.23%	2.60%	4.21%	5.40%	7.49%	8.10%	1.31%
Case6	291.0315	290.9794	286.3009	278.1714	211.3127	150.1316	109.9942	83.03464	69.19745	0.00%	0.00%	-0.42%	-0.10%	-1.22%	-1.08%	-0.81%	0.11%	-0.68%
Case7	291.0197	291.0484	293.6068	288.4346	227.5466	164.217	122.7935	92.78156	71.89132	-0.01%	0.02%	2.12%	3.58%	6.37%	8.20%	10.73%	11.86%	3.19%

16 mm (crack tip)	Hoop stress [MPa] t=6 s	Hoop stress [MPa] t=30 s	Hoop stress [MPa] t=300 s	Hoop stress [MPa] t=600 s	Hoop stress [MPa] t=1200 s	Hoop stress [MPa] t=2400 s	Hoop stress [MPa] t=3600 s	Hoop stress [MPa] t=4800 s	Hoop stress [MPa] t=6000 s	Hoop stress t=6 s	Hoop stress t=30 s	Hoop stress t=300 s	Hoop stress] t=600 s	Hoop stress t=1200 s	Hoop stress t=2400 s	Hoop stress t=3600 s	Hoop stress t=4800 s	Hoop stress t=6000 s
Case1	157.0024	146.0549	82.13977	96.8638	220.588	257.451	220.8348	178.9129	132.431	-0.18%	-1.21%	-11.68%	-10.84%	-12.19%	-2.46%	-2.07%	2.64%	9.93%
Case2	157.3789	147.9731	81.27159	97.14193	235.7219	255.5607	223.1331	176.0638	130.7793	0.06%	0.09%	-12.61%	-10.59%	-6.16%	-3.18%	-1.05%	1.00%	8.56%
Case3	157.292	147.8386	92.99978	108.6439	251.2081	263.9491	225.5073	174.3122	120.4667	0.00%	0.00%	0.00%	0.00%	0.00%	0.00%	0.00%	0.00%	0.00%
Case4	157.3784	147.7765	75.81684	92.94787	228.4437	251.2199	222.4994	175.7758	133.8294	0.05%	-0.04%	-18.48%	-14.45%	-9.06%	-4.82%	-1.33%	0.84%	11.09%
Case5	157.3789	147.9727	82.41297	89.05106	233.3767	255.862	222.9251	177.9154	132.1585	0.06%	0.09%	-11.38%	-18.03%	-7.10%	-3.06%	-1.15%	2.07%	9.71%
Case6	157.3795	148.0361	96.7818	108.9777	256.8088	264.8204	224.1822	170.977	119.6174	0.06%	0.13%	4.07%	0.31%	2.23%	0.33%	-0.59%	-1.91%	-0.70%
Case7	157.3784	147.7714	74.79291	82.08695	223.8555	251.0138	222.5577	179.0935	135.9854	0.05%	-0.05%	-19.58%	-24.44%	-10.89%	-4.90%	-1.31%	2.74%	12.88%

16 mm (crack tip)	Axial stress [MPa] t=6 s	Axial stress [MPa] t=30 s	Axial stress [MPa] t=300 s	Axial stress [MPa] t=600 s	Axial stress [MPa] t=1200 s	Axial stress [MPa] t=2400 s	Axial stress [MPa] t=3600 s	Axial stress [MPa] t=4800 s	Axial stress [MPa] t=6000 s	Axial stress t=6 s	Axial stress t=30 s	Axial stress t=300 s	Axial stress t=600 s	Axial stress t=1200 s	Axial stress t=2400 s	Axial stress t=3600 s	Axial stress t=4800 s	Axial stress t=6000 s
Case1	71.37985	66.47135	37.57105	57.43013	191.7026	240.7786	212.8636	175.4427	128.0677	-0.22%	-1.27%	-22.34%	-17.12%	-13.90%	-2.69%	-2.23%	2.63%	10.36%
Case2	71.56521	67.3502	36.57778	57.74446	207.0251	238.9794	215.2879	172.7048	126.4278	0.04%	0.03%	-24.39%	-16.67%	-7.02%	-3.42%	-1.11%	1.03%	8.95%
Case3	71.53604	67.3276	48.37658	69.29703	222.6589	247.4465	217.7105	170.9406	116.0406	0.00%	0.00%	0.00%	0.00%	0.00%	0.00%	0.00%	0.00%	0.00%
Case4	71.56463	67.16033	31.09879	53.53791	199.6984	234.6072	214.6472	172.4039	129.4882	0.04%	-0.25%	-35.72%	-22.74%	-10.31%	-5.19%	-1.41%	0.86%	11.59%
Case5	71.56524	67.34988	37.72331	49.60236	204.6727	239.289	215.0924	174.5636	127.8128	0.04%	0.03%	-22.02%	-28.42%	-8.08%	-3.30%	-1.20%	2.12%	10.14%
Case6	71.56578	67.41356	52.1566	69.58723	228.2818	248.3164	216.3701	167.5776	115.1932	0.04%	0.13%	7.81%	0.42%	2.53%	0.35%	-0.62%	-1.97%	-0.73%
Case7	71.56457	67.14756	30.06696	42.62489	195.0737	234.3907	214.6956	175.7414	131.6603	0.04%	-0.27%	-37.85%	-38.49%	-12.39%	-5.28%	-1.38%	2.81%	13.46%

Figure 2.6: Percentage and absolute differences in 7 cases compared to Case 3

The comparisons show that lower values of temperature are only observed in Case 6, where the circumferential angle is the same, but the elevation is higher (flange weld). For this reason, higher values are observed for the circumferential and axial stresses in Case 6. The difference between Case 3 (202.5°) and Case 4 (337.5°) is the circumferential position, from where the TH data are taken. As can be seen from the table, Case 3 shows higher stress values and therefore Cases 4 and Case 7 (ambient) have been excluded from the future simulations.

2.2.2 Comparison between the partners' results

As described in the previous section, Case 3 was chosen as the focus of Task 3.1, and the comparison of the partners' results is presented for this case.

The software or in-house codes used by the partners for the simulations were FAVOR, PROST, ABAQUS, ANSYS, MSC.Marc Mentat, Pre-PASCAL, SIF-Master, Systus and Verload.

Comparison of partners' results for temperatures, hoop and axial stresses as a function of time for the crack tip position is shown in Figure 2.7 to Figure 2.9. From the diagrams it can be seen that the final differences between the results of the partners are less than 5% compared to the previously introduced reference curve. The only exception is a 2D axisymmetric model which was done additionally to 1D model. The core weld is relatively far away from the conical part close to the RPV nozzles, therefore it only has minor effect on resulting stresses. According to other calculations, the conical part has a much more significant effect on the flange weld stress, see section 2.2.4.1

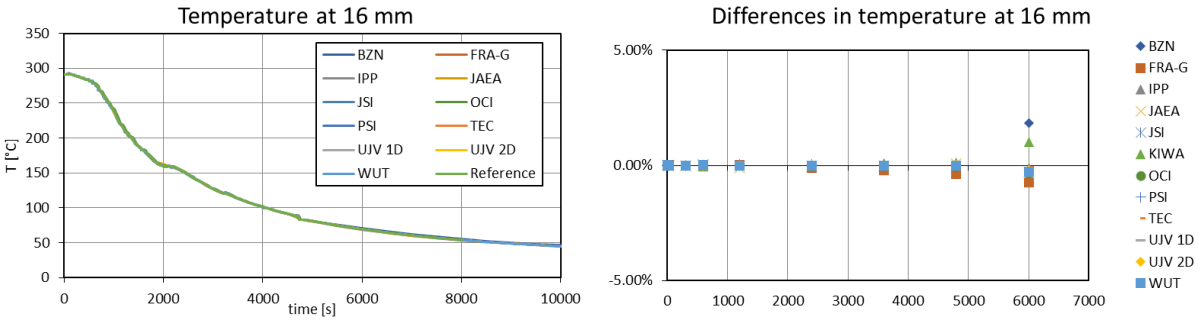

Figure 2.7: Comparison of partners' results of temperature as a function of time (Case 3)

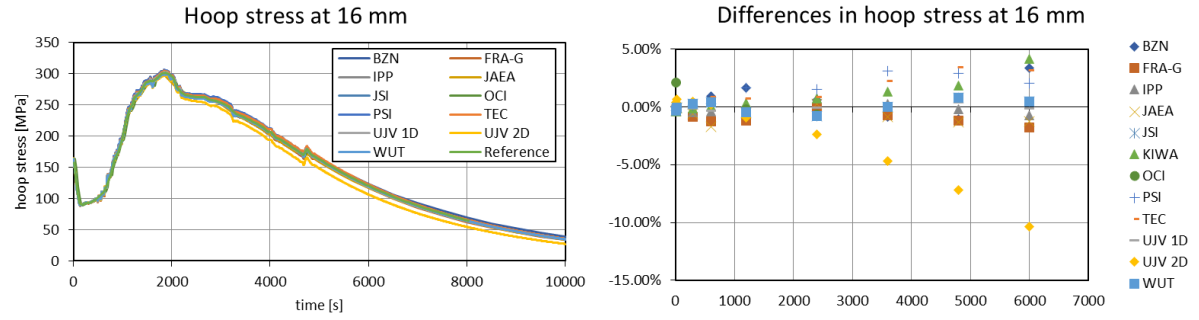

Figure 2.8: Comparison of partners' results of hoop stress as a function of time (Case 3)

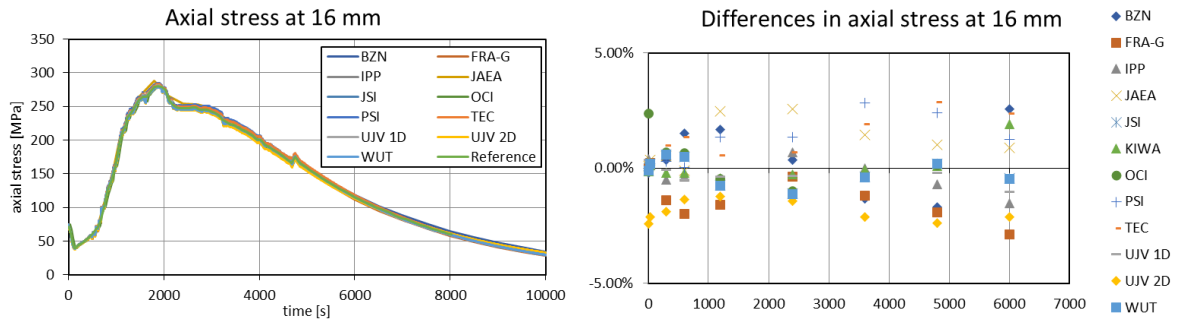

Figure 2.9: Comparison of partners' results of axial stress as a function of time (Case 3)

2.2.3 3D Simulations

Beside the 1D simulations of RPV 3D calculations were also generated by different partners. In the followings the models created by them, the boundary conditions used and some of the results are briefly introduced.

All of the following results were taken out from the core weld (2638 mm) and cold leg (202.5°) positions.

The first comparison was done with the same RELAP TH input data used by all partners. The comparisons of temperature and hoop stress distribution as function of time at the crack tip are shown in Figure 2.10.

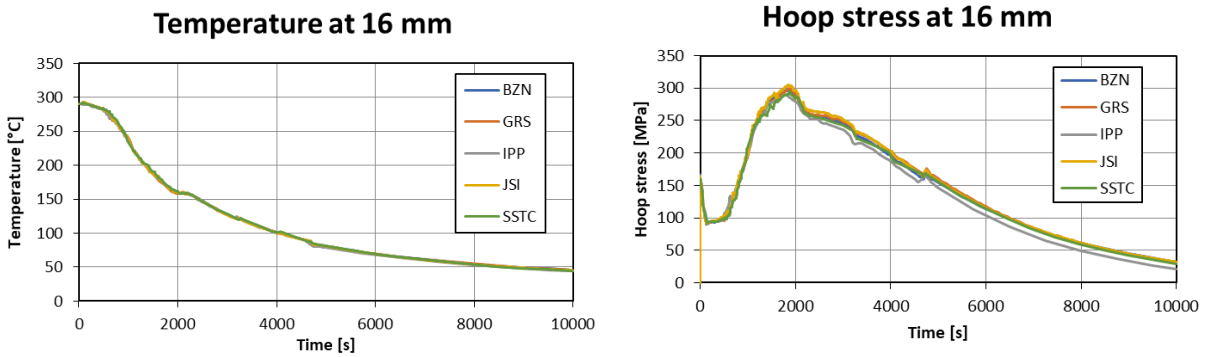

Figure 2.10: Temperature [°C] and hoop stress [MPa] distribution as a function of time for the same TH input data

The second comparison was done with the base case simulation versions of the partners. Here three types of TH data were used RELAP, KWU-MIX and TRACE. The comparisons of temperature and hoop stress distributions as function of time at the crack tip are shown in Figure 2.11. Even in case of the temperature large differences can be seen, which resulted of the different TH data. It has to be noted that in case of the TRACE results this large difference is due to the linear extrapolation of the results from the wall thickness of 26 mm and 46.5 mm as there were no other nodes between 6 mm and 26 mm. This should therefore be taken into account when interpreting the curve. Also in case of the KWU-MIX data the cold plume was also considered, therefore the data are taken from 180° where the coldest wall temperatures occur at the elevation of the core weld (2638 mm), which is the position of the merging cold plumes. In the case of the other TH data this analysed circumferential angle position was 202.5° (in-plume position).

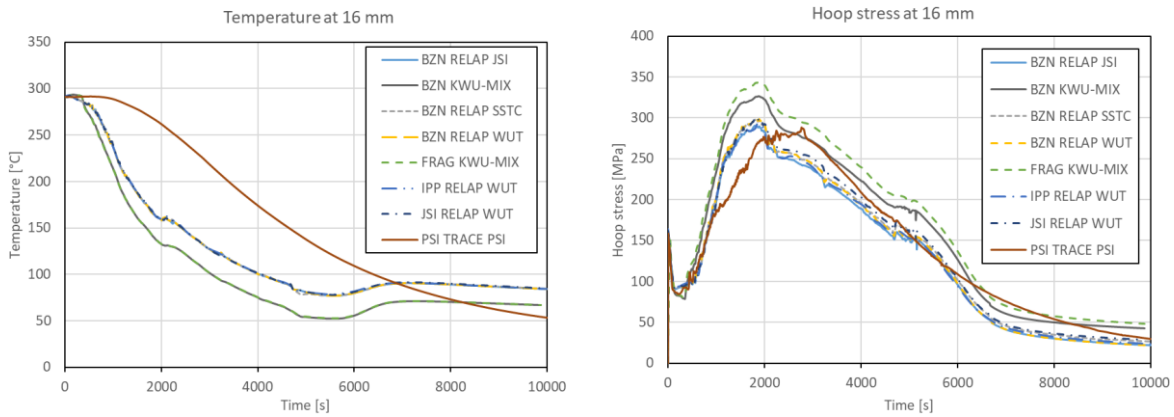

Figure 2.11: Temperature [°C] and hoop stress [MPa] distribution as a function of time with different TH input data

2.2.4 Other locations

2.2.4.1 Flange weld location

As mentioned previously, besides the investigation of the core weld the flange weld was also considered. The core weld is located at the elevation of 2638 mm where the thickness of the reactor pressure vessel wall is uniform. The flange weld is located at the elevation of 1350 mm which is already very close to the nozzle area. Furthermore, the thickness of the vessel starts increasing above the flange weld, which can influence the stress distribution in the location of the flange weld.

Several partners investigated the effect of the flange weld location with either 1D or 3D FE method and with either input from a system code (e.g. RELAP) or from a system code in combination with a mixing code. All the investigations showed the same trend, but with different quantities. The impact of flange weld location is illustratively shown in Figure 2.12 and Figure 2.13 (results considering RELAP input at relevant locations). The results for the flange weld location from 3D FE with input from RELAP in combination with mixing code are given in section 8.1.

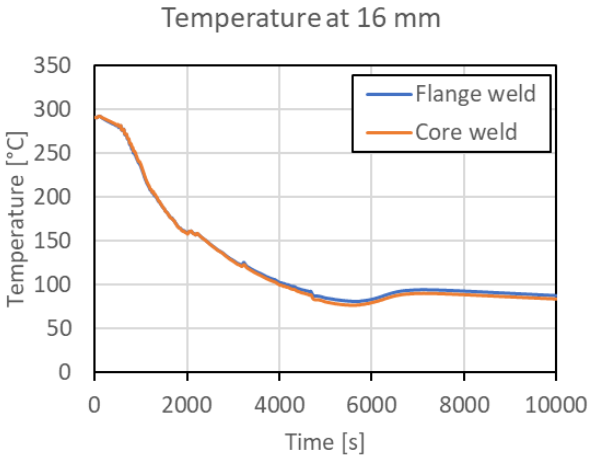

Figure 2.12: Temperature variation at crack tip of the RPV wall for the core weld and the flange weld below the cold leg

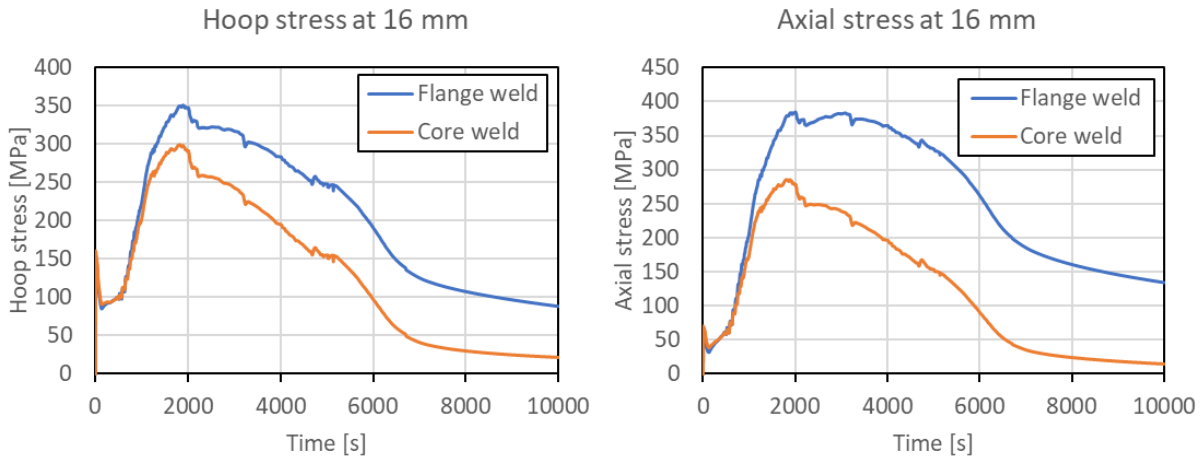

Figure 2.13: Hoop stress and axial stress variation at crack tip of the RPV wall for the core weld and the flange weld below the cold leg

2.2.4.2 Outside cold plume location

The location outside plume was chosen to be below CL4 at the azimuth 337.5° (far away from the cold injection legs CL2 and CL3), see section 2.2.1. Several partners investigated the effect of the outside plume location with either 1D or 3D FE method and with input either from a system code (e.g. RELAP) or from a system code in combination with a mixing code.

The results and the comparison with inside plume location showed, that temperatures below the CL2 and CL3 nozzles (volumes 094-05 and 095-05) where the ECC water is injected and the plume is formed, are lower than the temperatures below other nozzles during most of the transient. As expected, this yields higher stresses in the two cold plume locations than in the other locations. Results for outside plume location and comparison with inside plume location can be made by considering the results provided in section 8.1.1 and 8.1.3.

Figure 2.14 shows the comparison between 3D (ABAQUS) and 1D (FAVOR) results at the core and flange weld elevations, and both at the outside plume location below CL4 centreline and with the addition of the ABAQUS results for the alternative outside plume location below HL2. The results at the core weld elevation are presented in Figure 2.14-right, where it is shown that while the inner-surface temperatures of the 2 outside plume locations are practically identical, the stresses below HL2 are slightly lower than below CL4, the latter very well reproduced by FAVOR. Figure 2.14-left presents the results at the two outside plume locations, but at the flange weld elevation. While the temperatures are also very much the same, we can see again some discrepancy on the stresses. As concluded in D3.1 [1], FAVOR clearly delivers lower stresses at the flange weld since the 1D approximation cannot account for close proximity of the thicker part of the RPV and nozzles. The ABAQUS hoop stresses below HL2 are again lower than below CL4, however, the axial stresses are practically the same as can be seen in the figure inset.

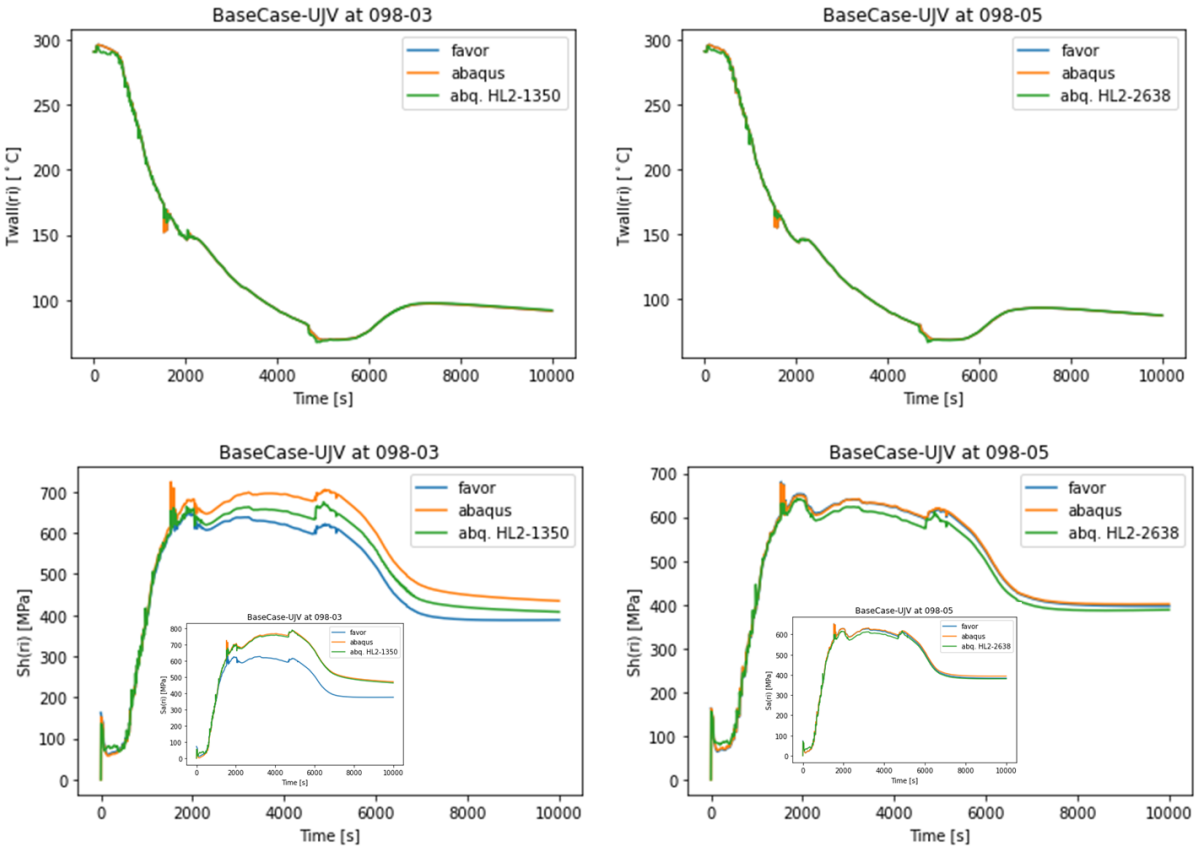

Figure 2.14: RPV inner-surface temperatures (top), hoop (bottom) and axial (bottom-inset) stresses at the core weld (right) and flange weld (left) elevations, both at the outside plume location below CL4 (favor and abaqus) and below HL2 (abq. HL2)

2.2.4.3 Nozzle corner

Stress and temperature fields for the nozzle corner (cold leg) have only been calculated with 3D FE. Results for nozzle corner location and comparison with inside plume location at core weld can be made by considering the results provided in section 8.1.1 and 8.1.4.

2.2.5 Mesh refinement

Several partners investigated the effect of mesh refinement. Different variants of mesh refinement in combination with linear or quadratic elements were selected and analysed. Details about all results from all partners are given in [1].

Illustratively the results on mesh refinement in case of the 3D simulation are presented, where the FE models listed in Table 2.6 were used. Two types of global model were created, one with linear elements where the full model was made and one with quadratic elements where only half of the reactor pressure vessel was modelled. Thereafter from the first version refined local models were also generated where the number of elements were increased as shown in the table.

Table 2.6: Properties of the investigated mesh types

Name	Model version	Order of refinement	Elements in the cladding	Elements in the base metal
Mesh 1	Linear model	Linear (full model)	3	10
Mesh 2		Linear (local model)	3	38
Mesh 3		Linear (Local model)	6	76
Mesh 4	Quadratic model	Quadratic (half model)	3	10

The temperature distribution for all 4 mesh versions were in excellent agreement, however in case of the hoop and axial stress small deviations could be noted as it is also illustrated in Figure 2.15 and Figure 2.16.

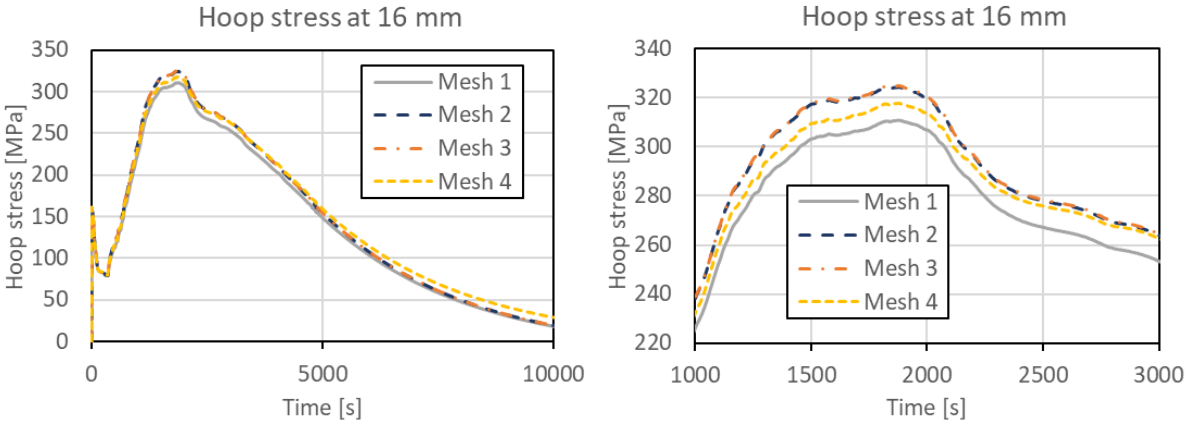

Figure 2.15: Influence of the mesh refinement on the hoop stress

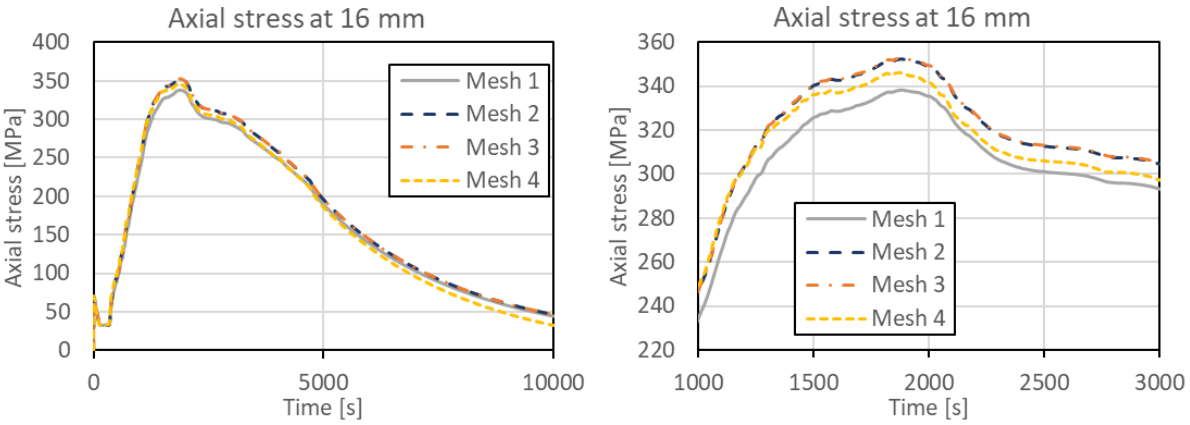

Figure 2.16: Influence of the mesh refinement on the axial stress

2.2.6 Time steps

The effect of the size of the time steps was investigated to see how the simplification of longer timesteps could be applied. The input data – results of TH calculations - had a duration of 10 000 s, where the time step was 1 s. This is not a major problem for 1D simulations, but the runtime of a 3D simulation would be too long, so input data simplification was considered. For both 1D and 3D simulations, we used the Case3 presented earlier. For the 1D simulation, 4 different time steps were considered: 1 s, 2 s, 5 s and 10 s. With these values the number of time steps can be reduced from 10000 to 5000, 2000 and 1000. Figure 2.17 and Figure 2.18 shows the difference between solution with 2 s, 5 s and 10 s time steps and solution with 1 s time steps of the hoop stress at the inner surface of the RPV and at the crack tip location (16 mm). This shows that the result obtained with 10 s time step is higher/lower than that one with 1 s time step by more than 20 MPa. This results in a relative difference of about 5%. The results obtained with the 2 s time step are in fairly good agreement with the original version, but the number of time steps seems to be too large in this case too.

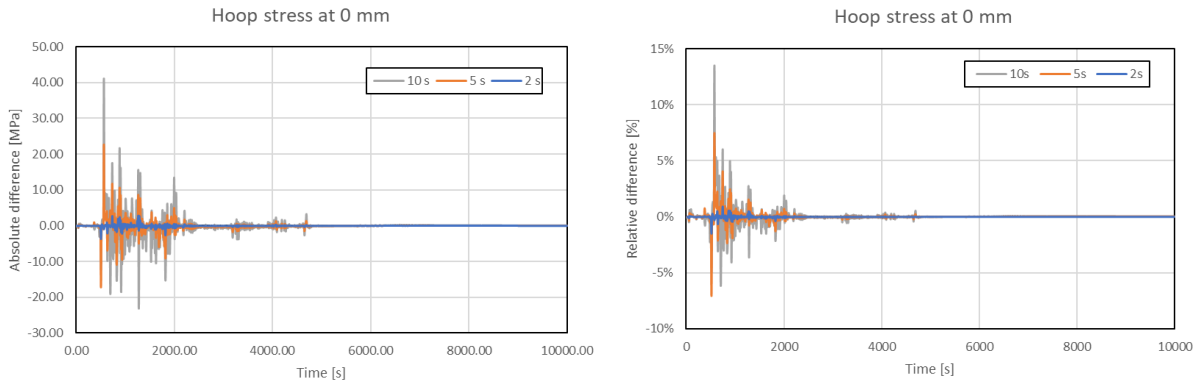

Figure 2.17: Absolute and relative difference of the hoop stress as a function of time step at the inner surface of the RPV

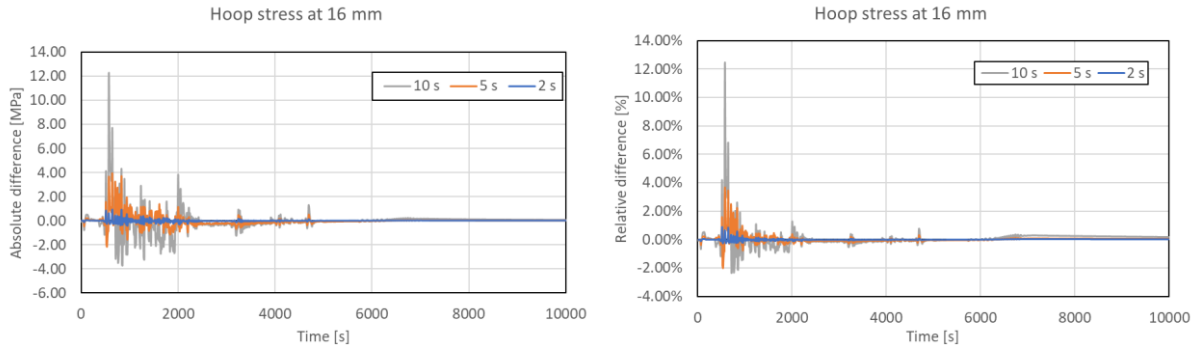

Figure 2.18: Absolute and relative difference of the hoop stress as a function of time step at the crack tip (16 mm)

2.3 LTO improvements

In WP2 nine types of long-term operation improvements and human actions were simulated which are listed in Table 2.7. The thermohydraulic simulations for the LTO improvements of Task 2.1 were performed with different system codes and mixing codes, namely ATHLET (including submodule ECC-MIX), RELAP5, TRACE and KWU-MIX. Further information is given in D2.1 [9].

Table 2.7: Investigated LTO improvements and human factors

Index Code	Naming in table	
1	LTO1	Heating of water in the HPIS tanks (T = 45°C)
2	LTO2	Heating of water in the ACCs (T = 50°C)
3	LTO3	Heating of water in the LPIS tanks (T = 45°C)
4	LTO4	Decreasing the HPSI head (75%)
5	LTO5	Decreasing the HPSI capacity (75%)
6	LTO6	Reduction of HPIS flow (operator action) at 1800 s
7	LTO7	Decreasing of ACC pressure (20 bar)
8	LTO8	Change of cooldown rate (operator action) to 200 K/h
9	LTO9	Isolation of ACCs (operator action) at 500 s

2.3.1 Results from 1D FE

For every LTO improvement included in **Table 2.7** 1D simulations were performed by different partners. In every 1D simulation the TH data were generated the same way as in Case 3 (see Table 2.3). In the following subsections the results from one partner are shown for exemplarily. More details about all results are given in [1].

2.3.1.1 LTO1 – Heating of water in the HPIS tanks (T = 45°C)

In case of the TH data the heating of water in HPIS tanks was simulated by increasing the injection temperature from the reference value of 15 °C to the LTO value of 45 °C. The calculations showed that the increased injection temperature results in a higher water temperature in the DC during the whole transient. The proposed LTO development until the ACCs start (about 2790 s) has an impact on the break flow and fluid levels. Therefore, it was preliminarily concluded in WP2, based on the TH results only, that the LTO improvement could potentially be beneficial for PTS.

The obtained hoop stress and temperature and the comparison with the base case result to see the impact of LTO improvement No. 1 are shown in Figure 2.19 (TH input from RELAP) and in Figure 2.20 (TH input from TRACE). The structural analysis results confirmed the expectations from TH calculations on beneficial effect of LTO improvement No. 1.

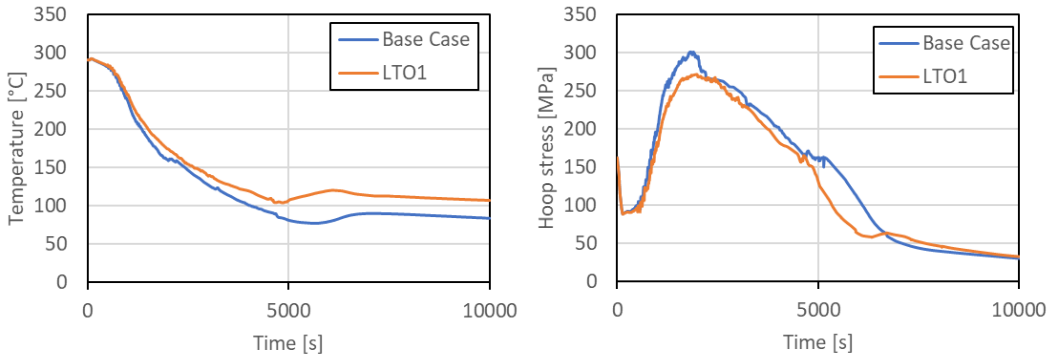

Figure 2.19: LTO1 results of JAEA interpolated to the 16 mm of RPV wall thickness, with RELAP (WUT) TH input data

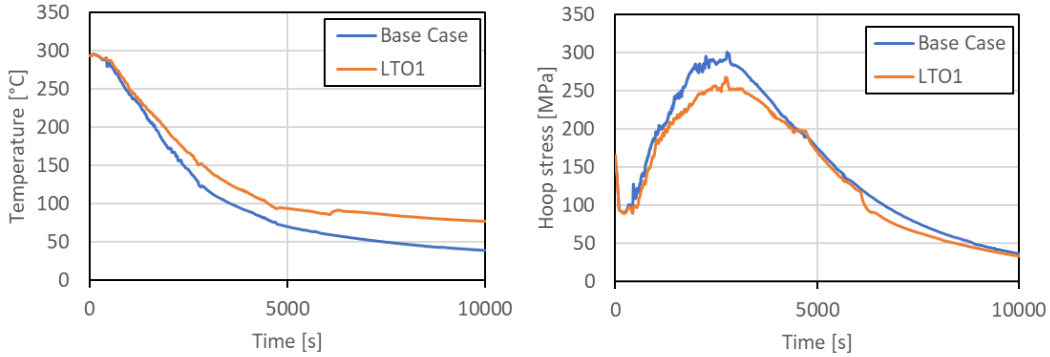

Figure 2.20: LTO1 results of TEC interpolated to the 16 mm of RPV wall thickness, with TRACE (PSI) TH input data

2.3.1.2 LTO2 – Heating of water in the ACCs (T = 50°C)

In case of the thermal hydraulic calculations the heating of water in the accumulator tanks (ACCs) was simulated by increasing the water injection temperature from the reference value of 20 °C to 50°C. The LTO improvement resulted in slightly higher temperature in the DC after the beginning of the flow

from ACCs. Therefore, from TH analyses in WP2 it was preliminarily concluded that this LTO improvement provides no significant benefit from a PTS perspective.

The obtained hoop stress and temperature and the comparison with base case result to see the impact of LTO improvement No. 2 are shown in Figure 2.21 (TH input from RELAP), in Figure 2.22 (TH input from TRACE) and in Figure 2.23 (TH input from ECC-MIX, plotted only up to 6000 sec.).

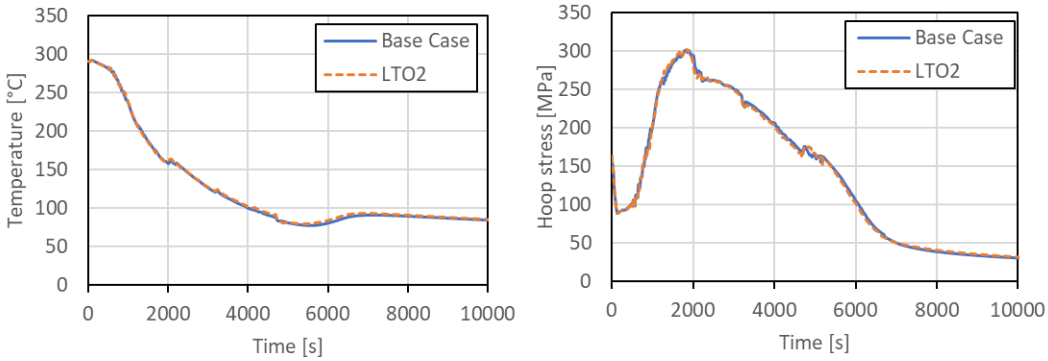

Figure 2.21: LTO2 results of JSI interpolated to the 16 mm of RPV wall thickness, with RELAP (WUT) TH input data

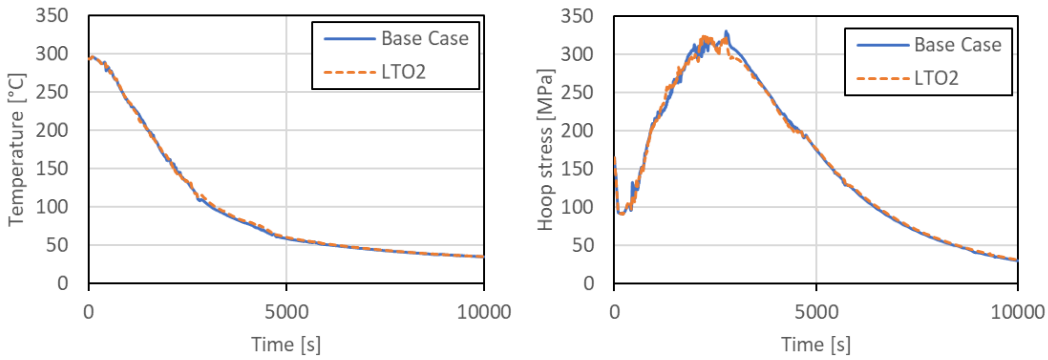

Figure 2.22: LTO2 results of PSI interpolated to the 16 mm of RPV wall thickness, with TRACE (PSI) TH input data

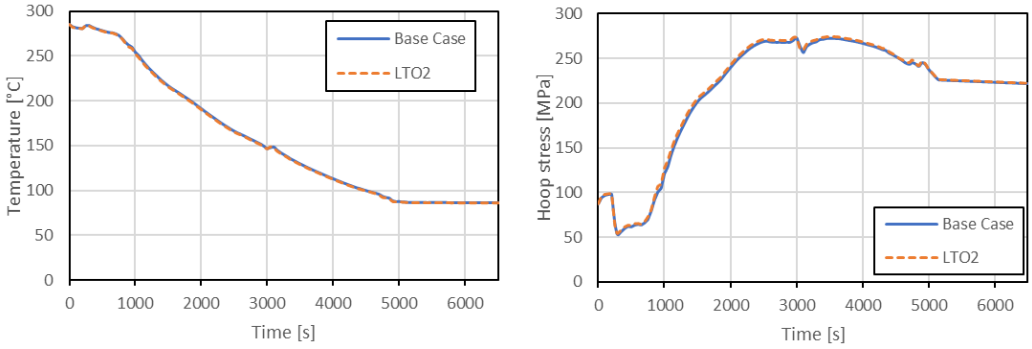

Figure 2.23: LTO2 results of GRS interpolated to the 16 mm of RPV wall thickness, with ECC-MIX (GRS) TH input data

2.3.1.3 LTO3 – Heating of water in the LPIS tanks (T = 45°C)

The heating of water in the LPI tanks was simulated by increasing the injection temperature from the reference value of 15 °C to 45 °C. The RELAP calculations showed that there is insignificant impact on the water level and water temperature in the DC till the end of the transient. Similarly to this, in case of the TRACE simulations, for this particular transient, heating of LPI had only a very small benefit. Therefore, the studied LTO improvement will probably not provide benefit from a PTS perspective.

The obtained hoop stress and temperature and the comparison with the base case result to see the impact of LTO improvement No. 3 are shown in Figure 2.24 (TH input from RELAP) and in Figure 2.25 (TH input from KWU-MIX).

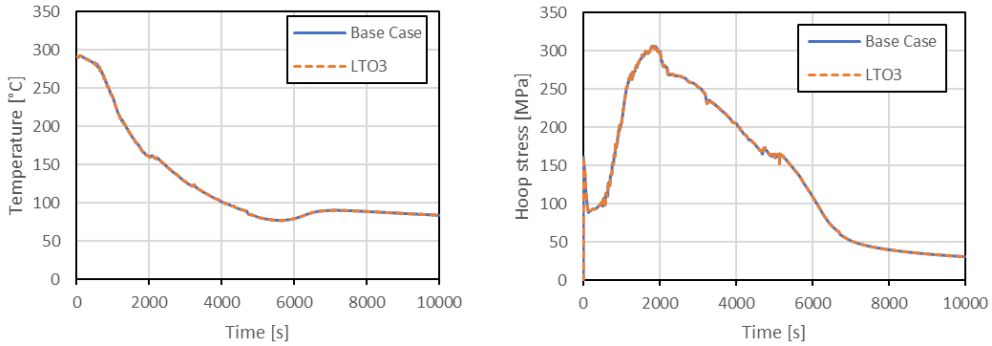

Figure 2.24: LTO3 results of BZN at the 16 mm of RPV wall thickness, with RELAP (WUT) TH input data

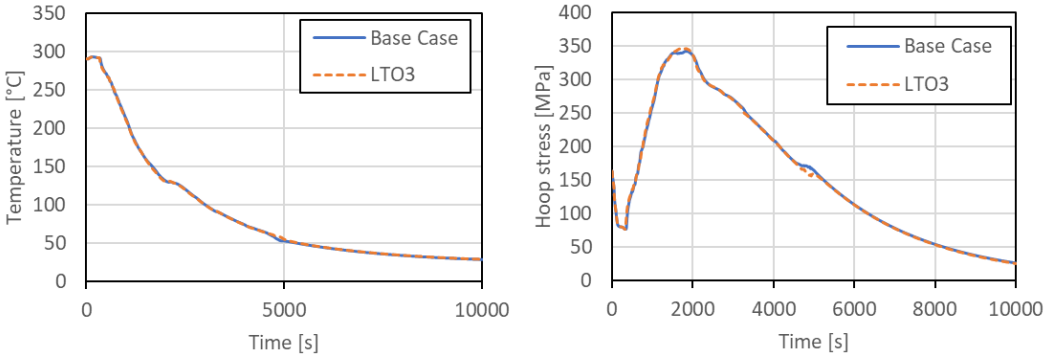

Figure 2.25: LTO3 results of IPP at 16 mm of RPV wall thickness, with KWU-MIX (FRA-G) TH input data

2.3.1.4 LTO4 – Decreasing the HPSI head (75%)

The decreasing of the HPI pump head was simulated by scaling the pressure component of the HPI pump curve down to 75% of its reference value.

The obtained hoop stress and temperature and the comparison with the base case result to see the impact of LTO improvement No. 4 are shown in Figure 2.26 (TH input from RELAP) and in Figure 2.27 (TH input from ECC-MIX).

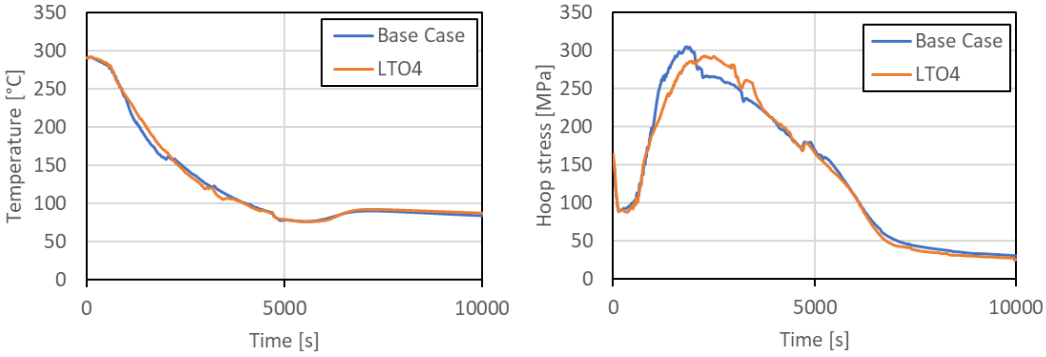

Figure 2.26: LTO4 results of KIWA at 16 mm of RPV wall thickness, with RELAP (SSTC) TH input data

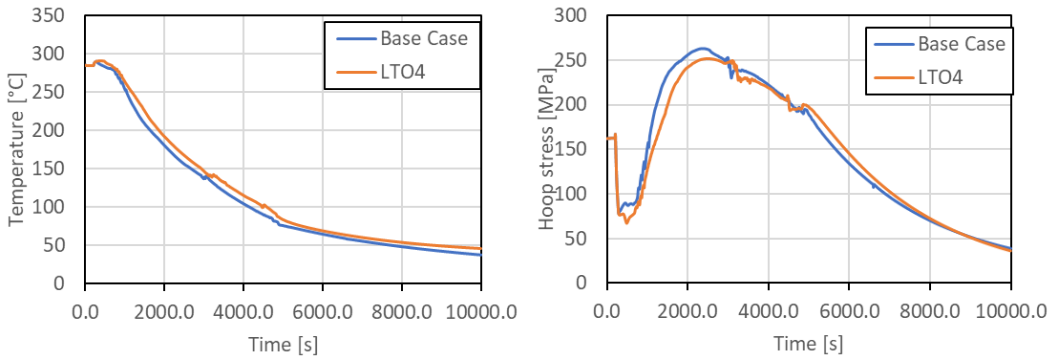

Figure 2.27: LTO4 results of TEC interpolated to the 16 mm of RPV wall thickness, with ECC-MIX (GRS) TH input data

2.3.1.5 LTO5 – Decreasing the HPSI capacity (75%)

The decreasing of the HPI pump capacity was simulated via scaling of the flow component of the HPI pump curve down to 75%. From the TH simulations it was concluded that by decreasing the rate of cooling (via HPI pumps) the coolant temperatures can be reduced to some extent as well. Based on the results the TH experts in WP2 assumed that the analysed LTO improvement may potentially affect the results of RPV integrity analysis. However, they stated that the effect needs to be confirmed using thermo-mechanical and fracture mechanics simulations.

The obtained hoop stress and temperature and the comparison with the base case result to see the impact of LTO improvement No. 5 are shown in Figure 2.28 (TH input from RELAP) and in Figure 2.29 (TH input from TRACE). The structural analyses results confirmed the expectations from the TH calculations that LTO improvement No. 5 has a beneficial effect.

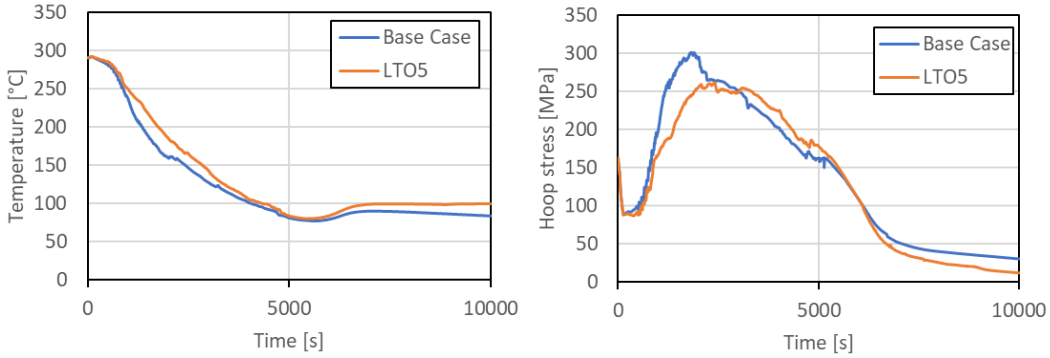

Figure 2.28: LTO5 results of JAEA interpolated to the 16 mm of RPV wall thickness, with RELAP (WUT) TH input data

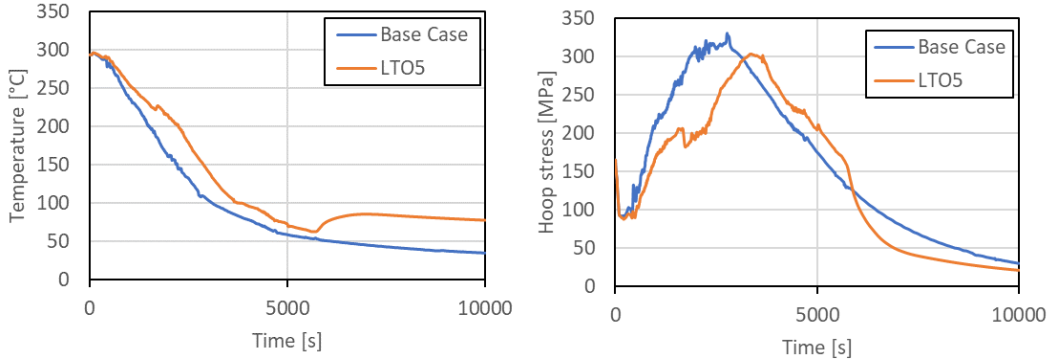

Figure 2.29: LTO5 results of PSI interpolated to the 16 mm of RPV wall thickness, with TRACE (PSI) TH input data

2.3.1.6 LTO6 – Reduction of HPIS flow (operator action) at 1800s

In the TH calculations the reduction of the HPIS flow by the operator was simulated by switching off 1 of 2 HPIS pumps 1800 s after the initiation of the break. The calculations showed that the reduction of HPI injection results in a higher temperature of the water in the DC starting at 1800 s. Additionally, the lower break flow, the lower water level in the DC and the higher void fraction is observed after this operator action. Therefore, in the WP2 it was concluded that this LTO improvement could potentially be beneficial from a PTS perspective.

The obtained hoop stress and temperature and the comparison with the base case result to see the impact of LTO improvement No. 6 are shown in Figure 2.30 (TH input from RELAP) and in Figure 2.31 (TH input from KWU-MIX). The structural analyses results could not fully confirm the expectations from TH calculations on beneficial effect of LTO improvement No. 6, as the global maximum of stress (reached approximately at the time 1800 s – the time of operator action) did not change and the reduction of stress at the late phase of transient is not significant. Therefore, fracture mechanics calculations are necessary for the evaluation of LTO improvement No. 6 effect.

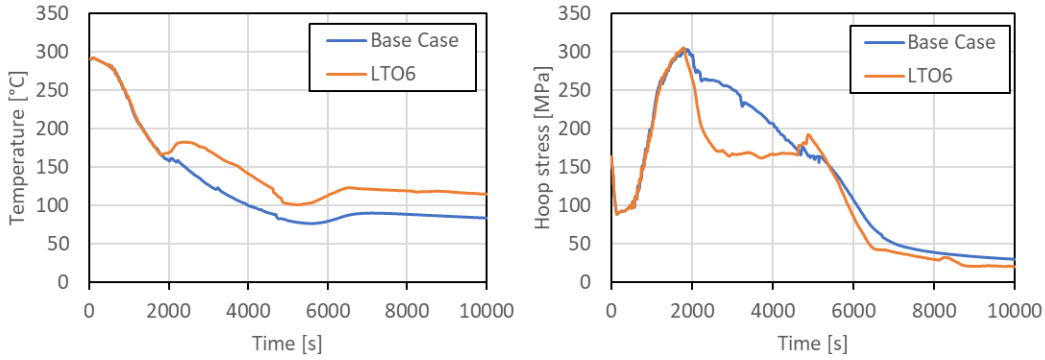

Figure 2.30: LTO6 results of UJV at 16 mm of RPV wall thickness, with RELAP (WUT) TH input data

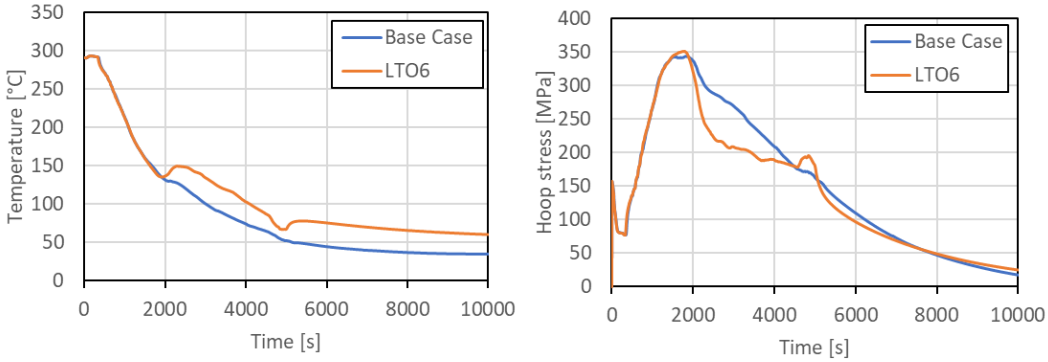

Figure 2.31: LTO6 results of BZN at 16 mm of RPV wall thickness, with KWU-MIX (FRA-G) TH input data in the middle of the plume

2.3.1.7 LTO7 – Decreasing of ACC pressure (20 bar)

In the TH calculations, the LTO improvement of decreasing of ACC pressure was modelled by decreasing the initial pressure opening setpoint in the ACCs from the nominal value of 2.6 MPa to 2 MPa. In case of the RELAP calculations the results showed that the decrease of the ACC pressure slightly increases the water temperature in the DC, however the TH experts in WP2 concluded that the studied LTO improvement provides no significant benefit from a PTS perspective.

The obtained hoop stress and temperature and the comparison with the base case result to see the impact of LTO improvement No. 7 are shown in Figure 2.32 (TH input from RELAP) and in Figure 2.33 (TH input from TRACE).

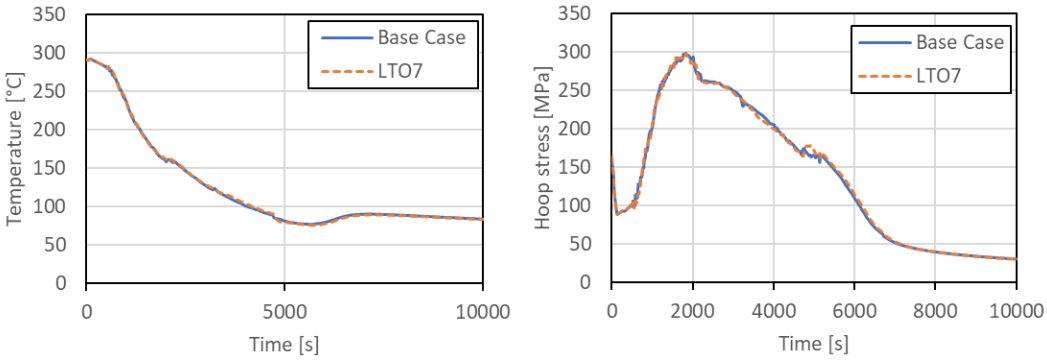

Figure 2.32: LTO7 results of WUT interpolated to the 16 mm of RPV wall thickness, with RELAP (WUT) TH input data

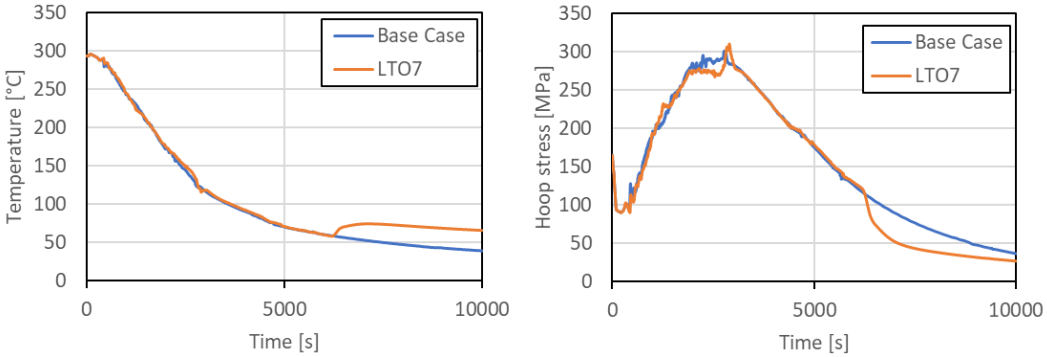

Figure 2.33: LTO7 results of TEC interpolated to the 16 mm of RPV wall thickness, with TRACE (PSI) TH input data

2.3.1.8 LTO8 – Change of cooldown rate (operator action) to 200K/h

During the TH calculation the increase of the secondary side cooldown rate by the operator was simulated by increasing the cooldown of the secondary side from 100 K/h to 200 K/h. The proposed LTO improvement resulted in the increase of the water temperature in the DC after 2000 s. In the D2.1 report it was stated that the studied LTO improvement could potentially be beneficial from a perspective of higher water temperature in DC, but at the same time, it could be detrimental from a perspective of the faster pressure drop in DC. Therefore, it was determined that the overall benefit of this LTO improvement should be verified by the structural analysis.

The obtained hoop stress and temperature and the comparison with base case result to see the impact of LTO improvement No. 8 are shown in Figure 2.34 (TH input from RELAP) and in Figure 2.35 (TH input from KWU-MIX). The structural analyses results could partially confirm the expectations from TH calculations on beneficial effect of LTO improvement No. 8, as the temperature increased, and the global maximum of stress decreased. Nevertheless, based on RELAP TH calculations, the stresses at the late phase of the transient slightly increased. Therefore, fracture mechanics calculations are necessary for evaluation of LTO improvement No. 8 effect.

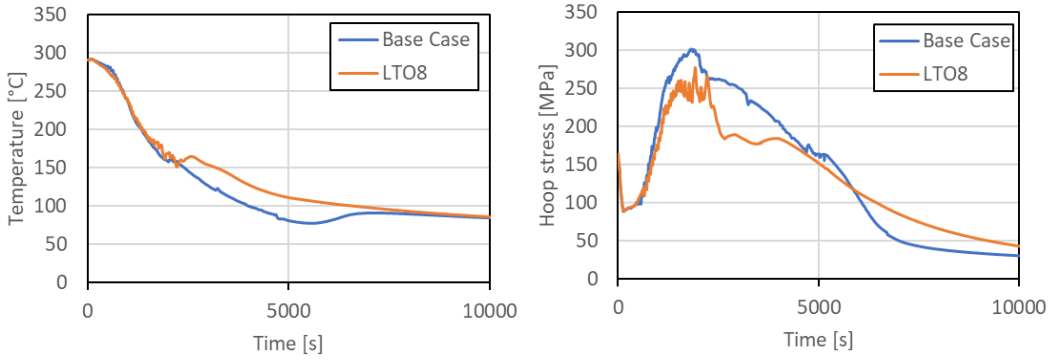

Figure 2.34: LTO8 results of JSI interpolated to the 16 mm of RPV wall thickness, with RELAP (WUT) TH input data

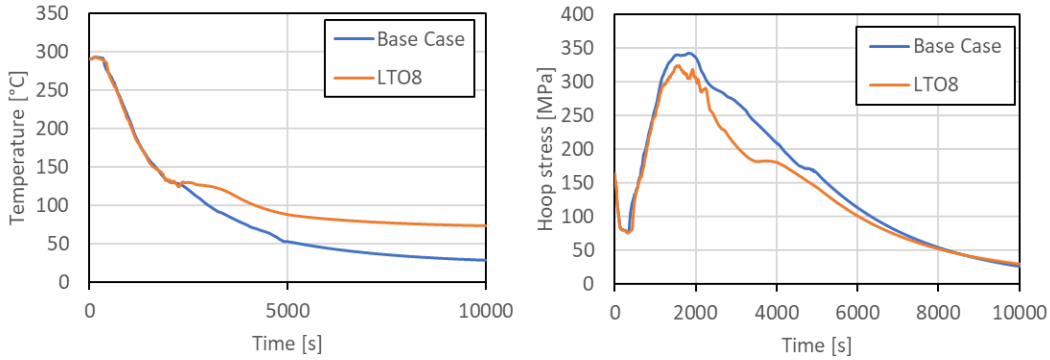

Figure 2.35: LTO8 results of IPP at 16 mm of RPV wall thickness, with KWU-MIX (FRA-G) TH input data

2.3.1.9 LTO9 – Isolation of ACCs (operator action) at 500s

In case of LTO9 the results from the system analysis performed with RELAP5, were repeated with the addition of a time for ACC isolation at 500 s. Because the pressure for this break size does not decrease to 26 bar until after 500 s, the ACCs were isolated before they could inject. In case of the TH calculations, it was concluded that this action has no significant effect.

The obtained hoop stress and temperature and the comparison with the base case result to see the impact of LTO improvement No. 9 are shown in Figure 2.36 (TH input from RELAP)

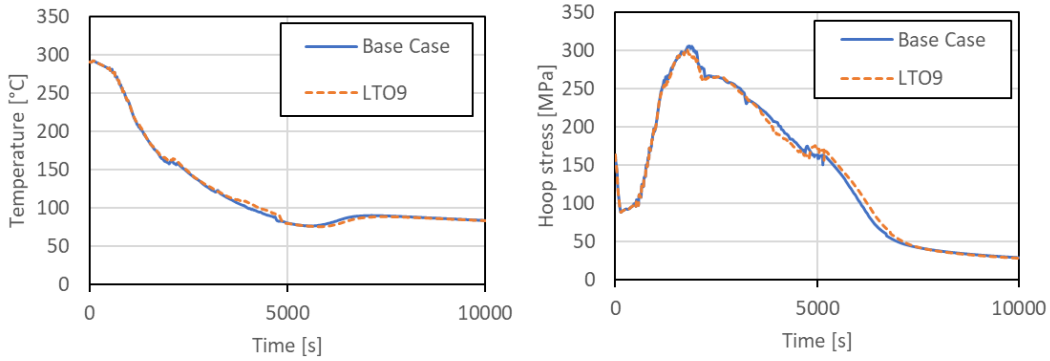

Figure 2.36: LTO9 results of IPP interpolated to the 16 mm of RPV wall thickness, with RELAP (WUT) TH input data

2.3.2 Results from 3D FE

Besides the 1D calculations, 3D simulations were also performed for the LTO cases. In the following subsections, results from 3D simulations are presented for the most important LTO cases (LTO1, LTO4, LTO5, LTO6 and LTO8) and for the other LTO cases can be found in [1]. In general, the results are similar

and show the same trend than those from 1D simulations shown in Section 2.3.1 The stresses and temperature profiles given are for core weld elevation under the cold leg position.

2.3.2.1 LTO1 – Heating of water in the HPIS tanks (T = 45°C)

The results at core weld elevation under the cold leg position from 3D calculations are given in Figure 2.37 (TH input from KWU-MIX), in Figure 2.38 (TH input from RELAP) and in Figure 2.39 (TH input from TRACE).

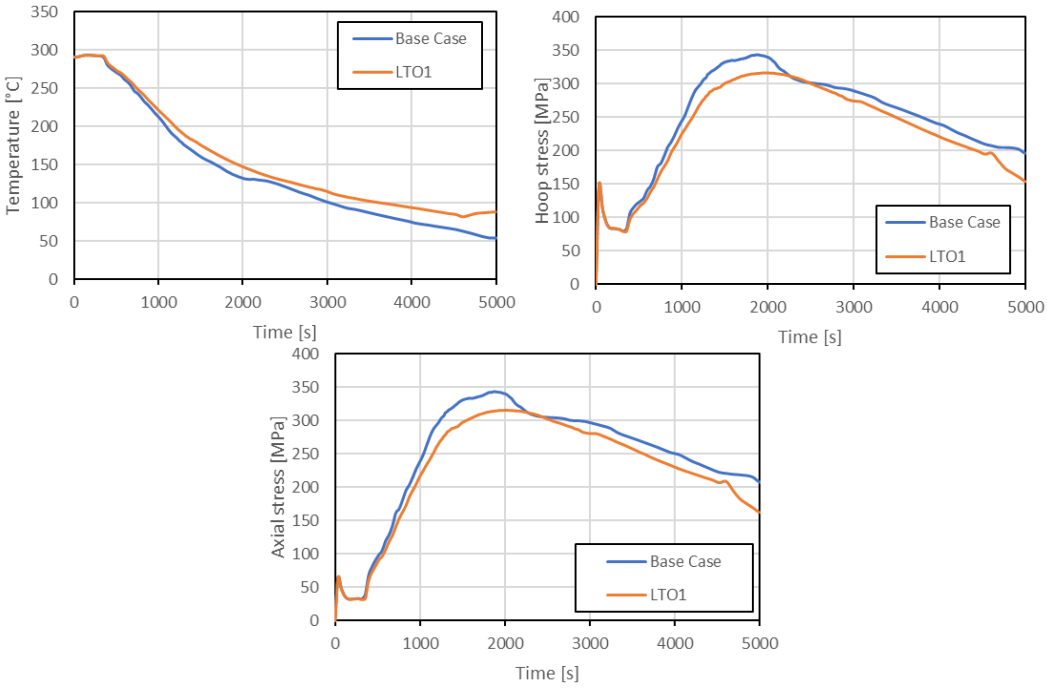

Figure 2.37: LTO1 results of FRA-G at 16 mm of RPV wall thickness, with KWU-MIX (FRA-G) TH input data

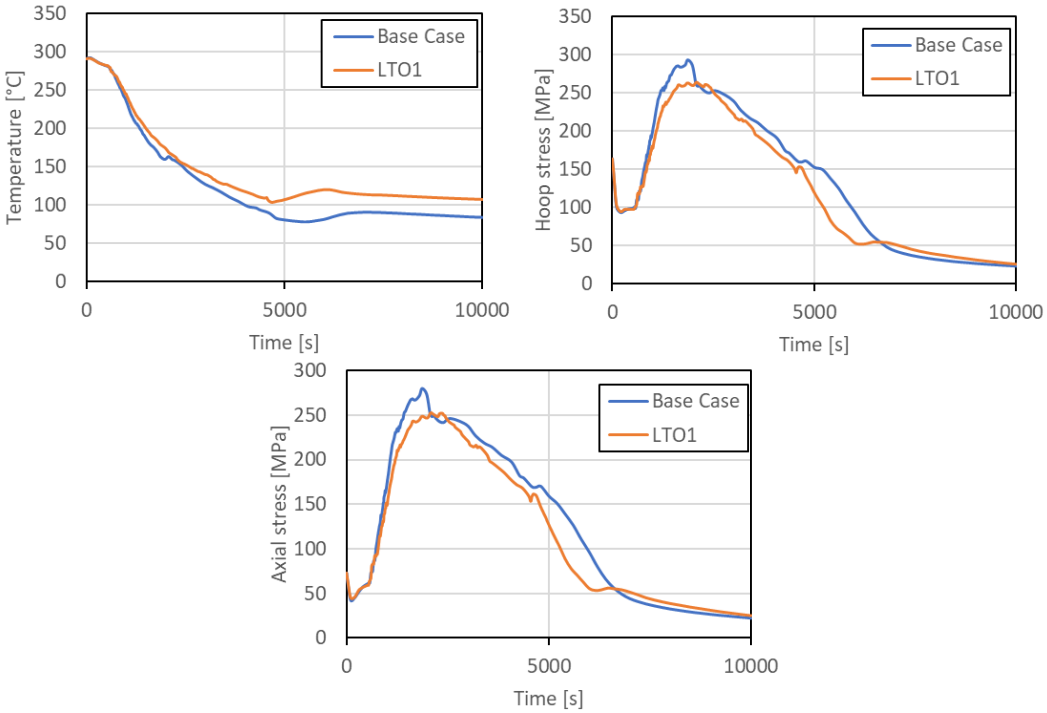

Figure 2.38: LTO1 of IPP at 16 mm of RPV wall thickness, with RELAP (WUT) TH input data.

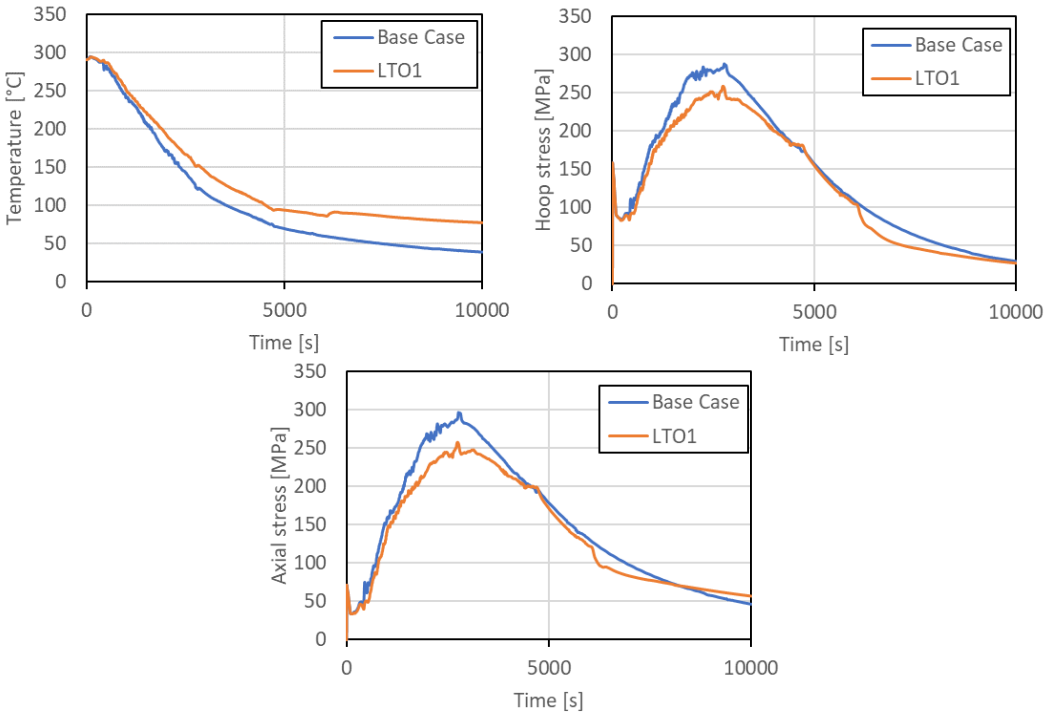

Figure 2.39: LTO1 results of PSI extrapolated to the 16 mm of RPV wall thickness, with TRACE (PSI) TH input data

2.3.2.2 LTO4 – Decreasing the HPSI head (75%)

The results at core weld elevation under the cold leg position from 3D calculations are given in Figure 2.40 (TH input from RELAP) and in Figure 2.41 (TH input from TRACE).

Interestingly in case of the simulations with RELAP input data the resulting temperature and stress fields similarly to the 1D results have some deviation from the base case, however no differences can be noted in case of the simulations done with TRACE input data.

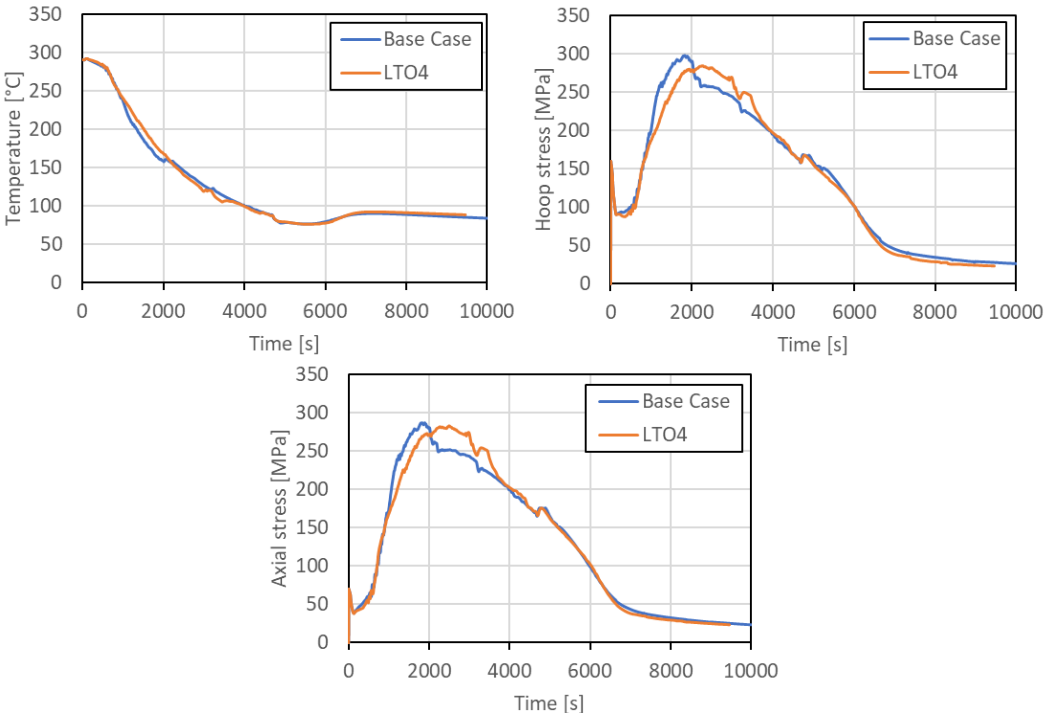

Figure 2.40: LTO4 results of BZN at 16 mm of RPV wall thickness, with RELAP (SSTC) TH input data.

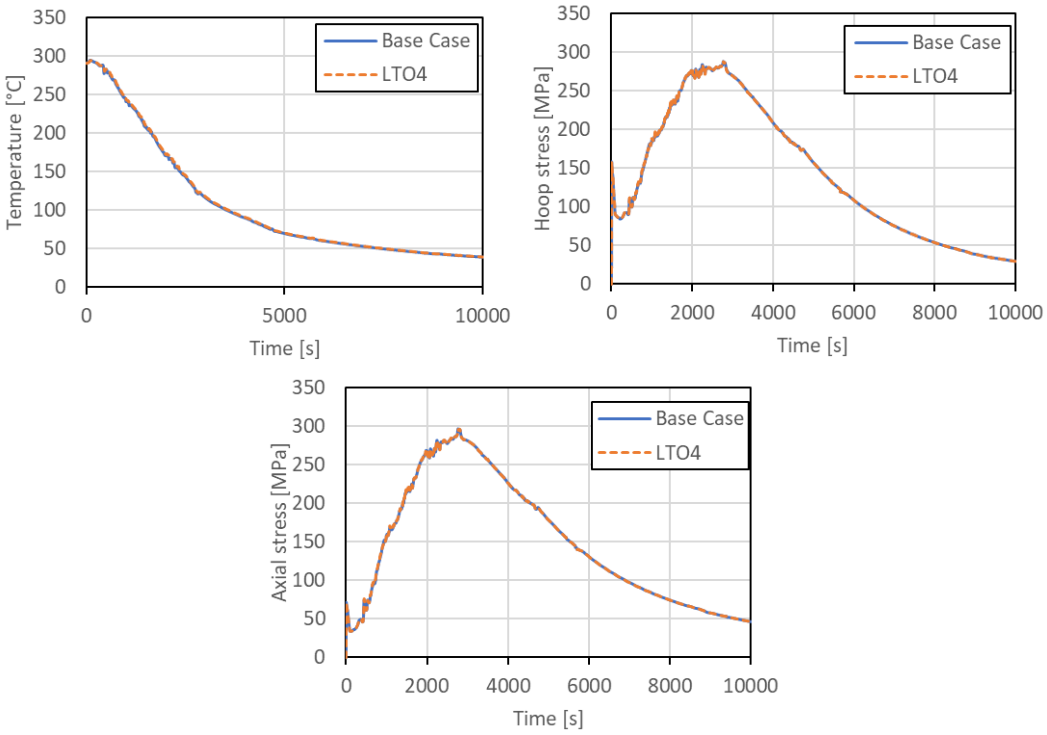

Figure 2.41: LTO4 results of PSI extrapolated to the 16 mm of RPV wall thickness, with TRACE (PSI) TH input data.

2.3.2.3 LTO5 – Decreasing the HPSI capacity (75%)

The results at core weld elevation under the cold leg position from 3D calculations are given in Figure 2.42 (TH input from RELAP).

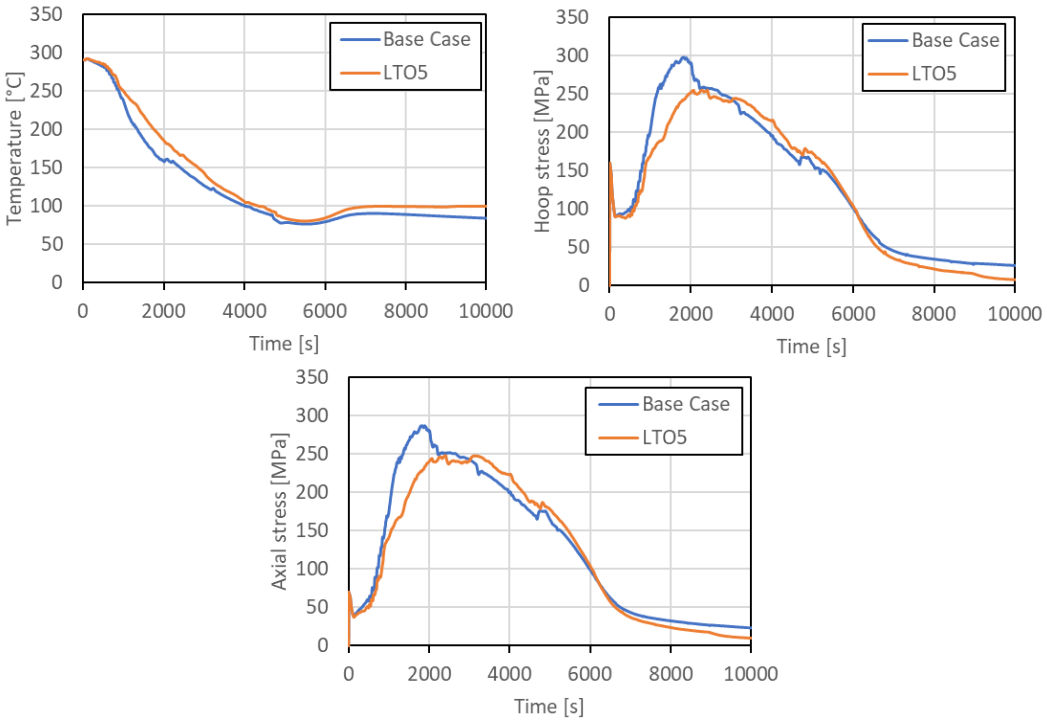

Figure 2.42: LTO5 results of BZN at 16 mm of RPV wall thickness, with RELAP (SSTC) TH input data.

2.3.2.4 LTO6 – Reduction of HPIS flow (operator action) at 1800s

The results at core weld elevation under the cold leg position from 3D calculations are given in Figure 2.43 (TH input from RELAP) and in Figure 2.44 (TH input from KWU-MIX).

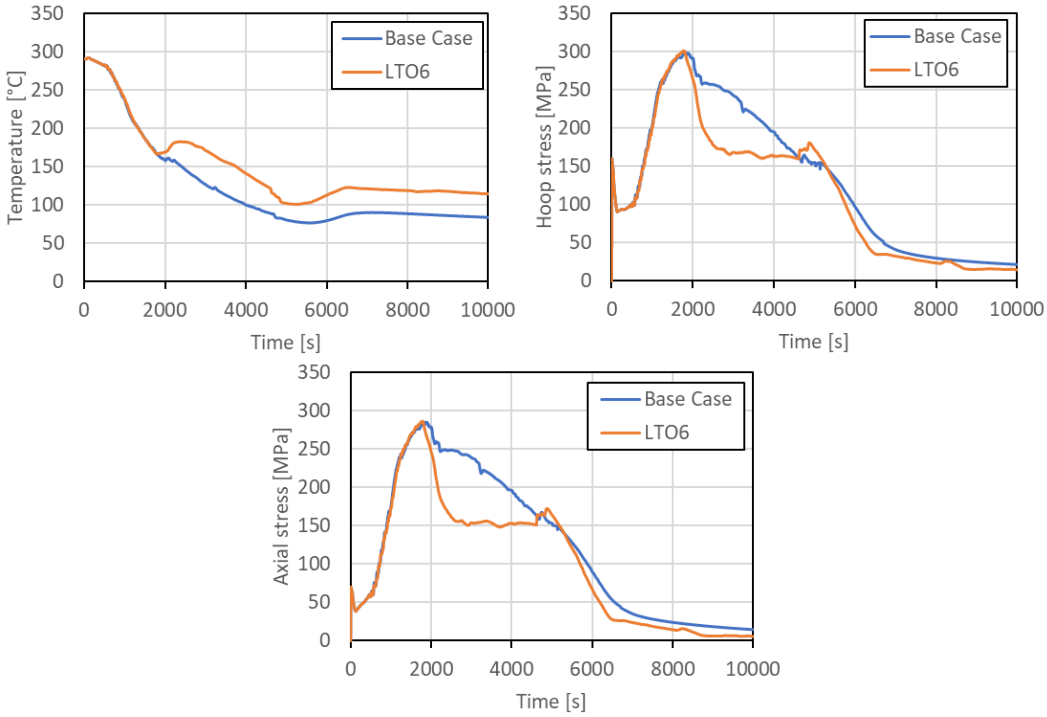

Figure 2.43: LTO6 results of BZN at 16 mm of RPV wall thickness, with RELAP (WUT) TH input data.

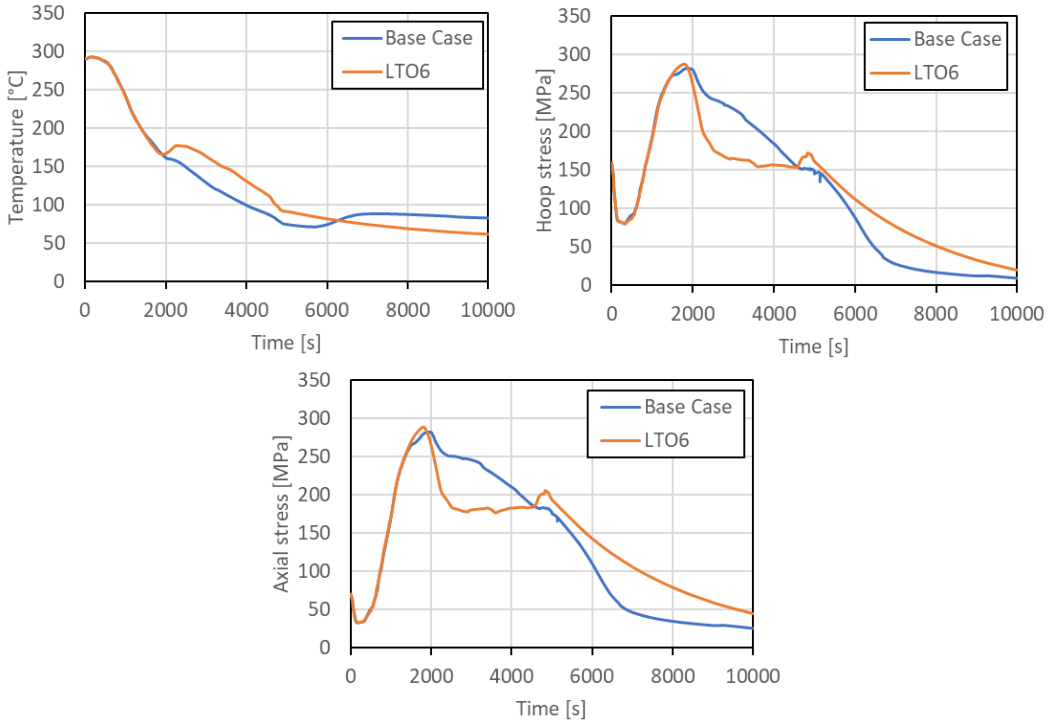

Figure 2.44: LTO6 results of SSTC interpolated to the 16 mm of RPV wall thickness, with KWU-MIX (FRA-G) TH input data.

2.3.2.5 LTO8 – Change of cooldown rate (operator action) to 200K/h

The results at core weld elevation under the cold leg position from 3D calculations are given in Figure 2.45 (TH input from RELAP) and in Figure 2.46 (TH input from KWU-MIX).

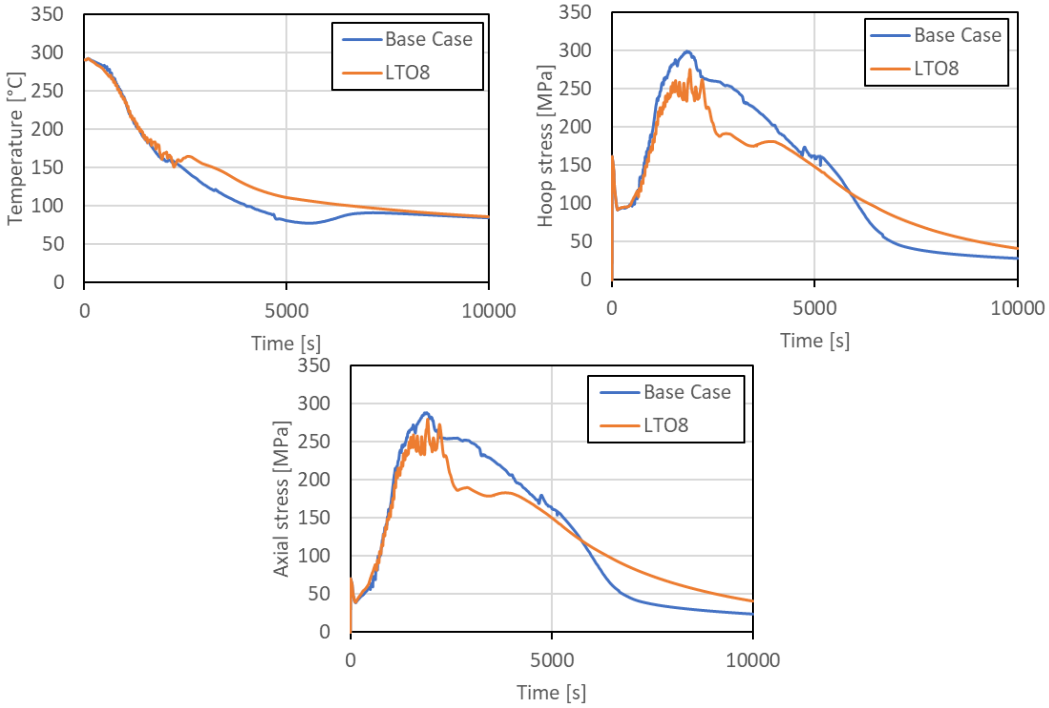

Figure 2.45: LTO8 results of JSI interpolated to the 16 mm of RPV wall thickness, with RELAP (WUT) TH input data

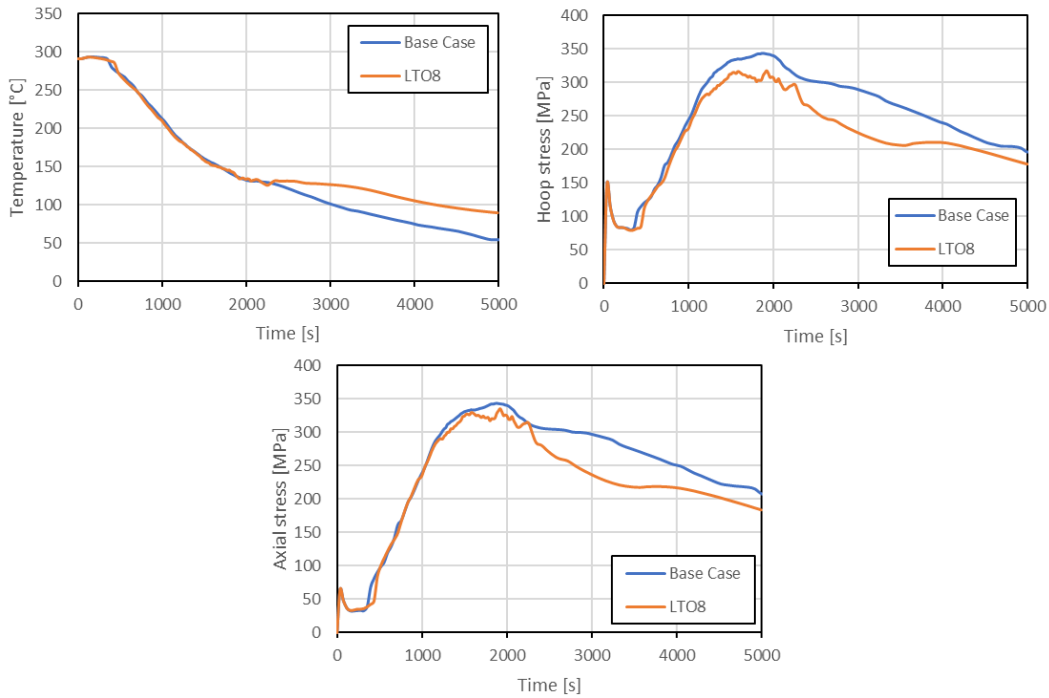

Figure 2.46: LTO8 results of FRA-G at 16 mm of RPV wall thickness, with KWU-MIX (FRA-G) TH input data

2.4 TH uncertainties

2.4.1 Uncertainties in TH data analyses for Wilks

Evaluation of TH uncertainties and their distributions have been performed in WP2 covering the model and computer-code uncertainties, plant uncertainties related to initial conditions, boundary conditions and parameters of the NPP systems. The TH uncertainties have been treated using statistical methods based on the Wilks approach allowing to define a statistical set of TH data with given confidence level and tolerance limits.

Thus, it was shown that using the Wilks method 59 simulations is required to achieve a one-sided tolerance interval with the tolerance limit of P=0.95, and the confidence level of $1-\alpha$=0.95. For achieving a double-sided tolerance interval for the same tolerance limit ($P = 0.95$) and the confidence levels of 0.95 or 0.99, Wilks simulations of 93 and 130 samples are required, respectively.

Several system TH codes (RELAP, ATHLET, TRACE) and one mixing TH calculation code (KWU-MIX) were used for TH analyses for best-estimate TH input parameters supplemented with statistically defined TH input data sets with propagated uncertainties according to the Wilks method. A summary of performed Wilks TH analyses by the APAL partners is presented in Table 2.8. The grey cells in the presented summary indicate which Wilks data sets have been used as the TH input data for structural analyses by different partners.

Table 2.8 Summary of TH data sets used for Wilks analyses (per partner).

TH code and partner	ATHLET from GRS	KWU-MIX from FRA-G	RELAP from JSI		RELAP from KIWA	RELAP from SSTC	RELAP from UJV		TRACE from PSI		RELAP from WUT
Wilks sets	59	93*	59	130	59	59	59	93	59	130	93
UJV							x	x			
FRA-G		x									
PSI									x	x	
JSI			x	x							
KIWA					x**						
IPP						x					
WUT											x
GRS	x										
BZN								x			
Tecnatom									x		

* First 59 Sets are treated as 59 Wilks sets.

** KIWA used Base Case from JSI TH data.

2.4.2 Typical Wilks TH input data for structural analyses

In general, all TH results from the Wilks analyses have a similar appearance but certain quantitative differences in the calculated results were observed. It can be explained by a variety of used TH codes, their functionality, differences in nodalisation of TH models and taken assumptions.

It is not feasible to represent all TH results that have been used as the input data for structural analyses. Therefore, typical TH data from the Wilks analyses based on US NRC system TH code TRACE is presented as an example in this Section.

The TH results presented in this report demonstrate the following TH cases:

- Base Case: The conservative reference case based on the conservative input data for the TH analyses in Task 2.1 as reported in the APAL Deliverable D2.1 [8] and also summarised in WP2 Public Summary [11].
- Best Estimate: The best estimate case based on the best-estimate input data (i.e. for all TH input parameters treated as statistically distributed the mean values were used) for the TH analyses in Task 2.3 as reported in the APAL Deliverable D2.3 [10] and also summarised in WP2 Public Summary [11].
- Wilks: The TH data set with random sampling of distributed selected plant parameters and boundary conditions. The random parameters and sampling methodology are described in D2.3 [10] and [11].

Fluid temperature, RPV pressure and heat transfer coefficient (HTC) time histories are shown for the Wilks sets with 59 and 130 samples in Figure 2.47-Figure 2.49. The grey curves in all plots represent individual results for each Wilks set.

It can be noticed from the presented TH results that the temperature and HTC time histories demonstrate a large scatter while the RPV pressure variation remains in a rather confined scatter band.

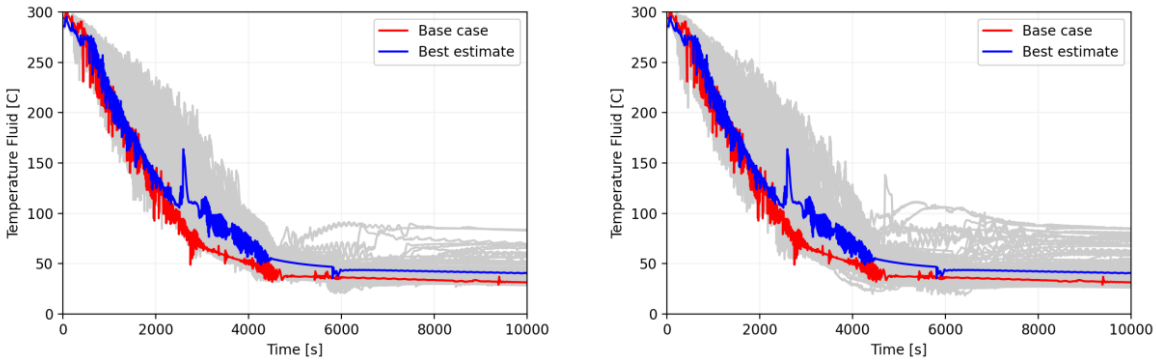

(a) (b)

Figure 2.47: Fluid temperature as a function of time for (a) Wilks-59 and (b) Wilks 130 data sets.

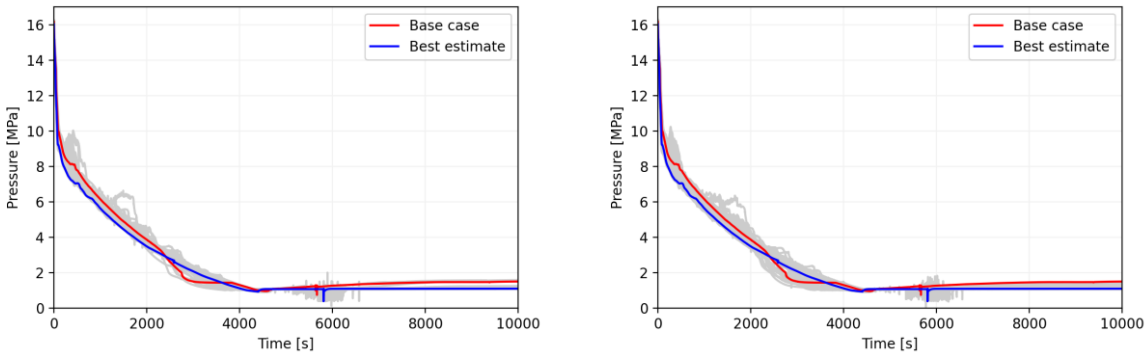

(a) (b)

Figure 2.48: Pressure in RPV as a function of time for (a) Wilks-59 and (b) Wilks 130 data sets.

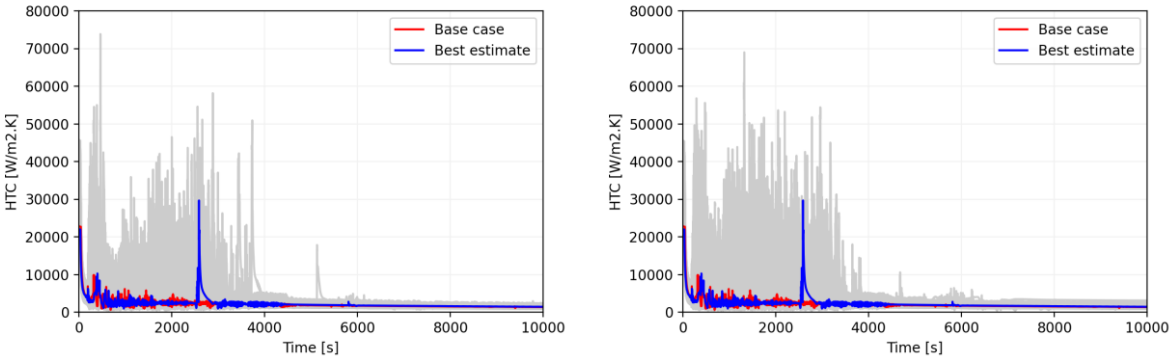

Figure 2.49: Heat transfer coefficient (HTC) as a function of time for (a) Wilks-59 and (b) Wilks 130 data sets.

2.4.3 Results for stress and temperature distributions through the RPV wall thickness

This section presents the structural analysis results in terms of transient stress and temperature distributions through the RPV wall. This task is part of WP4, see also [5]. The analyses have been performed by partners using the TH input data as given in Table 2.8. The calculated stress and temperature distributions through the RPV wall as a function of time are later used as the input data for fracture mechanics analyses within the deterministic and probabilistic benchmarks.

Again, it is not feasible to present all obtained results due to large amount of data. Only typical results are shown in the following subsections based on the analyses for two Wilks data sets with 59 and 130 samples. A discussion of main trends and deviations in the results from different partners is also provided in this report.

For facilitating a comparison of the results between different partners, the following result plots were requested from each partner;

- Inner RPV wet surface temperatures as a function of time,
- Hoop and axial stresses at the RPV inner surface as a function of time,
- Temperature, hoop and axial stresses at the crack tip as a function of time,
- Hoop and axial stresses at the crack tip as a function RPV wall temperature at the crack tip.

In the analyses the crack tip located at the distance of 16 mm from the inner (wet) surface of the RPV was assumed. The obtained stress distributions include weld residual stresses.

2.4.3.1 Results for Wilks set with 59 samples

The RPV wall temperature, hoop and axial stresses at the inner (wet) surface of RPV as a function of time are presented in Figure 2.50 - Figure 2.52. The temperature at the crack tip location (crack depth of 16 mm is assumed), hoop and axial stresses at the crack tip location as a function of time are presented in Figure 2.53 - Figure 2.55. The hoop and axial stresses at the crack tip as a function of crack tip temperature are shown Figure 2.56 and Figure 2.57.

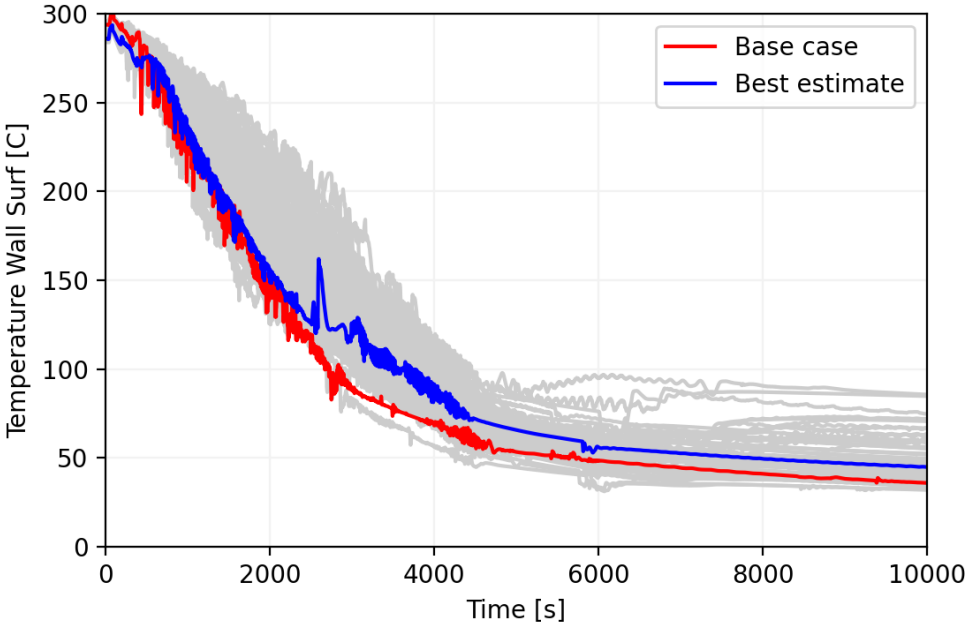

Figure 2.50: Inner surface temperature as a function of time for Wilks-59.

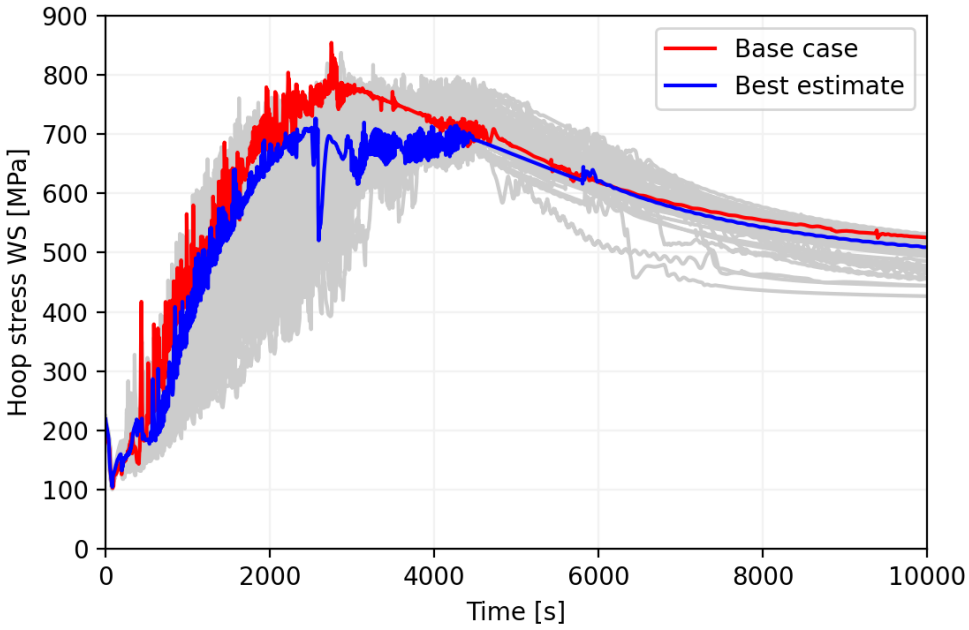

Figure 2.51: Hoop stresses at inner surface as a function of time for Wilks-59 with WRS.

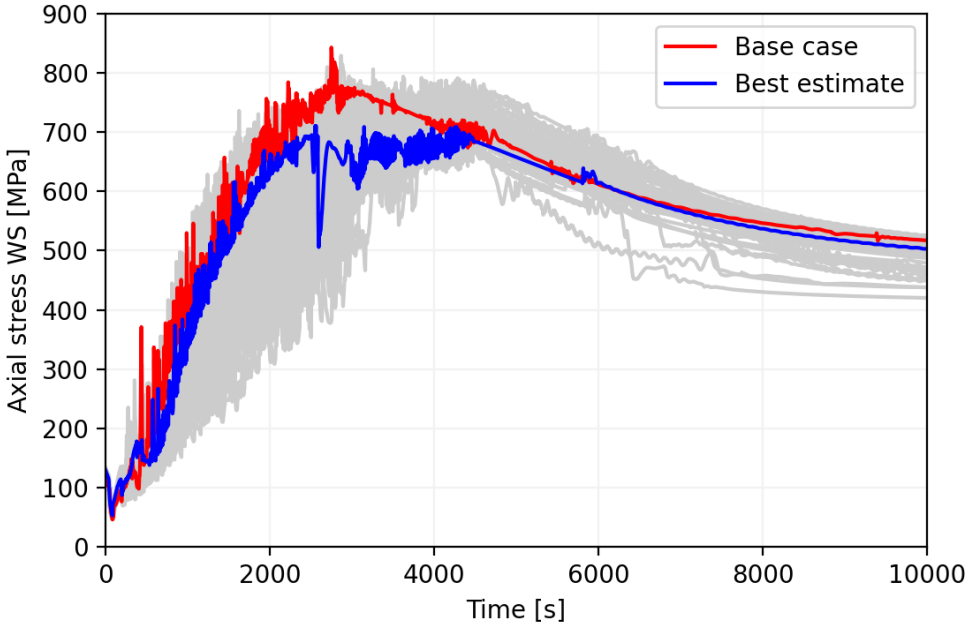

Figure 2.52: Axial stresses at inner surface as a function of time for Wilks-59 with WRS.

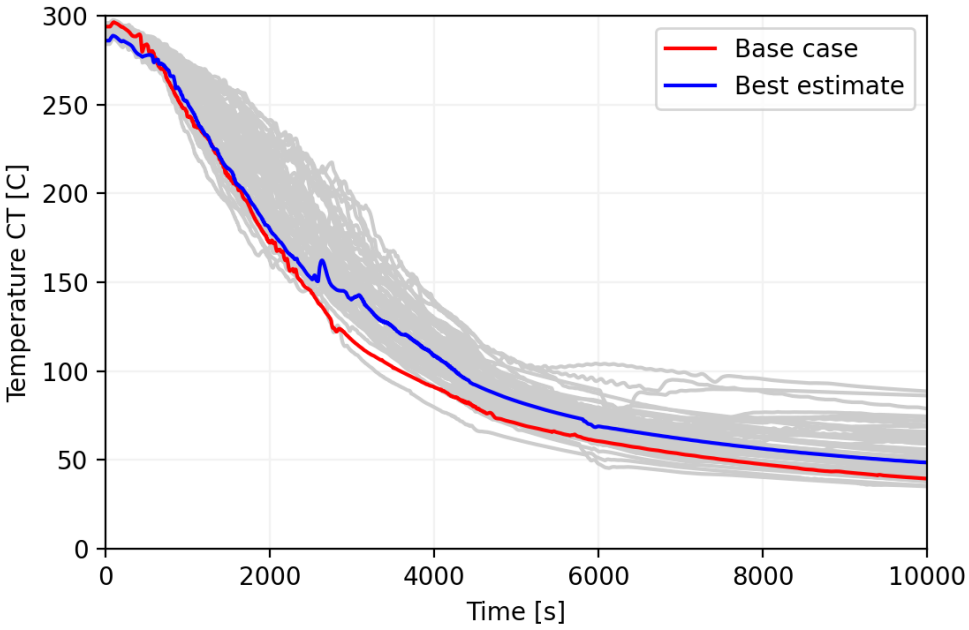

Figure 2.53: Temperature at the crack tip location as a function of time for Wilks-59.

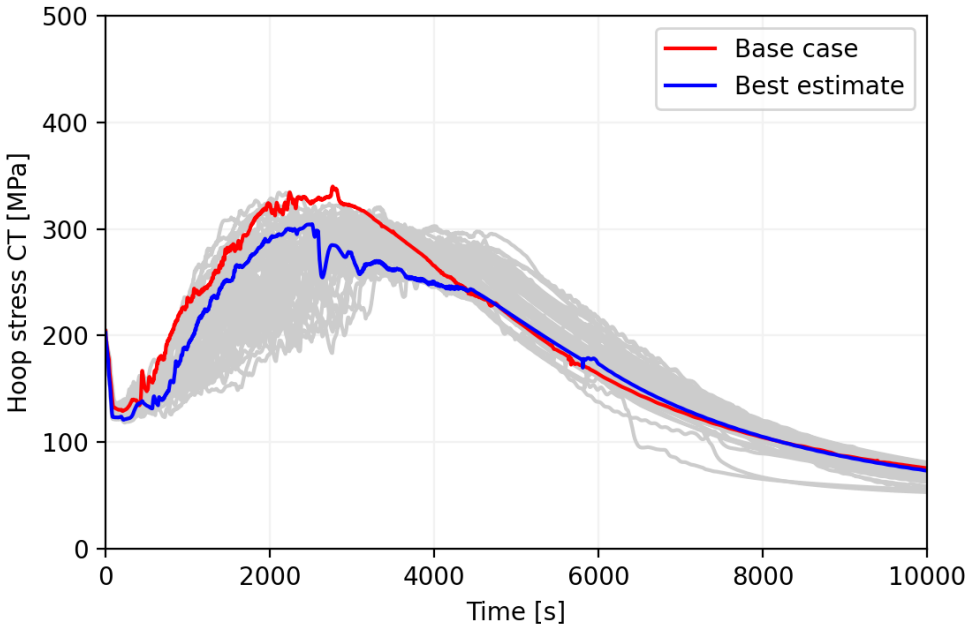

Figure 2.54: Hoop stresses at the crack tip location as a function of time for Wilks-59 with WRS.

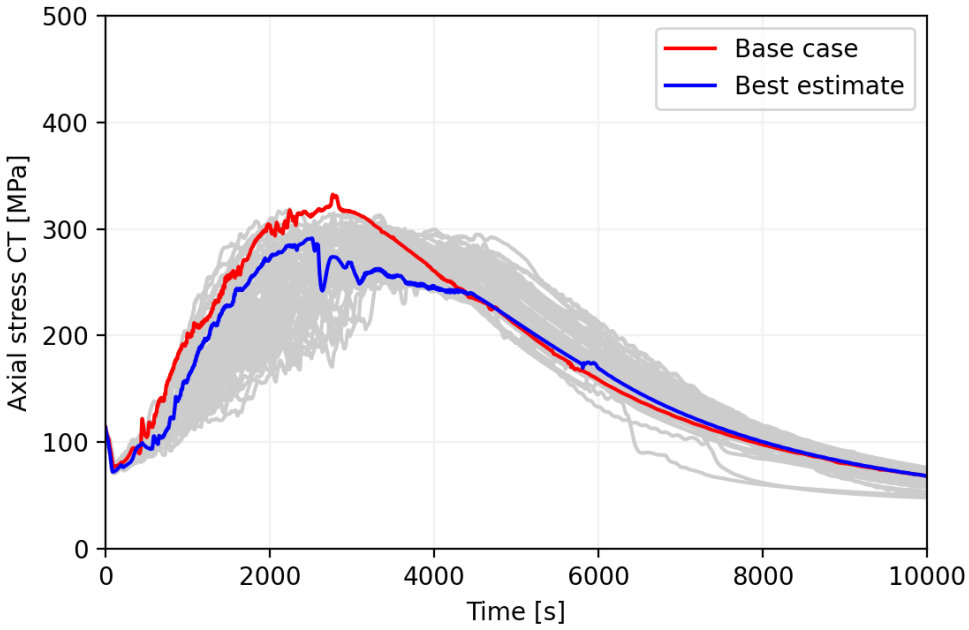

Figure 2.55: Axial stresses at the crack tip location as a function of time for Wilks-59 with WRS.

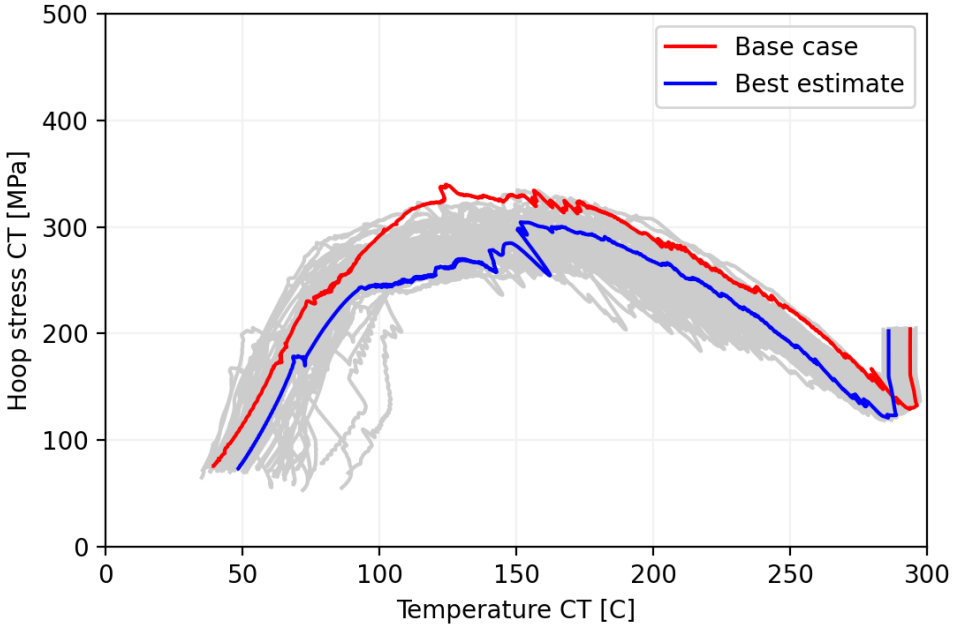

Figure 2.56: Hoop stresses at the crack tip as a function of crack tip temperature for Wilks-59 with WRS.

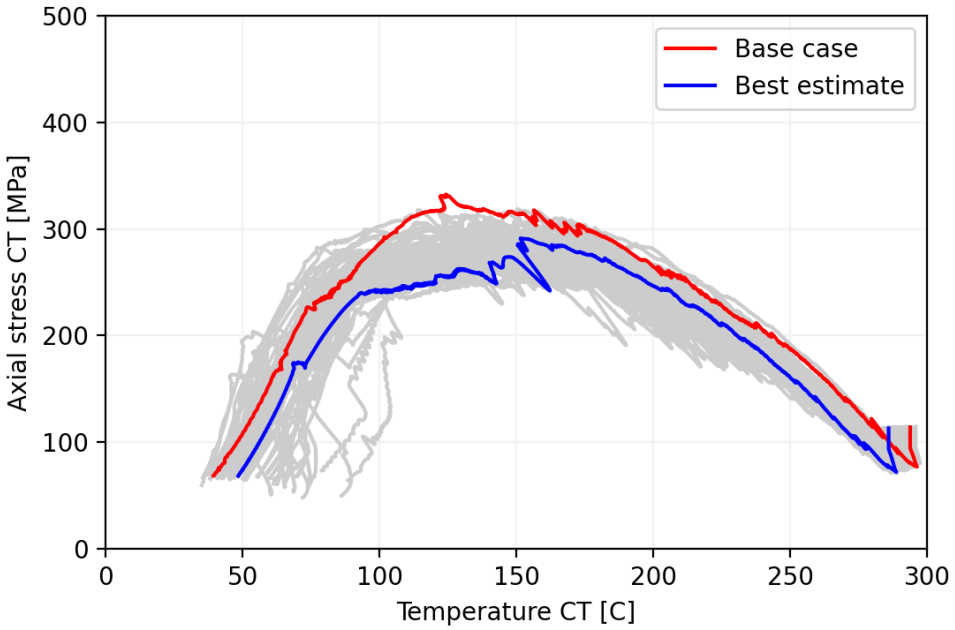

Figure 2.57: Axial stresses at the crack tip as a function of crack tip temperature for Wilks-59 with WRS.

2.4.3.2 Results for Wilks set with 130 samples

The RPV wall temperature, hoop and axial stresses at the inner (wet) surface of RPV as a function of time are presented in Figure 2.58 - Figure 2.60. The temperature at the crack tip location (crack depth of 16 mm is assumed), hoop and axial stresses at the crack tip location as a function of time are presented in Figure 2.61 - Figure 2.63. The hoop and axial stresses at the crack tip as a function of crack tip temperature are shown Figure 2.64 and Figure 2.65.

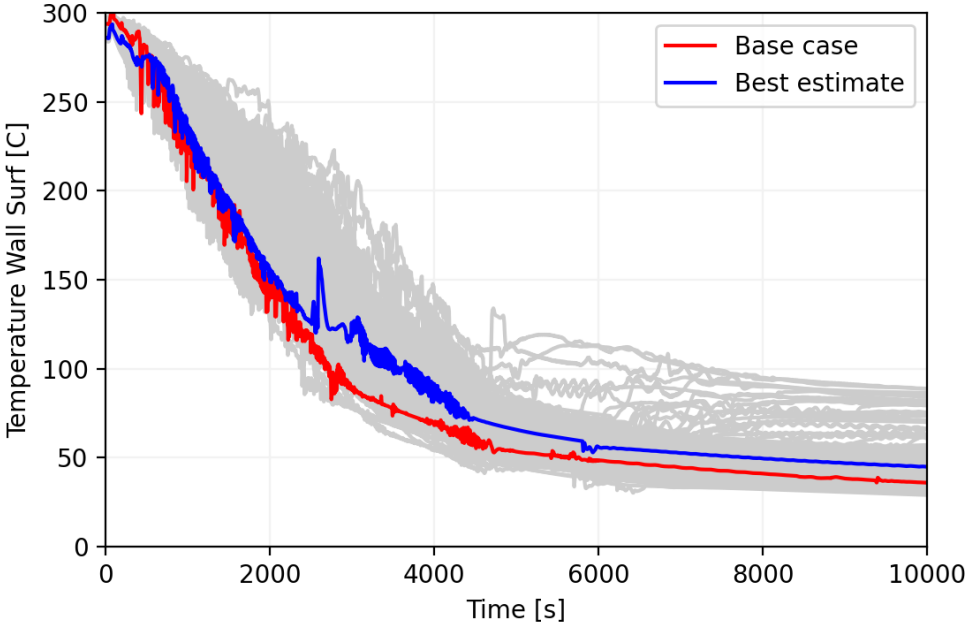

Figure 2.58: Inner surface temperature as a function of time for Wilks-130.

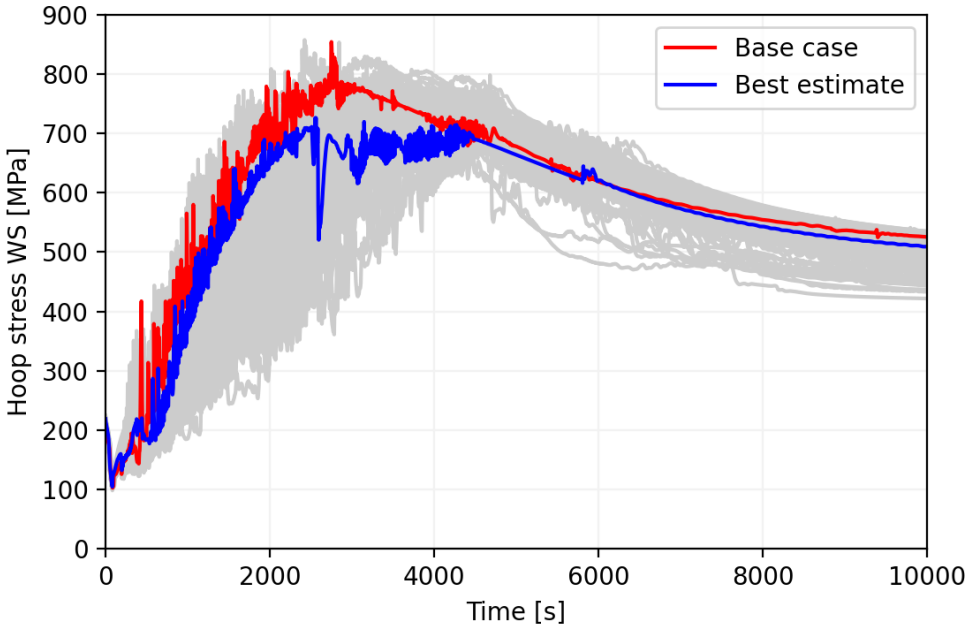

Figure 2.59: Hoop stresses at inner surface as a function of time for Wilks-130 with WRS.

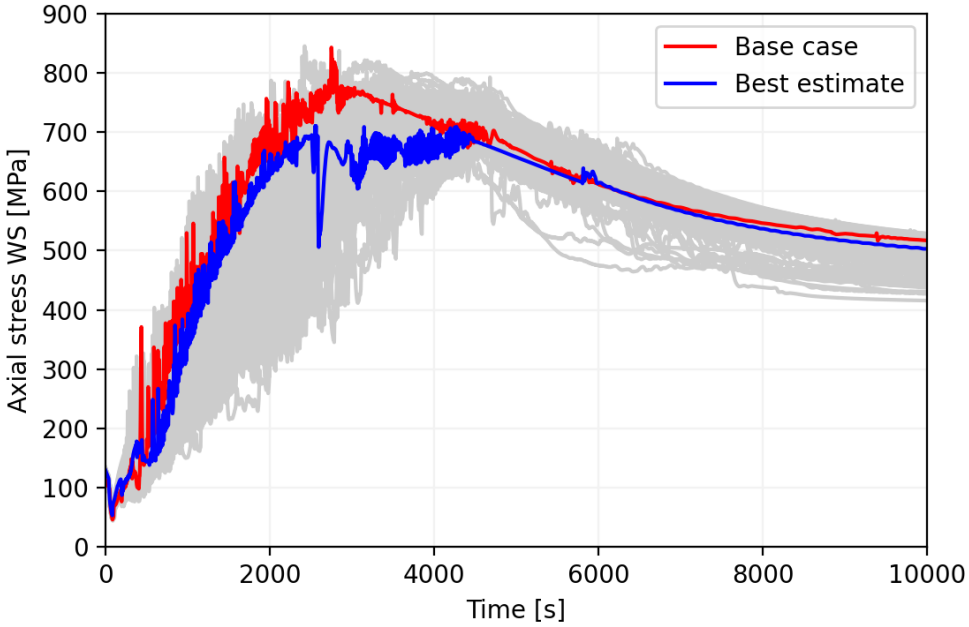

Figure 2.60: Axial stresses at inner surface as a function of time for Wilks-130 with WRS.

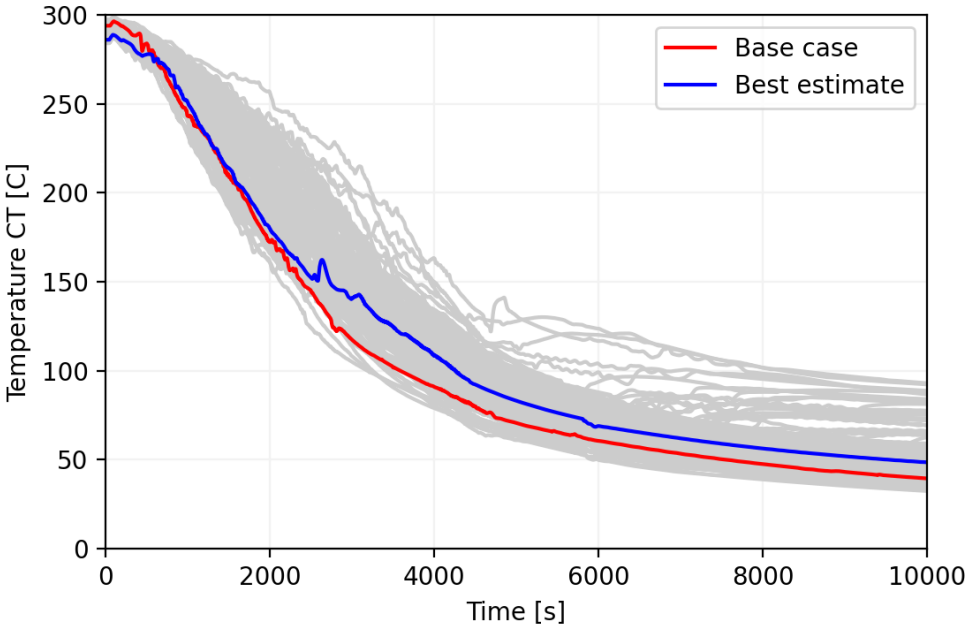

Figure 2.61: Temperature at the crack tip location as a function of time for Wilks-130.

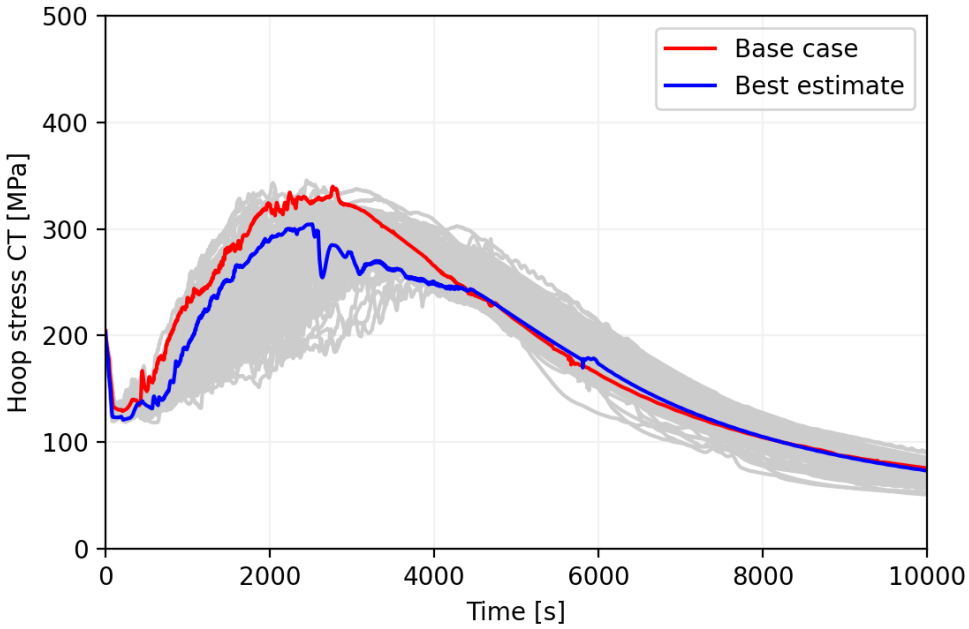

Figure 2.62: Hoop stresses at the crack tip location as a function of time for Wilks-130 with WRS.

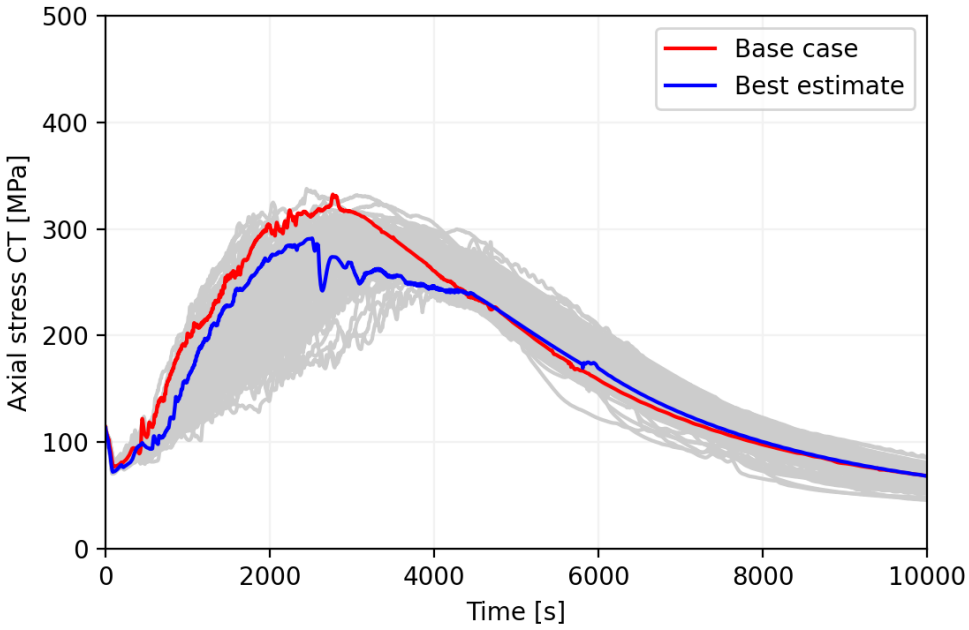

Figure 2.63: Axial stresses at the crack tip location as a function of time for Wilks-130 with WRS.

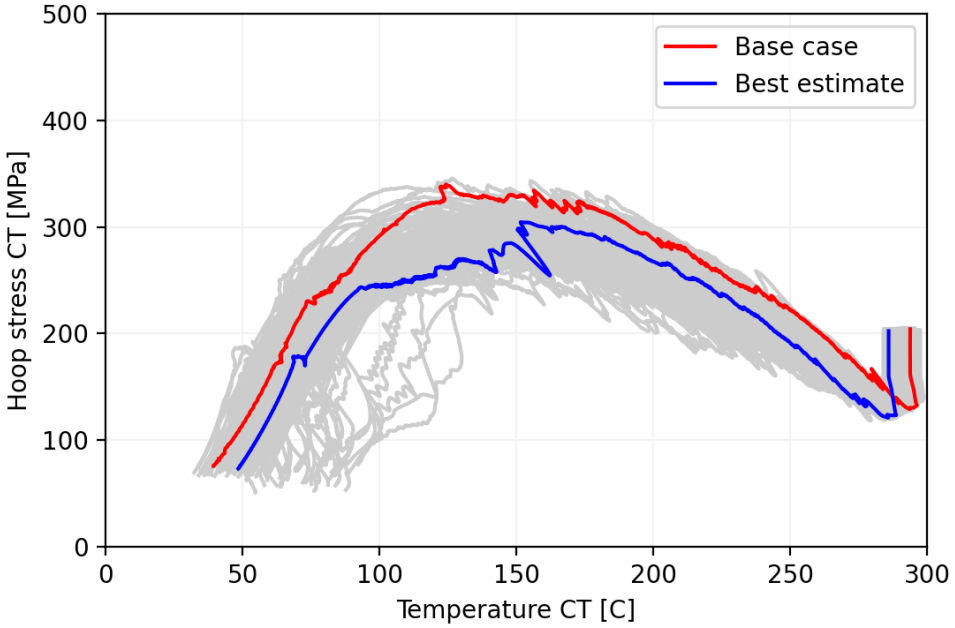

Figure 2.64: Hoop stresses at the crack tip as a function of crack tip temperature for Wilks-130 with WRS.

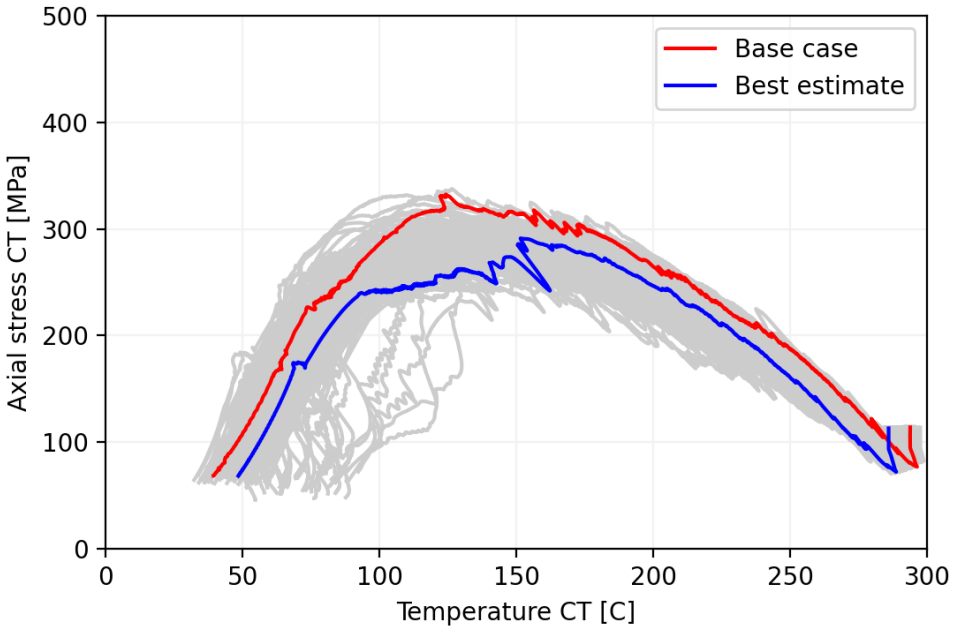

Figure 2.65: Axial stresses at the crack tip as a function of crack tip temperature for Wilks-130 with WRS.

2.5 Conclusions from structural assessment

2.5.1 General conclusions on structural assessment

In APAL Task 3.1 - Stress and temperature distributions for benchmark performance, structural assessments for the base case (SBLOCA with 50 cm^2 break in HL and with loss of offsite power) and for selected LTO improvements and operator actions were performed with different analysis methods.

The temperature and stress fields generated within Task 3.1 were delivered to Task 3.3, Task 3.4, Task 4.3 and Task 4.4 for benchmark performance and margin assessment.

The commercial software or in-house codes used by the partners for the simulations were FAVOR, PROST, ABAQUS, ANSYS, MSC.Marc Mentat, Pre-PASCAL, SIF-Master, Systus and Verload.

As a first step a round robin task was generated to determine how the TH data can be used in case of 1D finite element simulations. 7 cases were chosen where the TH data were averaged or, in some cases, taken from an exact location, thus leading to 0D, 1D and 2D TH data. The agreement of resulting temperatures and stresses among partners was good. It was also concluded that the 2D TH data version (TH data from a given location e.g., at core weld under the cold plume) gives the most conservative results. Therefore, in the later parts of the task this version was chosen for the further calculations. Any averaging of TH data leads to non-conservative solution.

In the case of the flange weld the effect of the geometry had to be checked as the position of this weld is close to the nozzle region with higher wall thickness. The results showed that in this case the 1D finite element simulations with 2D TH data do not deliver the correct results as compared to the 2D or 3D simulations, and they underestimate the stress fields. Due to this reason, it is recommended that future work is dedicated to generating new formulae to determine the stress values in the flange weld with consideration of this geometrical effect. Alternatively, a 2D FEM simulation can be recommended. Moreover, effect of the nozzle vicinity can be studied in the future.

Several sensitivity cases were analysed, and the effect of these cases will be mainly evaluated in Task 3.3. Nevertheless, in case of the stress distributions some conclusions can already be made. The results of location investigations showed that the stress values depend highly on where the stress values are taken from. As expected, the out of plume position resulted in lower stress values, while the flange weld and nozzle corner positions generated higher stresses. Beside the locations the thickness of the cladding, the mesh and the time step were also varied, which showed lower impact on the temperature and stress results.

2.5.2 Assessment of LTO improvements

The LTO improvements determined in WP2 were investigated with 1D and 3D finite element simulations. The structural assessment calculations were done for 9 LTO cases, 3 of them being operator actions (LTO6, LTO8 and LTO9).

Table 2.9 shows the evaluation of impact of the LTO improvements on the temperature and stress field. It should be noted that the evaluation was made based on the results of the temperature and stress field at the crack tip location (16 mm from the wet surface), therefore the final assessment of the effect of different LTO improvements was done in Task 3.4 (see chapter 5) and Task 4.4 (see [5]) of the APAL project based on deterministic and probabilistic fracture-mechanical assessment. It should be also noted that the evaluation of impact of LTO improvement is valid for the assessed PTS regime and can be different for different regimes.

Table 2.9: Evaluation of impact of LTO improvements on the temperature and stress fields

	LTO improvement	Temperature field	Stress field
LTO1	Heating of water in the HPIS tanks	Beneficial	Beneficial
LTO2	Heating of water in the ACCs	No impact	No impact
LTO3	Heating of water in the LPIS tanks	No impact	No impact
LTO4	Decreasing the HPSI head	Small impact	Small impact
LTO5	Decreasing the HPSI capacity	Beneficial	Beneficial
LTO6	Reduction of HPIS flow (operator action)	Unclear	Unclear
LTO7	Decreasing of ACC pressure	No or small impact	No or small impact
LTO8	Change of cooldown rate (operator action)	Unclear	Unclear
LTO9	Isolation of ACCs (operator action)	No impact	No impact

2.5.3 Structural Assessment for TH uncertainties

2.5.3.1 TH input data

TH input data for structural analyses was obtained from TH uncertainty analyses based on the Wilks method as described in Section 2.4.1. For the TH analyses, different TH codes were used such as RELAP5, ATHLET, TRACE and KWU-MIX (for mixing calculations) together with several tools for uncertainty evaluation, e.g. DAKOTA, SUSA, etc. TH uncertainty analyses were performed for 59, 93 and 130 Wilks data sets.

The TH analysis results used as input data for structural assessments (see also Task 4.1 [5]) are summarised for each partner in Table 2.8. A detailed review and comparison of the TH results from uncertainty analyses between different partners have been carried out in APAL Deliverable 2.3 [10]. However, it is worth to include a short summary of this comparison and point out some observed differences in the TH data as it has a direct bearing on some deviations in the calculated temperatures and stresses.

Figure 2.66 illustrates a comparison of fluid temperature as a function of time used by JSI, IPP and KIWA as the TH parameter used for the temperature and stress calculations. These partners have been chosen as they performed TH uncertainty analyses based on 59 Wilks data sets using RELAP5 in combination with the uncertainty evaluation software SUSA.

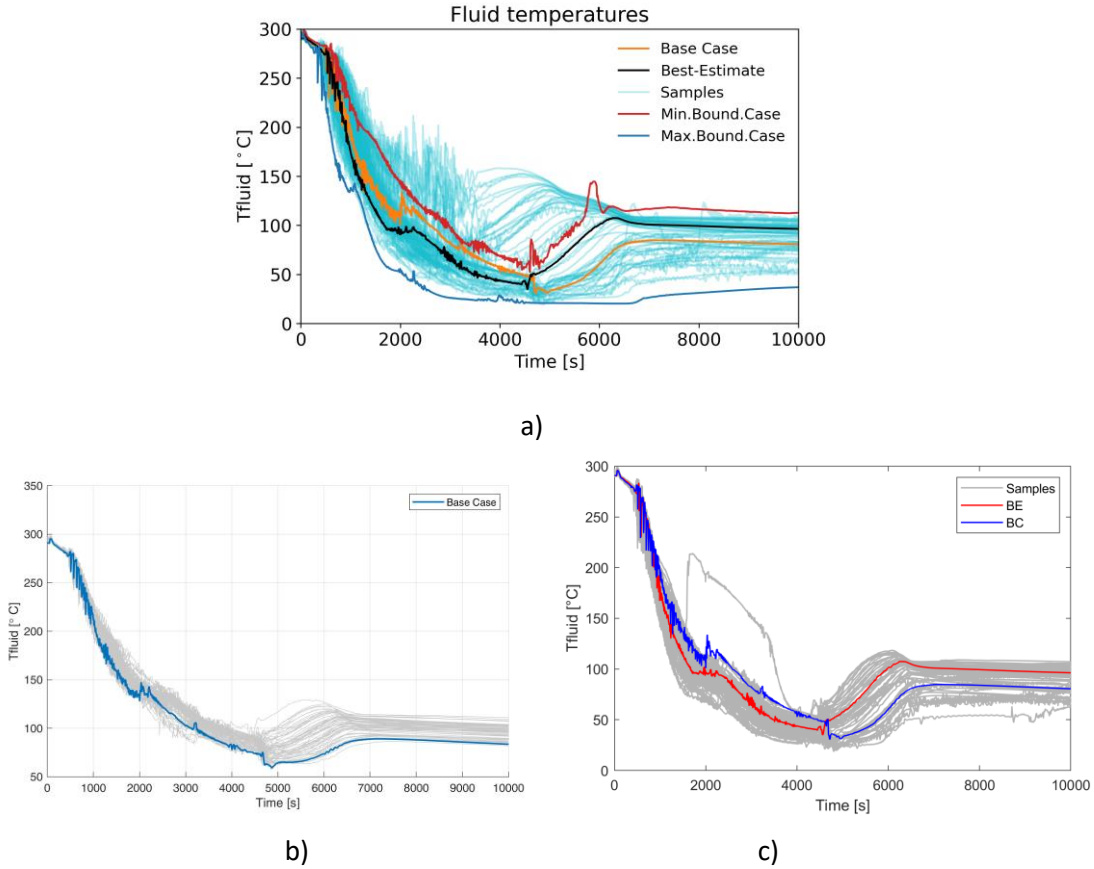

Figure 2.66: Comparison of fluid temperature as a function of time used for structural analyses by a) JSI, b) IPP and c) KIWA. Wilks 59 data samples.

Significant variations in Wilks results can be observed between JSI, IPP and KIWA. JSI results have much wider spread in the Wilks data samples in comparison to the IPP and KIWA data. One of the KIWA Wilks data samples demonstrates a clear deviation in the temperature trend when the fluid temperature increases in the time range between 1800 to 4000 s. Similar trend has also been observed in KIWA results from TH analyses for LTO improvements, namely LTO 05 for high pressure injection flow (HPSI)

reduction. KIWA performed the TH analyses by reducing HPSI flow from 100% down to 75% with 5% increments. The characteristic rise of temperature, similar to the one in Figure 2.66, was observed in the results for HPSI reduction to 75%. For higher HPSI levels (80%-100%) the temperature rise in this time range was not observed or it was much lower and less pronounced.

The temperature rise for HPSI at 75% may be explained by the following considerations. By reducing the emergency coolant quantity (HPSI flow) pumped into the reactor primary system the void fraction (ratio of steam to total volume) increases substantially. The void fraction in volume 9101 for HPSI 75% at 1500-3000 s is much larger than that for HPSI 80% which would support this assumption (void fraction values in HPSI cases 100%-80% at around 1500-3000 sec do not change much actually). It means that there is substantially more gas phase in downcomer which causes deterioration of heat transfer at certain conditions. This in turn leads to higher temperature rise in downcomer as it was obtained in the calculations for 75%. There should be a threshold somewhere between 75% and 80% HPSI reduction levels when the emergency coolant inflow is so low that most of it boils thereby deteriorating heat transfer.

Differences in fluid temperature can also be observed in the TH data for Wilks 93 data sets that have been calculated by FRA-G, UJV and WUT as shown in Figure 2.67.

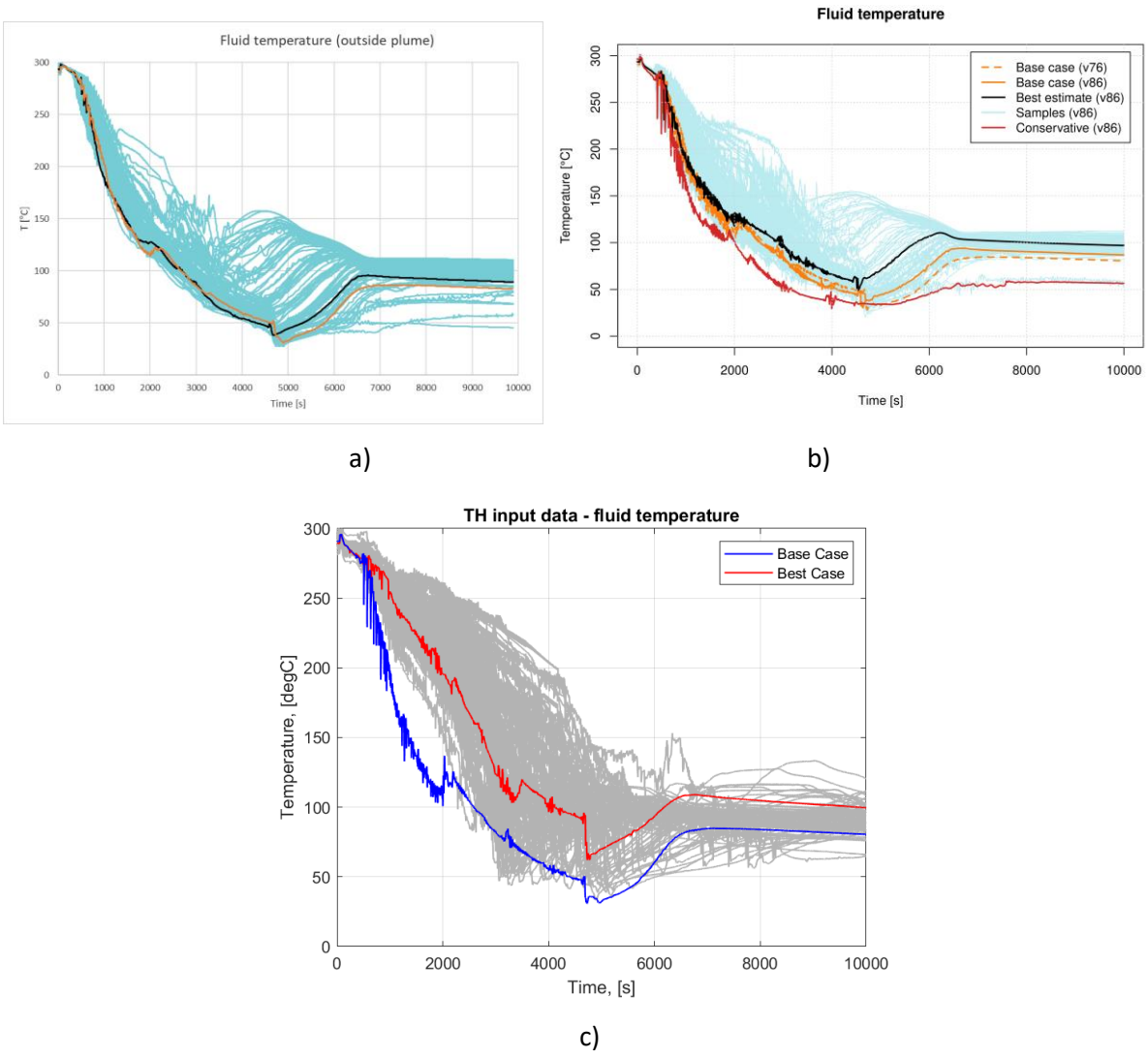

Figure 2.67: Comparison of fluid temperature as a function of time used for structural analyses by a) FRA-G, b) UJV and c) WUT. Wilks 93 data samples.

2.5.3.2 *Structural results*

It is somewhat cumbersome to make comparative plots containing results from all or several partners due to large amount of data curves. Therefore, only some qualitative comparisons and observed deviations in the structural results are provided herein.

Temperature at the RPV inner surface for the Best Estimate case analysed by PSI (TH code TRACE) exhibits a local peak with temperature increase at about 2600 s. This temperature peak results in local abrupt decrease in calculated stresses at the inner surface. Thus, hoop stresses exhibit a decrease by about 200 MPa as shown in Figure 2.68. Similar trends for the Best Estimate case can also be found in the results from TECNATOM who used the TH data from PSI for the structural analyses.

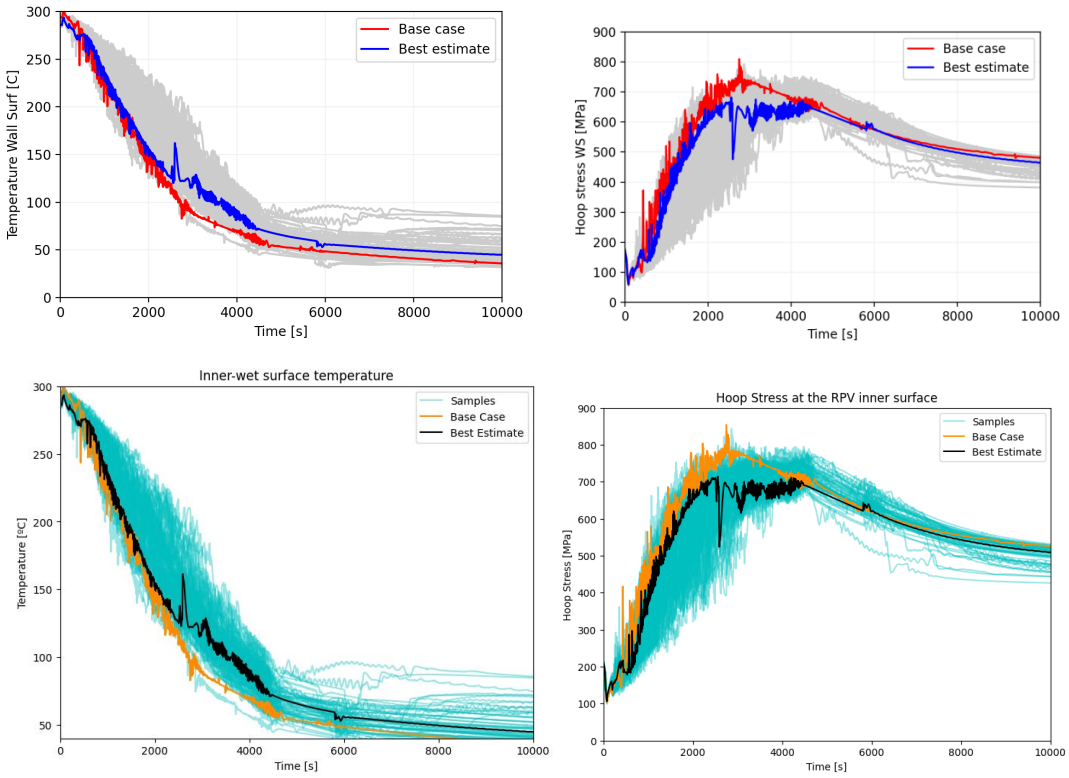

Figure 2.68: RPV inner-surface temperature and hoop stresses at the inner surface as a function of time. PSI vs Tecnatom results for Wilks 59 data samples.

In the previous section it was described that one of the KIWA Wilks TH data samples demonstrated a clear deviation in the temperature trend when the fluid temperature increased in the time range between 1800 to 4000 s, see Figure 2.66(c). This deviation in the TH data affects also the structural results leading to decrease of calculated stresses in the given time range. An example of this behaviour is presented in Figure 2.69.

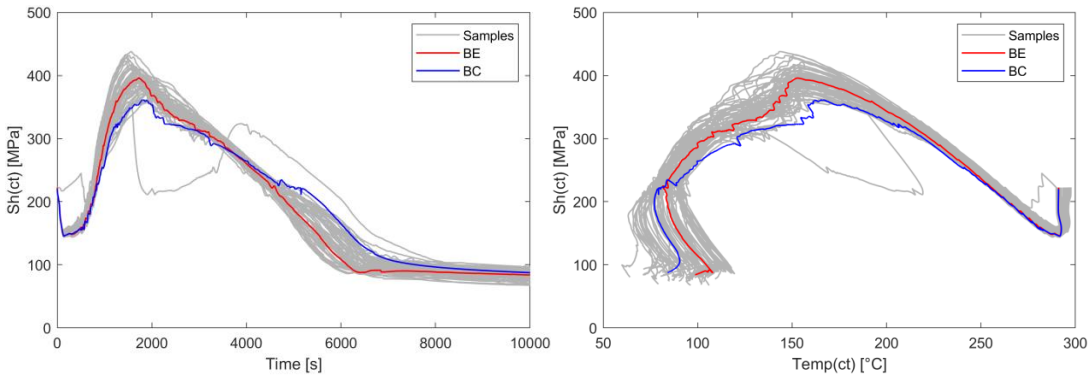

Figure 2.69: Hoop stresses at the crack tip location as a function of time and as a function of crack tip temperature. KIWA results for Wilks 59 data samples.

3 Benchmark Definition

A sound technical basis including experiences and conclusions from past projects with pre-requisite verification sub-tasks were defined to avoid misunderstanding and ensure a limited bias propagation into the final assessment of the max. all. ART for safety margin assessment. The realisation also supports exchange and knowledge transfer to engineers interested in RPV brittle fracture safety assessment.

The benchmark proposed in DEFI-PROSAFE[3] (see [14]) is the basis of the APAL benchmark definition. It was adapted to APAL while retaining its spirit with recommendations from former benchmarks (FALSIRE, ICAS, PROSIR, IAEA CRP9) on RPV fracture-mechanics assessment: **a necessary pre-requisite for successful benchmarking is to have a well-defined problem based on which a consensus solution could be achieved.**

3.1 Basic data for RPV fracture mechanics safety assessment

The main data required for the RPV fracture-mechanics safety assessment for the benchmark and for the margin assessments related to LTO improvements and TH uncertainties are summarized in Table 3.1.

Table 3.1 Overview of the input data required for the deterministic benchmark - Overview data sheet – deterministic

		Required for RPV fracture mechanics safety assessment (comparison of the max.all.ART with RPV specific predicted/measured ART_{xEFPY})	Required for determination of maximum allowable ART **Scope APAL**
RPV geometry	PWR 4-loop type	√	√
Properties of base metal, weld and cladding	Thermal	√	√
	Tensile	√	√
	Toughness: K_{IC} , J_{IC} versus temperature	√	√
	Chemical composition	√	
Irradiation effects	Fluence vs. EFPY	√	
	Initial RT_{NDT} or T_0 and Irradiation shift formula	√	
	Irradiation decrease through the RPV wall	√	
	Consequences on tensile properties	(√)[4]	
Defect	Position in RPV, Orientation	√	√
	Type: surface, underclad or embedded	√	√
	Size: depth, length, shapes	√	√
Transient loads	selected transient	√	√
Other loads	residual stresses	√	√
Fracture-mechanics model	K or J evaluation	√	√
RPV fracture-mechanics assessment	Crack initiation (brittle, ductile) Crack arrest	√	√

[3] DEFI-PROSAFE was a project under NUGENIA-PLUS funded by European Atomic Energy Community's (Euratom) Seventh Framework Programme FP7/2007-2013 under grant agreement No. 604965

[4] tensile properties variations with fluence and fluence effect on RPV brittle fracture assessment have been investigated in COVER project

limit condition for crack initiation and arrest and associated maximum allowable ART	Condition on KI, KIC, KIA for initiation and arrest limit on maximum allowed crack depth (75%)	√	√

3.1.1 RPV Geometry

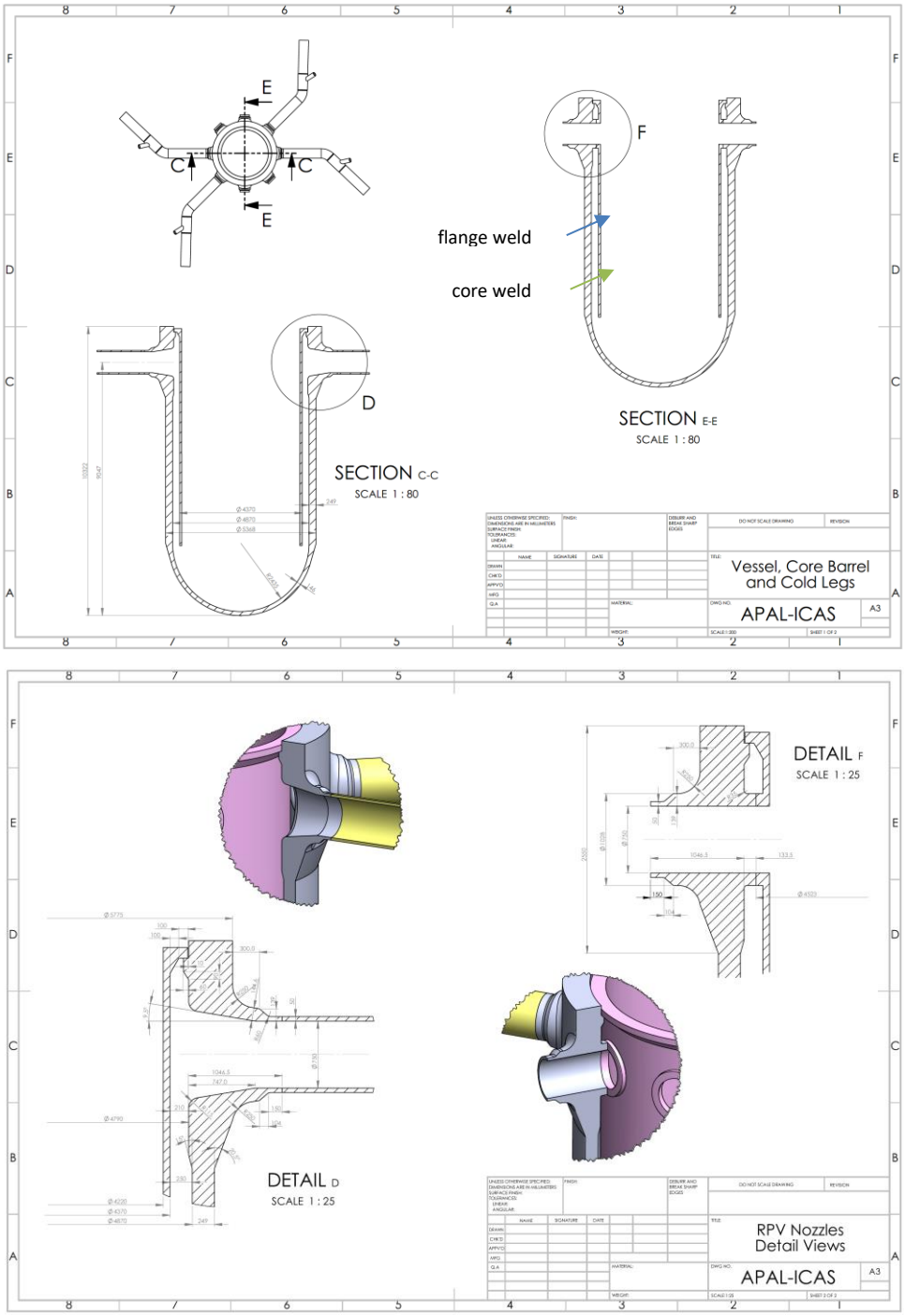

Figure 3.1 APAL RPV drawing with location of welds

The wall thickness given in Figure 3.1 includes the cladding (i.e., t = 249 mm = 243 mm ferritic part + 6 mm cladding). The location of welds (below nozzle center line – elevation 0 mm) are:

-1350 [5]mm (weld connection between cylinder and nozzle support flange), as non-mandatory task
-2638 mm (location of **belt line weld**, same as ICAS: -2638 mm),

Historically flaws were postulated primarily in welds, later also in base material or location where cracks have been found.

3.1.2 Material properties (mechanical and physical)

The material properties of the base metal 22NiMoCr37 and of the austenitic stainless-steel cladding

19 9NbSi (DIN 1.4551) from ICAS are considered with a density = 7800 kg/m² for base metal, weld and cladding. Strictly speaking, constant density that is independent of material temperature is in contradiction with nonzero thermal expansion coefficient of the material, however this fixed value is kept for the base case.

It is also assumed for the computation that:

- base material and weld metal have the same mechanical properties

- all the materials are isotropic

Table 3.2 Base metal / weld material properties

***T* [°C]**	**20**	**100**	**200**	**300**	**350**
***E* [MPa]**	206000	199000	190000	181000	172000
Poisson's ratio ν [–]	0.3	0.3	0.3	0.3	0.3
Thermal cond. [W/(m·K)]	44.4	44.4	43.2	41.8	39.4
Spec. Heat. Cap. C_p [J/(g·K)]	0.45	0.49	0.52	0.56	0.61
Mean thermal exp. α [10^{-6}/K] With T_{ref} = 20 °C	10.3	11.1	12.1	12.9	13.5
$R_{p0.2}$ [MPa]	450	431	412	392	--
E_T [MPa]	2000	2000	2000	2000	2000
density [kg/m³]	7800	7800	7800	7800	7800

Table 3.3 Cladding material properties:

***T* [°C]**	**20**	**100**	**200**	**300**	**400**
***E* [MPa]**	200000	194000	186000	179000	172000
Poisson's ratio ν [–]	0.3	0.3	0.3	0.3	0.3
Thermal cond. [W/(m·K)]	16	16	17	17	18
Spec. Heat. Cap. C_p [J/(g·K)]	0.5	0.5	0.54	0.54	0.59
Mean thermal exp. α [10^{-6}/K] With T_{ref} = 20 °C	15	16	17	19	21
$R_{p0.2}$ [MPa]	320	320	320	320	--
E_T [MPa]	2000	2000	2000	2000	2000
density [kg/m³]	7800	7800	7800	7800	7800

[5] the exact location of the flange weld center is -1275 mm but we choose -1350 mm for the evaluation due to the weld width and since the best TH data were not available for the -1275mm. It must be noted that RELAP has results for -1130 mm.

The initial temperature (starting temperature) of a calculation (transient) is usually not related to the reference temperature T_{ref} required by any particular FEM software. The initial temperature is related to the stress-free temperature in some FEM software (such as Marc, Abaqus), but not in all commercial software. A manual of any relevant FEM software should be consulted on what regards reference temperature T_{ref} and stress-free temperature T_{sf}, because the implementation of thermal stresses differs among various FEM codes.

Attention must be paid to the definition of the mean (linear) thermal expansion coefficient (TEC) especially if the starting temperature is different than the reference temperature used for measurement of mean linear TEC (which is usually the room temperature). This conversion shall be used in the case where the FEM code used for elastic and elastic-plastic stress analysis calculations does not correct it automatically to stress-free temperature T_{sf} (this may be different from reference temperature T_{ref} used for thermal expansion coefficient measurement). The formula for converting the TEC (usually given with a reference temperature of 20 °C) to a new T_{ref} is given as formula (11) of [12]. In ICAS the conversion had to be done for an initial temperature of 288 °C but in APAL the transient starts with a temperature of 291 °C. The conversion of TEC has been performed for an initial temperature (stress-free temperature) of 291 °C in

Table 3.4.

The partners are invited to perform their own calculation for verification and check whether their own code requires TEC conversion or not.

Table 3.4 Mean thermal expansion α (in 10^{-6}/K) at 20 °C (original reference temperature) and after conversion to a new T_{ref} (288 °C, 291 °C)

***T* [°C]**	***T_{ref}***	**20**	**100**	**200**	**300**	**350**
Ferritic 22NiMoCr37	20	10.3	11.1	12.1	12.9	13.5
Results from [12]	*288*	*12.8*	*13.5*	*14.2*	*15.1*	*16.5*
Calculation according to [12]	291.00	12.79	13.51	14.22	15.02	16.53
***T* [°C]**	***T_{ref}***	**20**	**100**	**200**	**300**	**400**
Austenitic (1.4551)	20	15	16	17	19	21
Results from [12]	*288*	*18.7*	*19.8*	*22.2*	*24.2*	*26.2*
Calculation according to [12]	291.00	18.73	19.90	22.31	24.30	26.29

3.1.3 Brittle fracture, crack initiation fracture toughness K_{IC} and crack arrest fracture toughness K_{IA}

The material allowable stress intensity factors K_{IC} (considering quasi static loading) and K_{IA} (considering dynamic loading as achieved during crack arrest investigation) are functions of the inherent material component specific index and the temperature at the considered location of the component. This is relevant for the base metal and weld metal. It is not relevant for cladding.

For ferritic vessels the usual indexes are linked with a specific concept:

- reference nil-ductility transition temperature RT_{NDT} based on indirect measurement of the fracture toughness with Charpy and Pellini measurement, RT_{NDT} is the index for K_{Ic} and K_{Ia}
- Master curve concept based on direct measurement of the fracture toughness with fracture-mechanics samples and consideration of statistics, T_0 is the index for K_{Jc} and T_{KIa} (related to T_0) is the index for K_{Ia}

A comparison between several concepts and approaches is shown in Figure 3.2 (from [20]). The curve MC-5% is indexed with T_0, the curve MC-5%-RT_{T0} is indexed with RT_{T0} ($RT_{T0} = T_0$+19.4 K).

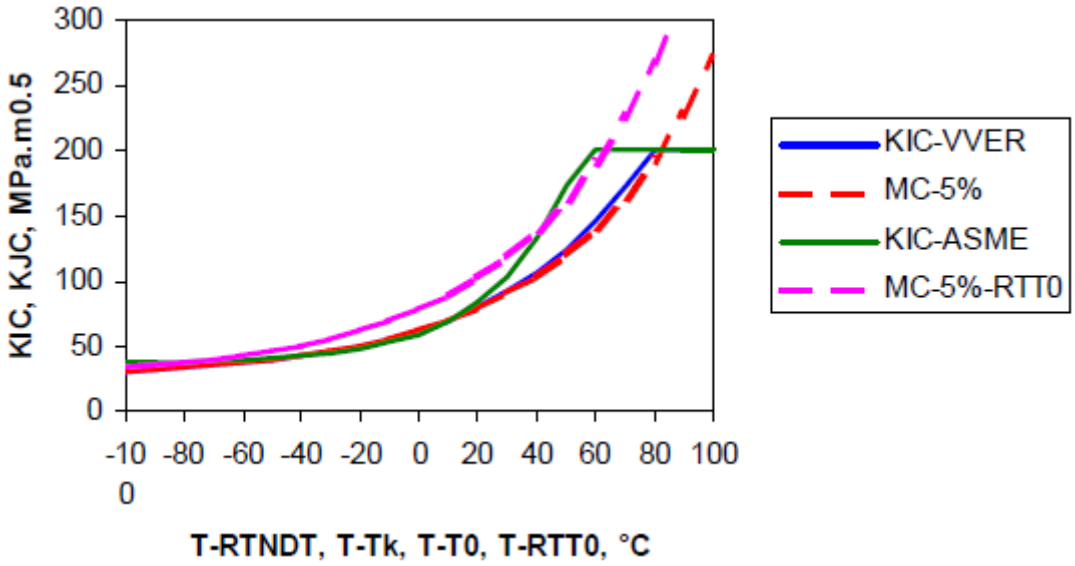

Figure 3.2 Fracture toughness based on RT_{NDT} concept and MC-approach

Remark: For one material, the values of RT_{NDT}, T_k, T_0 and RT_{T0} may differ substantially. K_{Jc} also depends on crack dimensions due to size correction.

The fracture toughness profile might not be homogeneous through the whole RPV thickness even after manufacturing because T_0 (or RT_{NDT}, or T_k) distribution is not homogeneous through the whole RPV thickness.

The initial RT_{NDT} or T_0 (after manufacturing before service operation) can have a certain profile across the thickness of forging (base material) and weld metal. Historical NDT and Kv measurements (for indirect measurement of RT_{NDT}) and direct T_0 measurements are performed at 1/4 thickness. Other locations have been investigated in the past for un-irradiated component, demonstrating that RT_{NDT} and T_0 at 1/4 thickness is higher compared to the locations near surface.

The highest initial reference temperature over the RPV wall thickness (up to 1/4 t) is considered for brittle fracture safety assessment with postulated crack size generally less than 1/4 t.

3.1.3.1 Critical stress intensity factors K_{Ic} and K_{Ia} based on RT_{NDT} concept and historical ASME curve

The toughness values of K_{IC} and K_{IA} are given in the ASME III Appendix G and ASME XI Appendix A code and can be considered as lower bound (5%) values for safety assessment.

$$K_{Ic\ ASME} = 36.5 + 3.1 \exp[0.036\ (T\text{-}RT_{NDT} + 55.5)]$$

$$K_{Ia\ ASME} = 29.4 + 1.4 \exp[0.026\ (T\text{-}RT_{NDT} + 88.9)\ ]$$

with T, RT_{NDT} in °C and K_{Ic}, K_{Ia} in MPa $m^{0.5}$.

According to the information delivered during the PROSIR project and elsewhere (ORNL), the K_{Ic} and K_{Ia} (for a given $T\text{-}RT_{NDT}$) as defined in ASME are normally distributed and it can be considered that:

Mean values - 2 standard deviations (SD) = ASME curves

$K_{IC\ ASME}$ and $K_{IA\ ASME}$ are considered as lower bound with 95% confidence (so p = 5%), corresponding to the mean value minus two standard deviations. Standard deviations for K_{IC} and K_{IA} of 15% and 10% (of the mean value), respectively, were considered in PROSIR and this will be also considered within APAL as:

$$K_{IC\ ASME} = K_{IC\ mean,\ ASME} - 2{\cdot}SD \text{ (with } 1{\cdot}SD{=}15\%),$$

then $K_{ICmean,\ ASME}$=1/0.7 $K_{IC\ ASME}$

and

$K_{IA\ ASME}$ = $K_{IA\ mean,\ ASME}$ - 2·SD (with 1·SD=10%),

then $K_{ICmean,\ ASME}$=1/0.8 $K_{IC\ ASME}$

3.1.3.2 Cleavage crack initiation fracture toughness K_{Jc} and arrest K_{Ia} based on T_0 Master Curve approach

The fracture toughness K_{Jc} based on T_0 Master curve approach is presented in Figure 3.3 and the equations for lower bound and mean K_{Jc} are taken from CC-N-830-1 [13] and given in Table 3.5.

Note that the RT_{NDT} concept is "adjusted" (contains margin) whereas T_0 is not adjusted (margin is not included).

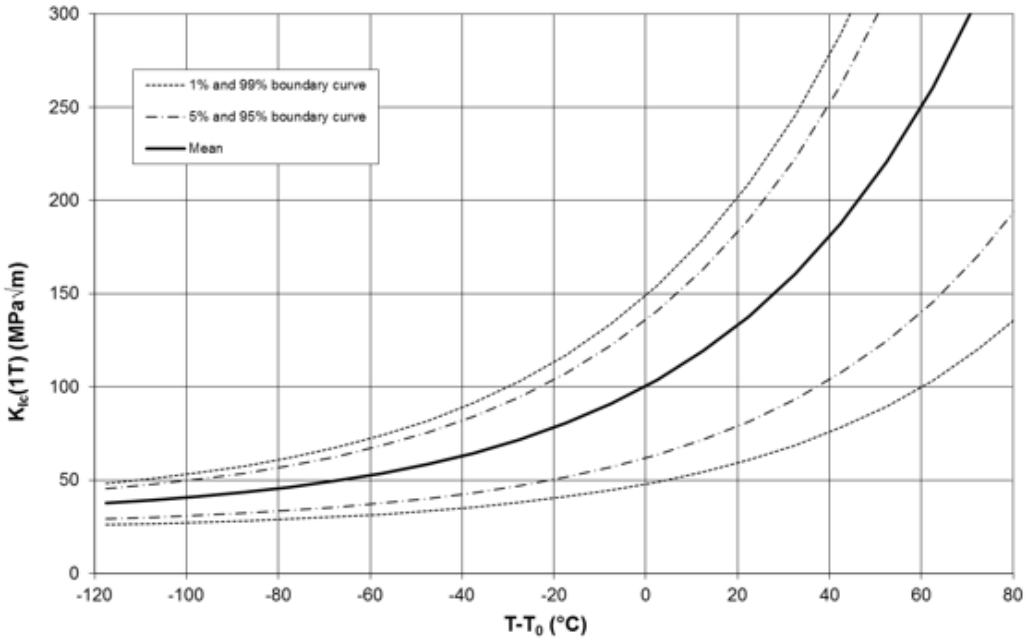

Figure 3.3 Fracture toughness based on T_0 MC-approach (for crack front length of 1 inch)

Table 3.5 Description of K_{Jc} based on MC approach

for lower bound curves with cumulative failure probability percentile p = 5%	$K_{Jc}^{p=0.05} = 25.2 + 36.6 \cdot \exp[0.019(T - T_o)]$
For median value with percentile p = 50%	$K_{Jc}^{p=0.5} = 30 + 70 \cdot \exp[0.019(T - T_o)]$

These equations are valid only for crack front length of 1 inch. For other sizes, a size correction must be applied (taken from [20]):

$$K_{Jc} = K_{\min} + (K_{Jc} - K_{\min}) \cdot \left(\frac{25\ \text{mm}}{B}\right)^{1/4}$$

with B being the crack front length and with K_{min} = 20 MPa $m^{0.5}$

The 5% lower boundary is close to design fracture toughness curves (K_{IC} ASME) if reference temperature RT_{T0} (=T_0+19.4K[6]) is used as index in the K_{IC} ASME (RT_{T0} concept [7]).

This is important when comparing both evaluations (RT_{NDT} concept and Master Curve).

Crack arrest K_{IA} based on T_0:

The crack arrest fracture toughness curve at percentile *p* is defined in [13] as follows:

Table 3.6 Description of K_{Ia} based on MC approach

for lower bound curves with percentile p = 5%	$K_{Ia}^{p} = K_{Ia}^{mean}\left(1 - 0.18M_p\right)$ with M_p = 1.64

Equation 1

For median value with percentile p = 50%	$K_{Ia}^{mean} = 30 + 70 \cdot \exp[0.019 \cdot (T - T_{KIa})]$ Where $T_{KIa} = T_0 + 44.97\exp[-0.00613 \cdot T_0]$

Equation 2

3.1.4 Upper shelf limit, ductile fracture toughness J / ductile tearing

It must be noted that the upper limit of K_{IC} and K_{IA} for the upper shelf is given rather arbitrarily, since the state of the art reflects that the historical limit of 220 MPa√m may not be adequate and a proper definition of the upper shelf limit can now be considered with limitation of ductile tearing (see Code case 830-R1 [13]). Limitation is usually due to the specimen geometry and standard validity range. Therefore, the largest amount of ductile crack growth (Δa) is usually limited to 2.5 mm. The description provided in the ASME CC-N-830 R1 is the basis for the benchmark.

In the transition region, the brittle and ductile fracture modes are in concurrence, and both must be investigated in a RPV fracture-mechanics safety assessment. Within APAL, competing mechanisms assessment is considered as a non-mandatory task for WP3 (nozzle or crack arrest). It must be noted that instability could also occur by small ductile crack growth for low crack resistance material (J-R curve with last slope being horizontal, limit load).

[6] The values RT_{T0} = T_0 + 19.4K is set by imposing that the ASME KIc curve indexed with RT_{T0} in place of RT_{NDT} will bound the majority of the actual material fracture toughness data. Reference for this snippet: Nuclear Power: Control, Reliability and Human Factors

[7] N-629, ASME CC 629, 1999, N-631, ASME CC 631, 1999 ; IAEA Guide TRS 429 ; VanDerSluys et al, 2001: Fracture toughness master curve development: Fracture toughness of ferritic steels and ASTM reference temperature (T0)

The risk of tearing in ferritic steel is low for small crack size in the cylindrical part of RPV. The risk may be higher for high loaded ferritic region (like surface crack at nozzle corner during PTS) or large crack (after cleavage initiation and arrest). The risk of tearing may be also higher for crack with tip located in the cladding (like UCC) during thermal shock. The limit of 220 MPaVm is only kept for the deterministic and probabilistic benchmark purpose (since we are interested by the margin in the brittle fracture assessment).

3.1.5 Crack types

Once a flaw has been detected by non-destructive testing, it has to be characterized and idealized for the flaw assessment by means of fracture mechanics during integrity assessment of RPV. Since uncertainty may occur during NDT to qualify the flaw as a crack, the assessment is performed in a conservative way by "transforming" the flaw with maybe non-sharp shape (no stress riser) into a sharp crack. The usual relevant types of flaws are listed hereunder. Please note that this is a general description and the specific crack types used for the benchmark are defined separately.

3.1.5.1 Through-clad crack in cladded component TCC:

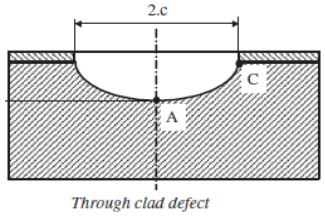

Figure 3.4 TCC

Shape for through-clad crack in cladded component:

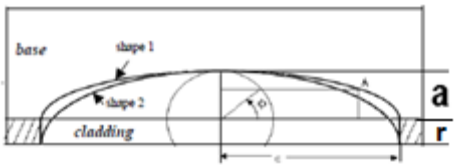

Figure 3.5 TCC shape

a is the depth in base metal, r is the cladding thickness, the total crack depth from free (wet) surface is a+r. TCC with extended (infinite) length will be used for crack arrest assessment (after crack initiation).

3.1.5.2 Semi elliptical underclad crack (UCC) and elliptical crack with crack tip located at clad-base metal interface in cladded component

Two shapes co-exist for underclad crack. The shape with half ellipse in the base metal in Figure 3.6 is representative for UCC.

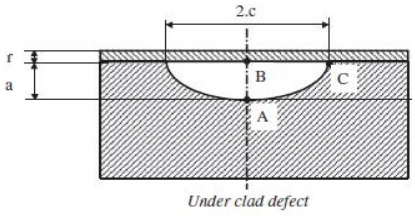

Figure 3.6 UCC with semi elliptic shape in base metal

In this special case the plasticity correction must be applied (see PROSIR [21]) because the small ligament in the cladding may produce additional crack driving forces during a thermal shock due to:

- the eventual increasing plasticity (of the cladding) during increasing load up to the maximal loading
- the remaining plasticity of the cladding after the maximal loading leading to restraint of the crack (stay open)

Therefore, the crack tip A and C are directly impacted by the level of plasticity (yielding) in the cladding (in front of the crack tip B).

The plasticity correction shall also apply to an elliptical crack with crack tip located at the clad-base metal interface (see Figure 3.7).

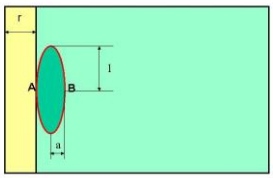

Figure 3.7 Elliptical crack with a crack tip located at the clad-base interface (from PROSIR [21])

3.1.5.3 Embedded (buried) crack

Such crack model is shown in Figure 3.8.

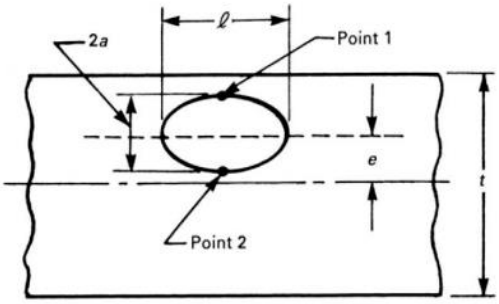

Figure 3.8 embedded (buried) flaw

The crack is fully inside bulk material, however one of the crack tips is close to the inner surface, which may influence the crack tip behaviour. If Point 1 is close to the inner surface it may be influenced by plastic deformation of the remaining ligament.

The risk of plastic deformation of the smallest ligament for embedded crack buried far away from inner surface is much lower due to the larger size of the remaining ligament. Furthermore, the local plasticity in front of the crack tip in the ferritic base material is lower compared to austenitic stainless steel.

The size of plastic deformation volume depends on the crack size and stress profile. A large embedded crack may lead to larger plastic zone than a small subcladding crack. For a subcladding crack, there is more plasticity in the austenitic material than in the ferritic material.

Several proximity rules are codified for characterisation of this type of flaw as a surface flaw (surface breaking crack = through clad crack in our case). This may be done if the ligament is small and the crack is too close to the surface.

3.1.5.4 Nozzle corner crack

Such cracks have initiated during thermal shock and have been investigated in the past HDR investigation (“Heiss Dampf Reaktor”, thermal shock on real denuclearized RPV) [22].

Nozzle corner crack at inlet nozzle has two possible postulated shapes:



Figure 3.9 Nozzle crack shapes

Remark. The nozzle corner cracks are relevant for both PTS (for safety assessment) and p-T curves (for limitation of pressure at lower temperature during normal operating condition).

3.1.6 Flaw orientation

If a flaw must be postulated, the orientation of the flaw leading to the maximum crack tip loading is usually selected. However, due to experience gained during the manufacturing of vessels and NDT as well as destructive examination, some orientations can dominate:

- In weld metal, flaws are generally oriented in the welding direction.
- In base metal, flaws can be oriented in all directions,
- In heat affected zone, flaws can be oriented in both directions.
- The UCC are oriented perpendicularly to the direction of welding for clad deposition, producing axially oriented cracks in the vessel beltline. They are clustered where the passes of strip clad contact each other.

The “new” type of flaws and records found recently (H2 flakes, metallurgic NDT records, high number of findings) will not be considered in the benchmark. These flaws are usually not significant for the RPV integrity due to their small through-wall dimension.

The usual procedure follows the ASME procedure (characterization, grouping for flaws close to each other, projection as planar flaw) and leads to the assessment of a flaw with maximized SIF. Other approaches with mixed mode SIF ($K_{equivalent}$) may be considered in detailed assessment. However, the material resistance has to be appropriately selected for the assessment (mixed mode).

3.1.7 Transient load

Typically, the TH loadings in the RPV result from a 3D system TH analysis. The pressure in the RPV is one of the loadings calculated by TH code. The thermal-hydraulic models of the fluid flow within the RPV have evolved during the last decades. In the past, the RPV downcomer was not nodalized in detail (only one volume was used for the downcomer), and the TH loading conditions passed to the structural assessment were averaged (height, azimuth) and smoothed over time.

However, mixing analyses were sometimes additionally performed to get more detailed information of the TH loading in the downcomer. The most detailed analysis is recently performed by a CFD code. All these predictions have different levels of detail and confidence compared to the reality (experiment or plant). An interface between TH- (output) and structural assessment (input) is required.

The results obtained from TH codes for a selected TH transient are quite extensive and simplified results (smoothing) are usually passed to the structural assessment.

In “0D” TH system analysis, this represents the “old” TH calculation (one volume), there is no cold plume, i.e., no temperature variation in circumferential direction, and thus temperature variation only

in radial direction. Also here, a choice of the data to be passed to the structural assessment has to be made like average temperature from all axial elevations.

In the 80s, RPV fracture-mechanics studies were more likely based on 1D TH data, for which a 1D structural assessment was logical. In practice, the RPV structural assessment was performed mainly considering an axisymmetric RPV TH-loading (neglecting plume). The 3D structural analysis of RPV with plume has been performed only based on TH-results from validated (against experiment) mixing code or originating from CFD.

Currently, the system codes (like RELAP) can provide 2D TH results for the reactor downcomer for which 1D to 3D structural analysis may also be performed. Based on such new results from the system code, we can calculate (maybe not enough conservatively) cold plume, considering 2D temperature map of downcomer. However, this should be validated against more detailed/reliable mixing analysis.

In mixing analysis, there are different types of output from the TH task, but mainly fluid or wall temperature in cold leg, in nozzle, in the downcomer (in cold plume and in ambient). Some codes provide also heat transfer coefficient and temperature variation in axial direction in DC (output in different levels).

The width of cold plume can be given by formulas from literature or output of the code. It can be dependent on axial position in DC and on time. Usually, conical shape of cold plume is considered. It is a difficult task to develop the data transfer for structural analysis if the mesh used in TH analysis is different from the FE mesh used in the structural analysis.

Questionable is the shape of temperature profile in circumferential direction between middle of cold plume and ambient. Two basic approaches – stepwise and Gaussian profile – are typically considered. Past benchmarks (outside APAL) showed small dependency of PTS results on this profile.

Even for one reactor and one TH code, different splits of DC in both axial and circumferential direction were used by different partners. This can cause troubles, when transferring data among the partners, e.g., many variants of TH analyses for LTO improvements (need for adjustments of auxiliary codes for data transfer).

The CFD calculations can provide full 3D and time dependent temperature map of the inner surface of RPV wall in the downcomer. However, a script for data transfer (mapping) into structural calculation is needed. Some smoothing in time and averaging/interpolation in space is needed for this data transfer from the CFD calculations to structural calculations. In APAL, only limited number of CFD solutions are available, and the mapping to FEA for structural calculation is still linked with large effort. FEA meshes for structural assessment considering TH data from system code or mixing code are usually coarse, as compared to FEA meshes required when using TH data from CFD analysis (more elements or finite volumes for fluid in CFD models close to the RPV surfaces, no symmetry, small time steps).

3.1.8 Other loads (residual stresses)

According to WP1 it is recommended to consider residual stresses (RS) in the RPV beltline welds, therefore they will be also included as input data for the baseline case.

Several recommended stress profiles are present in the literature (FAVOR) and normative documentation (KTA 3201.2 [23]) for the RS in RPV circumferential welds (connecting two forgings). When a cosine shape of RS is assumed, only their maximum levels may differ (56 to 70 MPa) for a circumferential crack (axial stress component). The situation is different for the circumferential stress (axial crack), there a constant stress may be considered. For the benchmark, the value relevant for the German RPV was considered (56 MPa), with a cosine shape for circumferential cracks and constant shape for axial cracks, see also [6]. Sensitivity studies were done for other profiles, i.e., the FAVOR residual stress profile.

In addition to the RS in weld, the RS in cladding and the RS in the base and weld metal due to cladding were discussed. The RS in intact cladding are unavoidable at low temperature due to the difference in thermal expansion coefficients between austenitic stainless steel and ferritic steel. The RS state in the HAZ region under the cladding can show tensile stresses due to post-weld heat treatment (PWHT). For the German RPV design used in ICAS, slight compressive stresses in the HAZ exist, therefore a tensile RS in the HAZ (under the cladding) can be neglected.

Elastic-plastic FEM calculations (not performed within APAL) with introduction of relevant RS before PTS loading either by direct introduction of the stresses or by introduction of strains as initial load are recommended as a good practice for deterministic RPV integrity assessment.

3.1.9 Stress intensity factors

The state of the art in 2010 has been described during the CRP 9, see IAEA Tecdoc [20]. To calculate the SIF, two basic options co-exist:

a) engineering methods, whereby use is made of analytic formulas or tabulated collections of stress intensity values for given defect, vessel geometries and loads,

b) cracked body finite element analyses, in which the crack is directly modelled in the mesh and subjected to the appropriate loadings.

While option b) allows detailed analysis of a specific defect, vessel geometry, material properties and transient conditions, the specialized engineering solutions (option a)) now available for RPV applications that have been developed from detailed cracked body FE analyses are highly accurate especially for elastic problems or dedicated elastic-plastic problems (UCC) and provide a rapid and essential tool for considering many transients and postulated defect geometries/orientations.

Other methods, such as XFEM, are also available, but will not be discussed here in more detail.

It must be emphasized that for RPV with inner cladding, solutions for cracks close to cladding have been developed recently with explicit consideration of stresses in cladding and in base metal. Such solutions are required for the benchmark to avoid discrepancies among partners in K_I estimation.

For the benchmark, a selection of K_I formulas (reference solutions) is given in [2].

For TCC, the solution provided in [17] based on the elastic stresses in cladding and base material (without additional plastic correction) is an envelope compared to the FEA elastic-plastic assessment. Therefore, it is assumed that a plastic correction is not required upon the domain of definition.

For UCC, it has been demonstrated that the correction for plasticity (due to cladding) is necessary to get envelope results.

It must be noted that FEA-based SIF formulas exist for UCC with semi-elliptical shape where crack fronts in the ferritic material AND in the cladding were modelled (see [17]). A K_I solution was provided during PROSIR project for crack with elliptical shape and one crack tip located at the clad-base region, a plastic correction was also prescribed. **The adoption of K_I solution of embedded cracks (as in FAVOR: elastic [15]) for UCC (elastic and plastic) is not straightforward because the solution implemented in FAVOR may be out of its validity range and nodalisation may lead to considering the stress discontinuity due to the cladding. Furthermore, plasticity in front of the crack tip located at the cladding-base metal interface (or near the cladding-base metal interface, if there is a small ligament) is not considered. The new CAPAL-version of FAVOR [26] is placing the embedded crack very close to (but not exactly at) the cladding-base metal interface and adopting the K_I solution of embedded cracks for UCC. This leads to a better approximation of the reference CEA solution of K_I at the deepest point of an UCC. However, the CAPAL results for UCC are not conservative, thus this approach is not recommended.**

SIF solutions for embedded (buried) cracks are codified in ASME Section XI, RSE-M. Details are also provided in [15] (FAVOR), see Figure 3.10.

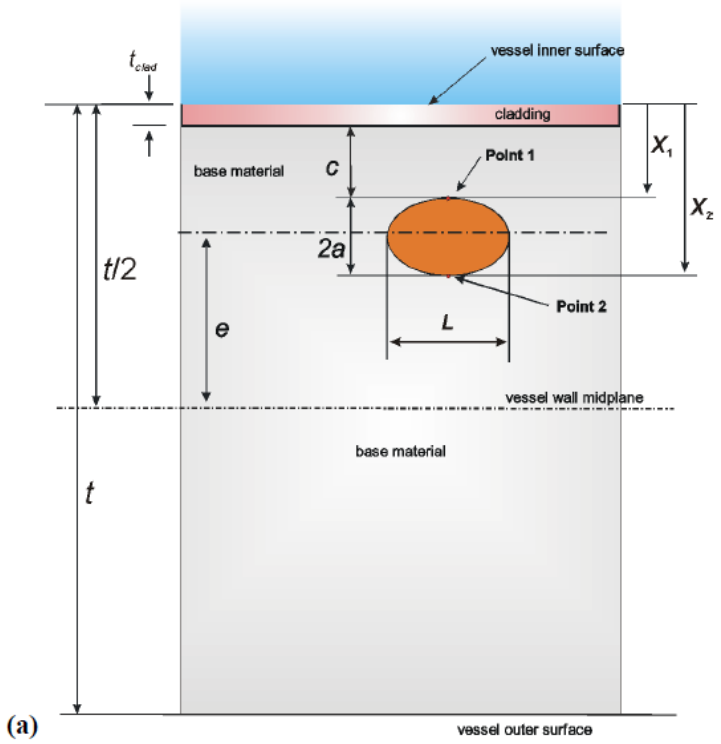

Figure 3.10 Model for buried flaw in FAVOR

Only evaluation of the Point 1 (shown in Figure 14) is implemented in FAVOR. The Point 1 is more relevant from fracture mechanics point of view in case of (inner RPV surface) overcooling transient.

Different crack surface proximity rules co-exist in the different codifications ASME, RSE-M, AME, JSME, API, and the comparison performed in [24] shows that the API is the most severe. According to [24], the stress intensity factor increases with a decrease in ligament size and with decrease in the aspect ratio depth/length. It is suggested, for a conservative structural integrity assessment of a cracked component, that the embedded crack shall be replaced by a surface crack when the ligament and the crack shape ratio are small. This interaction between cracks (or between crack and surface) increases in case of plastic deformation of the small ligament under loading.

The question of multiple flaws can arise. If the detected flaws are close to each other, flaws shall be combined. However, for the deterministic benchmark (addressed in this deliverable) with postulated flaw, only one flaw will be considered in the deterministic assessment.

Specific SIF solutions had to be developed for defect located in the nozzle region (surface crack at nozzle corner) due to the complex geometry (ASME Section XI; Chapuliot [25]). However, these solutions do not consider the cladding explicitly.

3.1.10 Fracture mechanics RPV safety assessment and limit conditions

The usual methodology is derived from the IAEA Tecdoc [20] and an illustration is given in Figure 3.11 considering the brittle crack initiation as criterion for the analysis. It helps to identify the final results to be provided during the benchmark, i.e., the maximum allowable adjusted reference temperature (RT_{NDT} concept or Master curve approach).

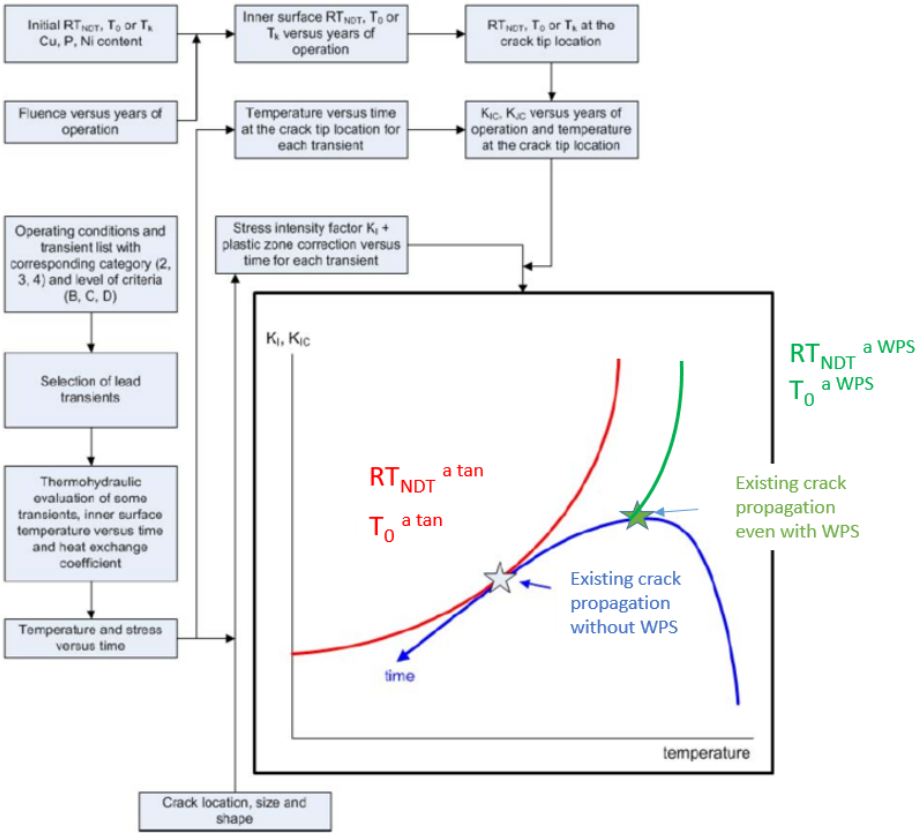

Figure 3.11 Schematic of a typical RPV integrity assessment process derived from IAEA TECDOC

For each individual analysed PTS sequence, the limiting material behaviour in terms of allowable stress intensity factor (K_{Ic}-curve that corresponds to max. all. index temperature $RT_{NDT}{}^{a}$ or $T_0{}^{a}$) and the crack loading path in terms of stress intensity factor (K_I) are considered as a function of temperature T and should be presented in a (allowable) stress intensity factor vs. temperature diagram. A schematic description of the assessment is provided in Figure 3.11. The figure does not show the actual fracture toughness (K_{Ic}) determined in a material testing but a K_{Ic}-curve that corresponds to a maximum allowable index temperature ($T_0{}^{a}$ or $RT_{NDT}{}^{a}$).

The calculated SIF must be enveloped (maximized to be conservative and on the "safe" side for a safety assessment, therefore a plastic correction must be applied in the case of defect located close to the cladding-base metal interface (UCC or embedded/buried crack) because the linear elastic solution may not consider the additional crack opening due to the cladding plastic deformation. For elastic-plastic calculation (using adequate tensile curves) with crack embedded in the mesh, the plastic correction is not needed.

3.1.10.1 Historical lower bound tangent approach limit condition

The max. all. ART for analysed transient corresponds to the allowable stress intensity factor curve (K_{IC} vs. T) shifted horizontally up to the point where it becomes a tangent to the crack loading path of the PTS transient (K_I vs. T). By the "tangent point" we mean the point, in which in the conventional inequality $K_I <= K_{IC}$ becomes an equality once the equality $K_I = K_{IC}$ is reached.

$$max.all.ART = \sup\{ART: \forall t\ K_J(t) \leq K_{Jc}(ART, T(t))\}$$

This equation defines max. all. ART for one transient, one fixed crack and one point on the crack front using the tangent approach and "crack initiation" as a failure criterion.

3.1.10.2 Limit condition with WPS benefit

As explained in detail in APAL D1.2 [7], the existence of the WPS effect is thoroughly established and its consideration in PTS evaluation can be seen as the state of the art. The following definition according to KTA3201.2 concerning crack initiation and WPS may be considered:

"*Crack initiation does not occur if this curve $K_I(t,T)$ does not reach the curve of static fracture toughness K_{Ic} (T). If the crack tip in course of the considered actual transient has been subjected to thermal loading beforehand (warm pre-*stress) *no crack initiation will occur if the crack resistance KFRAC upon warm pre-stress is not reached. If the stress intensity $K_I(t,T)$ is less than the crack arrest toughness $K_{Ia}(t,T)$ a running crack is arrested.*"

"*Upon warm pre-stressing of the crack front and in the case of a monotonously decreasing stress intensity factor (specimen cooling under sustained load), i.e. at dK/dt ≤ 0, crack initiation is to be excluded. Warm pre-stressing will also cause an increase in fracture toughness to exceed KIc to obtain KFRAC. Thus, crack initiation is excluded even in case of increase of stress intensity factor upon renewed warm pre-stressing (re-loading) if the stress intensity factor does not reach KFRAC."*

KFRAC is fracture toughness at reload (within a WPS cycle) and is not related to any specific WPS model. However, opposed to the physical KFRA value, the KFRAC value used in the assessment is dependent on the WPS model used for the calculation.

A simplified approach to WPS is chosen for APAL as provided in FAVOR code. The maximum allowable transition temperature for analysed PTS transient corresponds to the allowable stress intensity factor curve (K_{IC}) shifted horizontally up to the point where it intersects the K_I vs. T curve at the point relative to the maximum value of K_I during the PTS event if warm pre-stressing (WPS) approach is applied.

Following text in *italic* is taken from FAVOR manual [15]:

"*a flaw is assumed to be in a state of WPS when the following condition is met:*

- *a falling applied-KI field – the time-rate-of-change of the applied-KI is non positive (<= 0).*

If a flaw is in a state of WPS, it is not eligible for initiation (or re-initiation if it has arrested) until it leaves the WPS state.

Three conditions can be stated for a flaw <u>not to be</u> in the state of WPS and, thereby, to be eligible for initiation. These three conditions are:

> *Condition (1): the applied-KI is greater than KIc(min), where KIc(min) is defined by the fracture toughness model for the temperature at the flaw tip;*
>
> *Condition (2): a rising applied-KI field – the time-rate-of-change of the applied-KI is positive (dKI /dt > 0);*
>
> *Condition (3): in a rising applied-KI field, the driving force at the flaw tip must exceed some portion of the previously-established maximum applied-KI (designated as KI(max)) experienced by the flaw during the transient up to the current point in time under consideration – applied- KI $(\tau) \geq \alpha$ KI(max) (τ)* "

This is the "FAVOR approach". All the three conditions must be fulfilled simultaneously for a flaw to be eligible for initiation. The flaw initiates, if and only if all the three conditions are met together with $K_I > K_{Ic}$.

It must be stated that the time rate of change of the applied K_I is not always non-positive during the transient, however it must be distinguished between re-loading (real re-load due to significant pressure increase or due to a subsequent thermal shock loading) and small loading fluctuation (artefact) for which the WPS beneficial effect is not challenged. This is relevant to the so called "conservative approach" (which requires dK/dt<0 all the time after warm pre-stressing).

3.1.10.3 Limit condition with crack arrest

Several approaches exist for crack arrest analysis, from basic up to sophisticated, depending on the amount of data available as well as the adopted goal or confidence level, see Figure 3.12 from IAEA TECDOC [20].

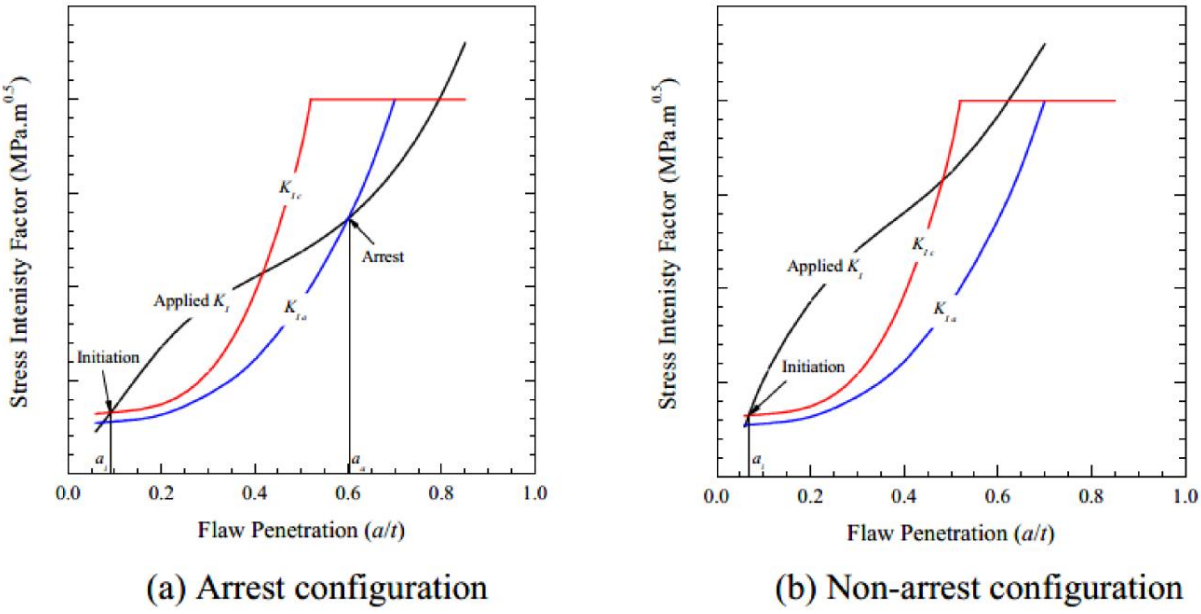

Figure 3.12 Arrest and non-arrest configuration according to [20] (at time of initiation)

The basic approach for crack arrest follows PROSIR (only brittle assessment): once the crack initiates at one of the crack tips, the crack is growing instantaneously (at the same time as the crack initiates) in all relevant directions of the crack plane:

- up to the inner surface without crediting an arrest potential in the cladding and becomes a TCC
- with a large length so a/c is assimilated to be zero without crediting an arrest potential in the azimuthal direction (for circumferential crack) or vertical direction (for axial crack)
- through the wall thickness from inside to outside in the case of an inner surface thermal shock

The temperature increases from inside to outside at time of initiation during an overcooling thermal shock due to safety injection in the RPV. Furthermore, the fluence is decreasing. Therefore, the fracture toughness (K_{IC} and K_{IA}) also increases through the thickness. As a conservative simplification it can be assumed that RT_{NDT} after several EFPY (= ART) is constant through the wall thickness. The through-wall crack propagation stops whenever the condition K_I (a, a/c=0, t) ≤ K_{IA} (T_t;$RT_{NDT\ x=a}$) is achieved.

Crack re-initiation is checked for later time in the transient, see Figure 3.13. If the crack does not initiate anymore (or is in WPS state) and remains within the inner 75% (APAL criterion) of the ferritic material wall thickness along the whole transient up to the end of the PTS event, then it may be stated that the crack achieved a stable arrest state. For the large LOCA, the depressurization occurs in the first 10 seconds but the whole PTS event up to stabilized cooling must be assessed (no large changes of temperature or pressure are allowed).

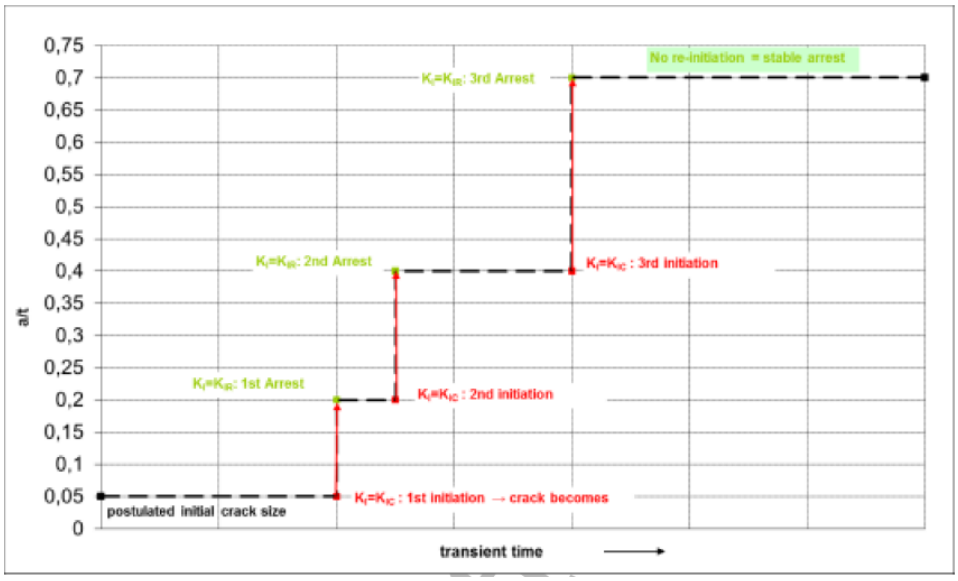

Figure 3.13 Schematic crack arrest procedure

Ductile tearing risk and risk of plastic collapse shall be checked once the crack achieves larger size after initiation/arrest, see also Initiation-Growth-Arrest procedure in FAVOR [15].

For APAL, simplifications will be made for the upper shelf by limiting K_{JC} at a level to be determined for German ferritic material (CARISMA EC project) for after 2.5 mm of stable crack growth (so allowance of ductile crack growth of 2.5 mm).

3.2 Description of first benchmark performance: Pre-Requisite deterministic analyses (PR-Det)

The first benchmark performance contains a series of pre-requisite analyses to allow partners to verify and validate their tools before they move to the benchmarks in tasks 3.4 (LTO) and 3.5 (TH uncertainties) for margin assessment, which require much more computation. This is to avoid misunderstanding in the different steps and to allow re-definition of the parts of the benchmark or input parameters if needed. The steps are separated into fracture-mechanics and margin assessment. The overall benchmark structure is quite simple: a common fracture mechanics assessment approach is the Pre-Requisite (PR) analysis, so this is the first step: PR-Det-1 (part 1), educational to learn state of the art (SOA) solutions (reference); PR-Det-2 (part 2), to compare other solutions with reference results for base case scenario, starting with the structural assessment (SA), see Spisák, 2024 [1] and the fracture mechanic analysis (FMA), see Angermeier (2024) [3]. In a second step the margin assessment is performed following the same verified approach between base case scenario and LTO improvements or for TH-uncertainties.

Table 3.7. Overview of deterministic benchmark (some non-mandatory tasks are not presented)

	Pre-requisite (**PR**)			**Margin** assessment	
	Part 1 Verification	**Part 2 (PR-Det.2)** Comparison of TH-code		**LTOs improvement**	**TH uncertainties**
Scenario	Not required, data are made available to partners	APAL-ICAS T2 Base Case			
TH global (system code)		System code results (RELAP, TRACE, ATHLET)		9 LTO improvements or human actions	59, 93, 130 simulations
TH mixing		Mixing code (ECC-MIX, KWU-MIX)		Some LTOs	93 simulations
Temperature & Stresses (SA)	Pre-defined, i.e. provided!	Simplified 1D/2D ***Task 3.1 PR Det.2.0***	Sophisticated 3D FEA ***Task 3.1 PR Det.2.0***	1D /2D Simplified, Sophisticated 3DFEA (selected LTOs), ***Task 3.1***	1D / 2D(cold plume) simplified ***Task 4.1***
Crack type	UCC, TCC	TCC, UCC (for non FAVOR user), Buried (for FAVOR/CAPAL user only)			
K_I model	Reference K_I: ***PR-Det 1.1.1*** And individual for comparison: ***PR-Det 1.1.2***	***PR-Det 2.1*** Ref. K_I Or Individual K_I	same	Same ***Task 3.4***	Same ***Task 3.5***
K_{IC} model + Limit condition+ Max all. ART	RT_{NDT}, T_0 Tang.: ***PR-Det 1.2.1*** WPS: ***PR-Det 1.2.2***	***PR-Det 2.2***	same	Same ***Task 3.4***	Same ***Task 3.5***
Crack arrest	***PR-Det 1.3***	***PR-Det 2.3***	same	Not mandatory	Not mandatory

Task 3.3:

3.2.1 PR-DET 1.1: Determination of SIF with provided temperature, stresses and pressure profiles

3.2.1.1 PR-Det 1.1.1: SIF solution provided

The objective of this task is to use the reference SIF solutions with explicit consideration of stresses in the cladding and base metal applied with input data provided (see Annex 8). The stresses and temperature are provided to allow K_I calculation in the pre-requisite (educational) part (PR-Det Part 1). These data are provided from a simplified structural assessment considering APAL-ICAS-T2 preliminary transient for an arbitrary location and are supplied in the form of digitized tables in a file. Stresses without / with weld residual stresses (WRS) were provided. Pressure loading on crack face shall be considered for TCC. E-modulus ratio (cladding / base metal) of 0.85 is kept constant for the sake of simplicity. Both crack orientations shall be considered. Flaw location in base metal and in weld (i.e. with weld residual stresses) shall be considered. Mandatory: TCC, UCC elastic, UCC with plastic correction, TCC a/c=0 if crack arrest is performed.

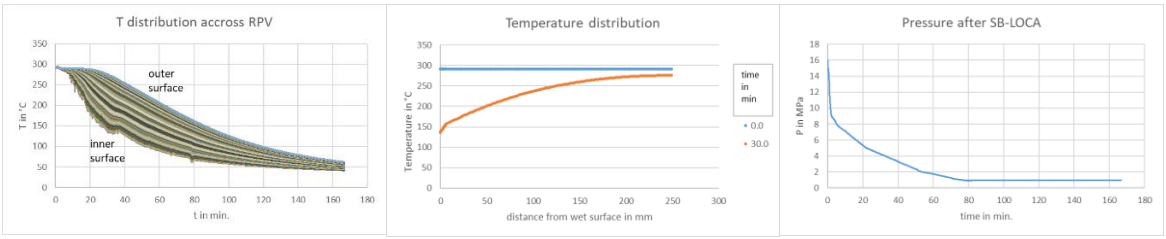

Figure 3.14. Temperature to be considered for PR-Det Part 1

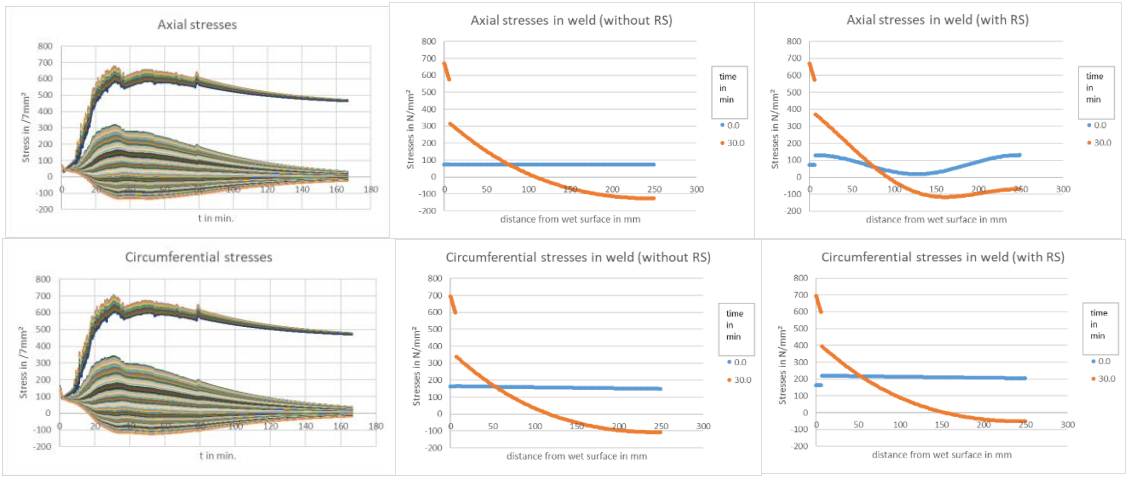

Figure 3.15. Stresses to be considered for PR-Det Part 1

Output: SIF results shall be provided for both crack tips A (deepest point) and C (interface clad-base/weld metal) as a function of time.

3.2.1.2 PR-Det 1.1.2: Individual/own SIF solutions

Since partners may use third party software (FAVOR/CAPAL/PASCAL) with own SIF solution different from the reference ones and without possibility to add the reference solution to the source code, the previous task is repeated with the SIF solution intended to be used in the benchmark. It is necessary for proper comparison and evaluation of bias compared with the reference SOA solutions for TCC and UCC (with plastic correction) crack type. For partner using third party software buried flaw shall be investigated.

3.2.1.3 PR-Det 1.1.3: SIF Sensitivity study (non-mandatory)

Consideration of buried crack (for non-commercial software user), TCC nozzle (crack shape: axial straight crack front in base metal), a/c=0 or circular with a/c=1. Stresses profiles from 3D non-uniform FEM structural assessment considering mixing TH loading shall be considered. This will be provided from D3.1 [1].

3.2.2 PR-DET 1.2: Determination of max. all. ART considering crack initiation

The max. all. ART is the value (calculated from PTS fracture mechanics safety assessment) being shifted in order to find the highest index fulfilling the limit condition (tangent or WPS). Partners will have to compute K_{Ic} = f(T at considered crack tip) for each crack tip for increasing RT_{NDT} and T_0 (starting from 0 °C) and perform the assessment of max. all. ART using the limit condition for the different approaches: tangent and WPS (simplified max WPS and sophisticated WPS for some partners). The required results are: max. all. ART (RT_{NDT} and T_0 concepts) for Tangent approach, simple WPS max. approach; corresponding K_{IC} (ASME), K_{IC} (Master curve 5% Lower Bound) and time of initiation. The non-mandatory tasks are: use of WPS model for K_{IC}, size correction for T_0 considering basic UCC size, embedded crack (for partners not using FAVOR/CAPAL), other location: nozzle crack, flange weld.

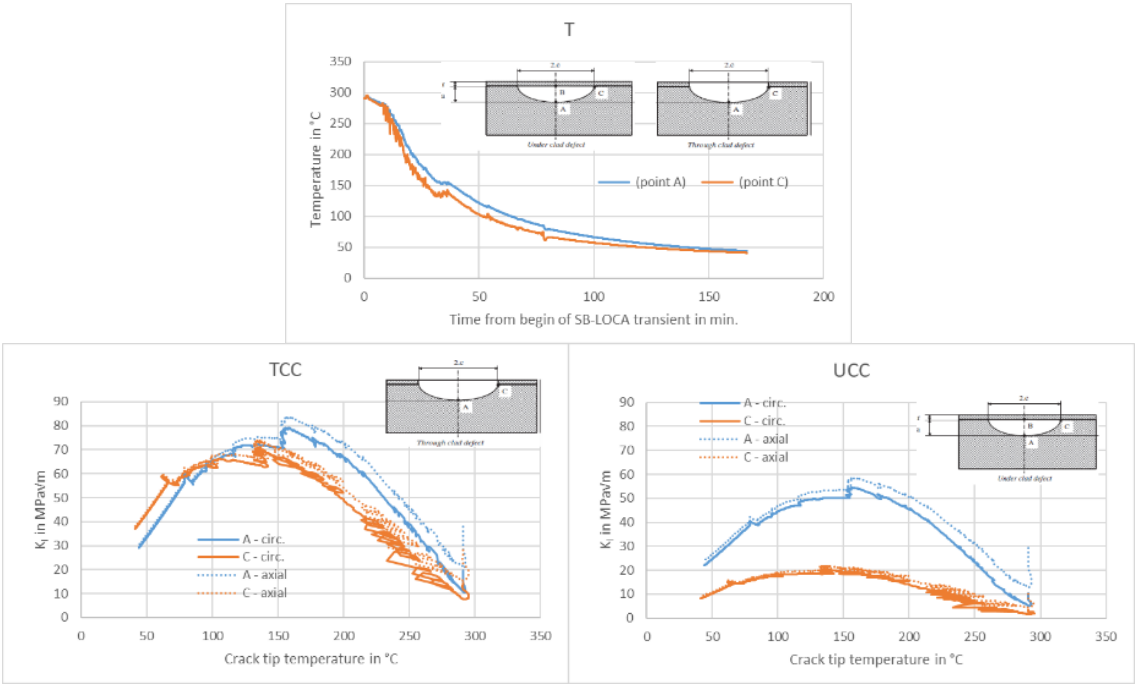

Figure 3.16. Input data for PR-Det 1.2

3.2.2.1 PR-Det 1.2.1: Tangent Approach

The max. all. ART can be obtained iteratively by increasing the RT_{NDT} index by a computational aging step of 1K (starting from non-irradiated T_0 or RT_{NDT}) and comparing the resulting K_{IC} curve with crack loading path for all times of the transient. Other ways shall be explained. Once the condition for crack initiation is achieved considering $K_I = K_{IC}$ (T, $RT_{NDT\,j}$) then max. all. ART is equal to estimated RT_{NDT} last index.

The tangent approach (no WPS) is considered using ASME curve: determination of max. all. ART ($RT_{NDT}{}^{a\,tan}$) with $K_I <= K_{IC}$; using Master Curve concept: determination of max allowable T_0 ($T_0{}^{a\,tang}$) with $K_I <= K_{IC}$ (5% Lower Bound). Comparison between max. all. ART for RT_{NDT} concept and MC concept i.e. $RT_{NDT}{}^a$ and $T_0{}^a$ can be done considering $RT_{T0}{}^a = T_0{}^a + 19.4K$.

3.2.2.2 PR-Det 1.2.2: WPS Approach

The conditions for the flaw not to be in a WPS state is: "*in a rising applied-KI field, the driving force at the flaw tip must exceed some portion to the previously-established maximum applied-K_I (designated as K_I(max)) experienced by the flaw during the transient up to the current point in time under consideration – applied- $KI(\tau) \geq 1 * KI(max)(\tau)$* "

The max. all. ART is obtained iteratively by increasing the RT_{NDT} index by a fictional "computational aging" step of 1K (starting from -33 °C non-irradiated T_0 or RT_{NDT}) and comparing the resulting K_{IC} curve with crack loading path for all times of the transient. Once the condition for crack initiation is achieved considering $K_{Imax} = K_{IC}$ (T, $RT_{NDT\,j}$), with K_{Imax} being the maximum value of K_I achieved at the crack tip during the transient, then max. all. ART is equal to estimated RT_{NDT} last index. The global maximum SIF is considered as simplified formulation: no fracture for a loading level lower than maximum loading at high temperature. Using ASME curve: determination of max. all. ART ($RT_{NDT}{}^{a\,WPS}$) with $K_{Imax} \leq K_{IC}$; using Master Curve concept: determination of max. all. T_0 ($T_0{}^{a\,WPS}$) with $K_{Imax} \leq K_{IC}$ (5% Lower Bound).

3.2.2.3 PR-Det 1.2.3/1.2.4: non-mandatory tasks with regards to WPS and ductile tearing

Alternative approaches are applied with different models to quantify the magnitude of the WPS effect, using codified K_{IC} WPS (for example Chell, KFRAC), WPS 90% $K_I$max (VERLIFE) or other national

approaches. Consideration of ductile initiation (tearing) is considered following CC-830 R1 approaches (T_0 based) for evaluation of ductile crack initiation risk at nozzle corner.

3.2.3 PR-Det 1.3: Determination of max. all. ART considering crack arrest (non-mandatory)

Allowance of crack initiation and arrest during the base case scenario is investigated. Data are provided, including temperature fields, K_I for TCC for initial geometry a=10mm, 2c=60 mm. After initiation a K_I matrix considering a fully surface extended (a/c=0) growing crack geometry is provided for several crack depths (starting with 10 mm up to $0.75t_{ferritic}$). RT_{NDT} is considered constant across thickness, azimuth and height. Limit condition are K_{IC}, K_{IA} ASME (5% Lower Bound). The maximum for both K_{IC} and K_{IA} is 220 MPa√m (only cleavage fracture consideration, no tearing check after arrest).

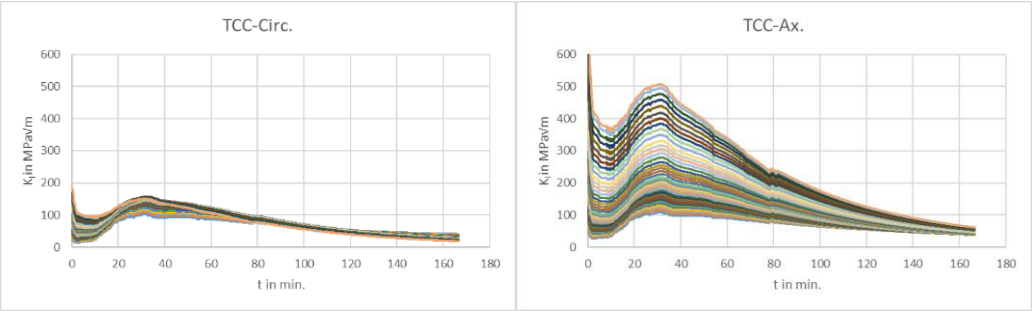

Figure 3.17. KI matrix for TCC extended (a/c=0) and increasing crack depth

3.2.4 PR-DET 1.4: Crack arrest analysis (non-mandatory)

K_{IC} ASME, K_{IA} (5% Lower Bound) at each potential crack tip location and each time of the transient shall be calculated by each partner, considering crack growth step of 0.5 mm. Basic approach for crack arrest analysis is: starting point: max. allowable ART+20 K from previous task considering WPS (so initiation is ensured); consideration of surface (ferritic material) and deepest point for crack initiation ; once $K_I >= K_{IC}$ then TCC with a/c=0 ; crack growth immediately and stopped if $K_I \leq K_{IA}$; fluence, chemical composition considered as constant upon thickness for this analysis, so the RT_{NDT} is considered constant too (starting with RT_{NDT} = max. all. ART $_{WPS}$ + 20K, re-initiation if $K_I > K_{IC}$, re-arrest if $K_I<K_{IA}$).

Output: Crack arrest results for first arrest (size of crack at first arrest, K_I shall be equal to K_{IA}!) for verification, check for further initiation for t>ti considering $K_I \geq K_{IC}$ for tangent approach; considering WPS (no-initiation by K_I decrease with $K_I(t>ti) <$ maximum K_I (t between initiation and end of transient). Present full results and diagrams (K_I, K_{IC}, K_{IA}) timely dependent + crack tip temperature dependent. Repeat the previous analysis but increasing starting ART by 1 K up to achieving the $ART_{no\ arrest}$ at which a stable crack arrest does not occur; max. all. ART $_{arrest}$ = $ART_{no\ arrest}$ -1 K ; Full results and diagram considering max. all. ART $_{arrest}$. Sensitivity studies with consideration of RT_{NDT} profile across thickness (RT_{NDT} at crack tip), with/without WPS after crack stop, T_0 basis for K_{IC}, $K_{IA,}$ check of plastic collapse and ductile tearing at crack stop.

3.2.5 PR-DET 2: Evaluation of max. all. ART based on different TH calculations and individual SA and methods

After reconciliation and verification of the tools for SA and fracture mechanics assessment (FMA) (especially K_I for TCC + UCC) is performed, qualified partners will share efforts to determine the max. all. ART from the different TH calculations output made available from WP2. All partners shall use the same methodologies as intended in WP4 probabilistic (part of the verification pre-requisite). All intermediate results shall be documented (task 3.1/4.1 for SA and task 3.3 for fracture mechanics assessment) and final results of max. all. ART shall be summarized in a table for each variant of the base line assessment.

The mandatory base line for the assessment of max. all. ART is:

- Axial and azimuthal location:
  - inside plume at elevation of the core weld -2638mm from the RPV nozzle centerline (system code)
  - inside merging plumes at elevation of the core weld -2638mm (local mixing)
- Crack types: TCC (shape 1) + UCC plastic, embedded/buried (FAVOR/CAPAL user group)
- Crack tips:
  - TCC (deepest point + point close to clad/base fusion line (FL)
  - UCC (deepest point + point close to FL in ferritic base/weld metal)
  - for FAVOR user group: embedded/buried crack (point close to FL)
- With/without weld residual stress
- both limit condition (tangent, simplified WPS max.)
- both fracture toughness concept (RT_{NDT}, Master Curve)

3.2.5.1 PR-Det in 2.0: Stress and temperature profiles (i.e. D3.1)

The mechanical analysis (structural assessment) is performed with increasing level of effort for the base case transient. The different type of TH results will be shared to the structural assessment. Preliminary assessment is based on the same TH-data from RELAP (Data-kwu76-WP34d.xlsx) to allow verification between partners. Simplified TH loading will be treated considering decreasing simplification and increasing level of effort in the SA. It results in SA assessment considering axisymmetric cooling with: 1D SA for each location, 2D or 3D geometry with thickness transition and both locations included with axisymmetric cooling. Decreasing the simplification results to non-uniform cooling consideration with: 2D SA for each elevation with both cold plumes and ambient regions, additional stresses due to cold plume considering eq.4.3 from IAEA TECDOC or with 2D FEA (ring), full 3D geometry and 3D TH. With System code RELAP results the width of the plume is set to 1/8 of the RPV inner circumference since only code with local mixing models are able to evaluate the cold plume width properly. Boundary conditions for the simplified assessment are: Generalized plane strain, Thermal outside adiabatic (or HTC=1 W/m² K, $T_{outside}$ = 40°C), $P_{outside}$ = 0 MPa.

The sophisticated assessment consists in the consideration of detailed (local) boundary conditions from detailed TH analysis from local mixing code able to consider cold plume merging or CFD mapped to 3D FEA mesh for the full RPV geometry analysis. Comparison of sophisticated analysis with simplified SA (1D / 2D / 3D with system code results; 1D and 2D with local mixing results for T/HTC/cold plume width) shall be performed with the goal to identify a safe level of simplification. Sensitivity studies: cladding thickness, mesh density, residual stress.

For the consideration of individual TH data the performance of SA (and sub-sequent analysis SIF, max. all. ART) shall focus on the aforementioned mandatory base line.

PR-Det 2.2: Determination of SIF (i.e. D3.3)

Tasks are similar to PR-Det 1.2 considering mandatory base line.

PR-Det 2.3: Determination of max. allowable ART (i.e. D3.3)

Tasks are similar to PR-Det 1.3 considering mandatory base line.

PR-Det 2.4: Non mandatory: determination of crack arrest (i.e. D3.3)

Tasks are similar to PR-Det 1.4 considering mandatory base line limited to TCCs.

3.3 Margin Assessment

3.3.1 Benchmark for tasks 3.4 considering LTOs improvement

LTO improvements listed in Table 3.8 will be investigated with regards to max. all. ART.

The SA and FMA are performed considering the mandatory baseline case. Intermediate results are documented in task 3.3 and final results shall be tabulated in a template for the different configurations.

Table 3.8. TH transient variants for LTO improvement investigation

LTO improvement / Human action	Simulated change
1. Heating of water in the HPIS tanks	Heated from 15 °C to 45 °C
2. Heating of water in the ACCs	Heated from 20 °C to 50 °C
3. Heating of water in the LPIS tanks	Heated from 15 °C to 45 °C
4. Decreasing the HPSI head	Decreased down to 75%
5. Decreasing the HPSI capacity	Decreased down to 75%
6. Reduction of HPIS flow (operator action)	Reduced at 1800 s to one pump
7. Decreasing of ACC pressure	Decreased from 26 bar to 20 bar
8. Different cooldown rate (operator action)	Changed from 100 K/h to 200 K/h
9. Isolation of ACCs (operator action)	Isolated at 500 s

Analysis with RT_{NDT} concept/$K_{IC\ best\ estimate}$ as well as MC concept/T_0 $K_{IC\ 50\%}$ shall be performed. The margin in max. all. ART against crack initiation can be made in a relative way by comparison with the max. all ART obtained with the base case: horizontally (difference between lower bound toughness and best estimate toughness) or vertically (difference in max. all. ART between LTO improvement and base case). The “best” LTO’s improvements to minimize the risk of brittle fracture of the RPV can be identified looking at the highest positive margin. The negative margins help to identify the PTS contra-productive measures and to propose counter measures.

3.3.2 Benchmark for task 3.5 considering TH uncertainties

The Wilks’ method provides a non-parametric (distribution-free) method to estimate the desired tolerance limit with a prescribed confidence that the estimate is conservative. Several runs will be considered: for N=59 simulations (fulfilling the population proportion and the confidence level of 0.95), N=93 and N 130 simulations. Proceed in analogy to PR-Det 2 and calculate max. all. ART for all N transients and report results for all configurations defined by the mandatory baseline case. The run leading to the minimum from all max. all. ART (for N=59) is the “true” bounding envelope transient for which TH parameter can be identified. A ranking of all runs based on max. all. ART has to be done as well as a counting for each range. Sensitivity study on range width shall be performed. Margin considering lower bound (P=0.95), best estimate and base case shall be determined.

4 First Benchmark Performance

The goal of the first benchmark performance is to have a well-established benchmark to be used in the margin assessments (task 3.4 and 3.5). This first benchmark performance was done stepwise to identify critical steps. This includes pre-requisite verification and validation to ensure valid and comparable solutions for a well-defined benchmark.

Therefore, the pre-requisite (PR) benchmark definition was given to all partners considering a limited number of parameters and limited choice of methods for the mandatory parts that will allow:

- to understand and permit **verification** for each step of the calculation chain following strictly the proposed solutions and providing input data (**part 1**) of PR-Det (PR-Det 1).
- a **comparison with partners' own solutions** for each step of the calculation chain but only providing the TH loading input (**part 2**) of PR-Det (PR-Det 2).

4.1 First benchmark performance part 1 results: Calculations based on provided temperature and stress distributions (PR-Det-1)

4.1.1 Description of the task

The first part of the benchmark defines a baseline enabling verification (considering prescribed calculation methodology) and comparison (considering own methodology) between the partners. This has to be performed gradually based on the same input data (provided) for all steps of the safety assessment: stress intensity factor (SIF), maximum allowable adjusted reference temperature (mandatory: considering initiation, non-mandatory: considering crack arrest).

Content:

- Part 1.1: Determination of SIF with provided Temperature & Stresses (1D)
  - Use of the same SIF solutions
  - Use of individual SIF solutions
  - Sensitivity study
- Part 1.2: Determination of max. all. ART with SIF provided
  - Use of tangent approach
  - Use of (simple) WPS-max approach
- Part 1.3 (non-mandatory): Determination of max. all. ART considering crack arrest with provided matrices of SIF and temperature

Temperature and stress distributions through RPV wall thickness for the whole time interval of the transient are provided in the Benchmark definition D3.2 for a given TH loading and shown in this report in section 3.2.1.

Baseline case (mandatory):

Assessment of TCC and UCC:

- Location: (provided for the middle of the plume under CL3, azimuth 202.5°C, at -2638mm from nozzle center line, belt line weld)
  - Temperature T and stresses distributions for cylindrical part of the RPV without and with residual stresses in weld (provided)
    - axial stress SigA; tangential stress SigT (circumferential, tangential and hoop stresses are synonyms for cylinder),
    - axial stress with residual stress in BM SigA+RS, tangential stress with residual stress in BM SigT+RS
  - Pressure p=f(time) to be applied on crack faces for through-clad crack TCC
- Cracks:

- Orientation: longitudinal and circumferential
- **TCC; a in base metal = 10 mm i.e., total depth = 16 mm (10mm + 6 mm cladding through)**; **a/c = 1/3**; **shape 1; 2c = 60 mm**
  no plastic correction (linear elastic)
- **UCC**; a in base metal = **10 mm**; **a/c = 1/3; 2c = 60 mm**
  no plastic correction (linear elastic)
  with correction to account plasticity
- **embedded/buried (FAVOR users)**; **2a = 20 mm; 2c = 120 mm; small ligament to base-clad interface = 5 mm, no plastic correction (linear elastic)**

Non-mandatory:

- buried crack (non-mandatory for non-FAVOR users) 2a = 20mm; 2c = 120 mm; small ligament to base-clad interface = 5 mm, without plastic / with plastic correction

Output:

- stress regression factors for axial and circumferential stresses = f(time)
- shape factors i for provided cracks
- K_I at two locations for TCC and UCC
  - closest to the fusion line with cladding (in ferritic material, i.e., point C)
  - at the deepest point of the crack (point A)
- Tabulated values of K_I and temperatures for all discrete times
- Plot of K_I as a function of the temperature at considered location

4.1.2 Results for part 1.1: Determination of SIF

In the following chapters the results without weld residual stresses are presented. Results with weld residual stresses are given in [3].

4.1.2.1 TCC

In Figure 4.1 and Figure 4.2 the K_I results of all participating partners without residual stresses are shown. The relative deviation is calculated by comparison with the Framatome results. The KI-calculations were done using the CEA-method by Chapuliot et al. [18] for TCC and UCC.

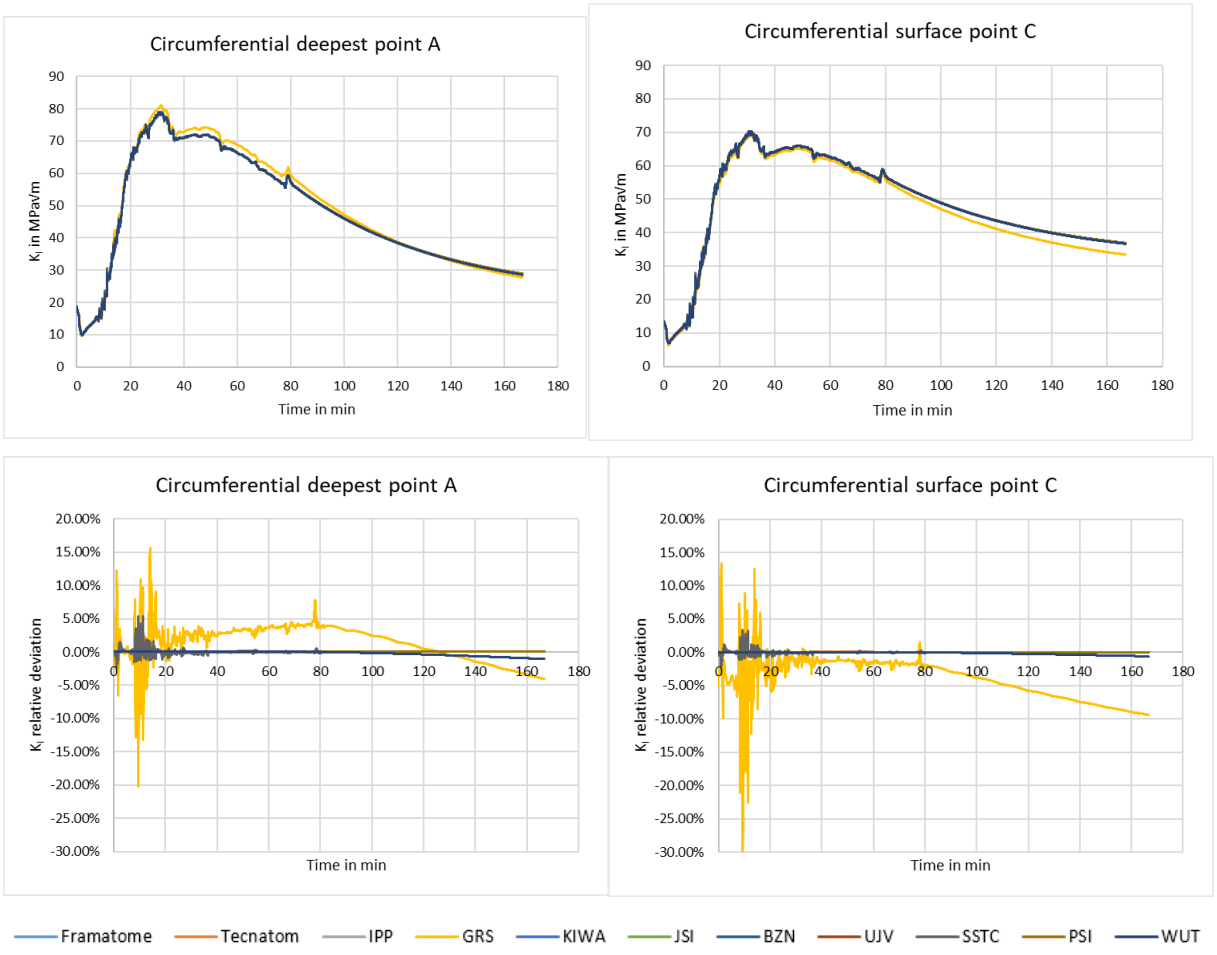

Figure 4.1: TCC Circumferential – K_I results absolute and relative values

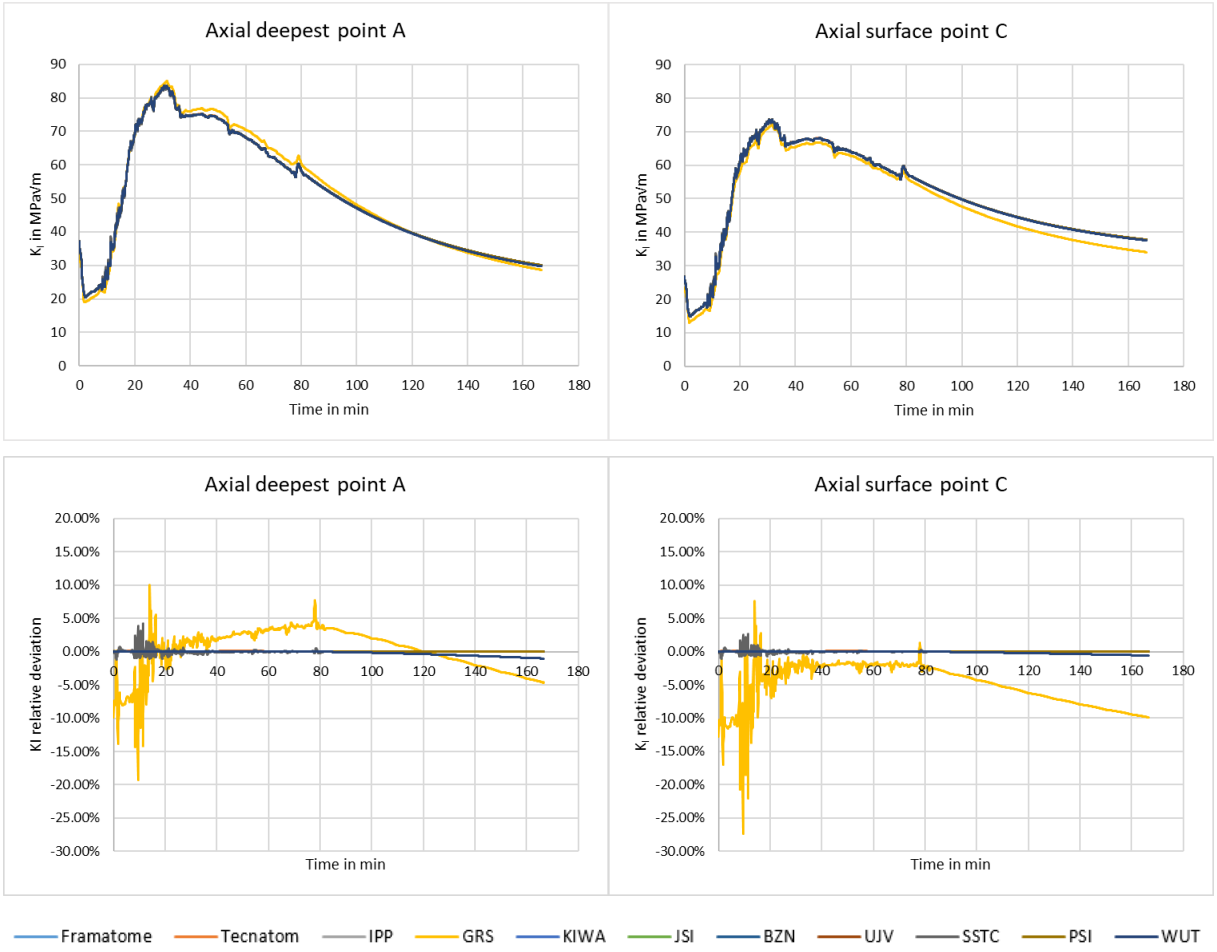

Figure 4.2: TCC Axial – K_I results absolute and relative values

Except for some punctual outliers the results agree well among the partners. GRS has overall, in the relevant timespan a relative deviation up to 5% for point A, for point C the deviation is up to 10%. This is due to the fact that they use their own stress calculations rather than the specified stresses.

Some partners used different K_I methods than the recommended CEA method for the following benchmarks (WP3.3 part 2, WP3.4+3.5, WP4), this concerns mostly the partners that were using FAVOR [15]. As far as the benchmark WP3.3 part 1 concerns, the results of all partners using their own solution for determination of SIF is shown in Figure 4.3. IRSN used the CEA method but without consideration of crack face pressure. The Framatome results are the same as before (CEA method) and are shown as a comparison. The Framatome and IRSN results are almost identical for most of the time in the transient. In the beginning of the transient the IRSN results are slightly lower since here the crack face pressure is not considered which has a larger effect when the other loading is small. The results for axial crack show the same behaviour.

The FAVOR results are different compared to the others since FAVOR is using the FAVOR program equations. The truncated stress distribution is approximated with a third order polynomial. K_I values are calculated for each of the individual terms and then added to obtain the total K_I value. Also, FAVOR can consider TCC with length (2c) to total depth ($a+t_{clad}$) ratios equal to 2, 6 and 10. The SIF results for the APAL TCC ratio of 3.75 (= 60/(6+10)) are obtained by linear interpolation of the values computed by FAVOR. A clear source of the discrepancy for FAVOR-TCC2 SIF results is thus the linear interpolation for length-to-total-depth ratios of 2 and 6 at the required value of 3.75.

The results from PSI were calculated using an in-house implementation in Python based on the FAVOR solution in FAVOR v16.1. Therefore, the PSI results are not the same as the other FAVOR results.

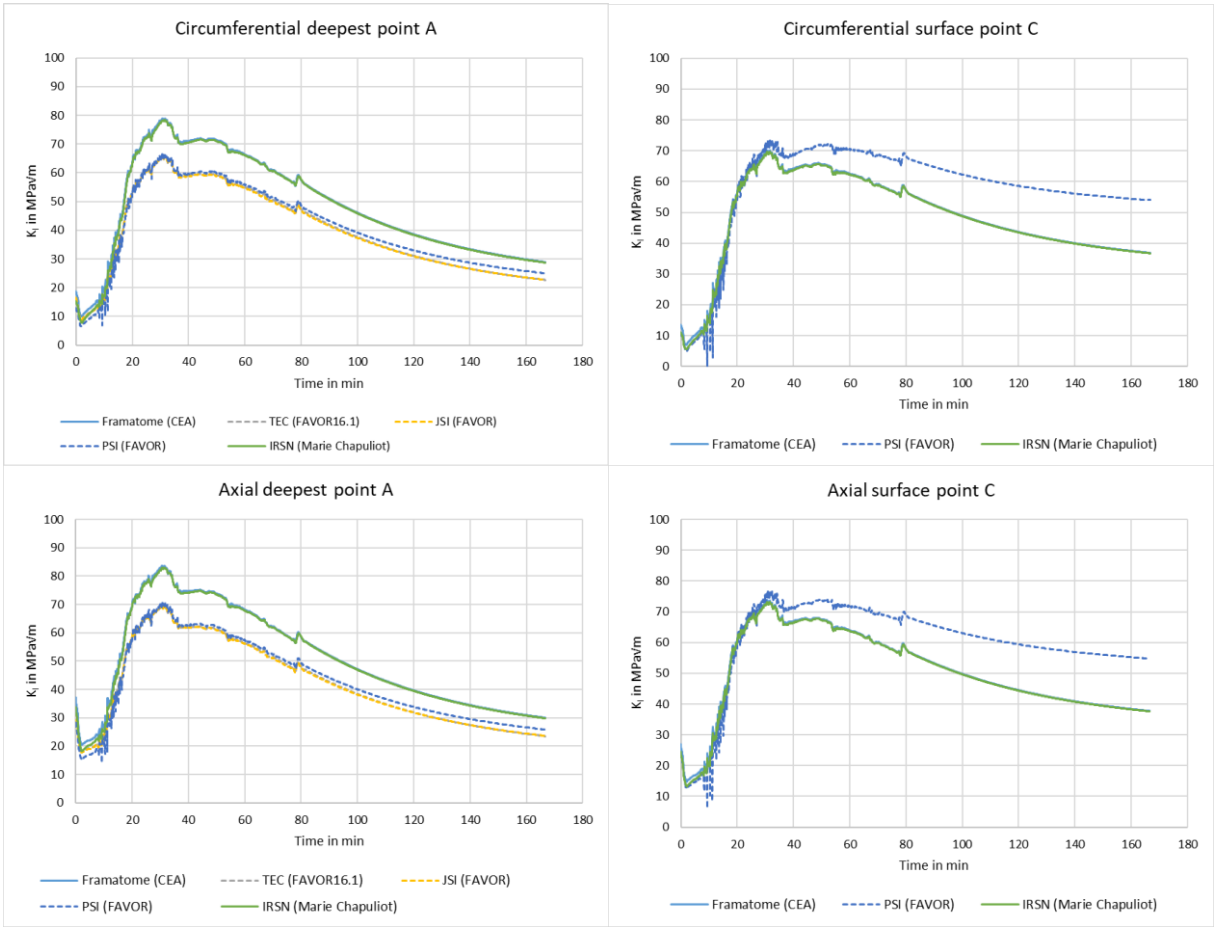

Figure 4.3: TCC circumferential and axial – K_I results own solution without residual stresses

4.1.2.2 UCC

For underclad cracks (UCC), a plastic correction on the stress intensity factor calculation must be applied to get enveloping results. The results shown here (Figure 4.4 and Figure 4.5) are first without and then with consideration of plastic correction (without = elastic results).

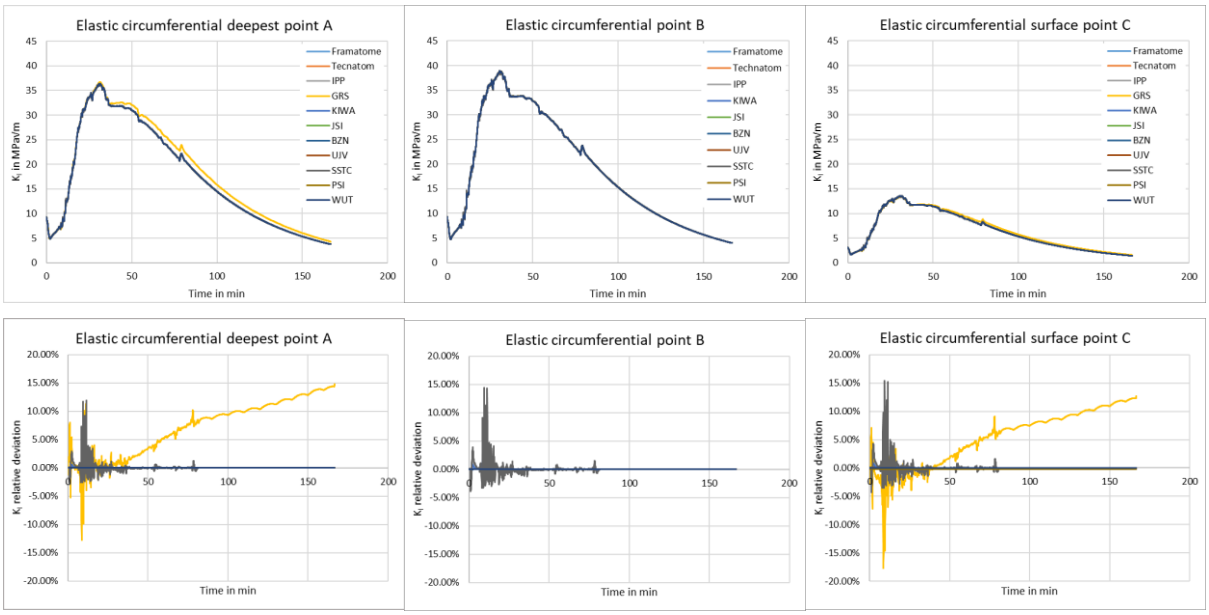

Figure 4.4: UCC Circumferential – K_I results absolute and relative values

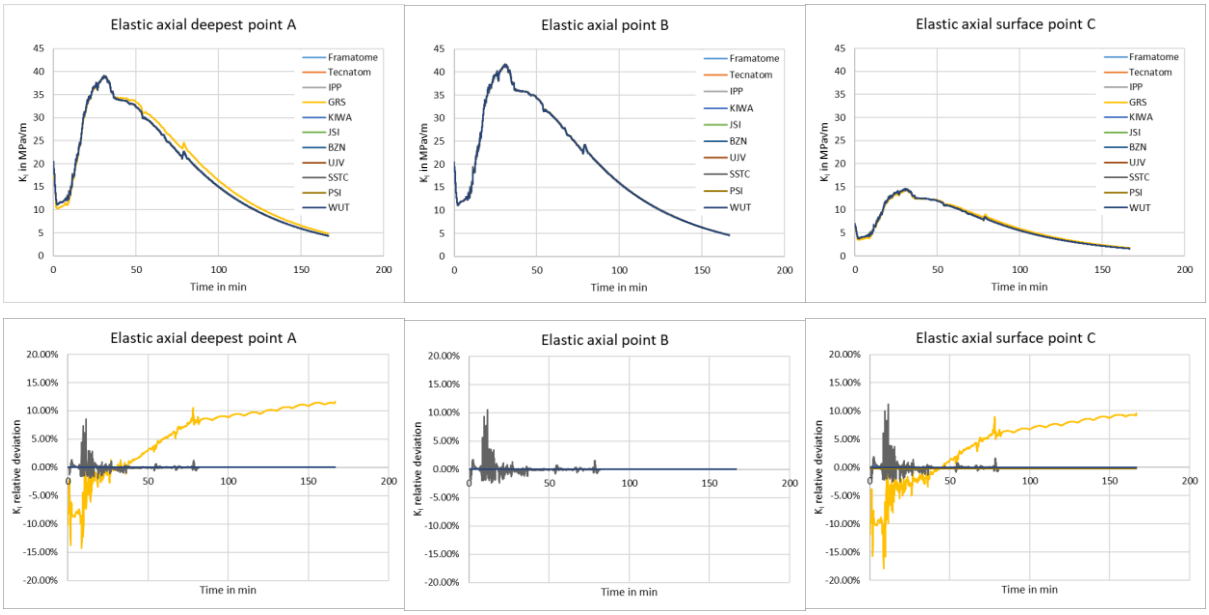

Figure 4.5: UCC Axial – K_I results absolute and relative values

Similarly as for TCC, the results for UCC are in quite good agreement between the partners. GRS again has some deviation, which is higher than for TCC (up to 15% relative deviation in the relevant timespan). The reason for that is the same as mentioned in chapter 4.1.2.1. The effect with the oscillations for KIWA, SSTC and IPP can be observed for both TCC and UCC. The "oscillation effect", which occurs primarily in the beginning of the transient is investigated in detail in chapter 4.1.5.2.

The results for points B and C for circumferential crack (Figure 4.4) show approximately the same behaviour as those for the axial crack (Figure 4.5). GRS has not performed calculations for point B and for K_I with plastic correction (for any of the points A, B, C).

The results for K_I with applied plastic correction are significantly higher than the elastic results. The results for circumferential crack point A are shown in Figure 4.6. The good agreement is confirmed by

the relative comparison, only a small deviation (<2%) for the PSI results can be observed, and again oscillations for the above-mentioned partners. The results for points B and C for circumferential crack (Figure 4.6) show approximately the same behaviour as those for axial crack (Figure 4.7).

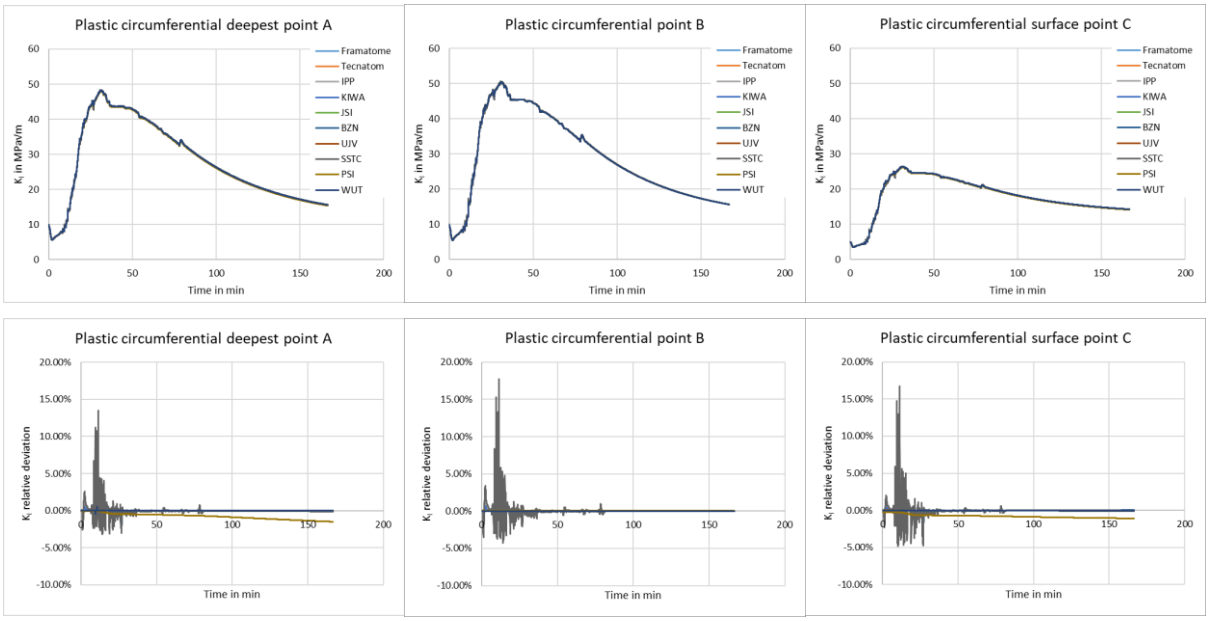

Figure 4.6: UCC Circumferential – K_I results absolute and relative values

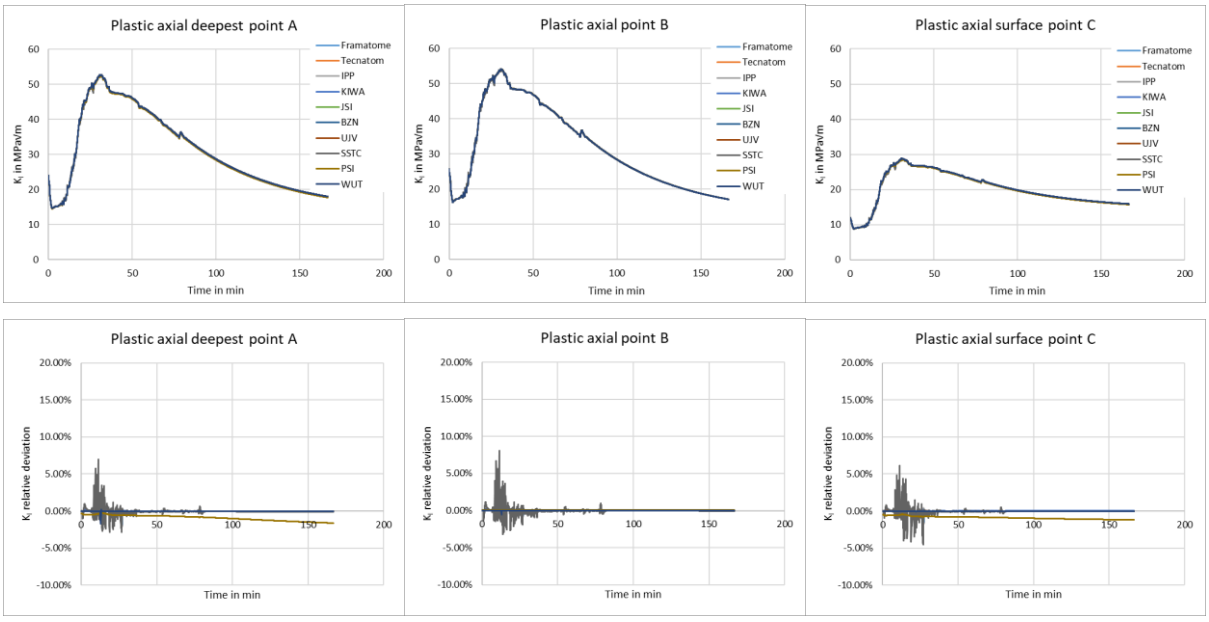

Figure 4.7: UCC Axial – K_I results absolute and relative values

The results of all partners using their own solution instead of the CEA method are shown in Figure 4.8. The Framatome results are the same as before (CEA method) and are shown as a comparison. The Framatome and IRSN results are almost identical for most of the time in the transient. The IRSN results are calculated with the RSE-M 2020 method. The results for axial crack show the same behaviour as for the circumferential crack.

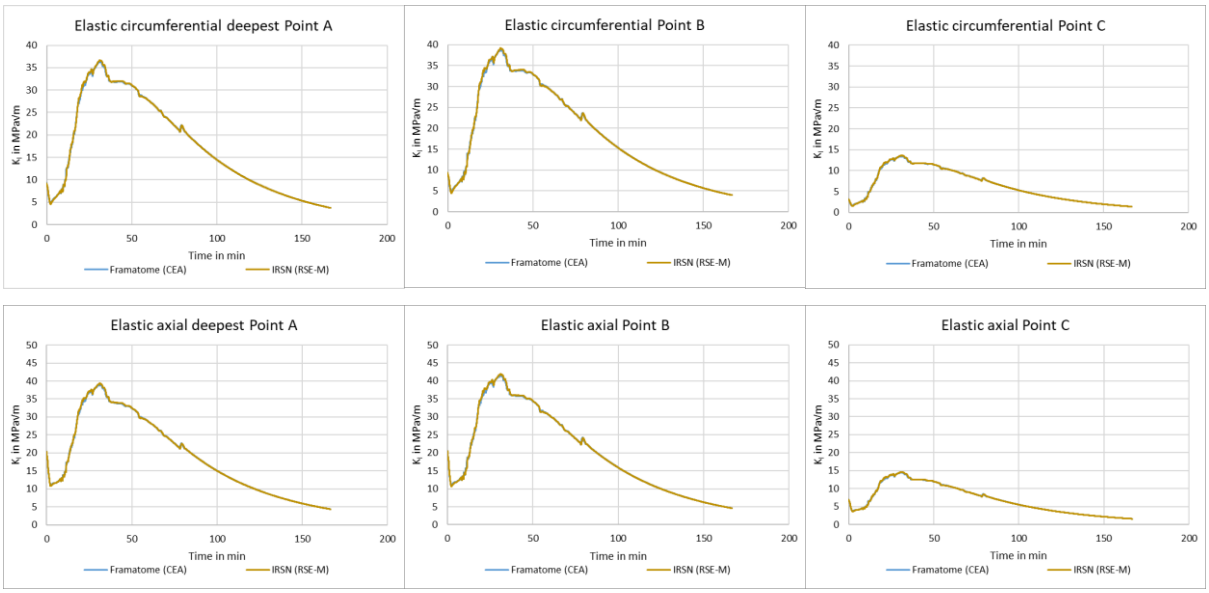

Figure 4.8: UCC circumferential and axial – K_I results own solution without residual stresses

4.1.3 Results for part 1.2: Determination of max. allowable ART considering crack initiation

For the benchmark part 1.2 a SIF distribution (K_I = f(t, x), where x indicates a point at the crack front (A, B, …)) as well as the temperature at each crack tip were provided. Please note that these values are different than in part 1.1. Partners had to compute the maximum allowable reference temperature with the given input data. For this purpose, K_{Ic} as a function of temperature for each crack tip for increasing RT_{NDT} and T_0 (starting from 0 °C) has to be calculated. To perform the assessment, the limit condition for the tangent approach (given by [7]), simplified WPS-max and sophisticated WPS for some partners had to be used. For a description of the different WPS approaches see deliverable 1.2 [7] and WP1 public summary report [8].

Baseline case (mandatory):

- Profiles (SIF and crack tips temperature) are provided for the assessment of the max. all. ART.
- Tangent approach and simple WPS max. approach.
- No size correction to be applied for T_0.

Non-mandatory:

- Sophisticated WPS model
- size correction for T_0 considering basic UCC size
- embedded crack (for partners not using FAVOR),

Output:

- Max. All. ART (RT_{NDT} and T_0 concepts) for Tangent approach, WPS approach
- Corresponding K_{IC} (ASME), K_{IC} (Master curve 5% Lower Bound) and time of initiation
- Diagrams showing crack load path K_I (provided) and fracture toughness curve K_{IC} to be calculated) over temperature and over time with index = max. all. ART

For the tangent approach the maximum allowable adjusted reference temperature $RT_{NDT}^{allow\ tan}$ can be obtained iteratively by increasing the RT_{NDT} index by a computational aging step of 1K (starting from unirradiated T_0 or RT_{NDT}) and comparing the resulting K_{IC} curve with crack loading path for all times of the transient. Once the condition for crack initiation is achieved considering

$K_I = K_{IC}(T, RT_{NDT\,j})$

then $RT_{NDT}^{allow\ tan}$ is equal to estimated RT_{NDT} last index.

The tangent approach (no WPS) is considered

- using ASME curve: determination of RT_{NDT} max allowable ($RT_{NDT}^{a\ tan}$) with $K_I <= K_{IC}$
- using Master Curve concept: determination of T_0 max allowable ($T_0^{a\ tan}$) with $K_I <= K_{IC}$ (5% Lower Bound)

The conditions for the flaw not to be in a WPS state (thereby to be eligible for initiation) are described in section 3.1.10 and in deliverable 1.2 [7]. The WPS-max approach ("simple approach") states, that a crack can only initiate if the current K_I is higher or equal to the maximum K_I up to that point in the transient.

The results presented in this chapter are in the following units if not stated differently: K_{IC} in MPa√m, Max. allow. ART in °C and time of initiation in minutes. The value of K_{IC} corresponds to the time of initiation.

4.1.3.1 TCC

The results for maximum allowable reference temperature considering crack initiation agree well between the partners, see Figure 4.9. The difference is below 1°C, this is because some partners have not rounded down to whole numbers as described in the benchmark definition. The difference between the tangent approach results and the simple WPS approach (Figure 4.10) is quite large, about 40°C. The difference between the ASME and the master curve approach is small, 4°C for the tangent approach and only 1°C for the simple WPS approach.

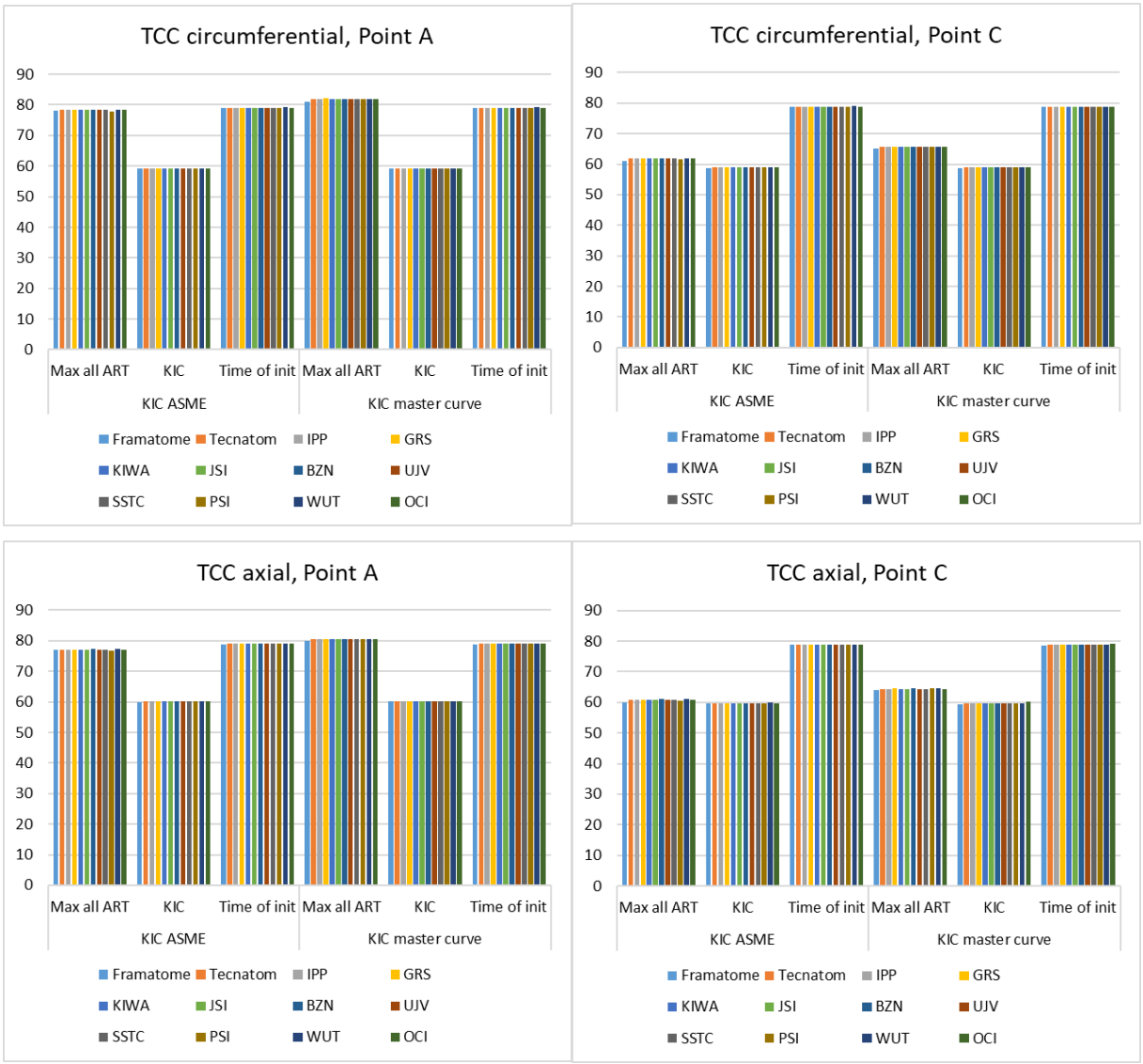

Figure 4.9: Maximum allowable ART (°C) considering crack initiation – TCC tangent approach

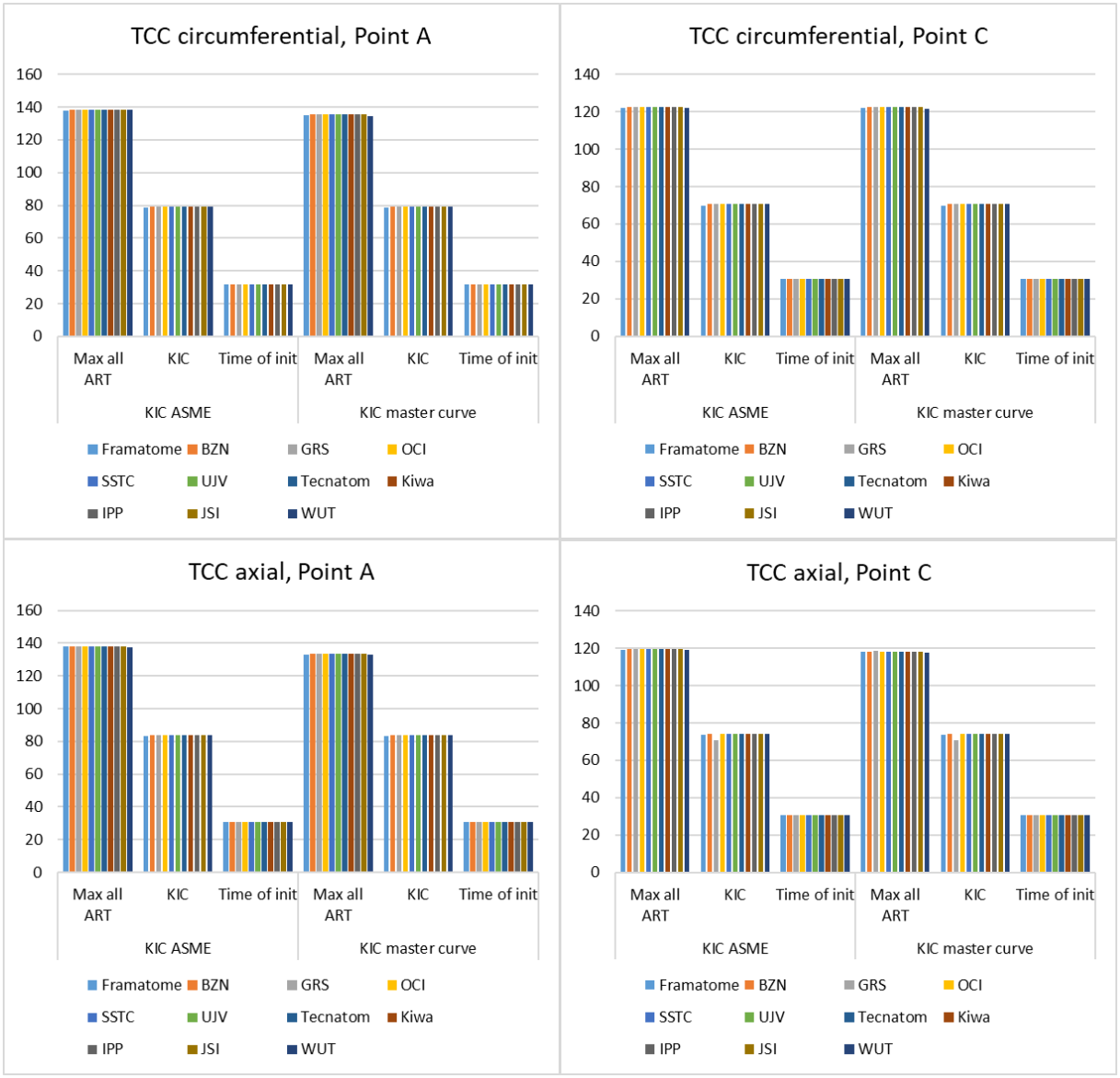

Figure 4.10: Maximum allowable ART (°C) considering crack initiation – TCC simple WPS approach

Some partners have performed additional calculations with sophisticated WPS approaches. In the results for TCC axial point C shown in Figure 4.11 three groups can be identified for this case: one that is identical to the tangent approach, one that is identical to the simple WPS approach, and one that lies approximately in the middle of both. IPP and BZN were using different versions of the Verlife approach, so their results are not the same (2008 and 2013 version).

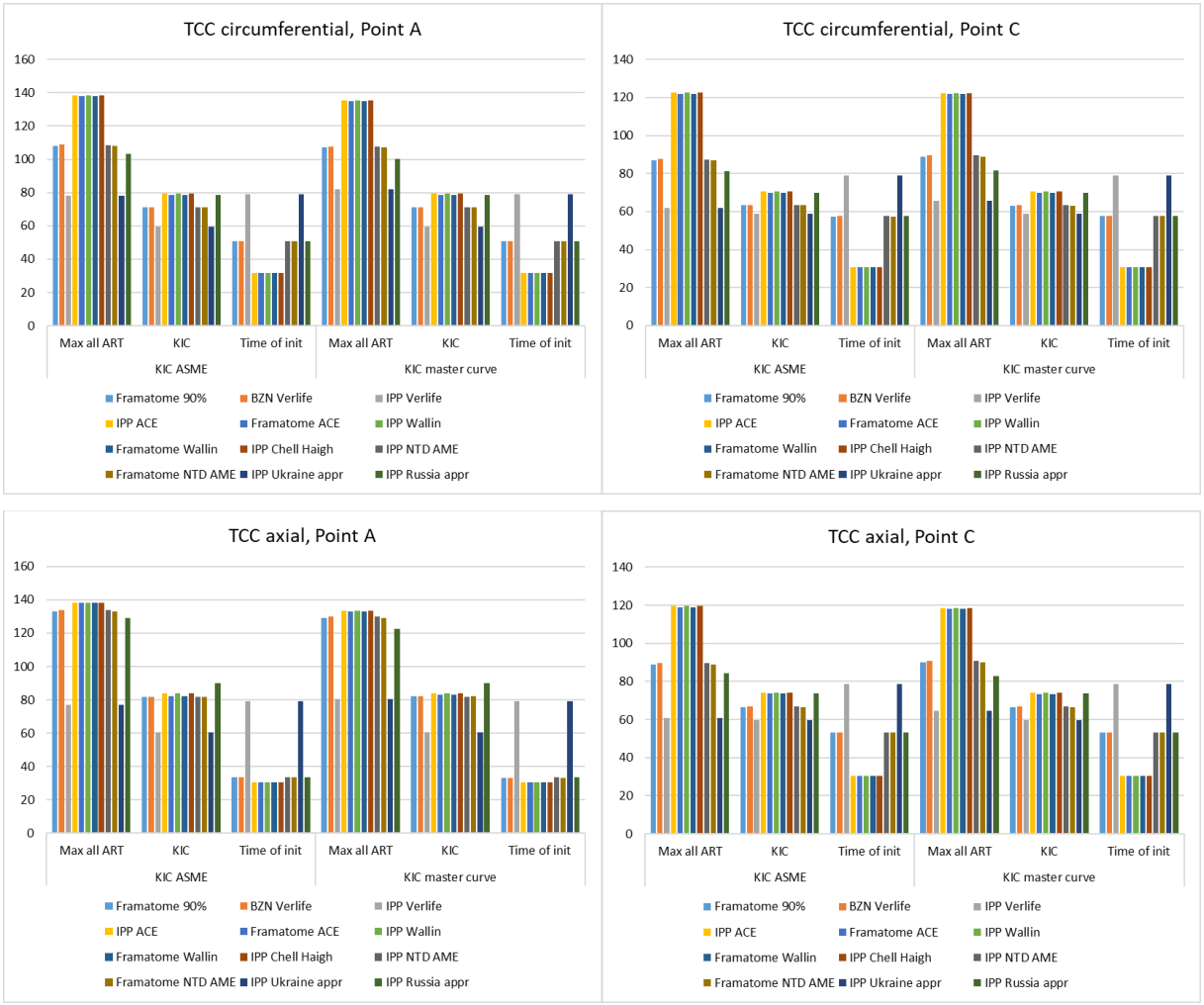

Figure 4.11: Maximum allowable ART (°C) considering crack initiation – TCC sophisticated WPS approaches

The results presented above confirm the conclusions that are also mentioned in deliverable 1.2 of the APAL project [7]. The tangent approach delivers the lowest results for max. allow. ART, whereas the simple WPS delivers the highest results. The results for the sophisticated approaches are either in agreement with the tangent or simple WPS approach; or lie in between for the investigated transient.

4.1.3.2 UCC

For UCC there is only a limit on the ART for point A, in point C there is no initiation. As for TCC, the differences for UCC between the partners are small and have the same reasons as previously explained, see Figure 4.12. The difference between the tangent approach results and the simple WPS approach (Figure 4.13) is again almost 40°C. The ASME and the master curve approach differ only by 3-4°C, where for the tangent approach the ASME results are higher for circumferential crack, and for the simple WPS approach the master curve results are higher for both axial and circumferential crack. The results for several sophisticated WPS approaches are shown in Figure 4.14.

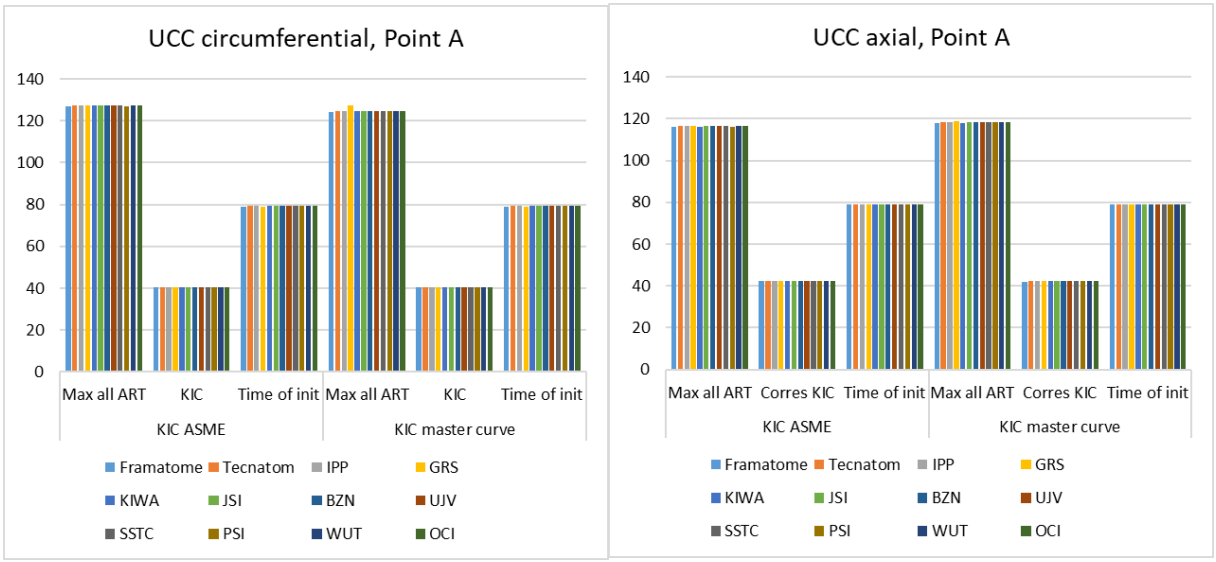

Figure 4.12: Maximum allowable ART (°C) considering crack initiation – UCC tangent approach

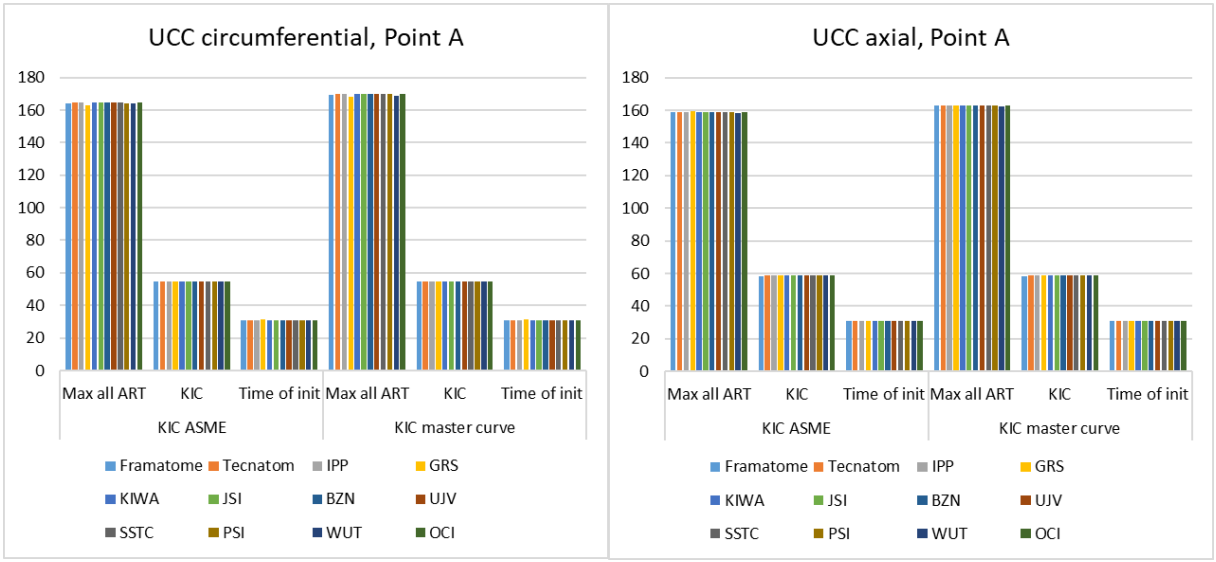

Figure 4.13: Maximum allowable ART (°C) considering crack initiation – UCC simple WPS approach

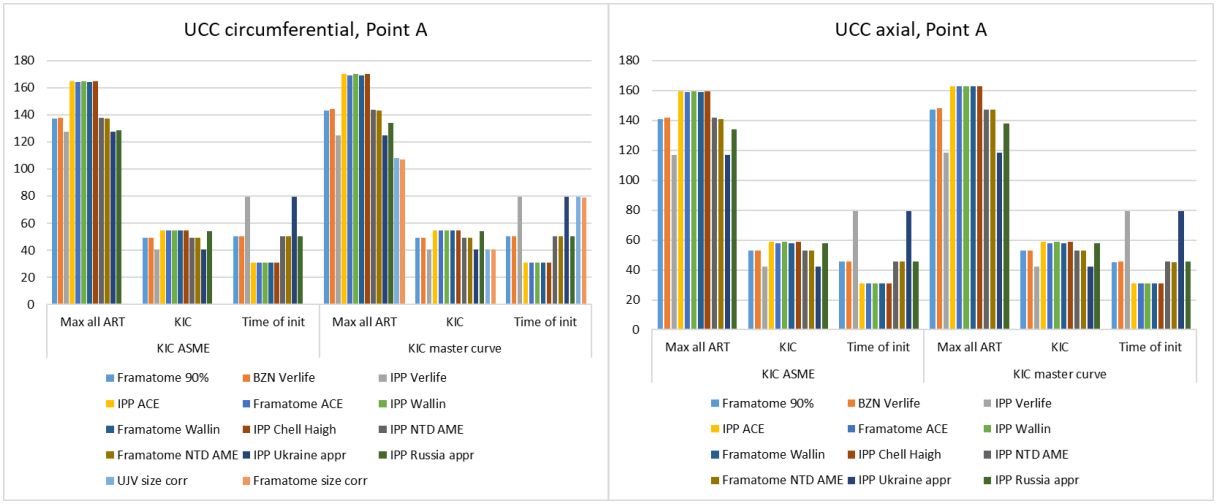

Figure 4.14: Maximum allowable ART (°C) considering crack initiation – sophisticated WPS approaches

The results presented above confirm the conclusions that are also mentioned in deliverable 1.2 of the APAL project [7]. The tangent approach delivers the lowest results for max. allow. ART, whereas the simple WPS delivers the highest results. The results for the sophisticated approaches are either in agreement with the tangent or simple WPS approach; or lie in between for the investigated transient.

4.1.4 Results for part 1.3: Determination of max. allowable ART considering crack arrest (non-mandatory)

Input:

- Provided temperature field and TCC K_I values along time in the transient, for a/c = 1/3 (fixed crack depth a = 10 mm) and a/c=0 (for several crack depths starting with 10 mm up to 0.75*t, measured only in the ferritic material)
- RT_{NDT} is for simplicity considered constant across thickness, azimuth, height
- limit condition K_{IC}, K_{IA} ASME (5% Lower Bound)
- K_{IC} , K_{IA} both max = 220 MPa√m (only cleavage fracture consideration, no tearing check after arrest)

Basic approach for crack arrest analysis:

- Starting point: max. allowable ART+20 K from previous task considering WPS (so initiation is ensured)
- Scenario:
  - TCC as basis
  - consideration of surface (ferritic material) and deepest point for initiation
  - once $K_I >= K_{IC}$ then crack converts to TCC with a/c=0
  - crack grows immediately and stops if $K_I <= K_{IA}$
    - fluence and chemical composition considered as <u>constant through the wall thickness</u> for this analysis, so the RT_{NDT} is considered constant too
  - re-initiation if $K_I > K_{IC}$, re-arrest if $K_I < K_{IA}$
  - stable arrest if through-wall extension remains < 75% RPV wall thickness (ferritic material)

Output:

- K_I (TCC a/c = 0) = f (t,a) for increasing crack depth *a* (up to 75% of ferritic thickness)

- K_{IC} and K_{IA} in dependence on crack depth *a* (and temperature at the crack tip) at each time *t* following initiation for some given levels of RT_{NDT} (starting with ART_{ini} + 20 K)
- Crack arrest results for first arrest considering max. allow. ART_{ini} + 20 K
    - size of crack at first arrest, K_I (following limit condition for crack arrest/cleavage: must be equal to K_{IA}!)
- Check for further initiation for t>ti (ti = time of arrest) considering K_I >=K_{IC} for tangent approach; considering WPS (no-initiation for K_I decrease with K_I(t>ti) < maximum K_I (t between initiation and end of transient)
- full results and diagrams; K_I = f(t); Diagram of development of K_{IC}, K_{IA} in time at the crack tip for the first initiation-arrest) for the crack arrest analysis K_I; K_{IC}; K_{IA} = f(t,a,T(t,a))
- repeat the previous analysis but increasing starting ART by 1 K up to achieving the $ART_{no\ arrest}$ at which a stable crack arrest does not occur
    - max. all. ART_{arrest} = $ART_{no\ arrest}$ -1 K
    - full results and diagram considering max. all. ART_{arrest}

The results presented in this chapter are in the following units if not stated differently: K_{IC} in MPa√m, Max. allow. ART in °C, time of initiation in minutes, depth at first arrest in mm and corresponding K_I (≤ K_{Ia}) in MPa√m. The value of K_{IC} corresponds to the time of initiation and K_I to the time of the first arrest.

In the non-mandatory part of calculation max. allow. ART with consideration of crack arrest, four partners have participated. The results are shown in Figure 4.15. In the case of an axial crack the results are the same as without consideration of crack arrest, since once the crack initiates no crack arrest occurs. Please note that a slightly different transient of temperature and K_I has been used compared to part 1.2.

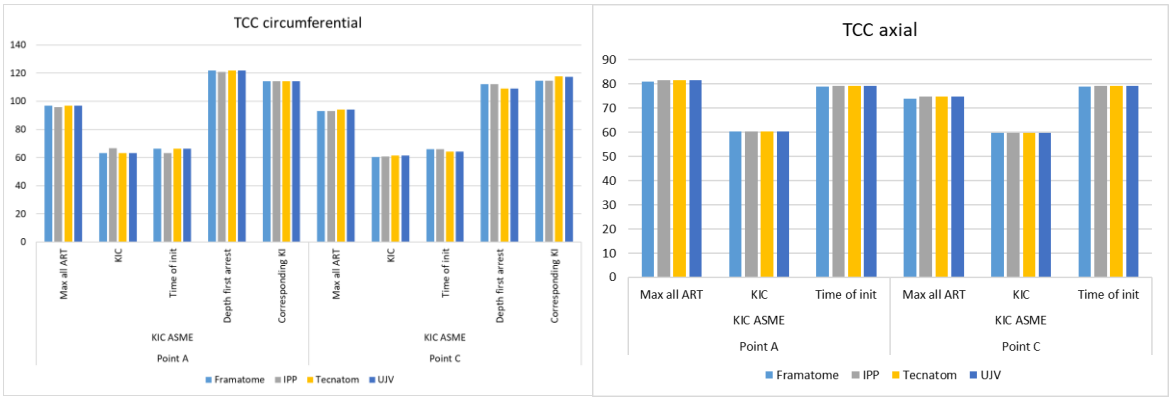

Figure 4.15: Maximum allowable ART (°C) considering crack arrest

4.1.5 Observations and recommendations

During the calculations for the benchmark there were numerous fruitful discussions on the methodology. The main findings and lessons learned are described in this chapter.

4.1.5.1 Observed uncertainties/scatter of results

For the results that are comparable in terms of input data and method used the overall scatter in K_I is in a range of ±5% in most parts of the transient. Some oscillations and other deviations are observed and can be associated with the different implementation of the same method. In summary, within part 1 of the benchmark a common understanding of the tasks and the methods could be established.

4.1.5.2 Oscillations

It was noticed that some partners seem to have the same "oscillations" in the beginning of the transient in a different order of magnitude. The plot for the beginning of the transient is shown in Figure 4.16.

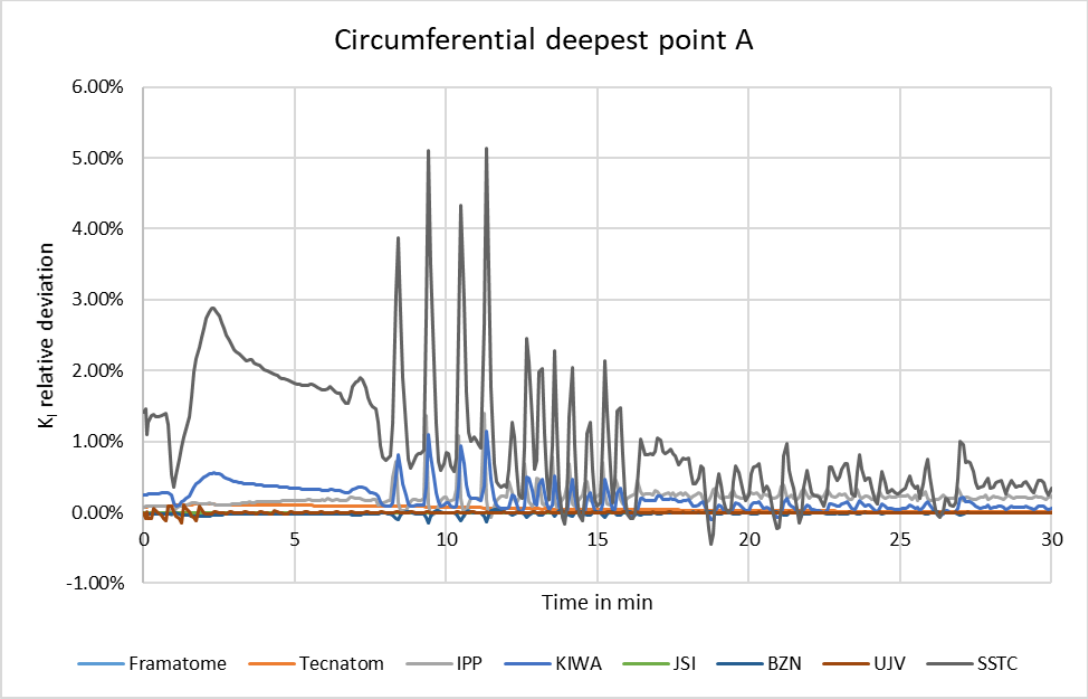

Figure 4.16: TCC Circumferential deepest point A – K_I results relative deviation (with RS)

KIWA has checked this effect for TCC, the same should be true for UCC. The reason for the oscillations is that the tool ISAAC, which KIWA is using, requires stresses to be defined over the full section that is to be analyzed while the input data given in Part 1.1 omits a small region at the intersection between cladding and base metal. Stresses in the cladding are given for 0 – 5.7 mm while stresses for the base metal are given for 7.1 – 249 mm from the inside.

To handle this, KIWA has extrapolated data from each material to the intersection. For the base metal side, both linear and 4th degree polynomial extrapolation was tested, which gave quite an insignificant difference. The largest deviations are observed at a time of 11.3342 minutes. The given as well as extrapolated stresses near the material intersection are shown in Figure 4.17 below.

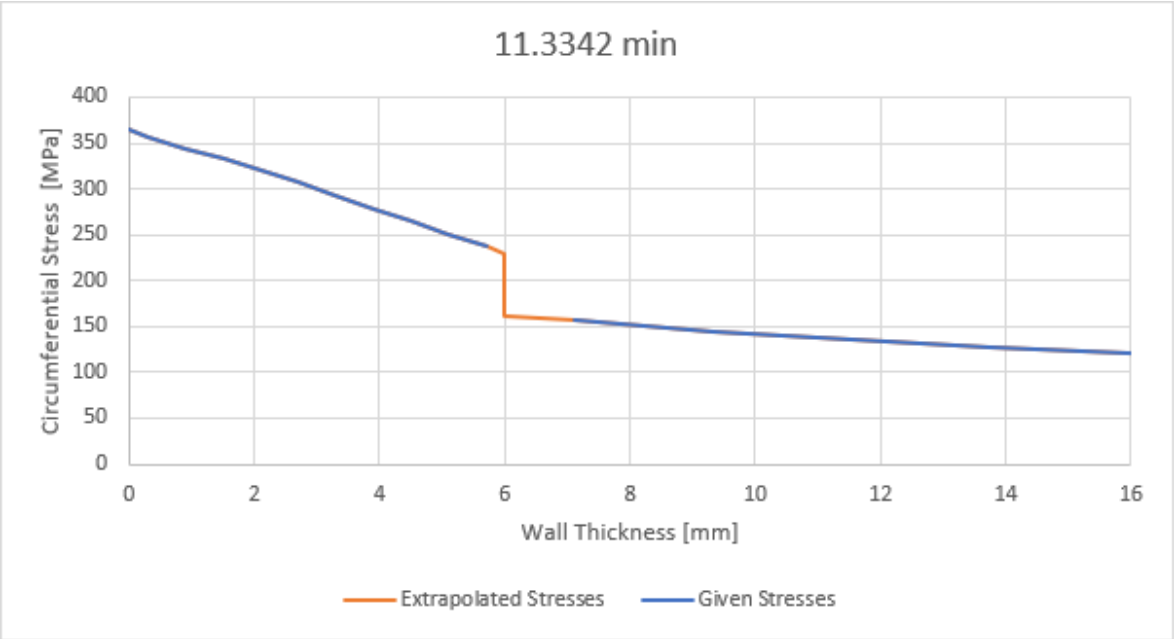

Figure 4.17: Extrapolation of given stress data

When doing a curve fit over the full wall thickness (base metal), it was seen that this small difference in treatment of stresses has a noticeable impact for time steps where a 4th degree polynomial cannot describe the stress state in an accurate manner. Figure 4.18 shows the stress state at the time 11.3342 minutes as well as fitted stresses for both the original data given in part 1.1, as well as the stresses including extrapolated values at the material intersection.

The curve fit using given stresses results in K_I-values according to the reference solution while the curve fit using extrapolated stresses results in K_I-values according to ISAAC.

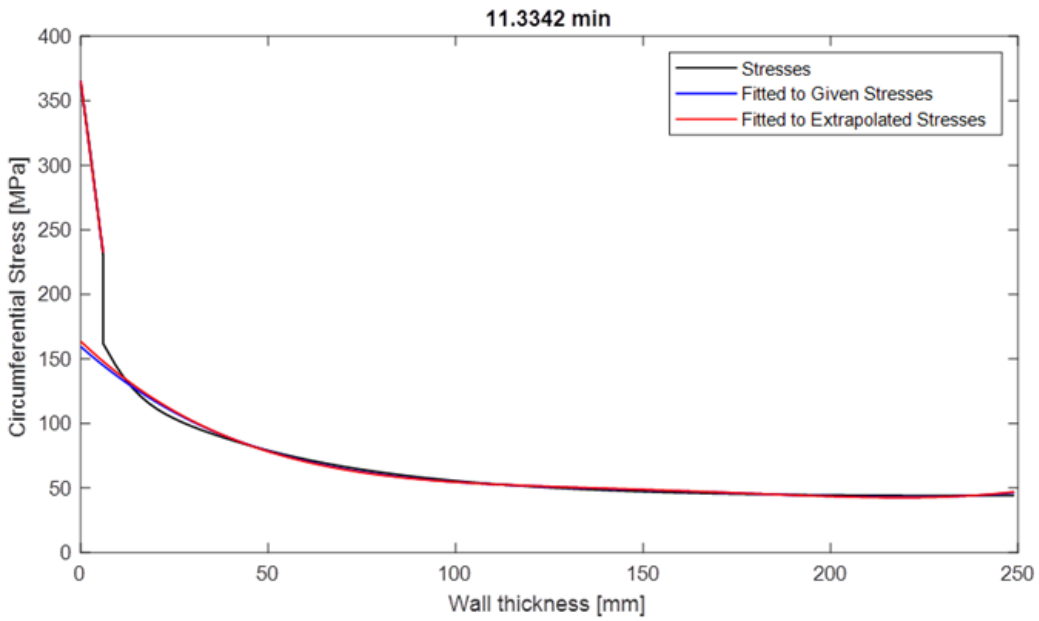

Figure 4.18: Comparison of stresses fitted with a 4th degree polynomial, both fitted to the stress state given in part 1.1 as well as to the stress state including additional extrapolated values

The reason for the deviations to act in an oscillating manner can be explained by the oscillations of the stress state leading to oscillating K_I-values as shown in Figure 4.19.

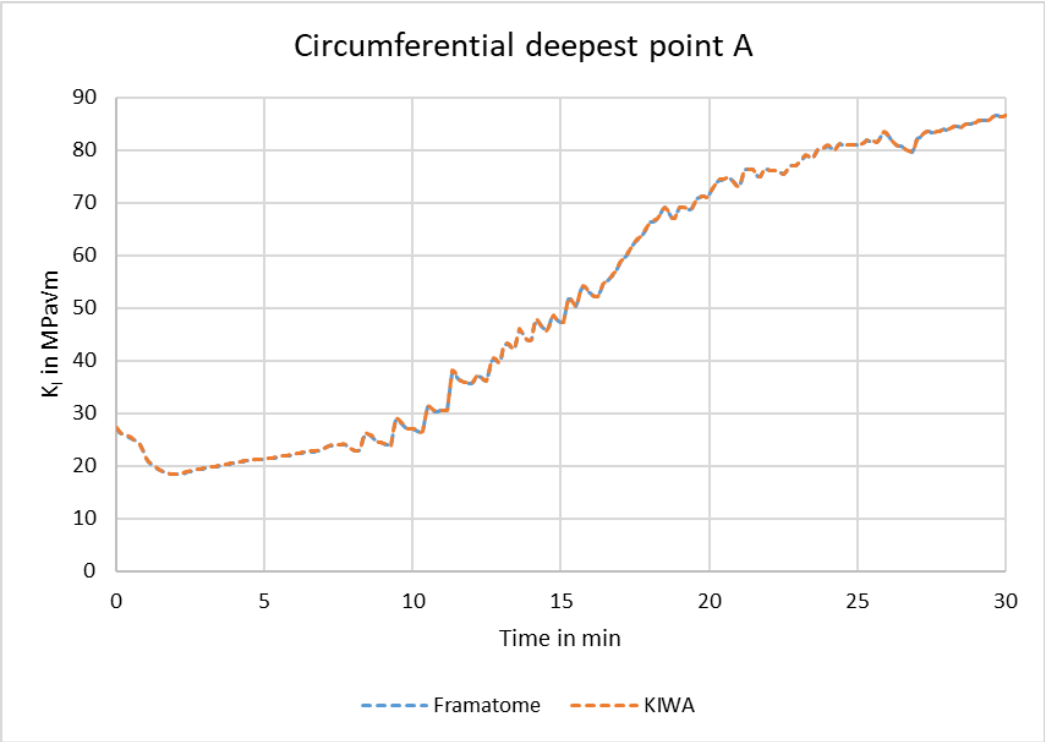

Figure 4.19: TCC circumferential deepest point A – K_I results (with RS)

From the investigation above it was concluded that the oscillations observed in results from KIWA are caused by the different treatment of stresses within ISAAC that requires the full stress state over the full section to be defined. This requirement is included to avoid incorrect treatment of stresses due to incomplete input data.

When stresses change fast, the gradient through the thickness may not be possible to be accurately described with a 4th degree polynomial. For such cases, curve fits based on different inputs may deviate from each other more than for cases when they can describe the gradient accurately. If the curve fit were to be done over the crack depth only, instead of the full wall thickness, it would be easier to get a good description of the stress state using a 4th degree polynomial for the full transient. This should lead to a much smaller impact of the different treatment of the stress states.

4.1.5.3 Plastic correction

The proposed plastic correction for UCC within the APAL project is from Marie, Nedelec [19]. The formulas given are different for times in the transient after the maximal value of K_{el} was reached and before. The passage in the paper is shown in Figure 4.20.

Once the maximum value of K_{el} reached, the corrected stress intensity factor K_{ep} is then obtained from :

- at point A : $K_{epA} = K_{elA} + (K_{epA} - K_{elA})_{max}$ where $(K_{epA} - K_{elA})_{max}$ is the value of $(K_{epA} - K_{elA})$ when the maximum K_{elA} is reached.

- at point B : $K_{epB} = K_{elB} + (K_{epB} - K_{elB})_{max}$ where $(K_{epB} - K_{elB})_{max}$ is the value of $(K_{epB} - K_{elB})$ when the maximum K_{elB} is reached.

Figure 4.20: Text snippet from [19]

Within the APAL project it was found that this formulation is ambiguous in the sense that it is at first not clear if the maximum K_{el} in the whole transient or the maximum K_{el} up to the evaluated point in the transient should be considered. When looking at the physical effect of plastification it becomes clear that the maximum K_{el} up to the evaluated point in the transient is the relevant one for the calculations. For the APAL transient this means, that up to approximately 10 min in the transient the maximum of K_{el} is the one at the beginning of the transient. Thus, in the first low of K_I the formula from Figure 4.20 must be used.

Another finding within the work for APAL was that in the 2006 PVP paper of Marie and Nédélec in the formula for β a factor of two is missing. The comparison of the two formulas is shown in Figure 4.21.

$$\beta = \frac{K_{I,A} + K_{I,A_u_{y,pl}}}{K_{I,A}} = 1 + \frac{1}{2.(1-\nu^2)} \cdot \sqrt{1 - \left(\frac{1}{1 + \frac{r_{y,B}}{a}} \right)^2} \qquad \beta = \frac{K_{I,A} + K_{I,A_u_{y,pl}}}{K_{I,A}} = 1 + \frac{1}{2.(1-\nu^2)} \cdot \sqrt{1 - \left(\frac{1}{1 + \frac{2r_{y,B}}{a}} \right)^2}$$

Figure 4.21: Formula for β from PVP paper (left) and [19] (right, correct version)

4.1.5.4 Crack face pressure

In the reference method for stress intensity factor calculation [17] the application of crack face pressure for TCC is described. The internal pressure must be added to the stresses. In the reference it is stated that the stress approximation is a polynomial expression of the 4th order for the base metal, and a linear approximation for the difference of the stresses in the cladding. The two approximations are illustrated in Figure 4.22.

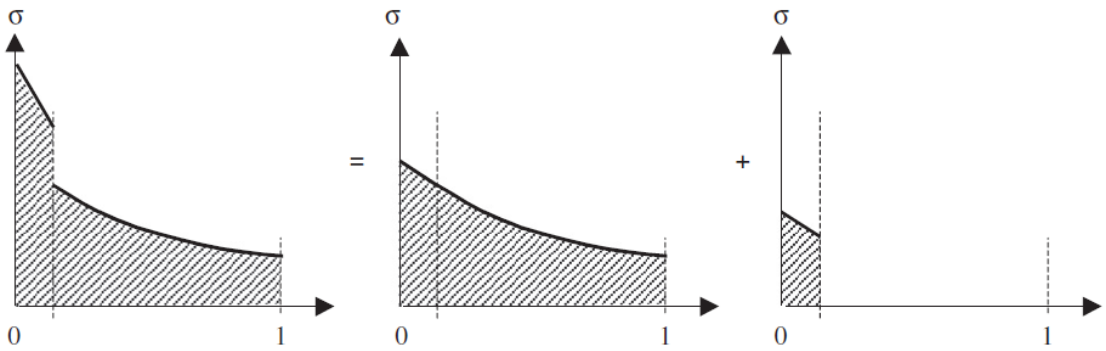

Figure 4.22 Stress decomposition for analytical K_I calculation [17]

The formula for K_I calculation is the following:

$$K_I = \left(\sum_{j=0}^{4} \sigma_j i_j \left(\frac{a+r}{h+r} \right)^j + \sum_{j=0}^{1} \sigma_{jr} i_{jr} \left(\frac{a+r}{h+r} \right)^j \right) \sqrt{\pi(a+r)}$$

The application of crack face pressure is described in the snippet below:

> According to the principle of superposition, the shape factors are then calculated one by one, applying the load cases as corresponding pressures on the crack face:
>
> - Imposed pressure on the whole crack face for the coefficients corresponding to the polynomial fit in the ferritic material.

This means, that the crack face pressure p in MPa has to be added to the constant part of the approximation in the KI formula, which is $\sigma_0 \leftarrow (\sigma_0 + p)$. During the calculations for the benchmark the question arose whether p has only to be added to σ_0 of the base metal approximation or also to σ_{0r} of the cladding. After discussing the topic and consulting the author of the original source it could be clarified that p is only to be added to σ_0, for cladding and base metal, but not to σ_{0r} that only treats the difference in stresses within the cladding.

4.2 First benchmark performance part 2 results: Calculations based on several TH calculations and individual structural and FM methods (PR-Det-2)

In Part 2, partners performed the structural analysis based on available TH calculations output, i.e., with their own temperature and stress distributions (see [1]) and with their own SIF solutions for TCC, UCC or embedded/buried cracks. For the FAVOR group, beside the TCC, the buried flaw must be considered instead of UCC. Final results are max. allowable adjusted reference temperatures.

Part 2 is based on the base case (APAL-ICAS-T2) TH data set (RELAP, ATHLET, FLUENT, TH mixing Codes, CFD). The base case data set from RELAP5+KWU-MIX was provided to the partners (reference TH data for system and mixing analysis). Each partner was free to choose an additional data set (TH-calculation output for SA) from the available TH data sets.

In part 2, the partners use the same methodology in structural assessment as intended in WP4 (for calculation of temperature, stresses, SIF, K_{IC} using RT_{NDT}/T_0, Tangent/WPS approach, etc.). The effect of different TH calculations (e.g., different TH mixing codes) is assessed in APAL up to K_I and max. all. ART.

Content:

- Part 2.0: Stress and temperature calculation including sensitivity studies for reference TH-data (RELAP, KWU-MIX)
- Part 2.1: Determination of SIF
- Part 2.2: Determination of max. allowable ART (RT_{NDT} $^{a\ tan\ /\ WPS}$, T_0 $^{a\ tan\ /\ WPS}$)

Parts 2.1 and 2.2 are based on the same approach as described in Part 1 but using participants' own stress and temperature calculations (simplified 1D, simplified plume from system code or from TH mixing-code combined with formulas, sophisticated 3D FEA) and on their own SIF implementation of the mandatory cracks. The mandatory cases (crack geometry etc.) from part 1 remain mandatory.

The numerous possible sources for discrepancies between the results are listed below:

- TH data used (partner, code, 1D/2D/3D TH run)
- Mixing code on TH data (code)
- Formulas to consider cold plume effect when using 1D model for stress calculation
- 1D/3D structural analyses

- 1D/3D stresses used with K_I analytical calculation
- K_I solution (FAVOR, CEA, 3D FEA)
- With/without WRS, and which residual stresses applied (FAVOR, APAL, etc)
- Plasticity correction for UCC
- Crack face pressure for TCC
- Cap pressure boundary

The examined locations are:

- Core weld inside plume (CW-CL, A95-V05)
- Core weld outside plume (CW-A, A98-V05)
- Flange weld inside plume (FW-CL, A95-V03)

4.2.1 Results for part 2.1: Determination of SIF

The task for part 2.1 was to repeat PR Det 1.1 (the same crack types, orientations, size) considering APAL-ICAS T2 transient, -2638 mm location and highest loaded azimuth 202.5° i.e., below injection nozzle or in the merging plume area (mixing case, azimuth 180°), but with participants' own SIF solution (the same as for probabilistic assessment WP4) and from their own structural assessment for stress and temperature distributions.

SA results were shared between the partners for those that cannot perform a sophisticated SA.

In the following chapters the results with weld residual stresses are presented. Results without weld residual stresses are given in [3].

4.2.1.1 TCC

The results for TCC with residual stresses are shown in this chapter. The results for the CW-CL location (base case) are shown first. Please note that for BZN the IP and IMP results are taken from a slightly different position, IP is at 202.5° and IMP is taken from 180°.

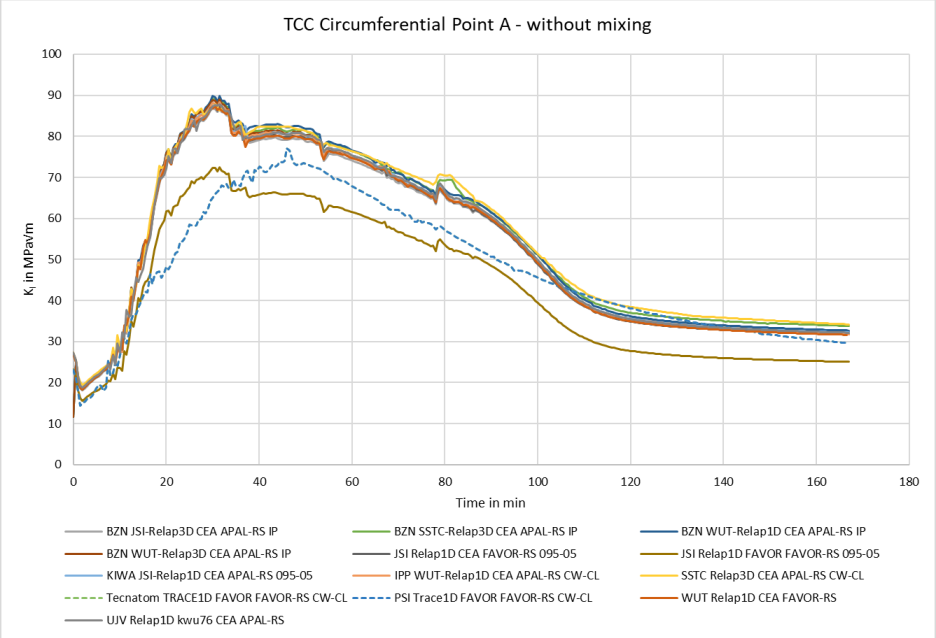

Figure 4.23: TCC Circumferential Point A – CW-CL without TH mixing

In Figure 4.23 the only results that differ from the others are the ones calculated with FAVOR and/or Trace TH-data. The difference of about 20 MPavm for the FAVOR results was already seen in the

benchmark part 1. The difference between stresses based on Relap and Trace TH codes was already observed in Deliverable 3.1 [1], the corresponding plot is shown in Figure 4.24.

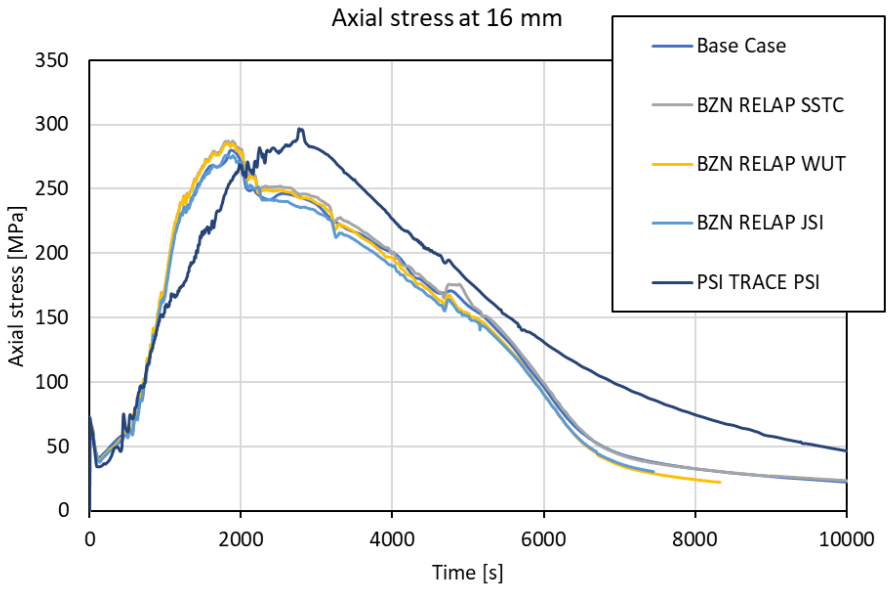

Figure 4.24: Comparison of stresses based on Relap and Trace TH codes

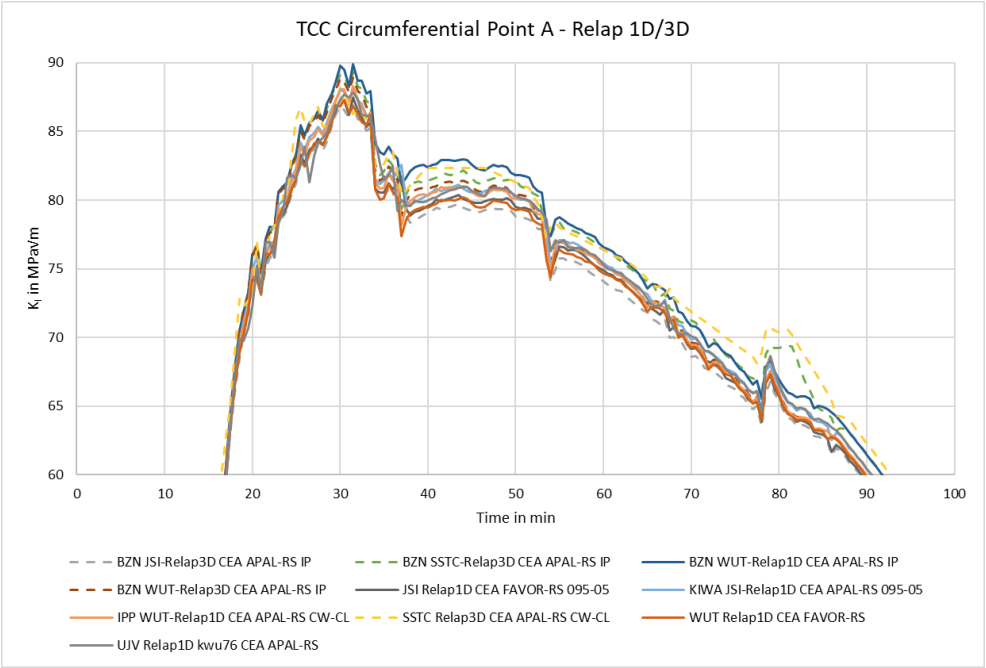

Figure 4.25: TCC Circumferential Point A – CW-CL Zoom on Relap results without TH mixing

In the detailed comparison in Figure 4.25 the 3D results are marked with dashed lines. There is no clear difference between the 1D and 3D structural analysis results. In the SSTC Relap, the results are slightly higher at 80 minutes in the transient. This could be relevant for the determination of max. allow. ART by the tangent approach. The results “BZN WUT-Relap1D CEA APAL-RS IP” and “WUT Relap1D CEA

FAVOR-RS" differ only in the type of residual stresses used. In the plot it can be seen that the results for FAVOR-RS are lower than for APAL-RS.

For the determination of the max. allow. ART not only the K_I curve over time but also over temperature is to be considered. In Figure 4.26 and Figure 4.28 K_I results over temperature are plotted to help understand the results in chapter 4.3.

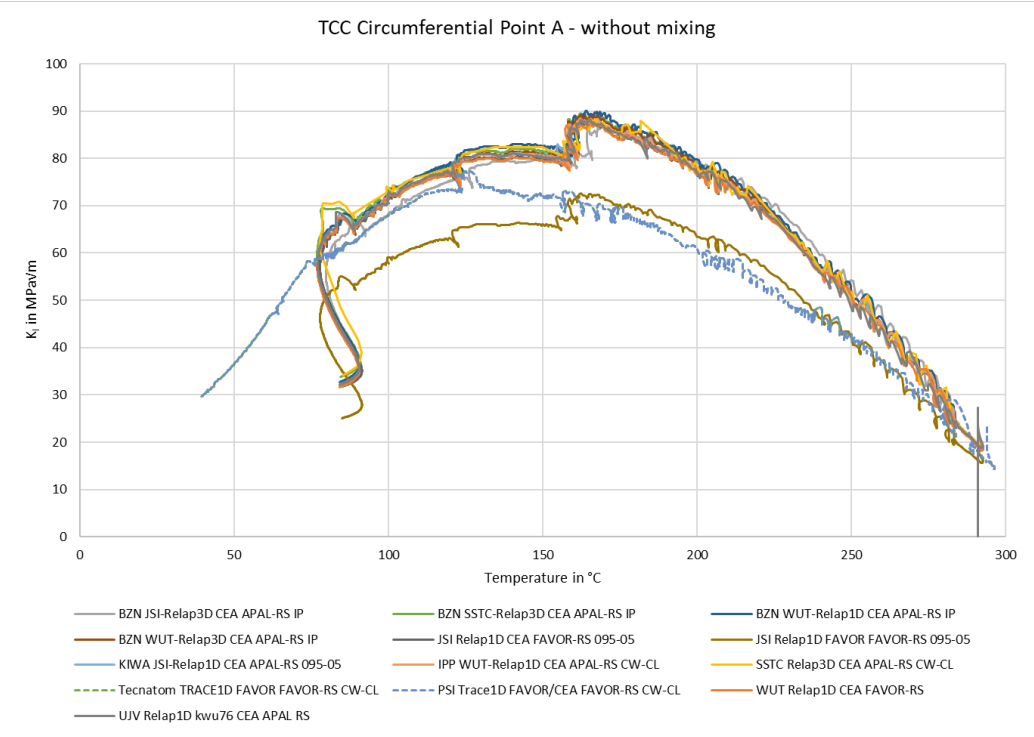

Figure 4.26: TCC Circumferential Point A – CW-CL without TH mixing, K_I over temperature

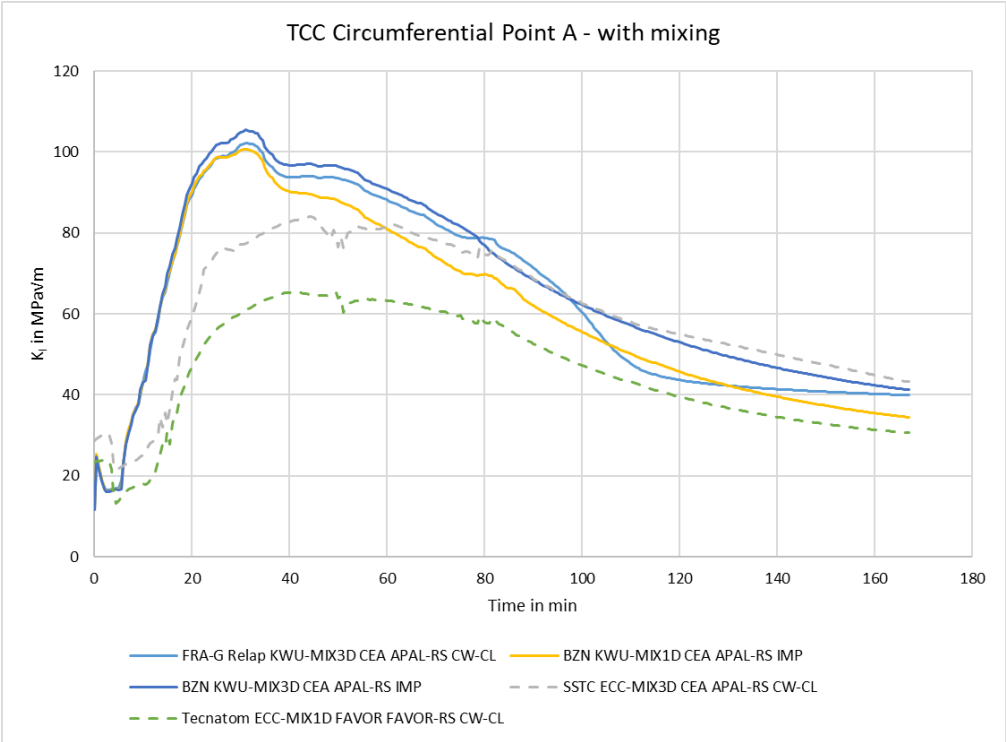

Figure 4.27: TCC Circumferential Point A – CW-CL with TH mixing

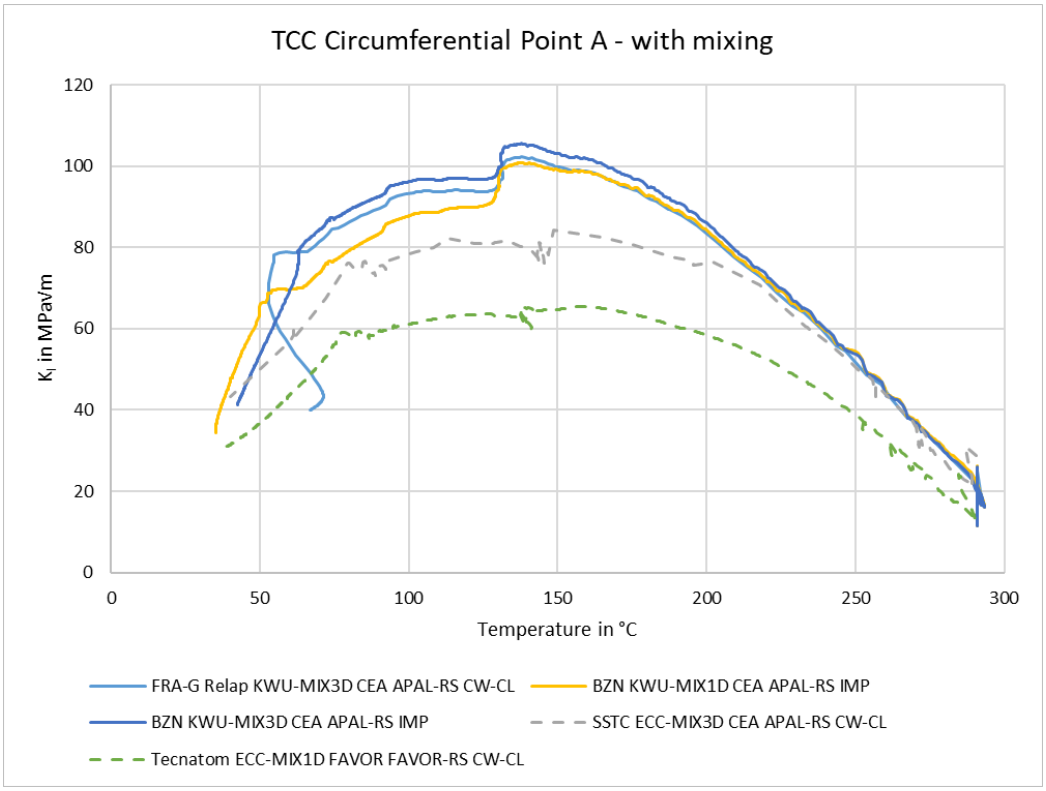

Figure 4.28: TCC Circumferential Point A – CW-CL with TH mixing, K_I over temperature

The results with TH mixing (see Figure 4.27) are higher than the results that do not consider TH mixing for the CW-CL inside plume location. The results of BZN are different from the Framatome results beginning at 83 minutes since BZN performed an extrapolation of the input data from that point in time. The ECC-Mix based stresses have a different shape than the KWU-Mix based stresses, for the stress calculations, see Deliverable 3.1 [1].

The results for point C show the same tendencies as for point A, while they are in general lower than those for point A. Details for the results for point C are given in [3].

The results for TCC with axial orientation are given in [3]. The same observations and explanations as for the circumferential crack are true. In general, the results for the axial crack are slightly higher.

The results for CW-A outside plume are shown in Figure 4.29 and are slightly lower than the results inside plume without TH mixing, but a lot lower than for the case considering TH mixing. This could be expected, since at the location outside plume the influence of the TH mixing is small.

The difference between the Framatome and JSI Relap results was examined in detail to fully understand the deviations. Comparisons were performed and concluded that the input pressures and temperature are quite similar. Also, the use of either APAL or FAVOR residual stresses does not make noticeable difference for the K_I result. It was concluded that the differences in the stress intensity factor values result from differences in the structural assessment (see also [1])

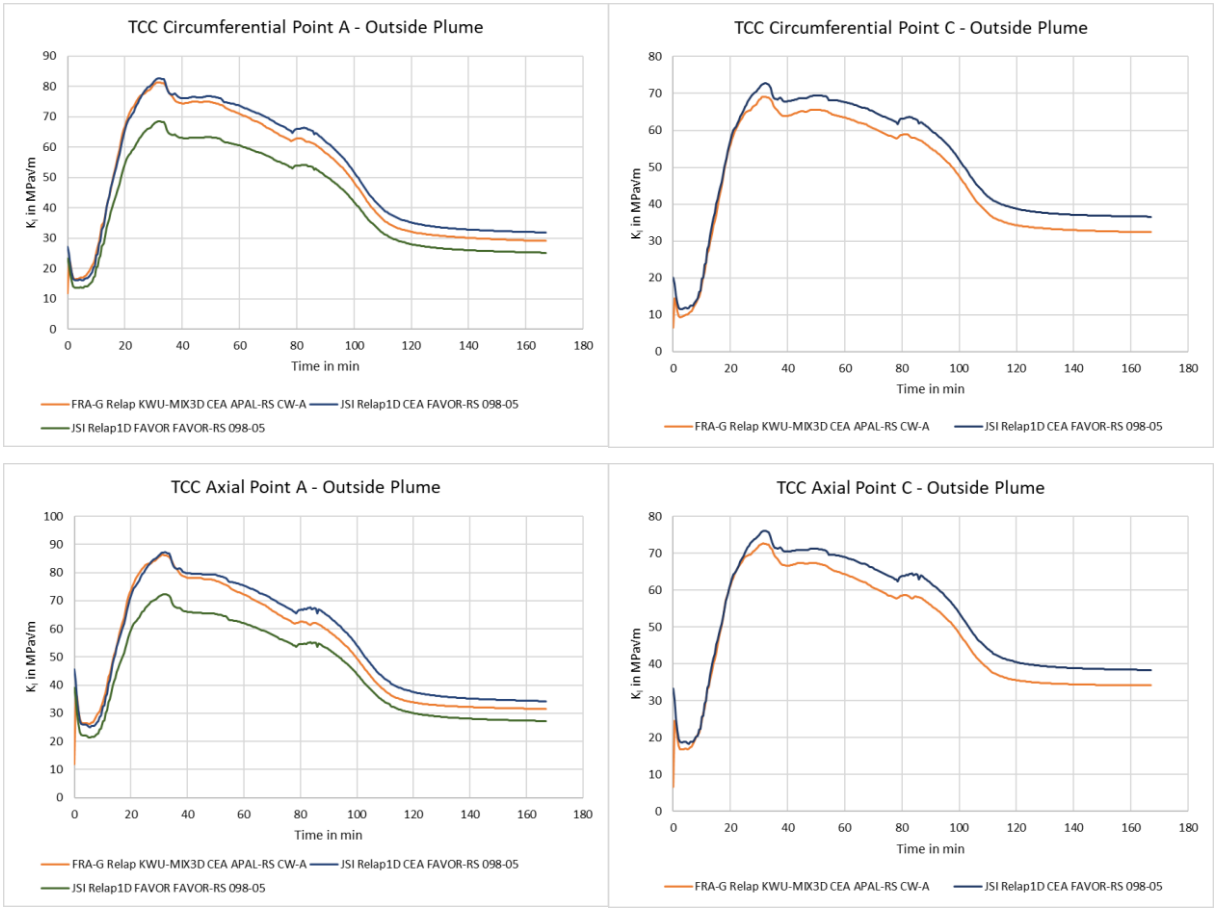

Figure 4.29: TCC at CW-CL outside plume

4.2.1.2 UCC

In this chapter the results for UCC at the CW-CL location are presented. The results for a circumferential crack UCC, point A and C are shown in Figure 4.30 to Figure 4.31.

The results for point B and C as well as for an axial crack are given in [3]. There are no FAVOR results, since there is no option to consider UCC in FAVOR.

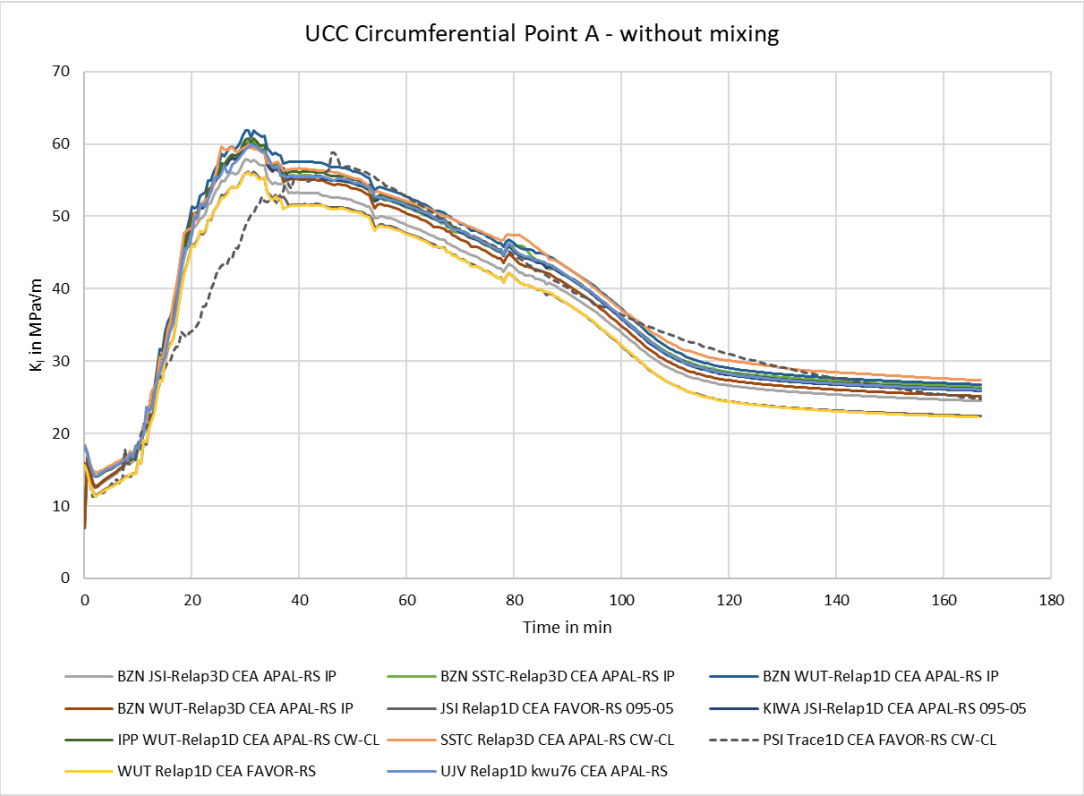

Figure 4.30: UCC Circumferential Point A – CW-CL without TH mixing

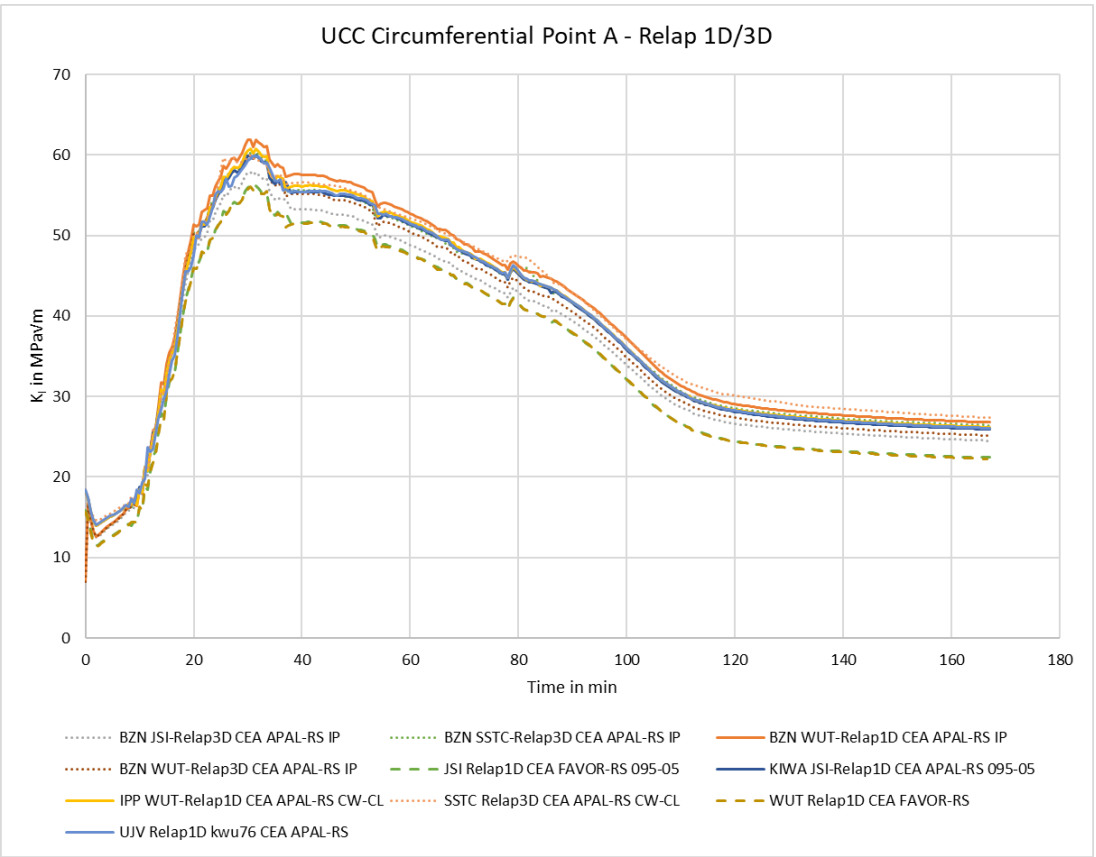

Figure 4.31: UCC Circumferential Point A – Comparison of Relap results

The comparison of only the Relap results is shown in Figure 4.31. The 3D results are marked with a dotted line, the results with FAVOR residual stresses are marked as a dashed line. There is no clear

difference between the 1D and 3D results, overall, the 1D results seem to be higher. It can be also seen that the results with FAVOR residual stresses are lower, this is consistent with the definition of the APAL and FAVOR residual stresses.

The scatter of the results without TH mixing for UCC (Figure 4.31) is larger than for TCC, where the results without TH mixing were closer together (Figure 4.23, only results based on Relap). As for TCC, the results with TH mixing (Figure 4.27, only results based on KWU-Mix) are a lot larger than the results that do not consider TH mixing (Figure 4.23, only results based on Relap and simultaneously using CEA method). The curve of SSTC is different since they are using data from ECC-Mix.

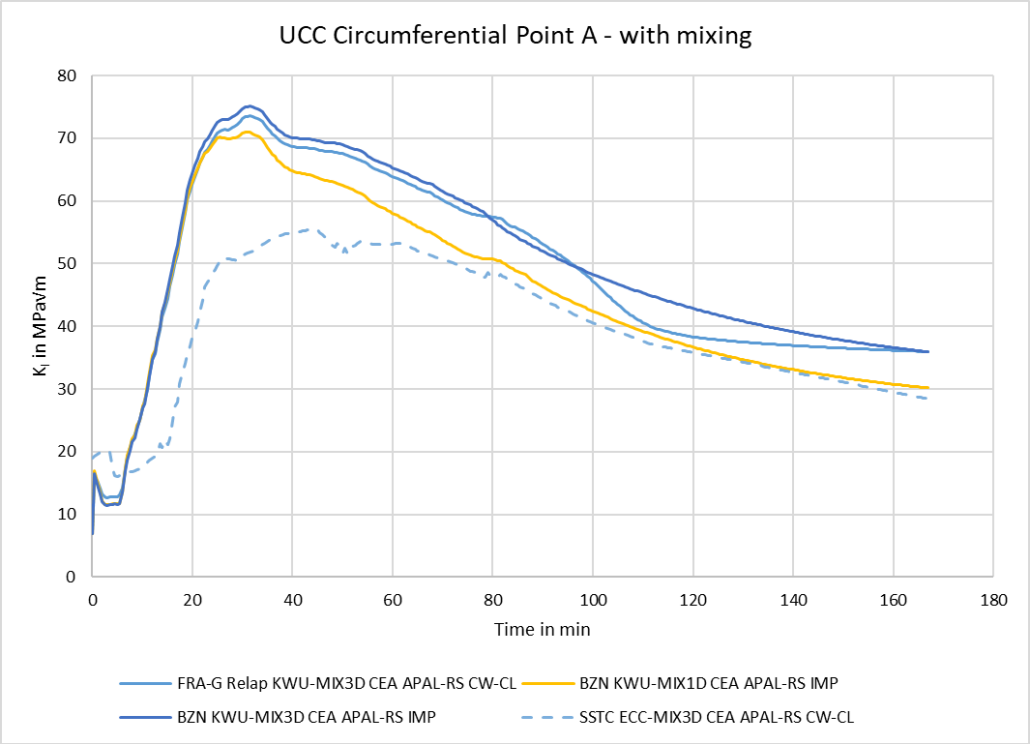

Figure 4.32: UCC Circumferential Point A – CW-CL with TH mixing

The results of BZN are different from the Framatome results beginning at 83 minutes since BZN performed an extrapolation of the input data from that point in time. On top of that there is a larger difference for UCC in axial orientation due to different stresses caused by the structural assessment.

Similar as for TCC, the UCC results outside plume are slightly lower than the results inside plume (see Figure 4.33). Again, the consideration of TH mixing does not play a big role for the results outside plume.

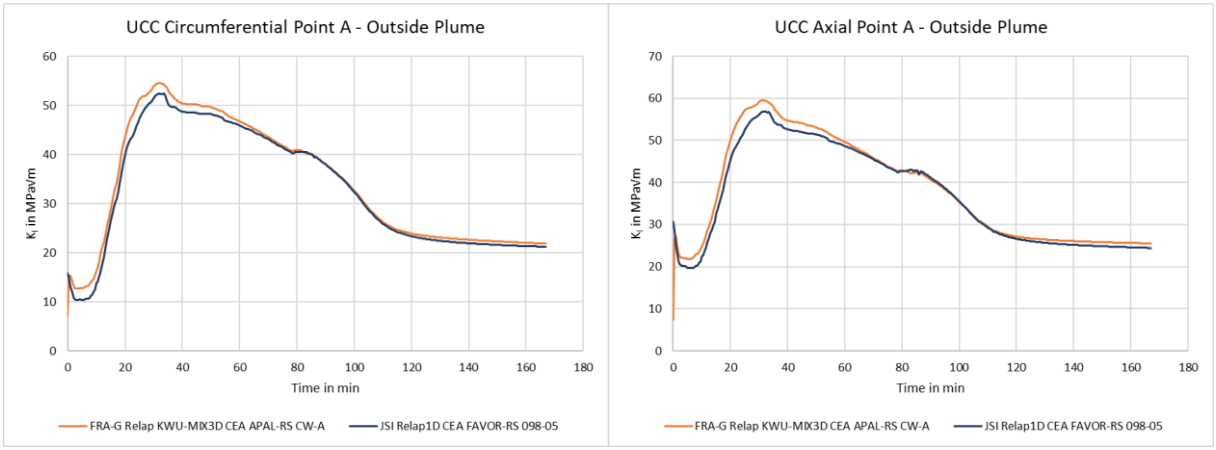

Figure 4.33: UCC at CW-CL outside plume

4.2.1.3 Embedded crack

The assessment of embedded cracks was performed by the FAVOR users. The results for a circumferential crack are shown in Figure 4.34 and results for an axial crack are given in [1]. All results were calculated with FAVOR but using three different TH inputs. The two results for Trace are almost identical.

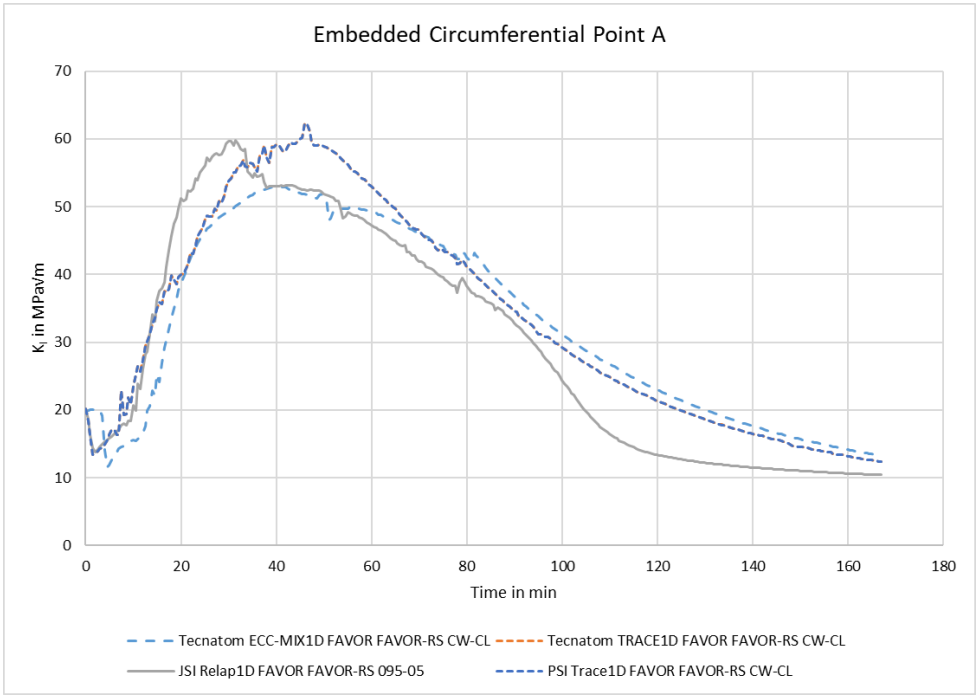

Figure 4.34: Embedded Crack Circumferential Point A – CW-CL

4.2.1.4 Other locations

In this chapter, the results for the flange weld (FW) location (inside and outside plume) are shown. The results for the outside plume location are marked as dashed lines. The results with different TH data (Trace) are marked with short-dashed lines.

For TCC, point A the results are shown in Figure 4.35 and Figure 4.36 and for TCC, point C the results are given in [3]. For the circumferential crack the results with TH mixing for the inside plume location are a lot higher than the other results, for the axial crack the TH mixing does not play a big role. The

results for the FW outside plume location are close to the FW inside plume results without mixing for the circumferential crack, for the axial crack the outside plume results are a bit lower.

The results from PSI are lower than the rest, not only because they used Trace for the TH input but also because the stress intensity factor calculation was done with FAVOR. It was already identified in deliverable 3.1 [1] that the 1D stresses are not correct and underestimate the real stresses at the flange weld.

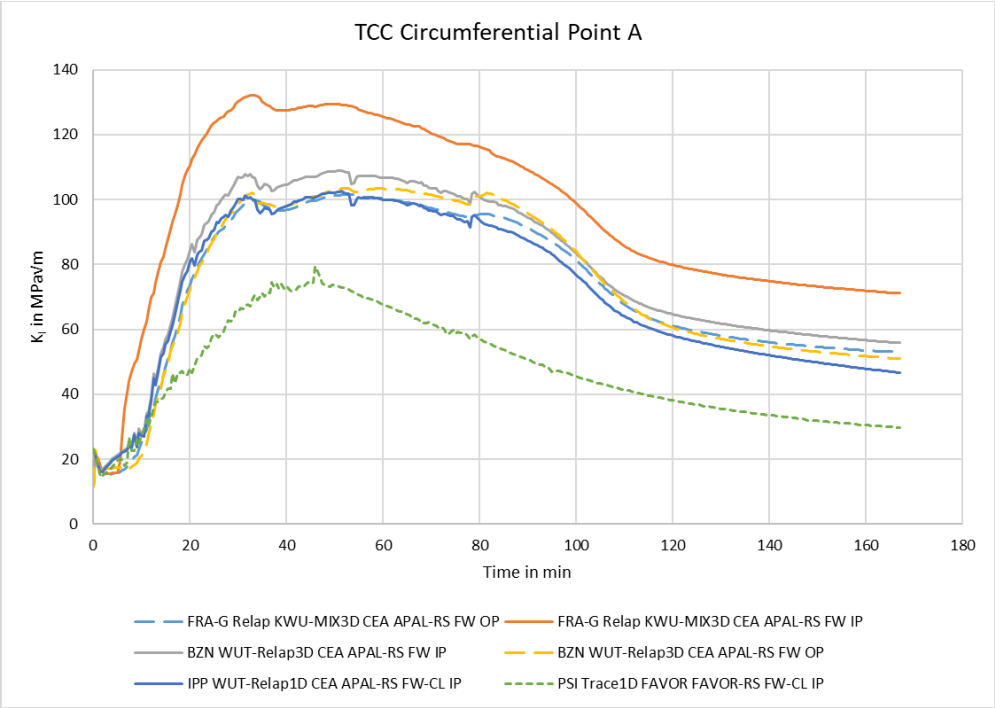

Figure 4.35: TCC Circumferential Point A – FW location

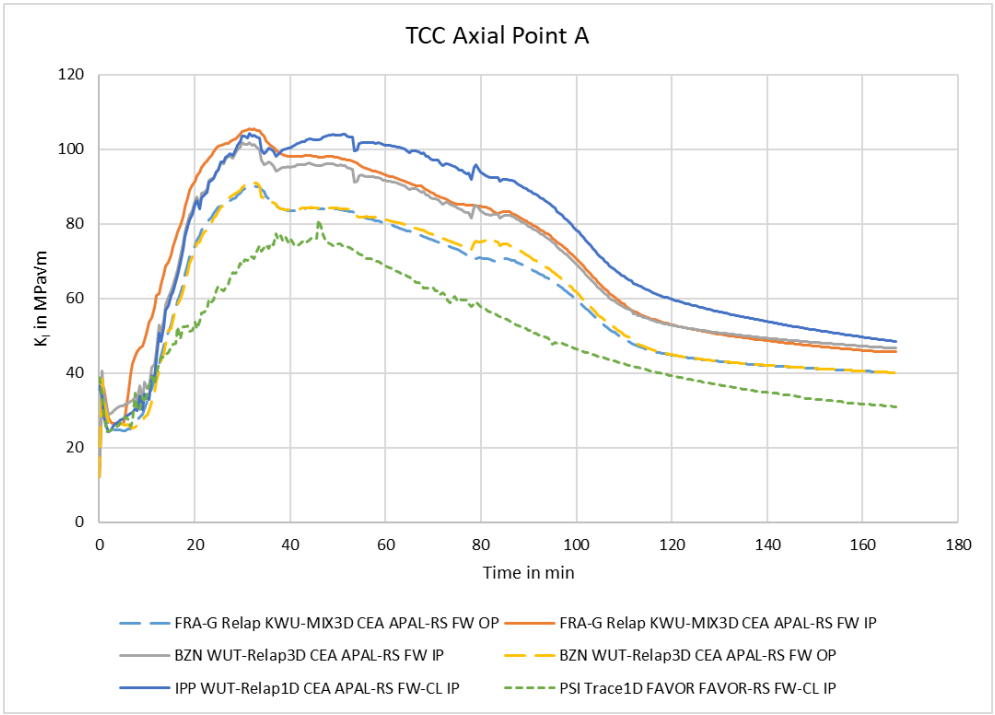

Figure 4.36: TCC Axial Point A – FW location

The difference between the BZN and IPP results is only that BZN is calculating with the 3D Relap data, where IPP is using 1D Relap data. The difference in KI follows the difference in the stresses, see Figure 4.37.

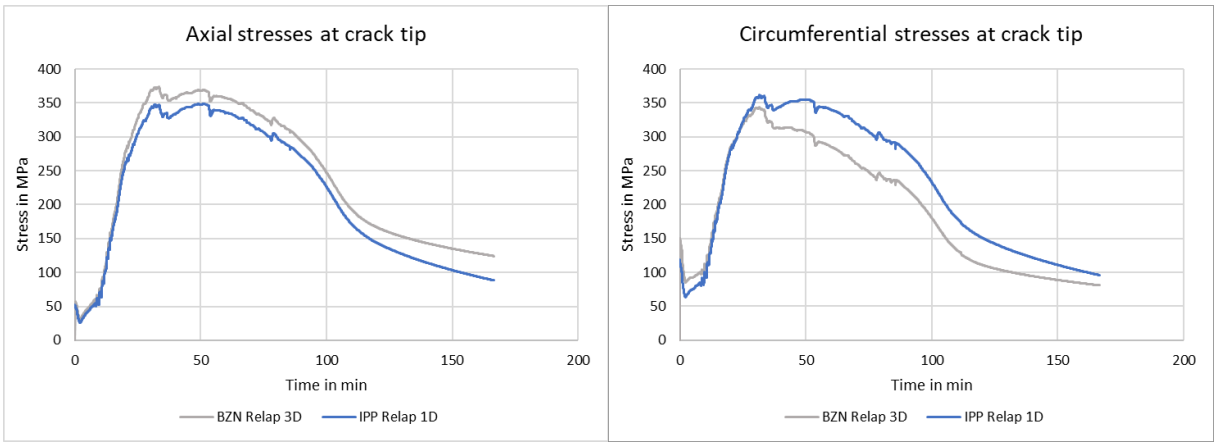

Figure 4.37: Comparison of Relap 1D and 3D stresses at FW location

For UCC, point A the results are shown in Figure 4.38 and Figure 4.39 and for UCC, point B and point C the results are given in [3]. For the circumferential crack the results with TH mixing for the inside plume location are a lot higher than the other results, for the axial crack the TH mixing does not play a big role. The results for the outside plume location are close to the inside plume results without mixing for the circumferential crack, for the axial crack the outside plume results are a lower.

The results from PSI were obtained by interpolating the stresses from the FAVOR results for the stress intensity factor calculation. The interpolation of the stresses in the cladding is inexact.

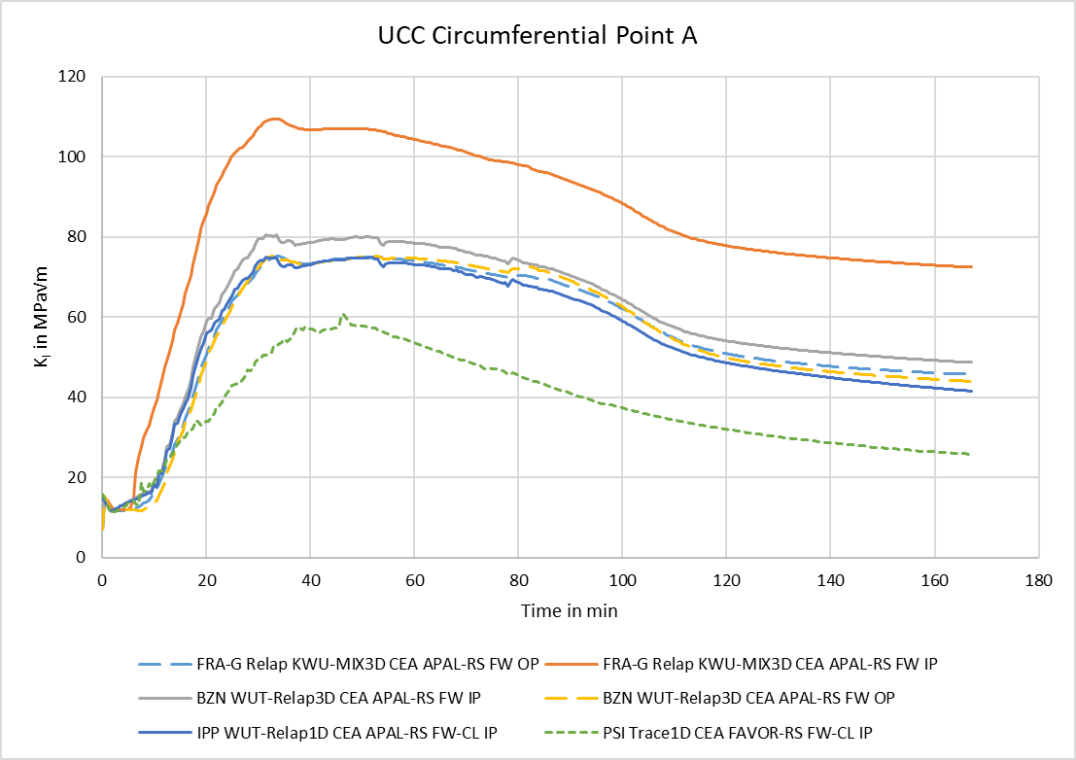

Figure 4.38: UCC Circumferential Point A – FW location

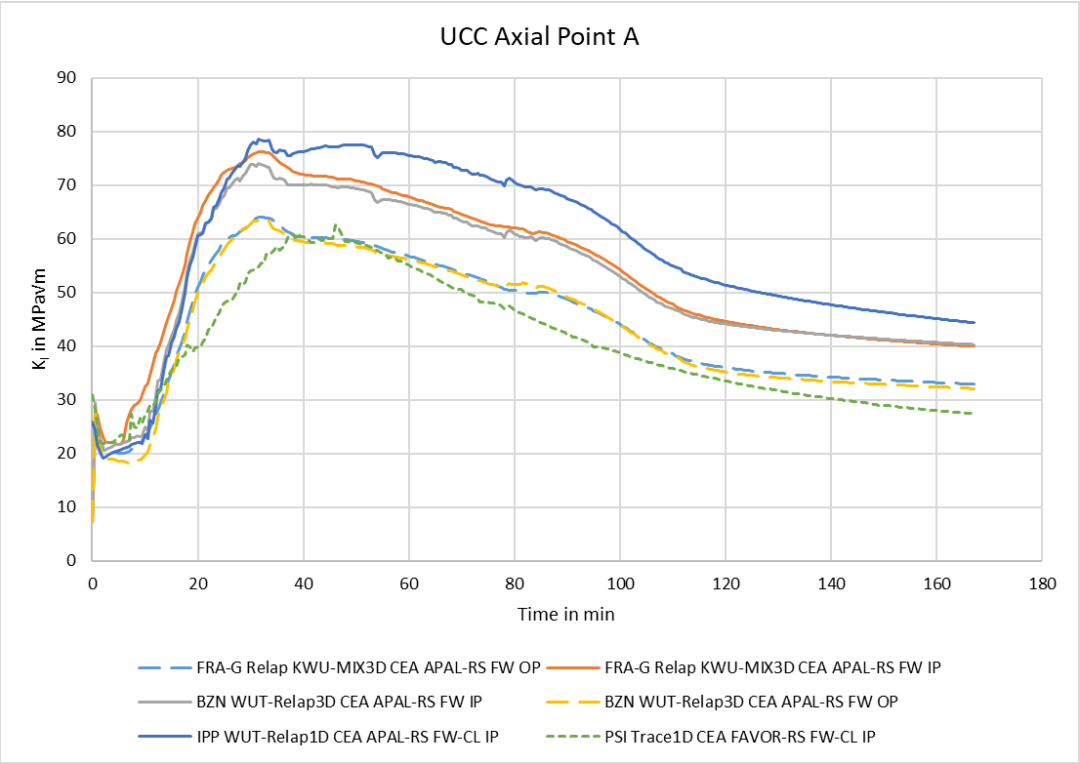

Figure 4.39: UCC Axial Point A – FW location

4.2.2 Observations and recommendations

The results for the benchmark part 2.1 show that the choice of TH code, K_I formula and consideration of TH mixing can have a considerable influence on the obtained K_I results. The different stresses for different TH codes are shown in more detail in deliverable 3.1 [1]. The FAVOR calculation of K_I leads to a lower K_I of up to 20 MPaVm compared to the CEA method. A part of that difference is probably caused by the required interpolation of crack depth/crack length ratios in FAVOR.

The consideration of TH mixing is less relevant in the locations outside of plume. For the inside plume locations TH mixing can play an influential role, the difference is large for circumferential crack and not so large for the axial crack.

4.3 Results for part 2.2: Determination of max. allowable ART

The task for part 2.2 was to repeat PR Det 1.2 but with SIF from PR Det 2.1 for determination of max. allowable ART.

TCC, UCC, surface and deepest point, K_{IC} ASME and T_0, Tangent and WPS-max approach, lower bound K_{IC} and mean K_{IC} were mandatory to allow comparison of results and provide an evaluation of the bias due to the use of different methodologies (e.g., different SIF solutions, different temperatures, and stress structural calculations).

Baseline case (mandatory):

Assessment of TCC (shape 1), UCC plastic, embedded/buried (FAVOR user group):

- Location:
  - inside plume at height of the core weld -2638mm from nozzle centerline
  - inside merging plumes at elevation of the core weld -2638mm
- Use of KI transient (KI versus time and temperature) for
  - TCC (deepest point, point close to clad/base fusion line (FL) = f(t,T))
  - UCC (deepest point, point close to FL in ferritic base/weld metal)

- for FAVOR user group: embedded/buried crack (point close to FL)

Non-mandatory:

- embedded crack (for non-FAVOR users),
- elevation -1350mm (flange weld)
- outside plume (same as in part 1.1)

Output:

- Maximum allowable adjusted reference temperature ART (RT_{NDT} and T_0 concepts)
- Lower bound and mean for ASME (RT_{NDT}) concept, 5% and 50% (median) for Master Curve concept
- Corresponding K_I, K_{IC} and time of initiation
- for tangent and WPS (FAVOR + model) approach

The results presented in this chapter are in the following units if not stated differently: K_I in MPa√m, max. allow. ART in °C and time of initiation in minutes. The value of K_{IC} corresponds to the time of initiation.

4.3.1 Tangent approach

In this chapter the results for the tangent approach with the lower bound ASME and master curve concepts are shown. In addition, the tangent approach was also applied taking into account ASME and master curve mean curves. These results are given in [3] and lead to the same conclusions as the lower bound application.

4.3.1.1 TCC

The results match the K_I results from chapter 4.2.1 well when looking at the K_I value at the time of initiation. For example, the result for max. all. ART with FAVOR is about 15-20 °C higher than with the CEA method as can be seen in Figure 4.40 and Figure 4.41. However, the combination of using Trace for the structural assessment and the FAVOR approach for the fracture mechanics does not make a large difference compared to the Relap and CEA approach. The reason for this is that at the relevant temperature of 75-80°C the Trace and Relap results for K_I over temperature are quite close together, see chapter 4.2.1.1. For point C (no FAVOR results) the max. all. ARTs agreement is good in general (Figure 4.42), only the ECC-MIX results are noticeably higher (Figure 4.43). For the axial crack the same tendencies can be seen as for the circumferential crack (Figure 4.44 to Figure 4.47).

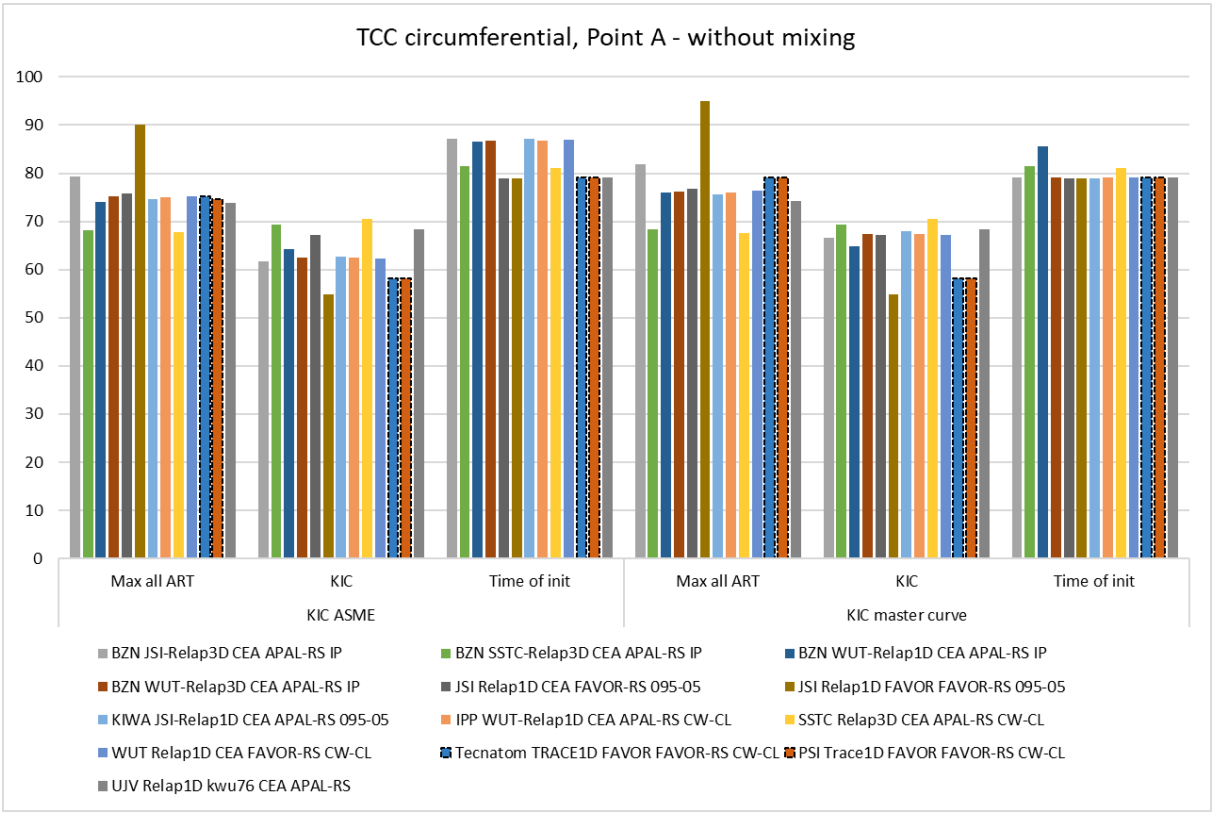

Figure 4.40: Maximum allowable ART (°C) tangent approach lower bound – TCC circumferential point A without TH mixing

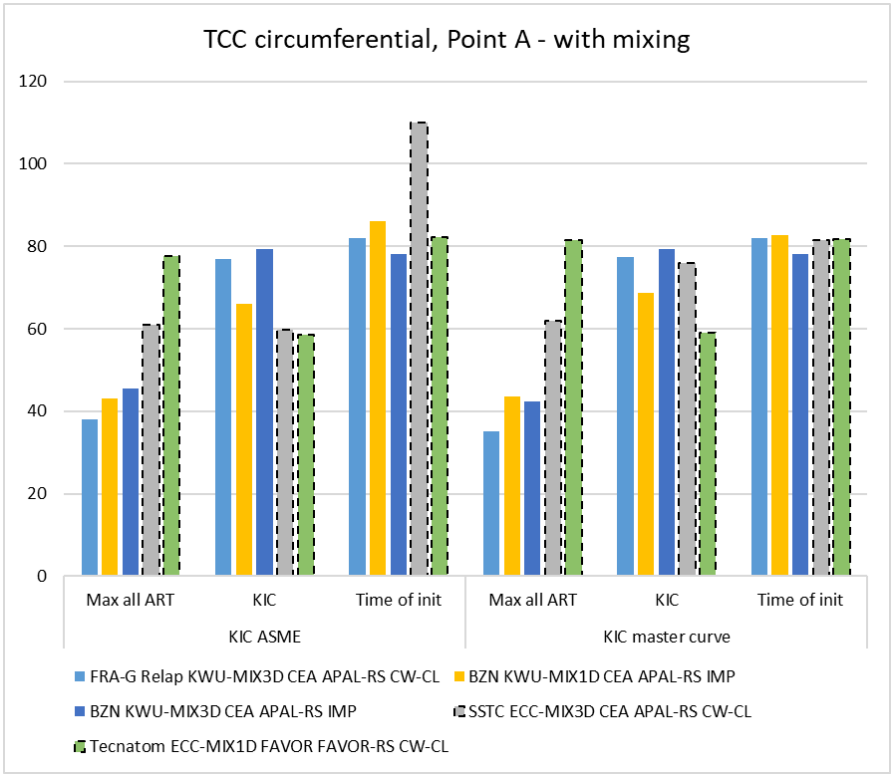

Figure 4.41: Maximum allowable ART (°C) tangent approach lower bound – TCC circumferential point A with TH mixing

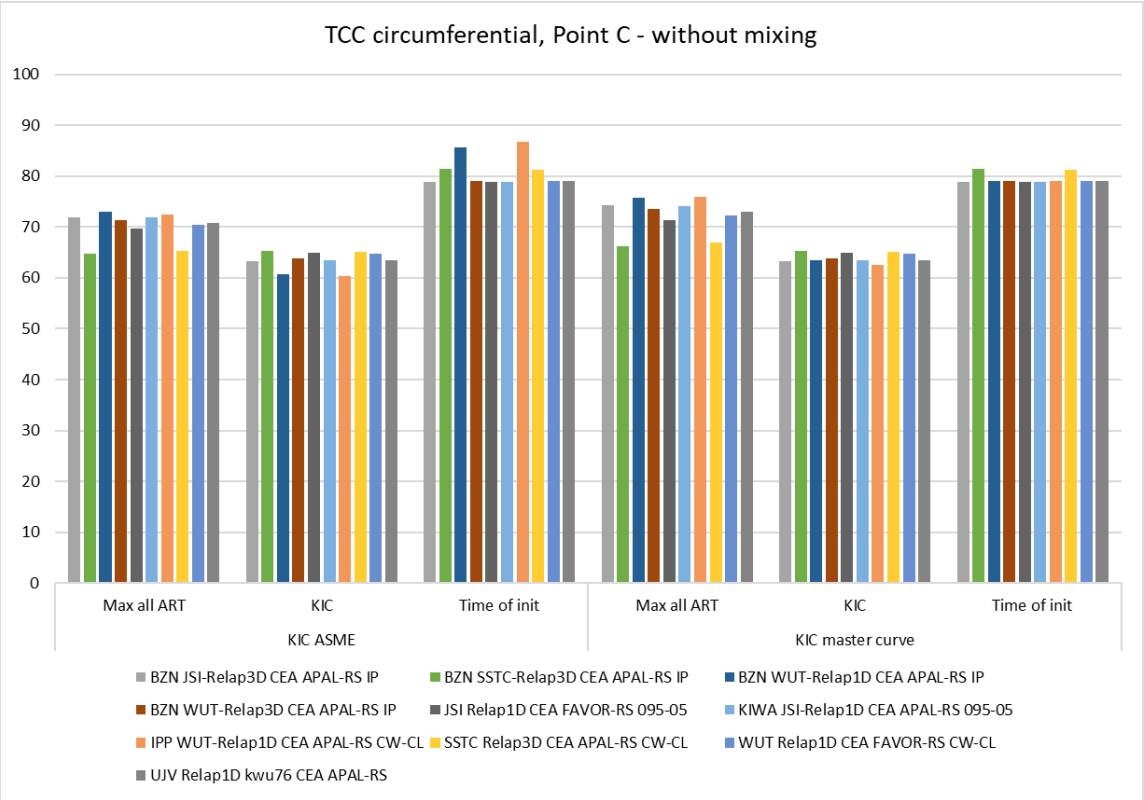

Figure 4.42: Maximum allowable ART (°C) tangent approach lower bound – TCC circumferential point C without TH mixing

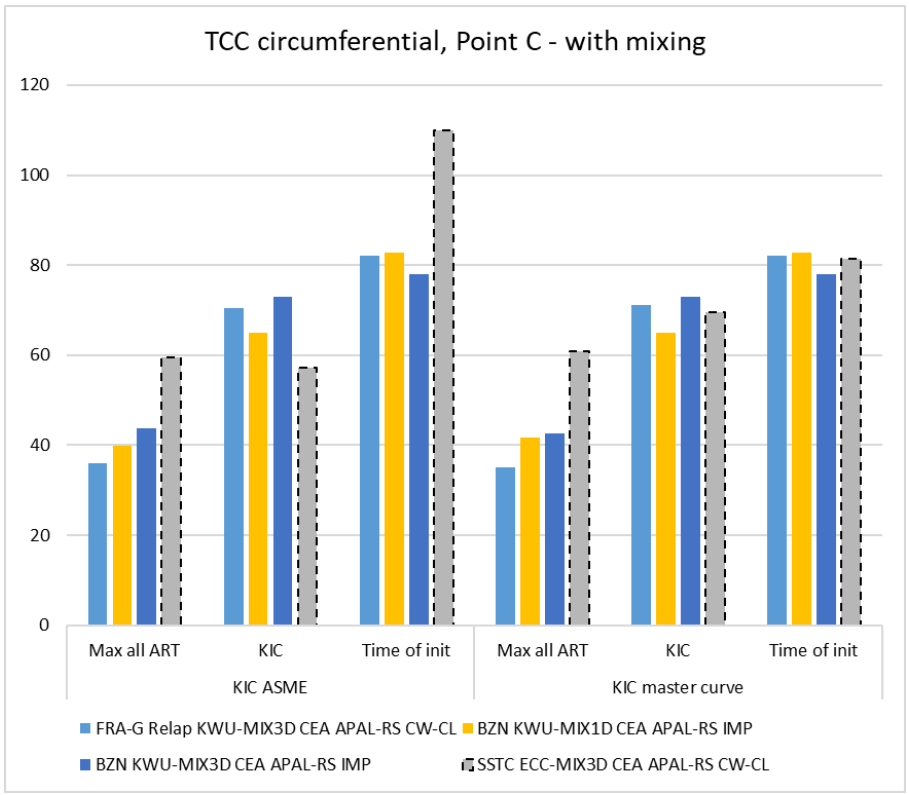

Figure 4.43: Maximum allowable ART (°C) tangent approach lower bound – TCC circumferential point C with TH mixing

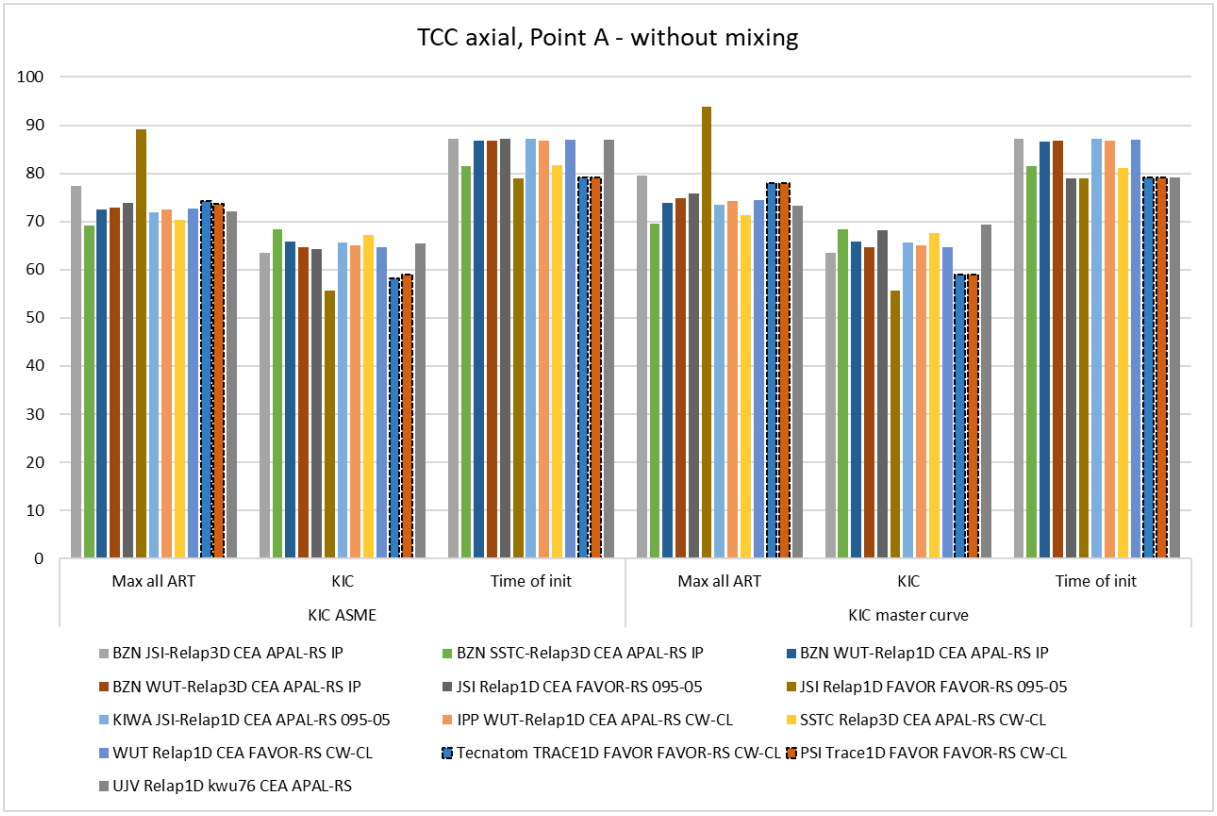

Figure 4.44: Maximum allowable ART (°C) tangent approach lower bound – TCC axial point A without TH mixing

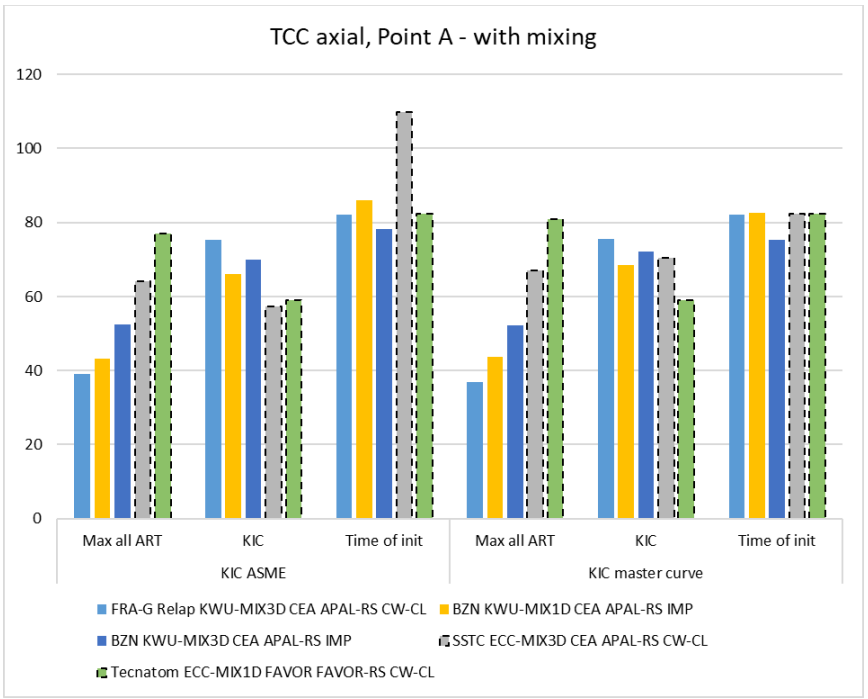

Figure 4.45: Maximum allowable ART (°C) tangent approach lower bound – TCC axial point A with TH mixing

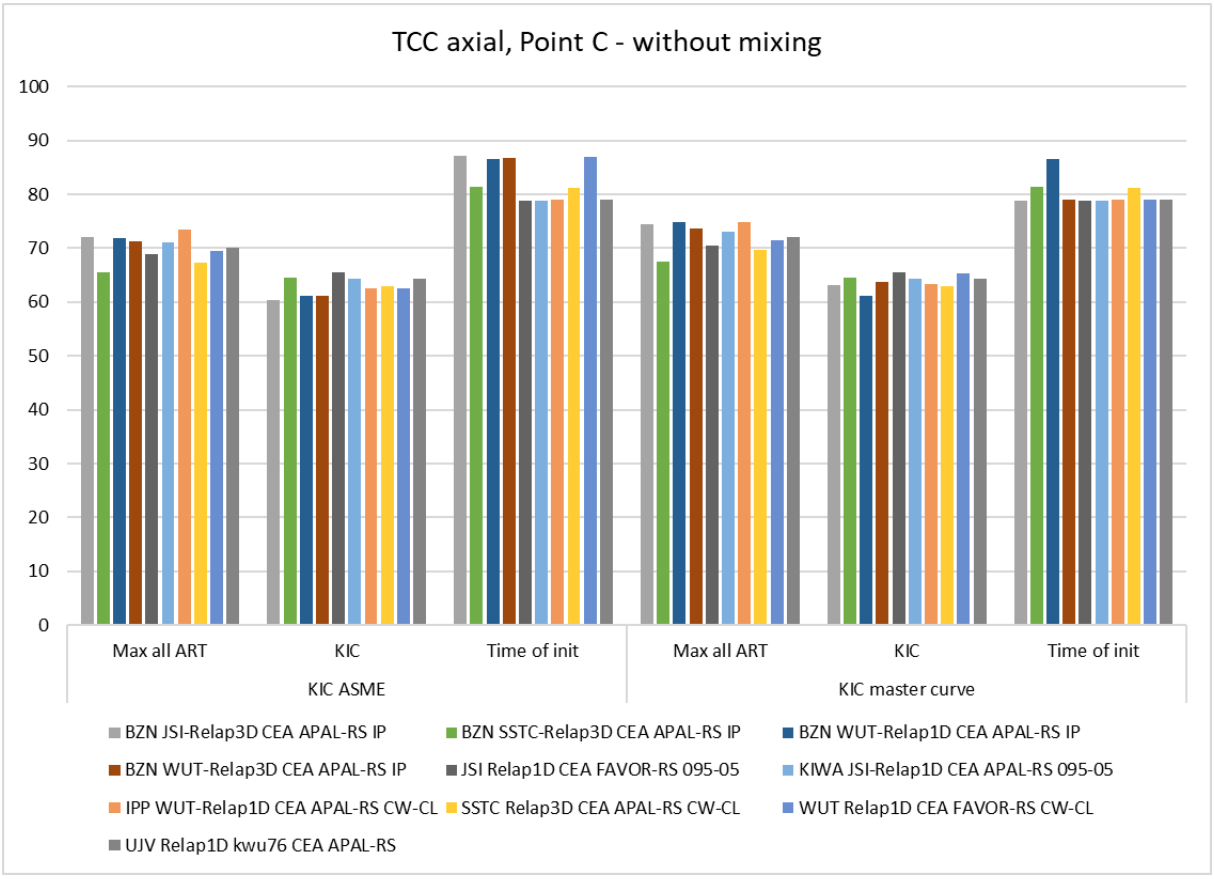

Figure 4.46: Maximum allowable ART (°C) tangent approach lower bound – TCC axial point C without TH mixing

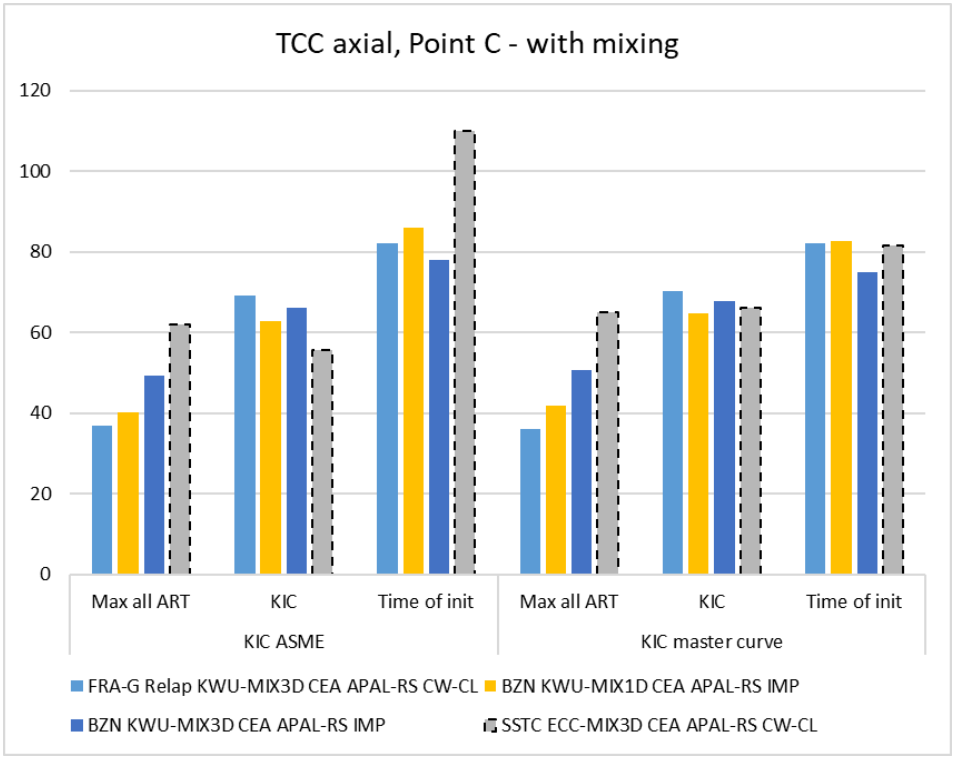

Figure 4.47: Maximum allowable ART (°C) tangent approach lower bound – TCC axial point C with TH mixing

For the outside plume location (Figure 4.48 and Figure 4.49) there is some small scatter and larger deviation for the FAVOR results which are again higher than the CEA results.

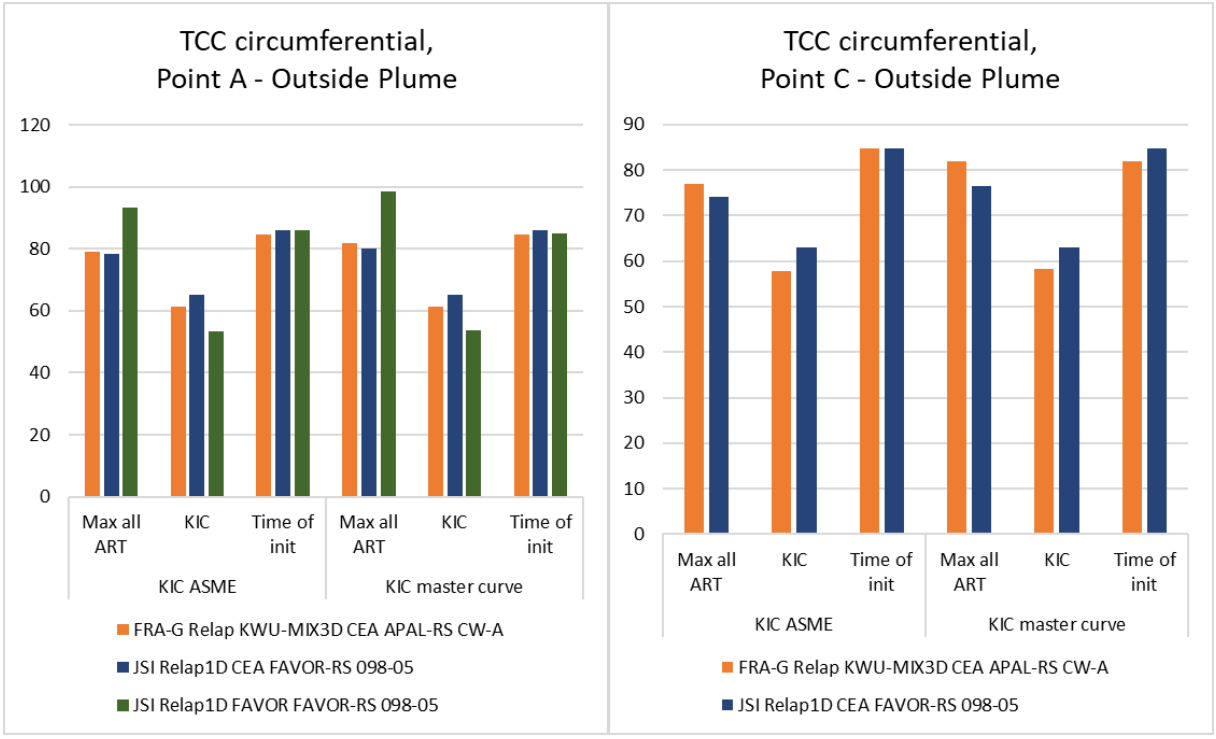

Figure 4.48: Maximum allowable ART (°C) tangent approach lower bound – TCC circumferential outside plume location

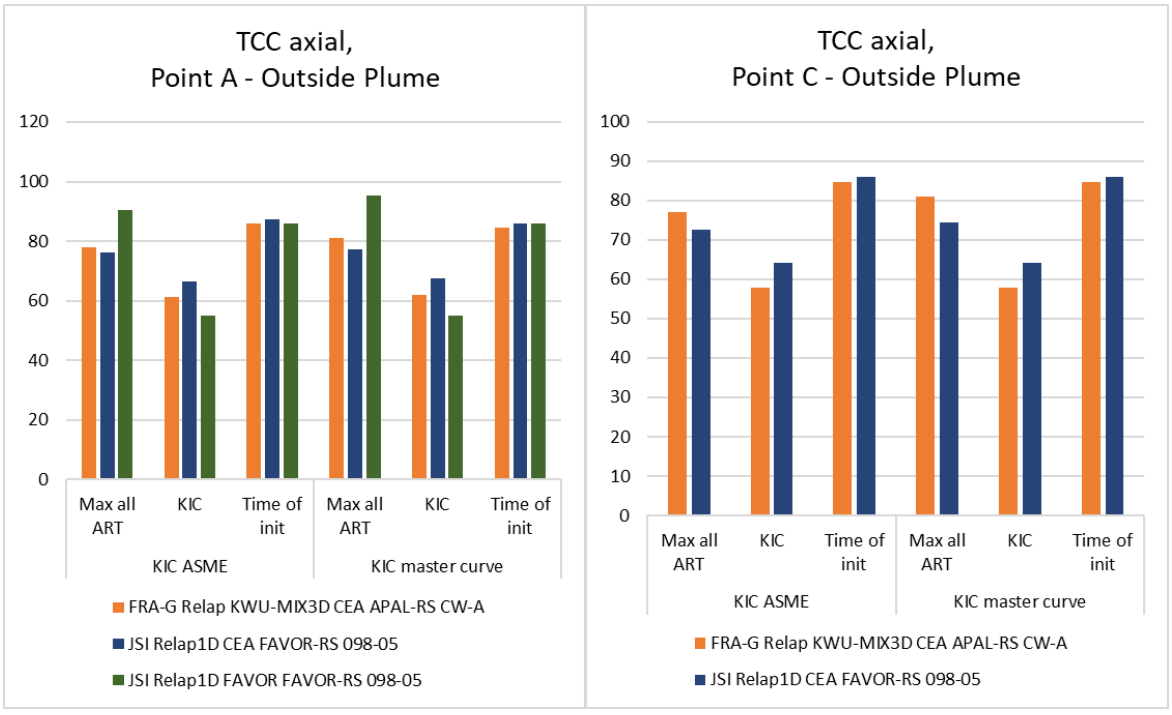

Figure 4.49: Maximum allowable ART (°C) tangent approach lower bound – TCC axial outside plume location

4.3.1.2 UCC

The results for UCC again reflect the results of part 2.1 (chapter 4.2.1). It can be noted that the Trace results are slightly lower than the Relap results, also between the Relap results some small differences in K_I can lead to over 10 °C difference in max. allow. ART (Figure 4.50).

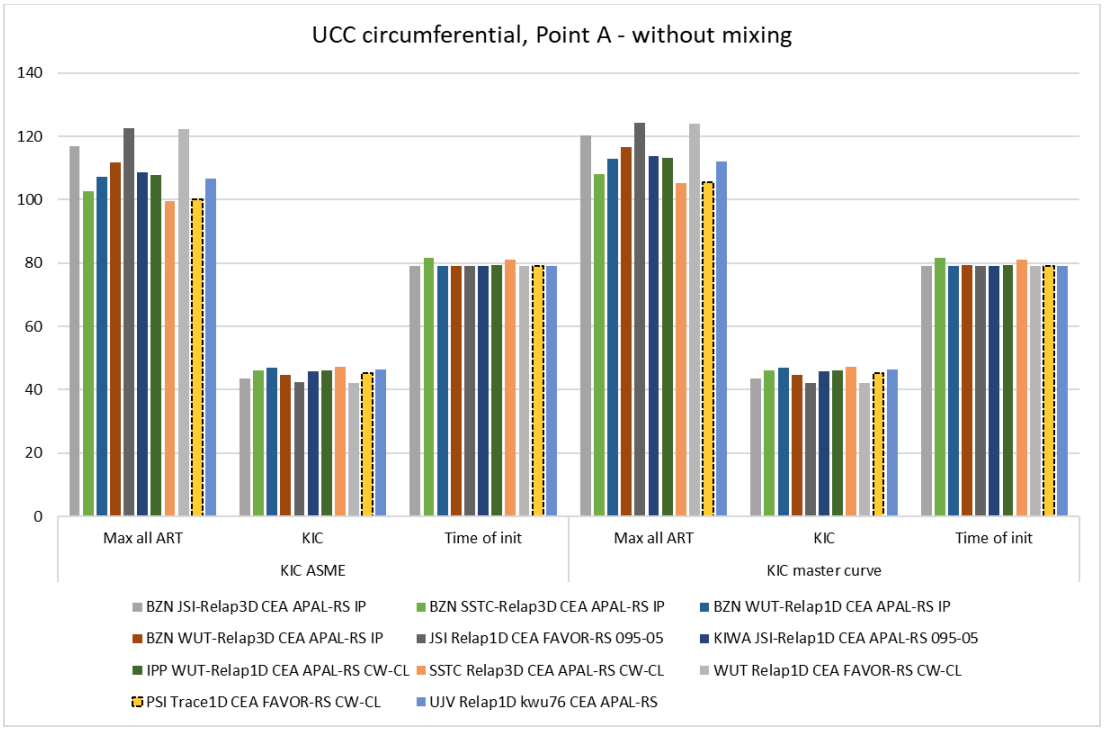

Figure 4.50: Maximum allowable ART (°C) tangent approach lower bound – UCC circumferential point A without TH mixing

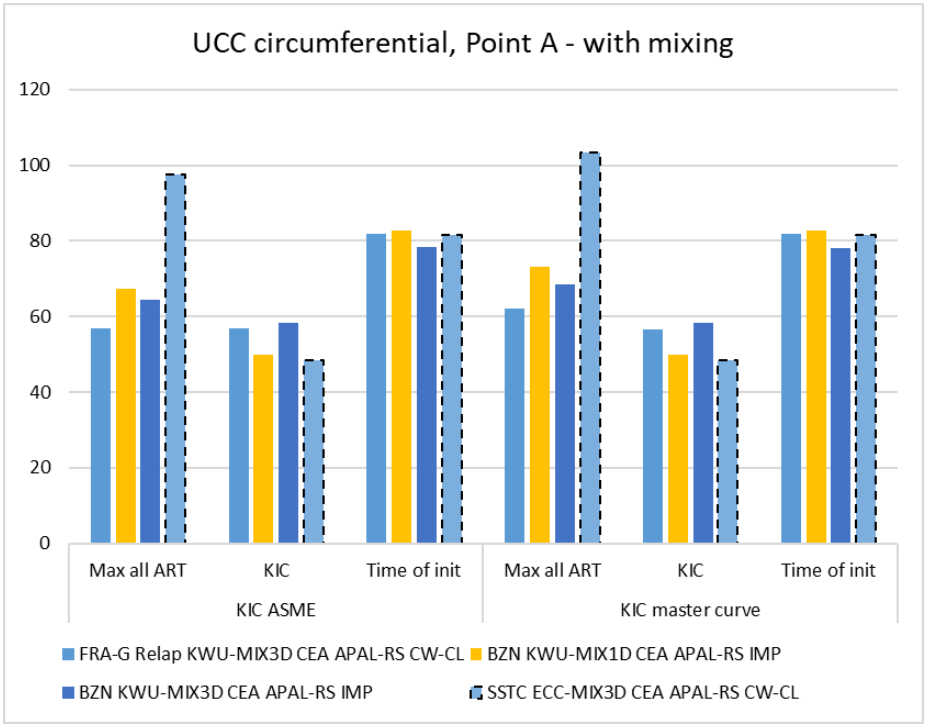

Figure 4.51: Maximum allowable ART (°C) tangent approach lower bound – UCC circumferential point A with TH mixing

For the results with consideration of TH mixing there is again a larger difference between KWU-MIX and ECC-MIX (Figure 4.51).

Most of the UCC results for point C only have a limit for the master curve approach and no limit for the ASME approach. The results without TH mixing are therefore only shown for the master curve approach (Figure 4.52, Figure 4.56). For the results with TH mixing also the ASME results are shown, here infinite results are represented by bars that reach the limit of the y-axis in the diagram (Figure 4.53, Figure 4.57). The other results show the same tendencies as for the circumferential crack (Figure 4.54, Figure 4.55)

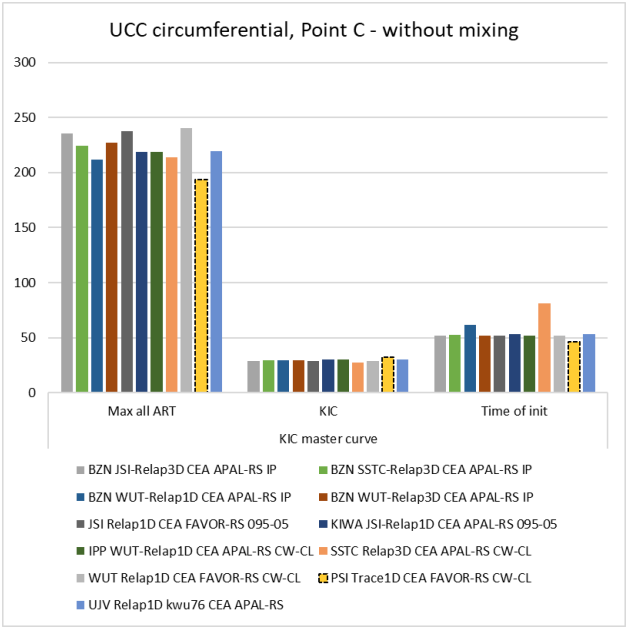

Figure 4.52: Maximum allowable ART (°C) tangent approach lower bound – UCC circumferential point C without TH mixing

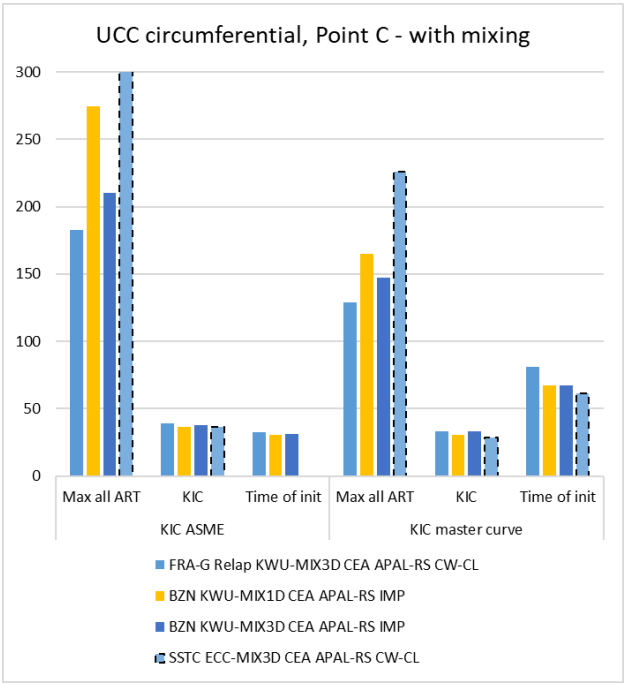

Figure 4.53: Maximum allowable ART (°C) tangent approach lower bound – UCC circumferential point C with TH mixing

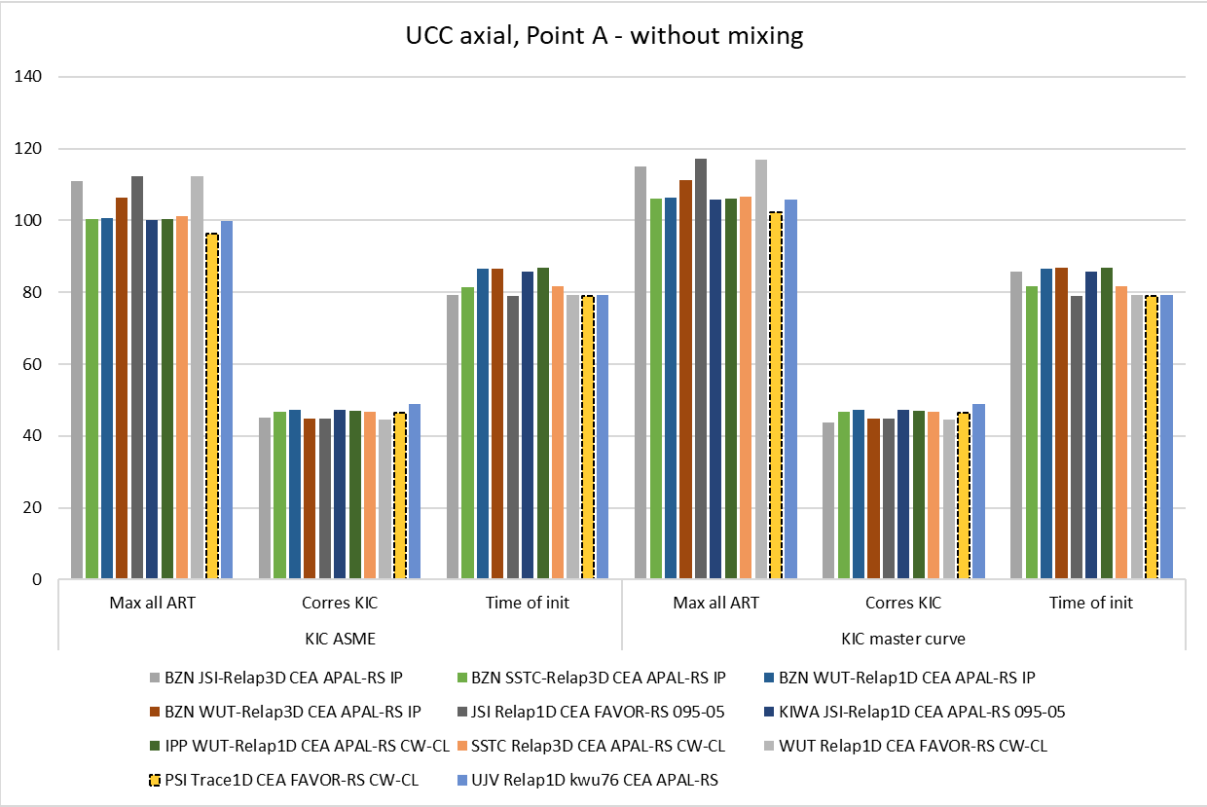

Figure 4.54: Maximum allowable ART (°C) tangent approach lower bound – UCC axial point A without TH mixing

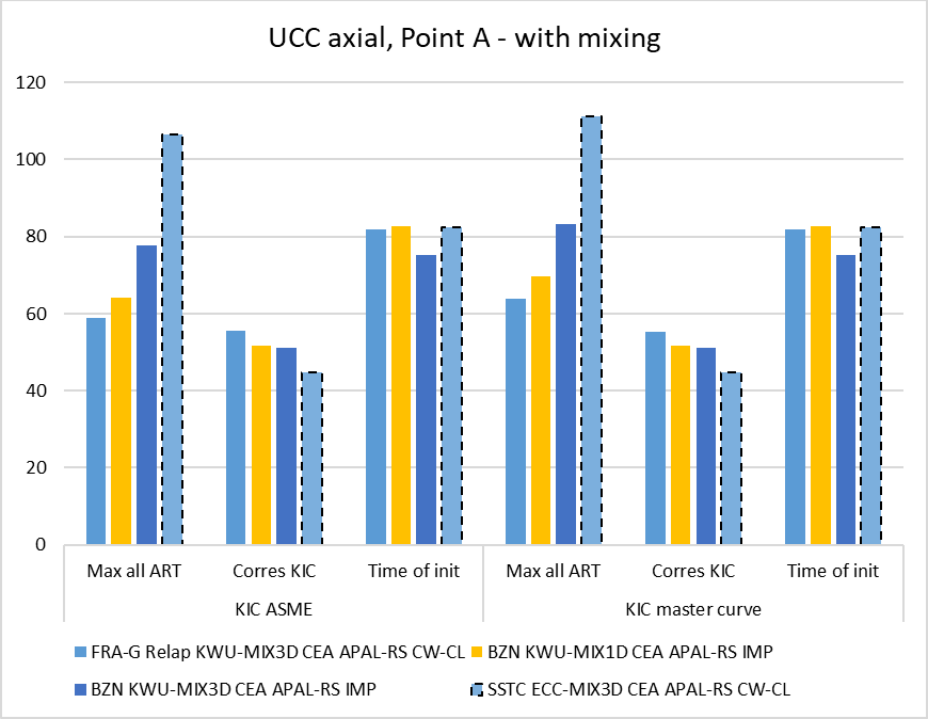

Figure 4.55: Maximum allowable ART (°C) tangent approach lower bound – UCC axial point A with TH mixing

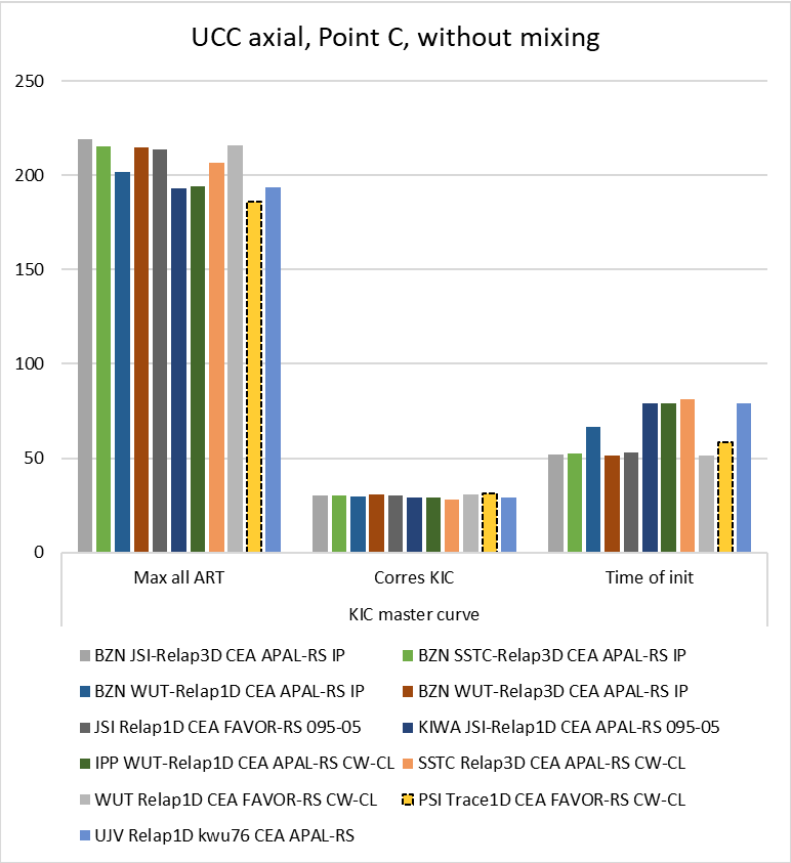

Figure 4.56: Maximum allowable ART (°C) tangent approach lower bound – UCC axial point C without TH mixing

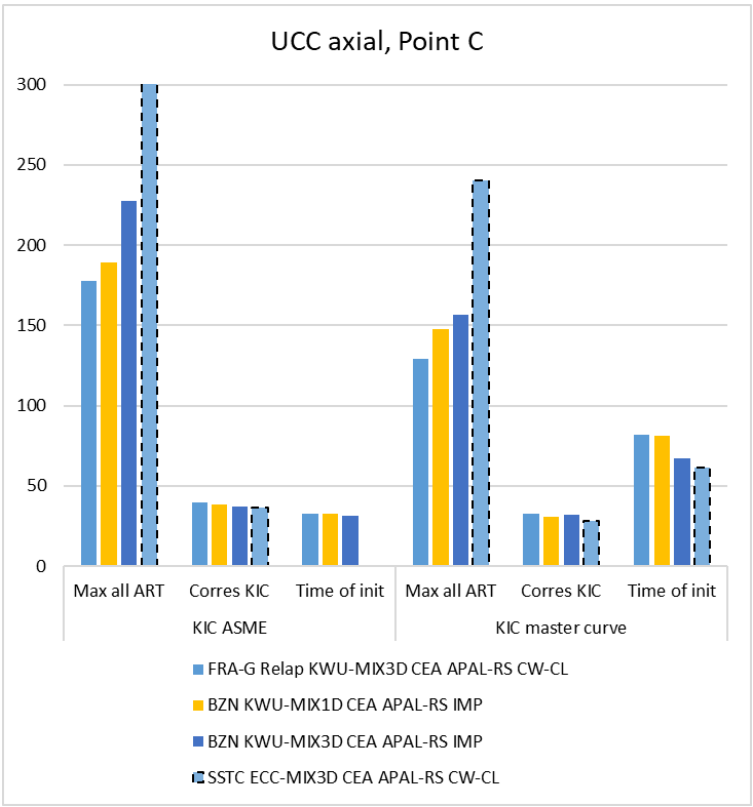

Figure 4.57: Maximum allowable ART (°C) tangent approach lower bound – UCC axial point C with TH mixing

For the outside plume location, the results of Framatome and JSI are close together since for this location mixing does not play a major role, see Figure 4.58.

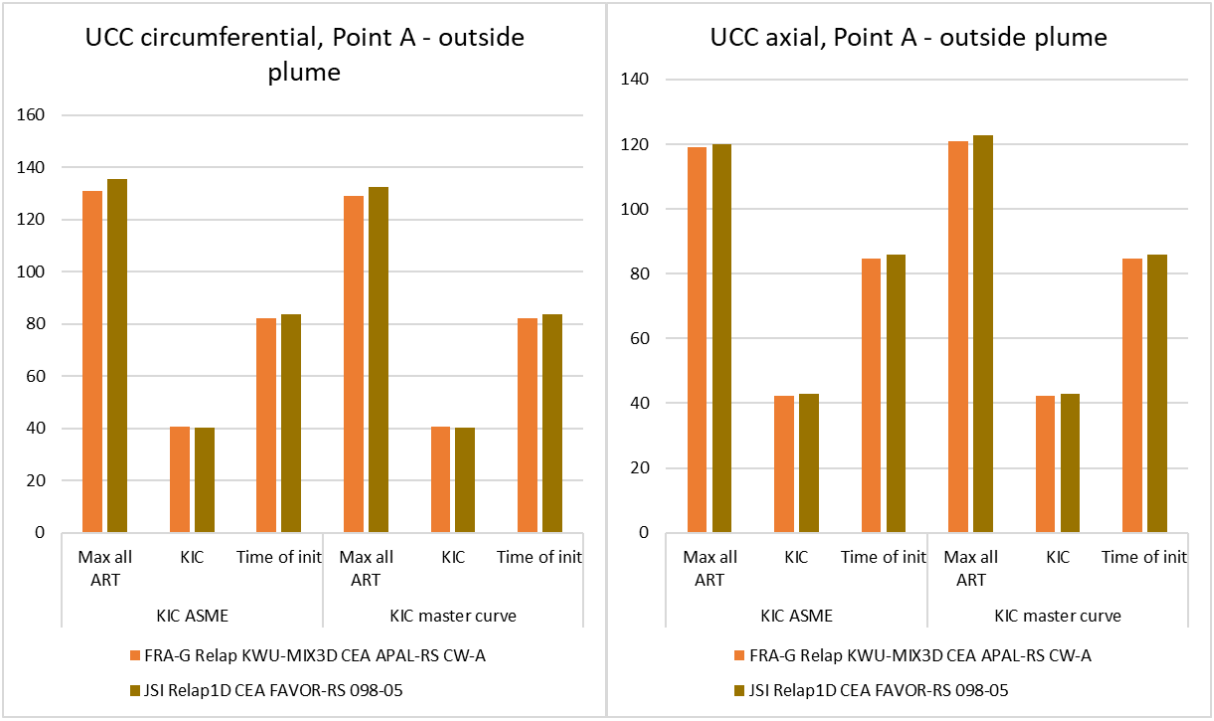

Figure 4.58: Maximum allowable ART (°C) tangent approach lower bound – UCC outside plume location

4.3.1.3 Embedded crack

The embedded crack results, all calculated with FAVOR, are shown in Figure 4.59 and Figure 4.60. The Trace results are close to the ECC-MIX results, the Relap result is higher.

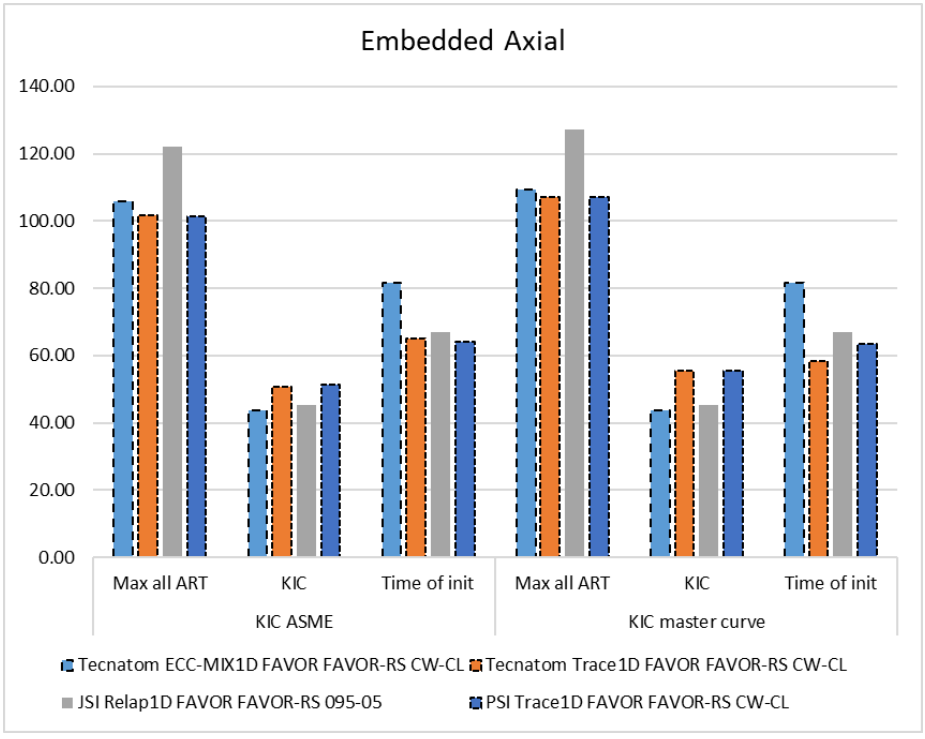

Figure 4.59: Maximum allowable ART (°C) tangent approach lower bound – Embedded crack axial

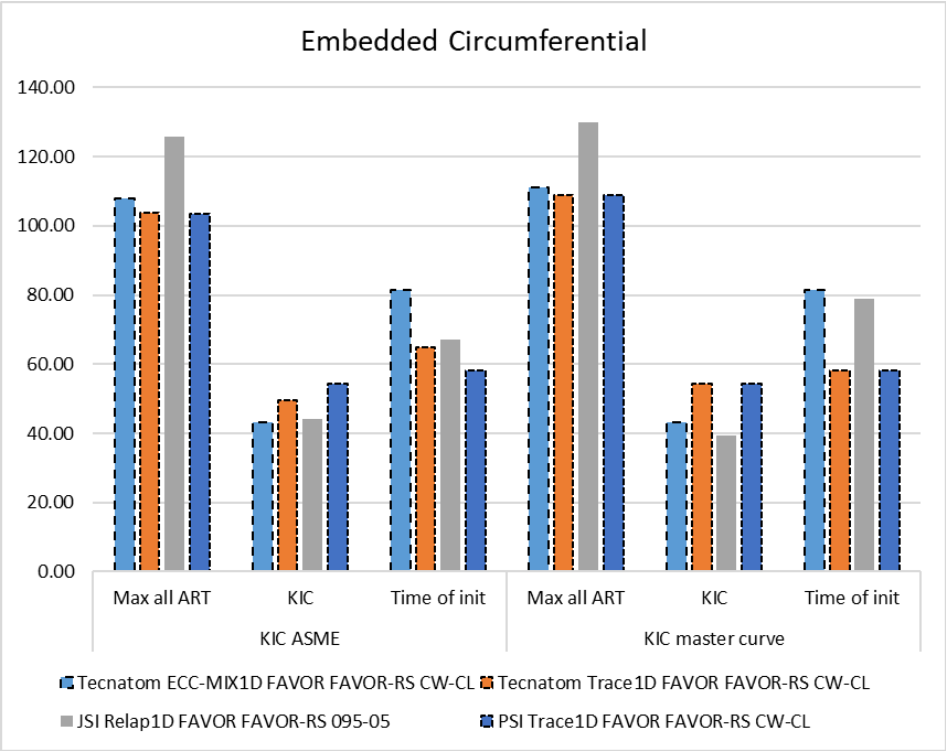

Figure 4.60: Maximum allowable ART (°C) tangent approach lower bound – Embedded crack circumferential

4.3.2 Simple WPS-max. approach

In this chapter the results for max. allow. ART using the simple WPS-max. approach are presented. There are results for both the ASME and the master curve concepts, for each using the lower bound. In addition, the simple WPS-max. approach was also applied taking into account ASME and master curve median curves. These results are given in [3] and lead to the same conclusions as the lower bound application.

4.3.2.1 TCC

In general, the max. all. ART is higher than for the tangent approach. For TCC point A without mixing (Figure 4.61 and Figure 4.65) the two lowest results are using Trace data and the FAVOR method. The highest result is using Relap and FAVOR. The results with mixing (Figure 4.62, Figure 4.64, Figure 4.66, Figure 4.68) show that the ECC-MIX are over 20 °C higher than the KWU-MIX results. For ECC-MIX the difference between CEA and FAVOR method is lower than 10 °C for the circumferential crack but a lot higher for the axial crack. The results for point C exclusively using Relap and CEA method are in good agreement (Figure 4.63 and Figure 4.67).

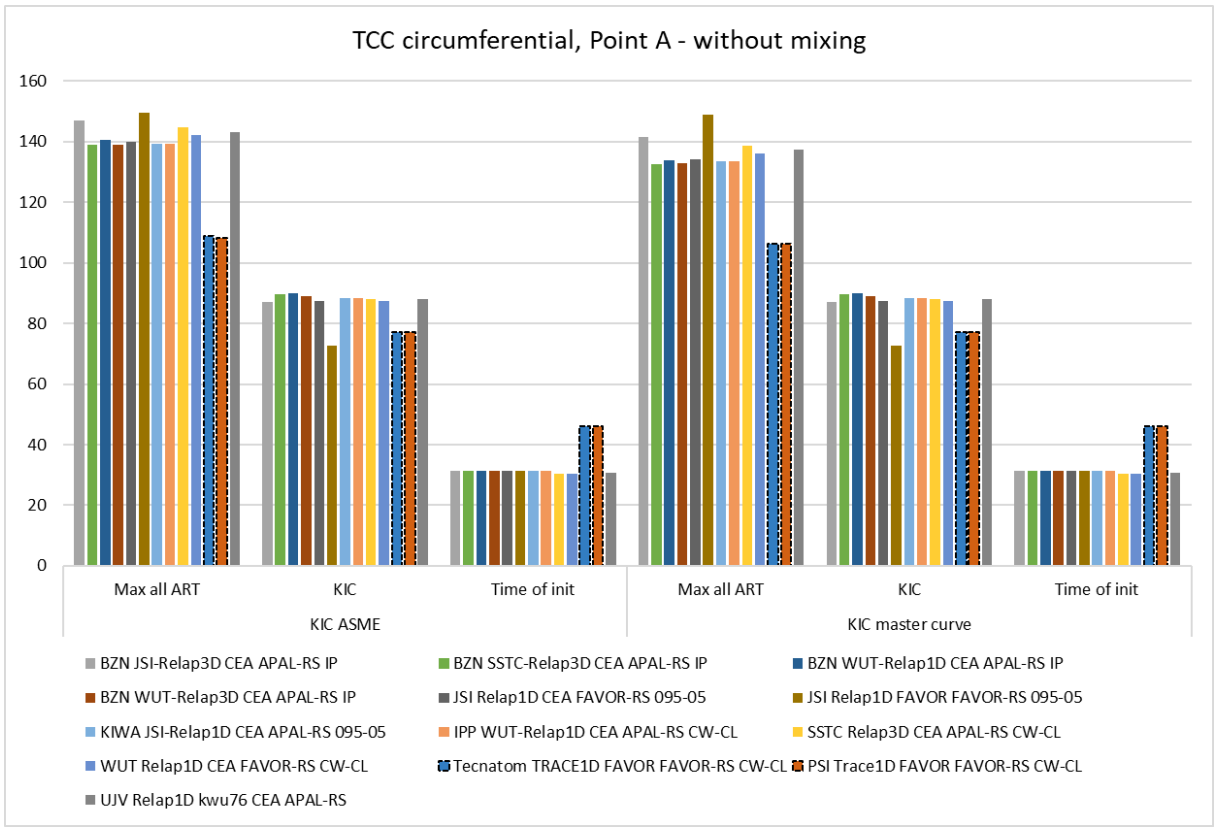

Figure 4.61: Maximum allowable ART (°C) WPS-max approach lower bound – TCC circumferential Point A without TH mixing

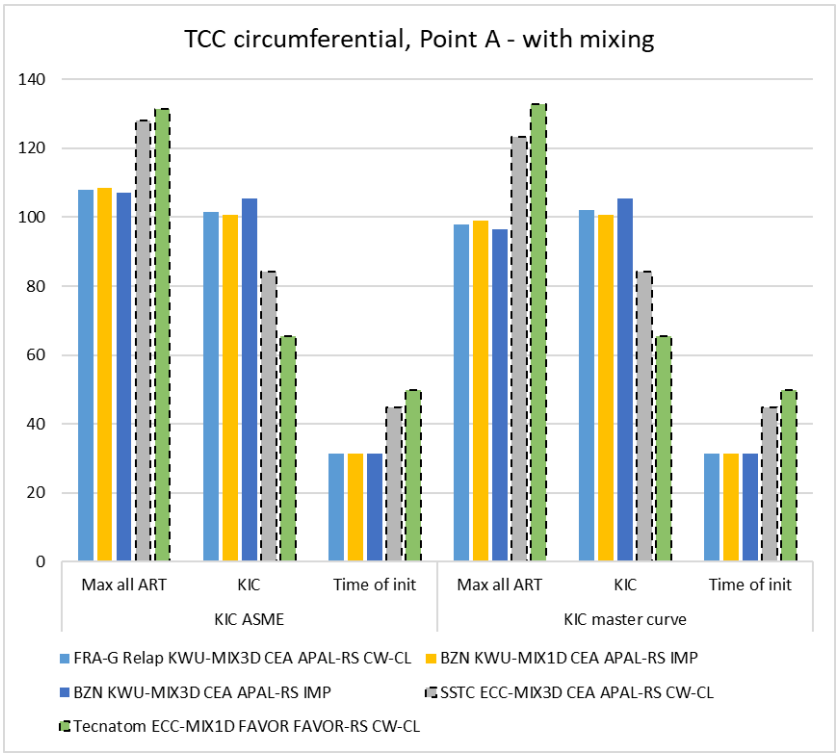

Figure 4.62: Maximum allowable ART (°C) WPS-max approach lower bound – TCC circumferential Point A with TH mixing

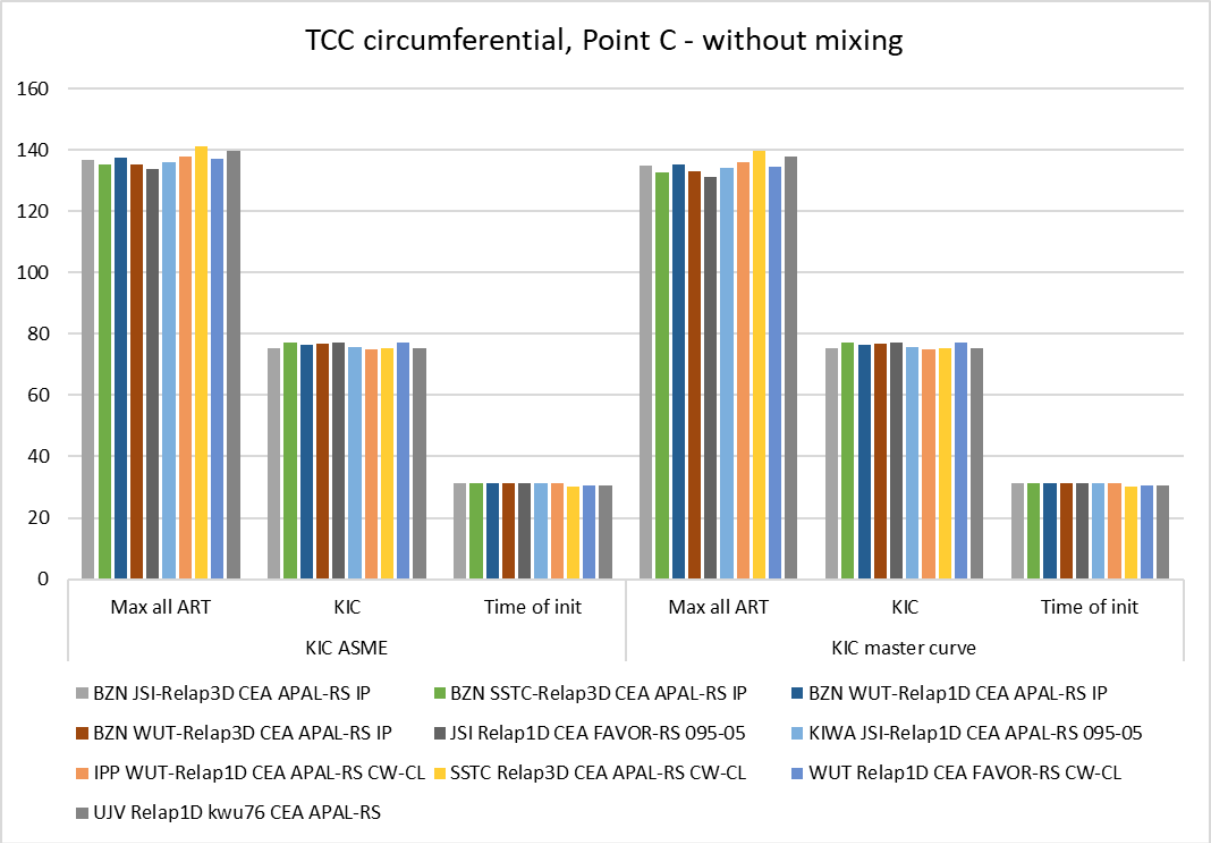

Figure 4.63: Maximum allowable ART (°C) WPS-max approach lower bound – TCC circumferential Point C without TH mixing

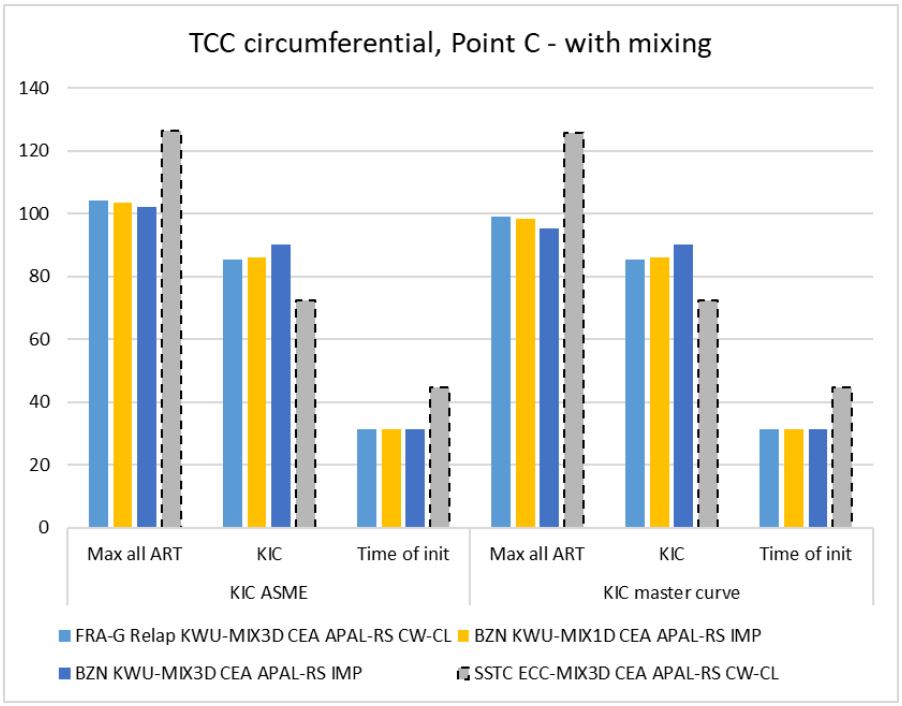

Figure 4.64: Maximum allowable ART (°C) WPS-max approach lower bound – TCC circumferential Point C with TH mixing

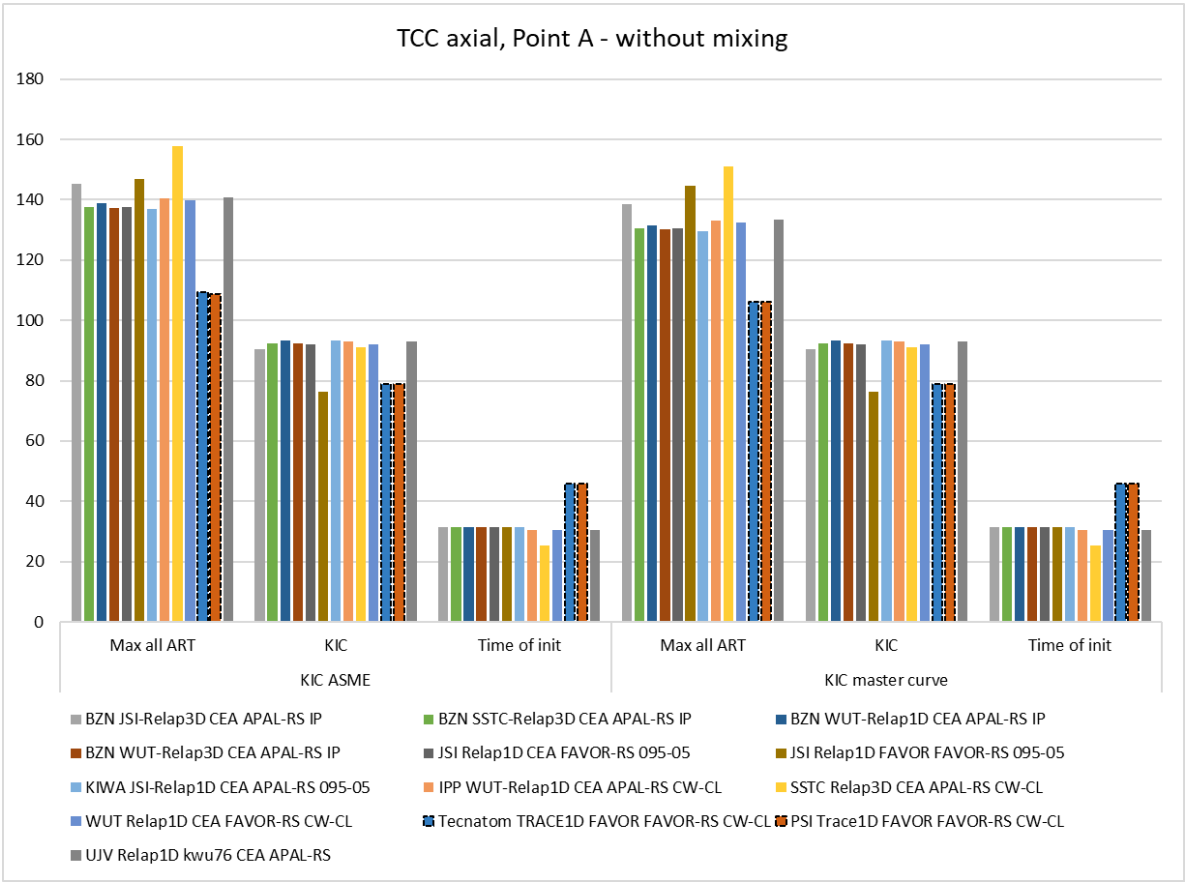

Figure 4.65: Maximum allowable ART (°C) WPS-max approach lower bound – TCC axial Point A without TH mixing

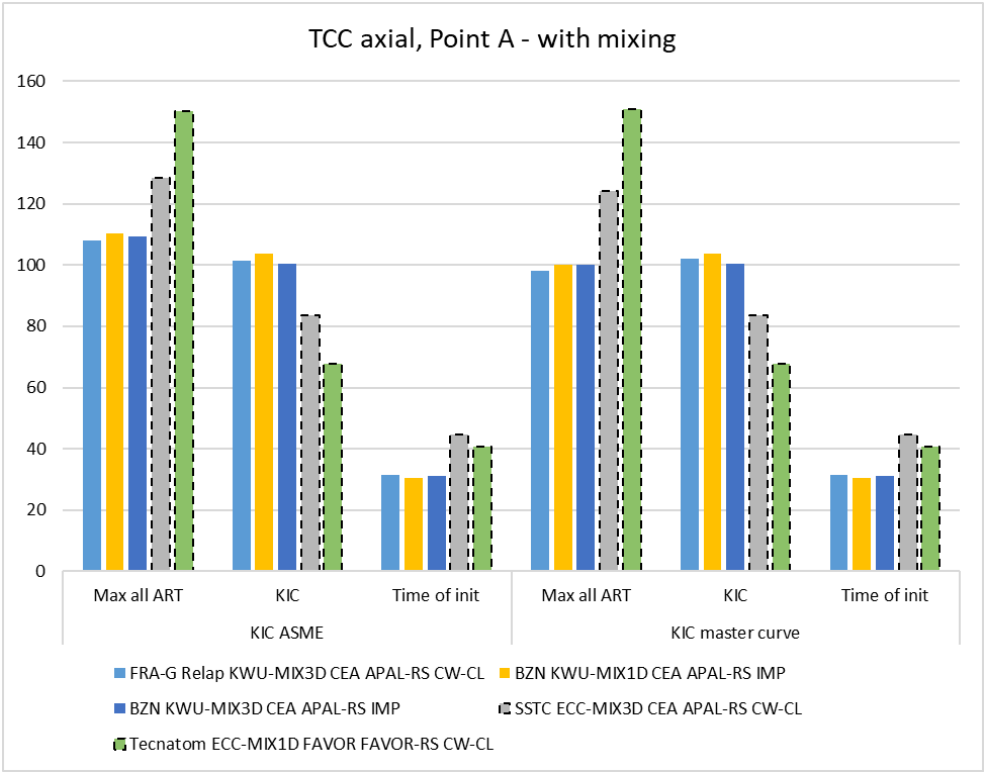

Figure 4.66: Maximum allowable ART (°C) WPS-max approach lower bound – TCC axial Point A with TH mixing

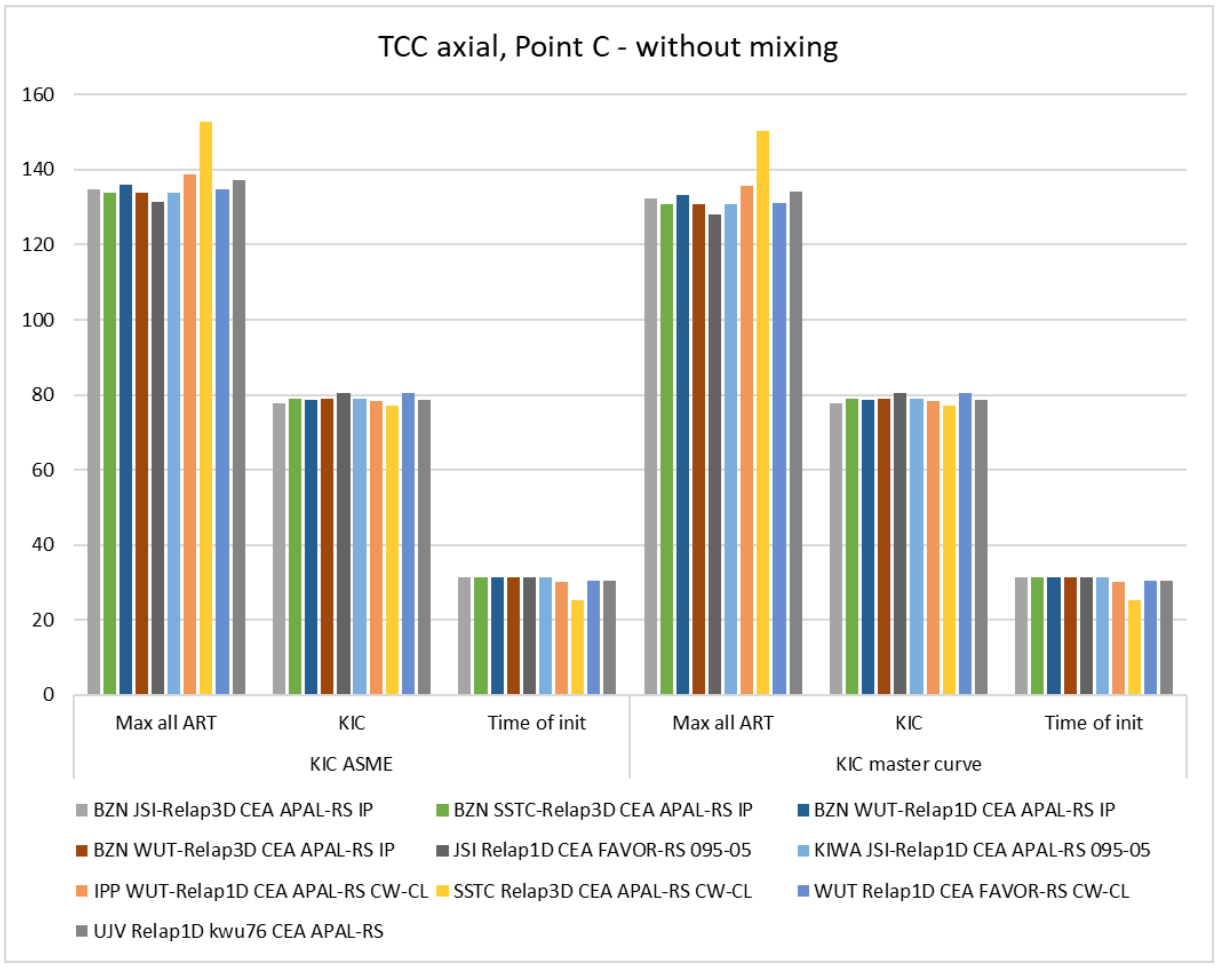

Figure 4.67: Maximum allowable ART (°C) WPS-max approach lower bound – TCC axial Point C without TH mixing

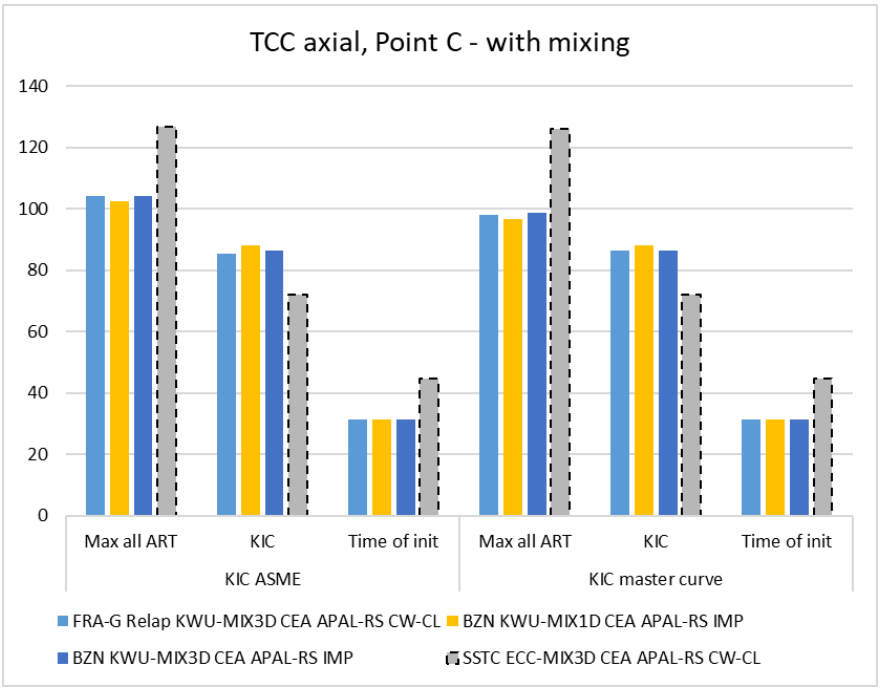

Figure 4.68: Maximum allowable ART (°C) WPS-max approach lower bound – TCC axial Point C with TH mixing

The results for the outside plume location (Figure 4.69) are in good agreement. The differences mixing/no mixing and FAVOR/CEA do not play a large role in relative terms, however in absolute terms the difference is up to 15 °C.

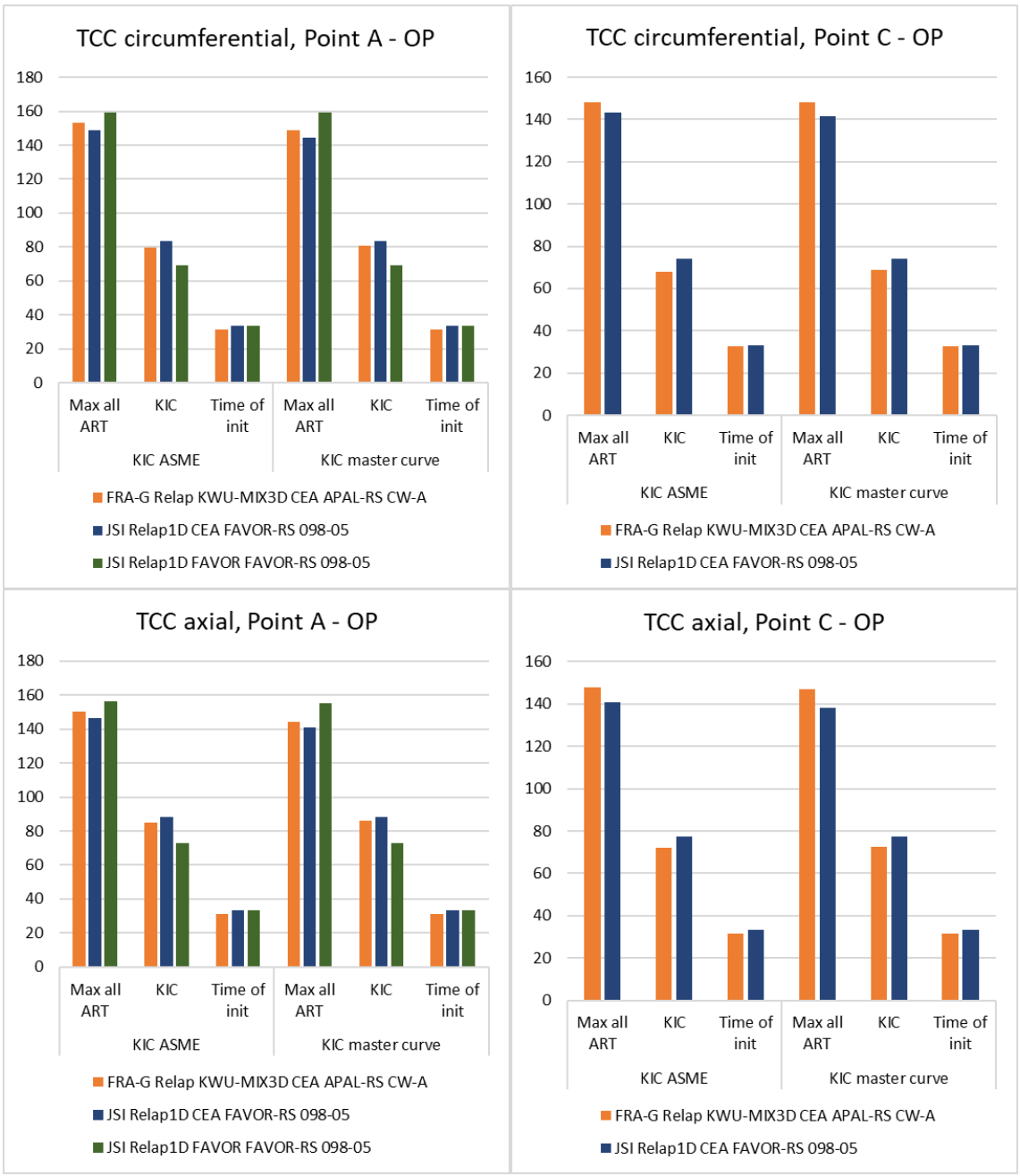

Figure 4.69: Maximum allowable ART (°C) WPS-max approach lower bound – TCC outside plume location

4.3.2.2 UCC

The UCC results (Figure 4.70 to Figure 4.78) reflect the results of part 2.1 (chapter 4.2.1). The Relap results are in good agreement. The Trace results are about 40 °C lower, the ECC-MIX results up to 40 °C higher than the Relap results.

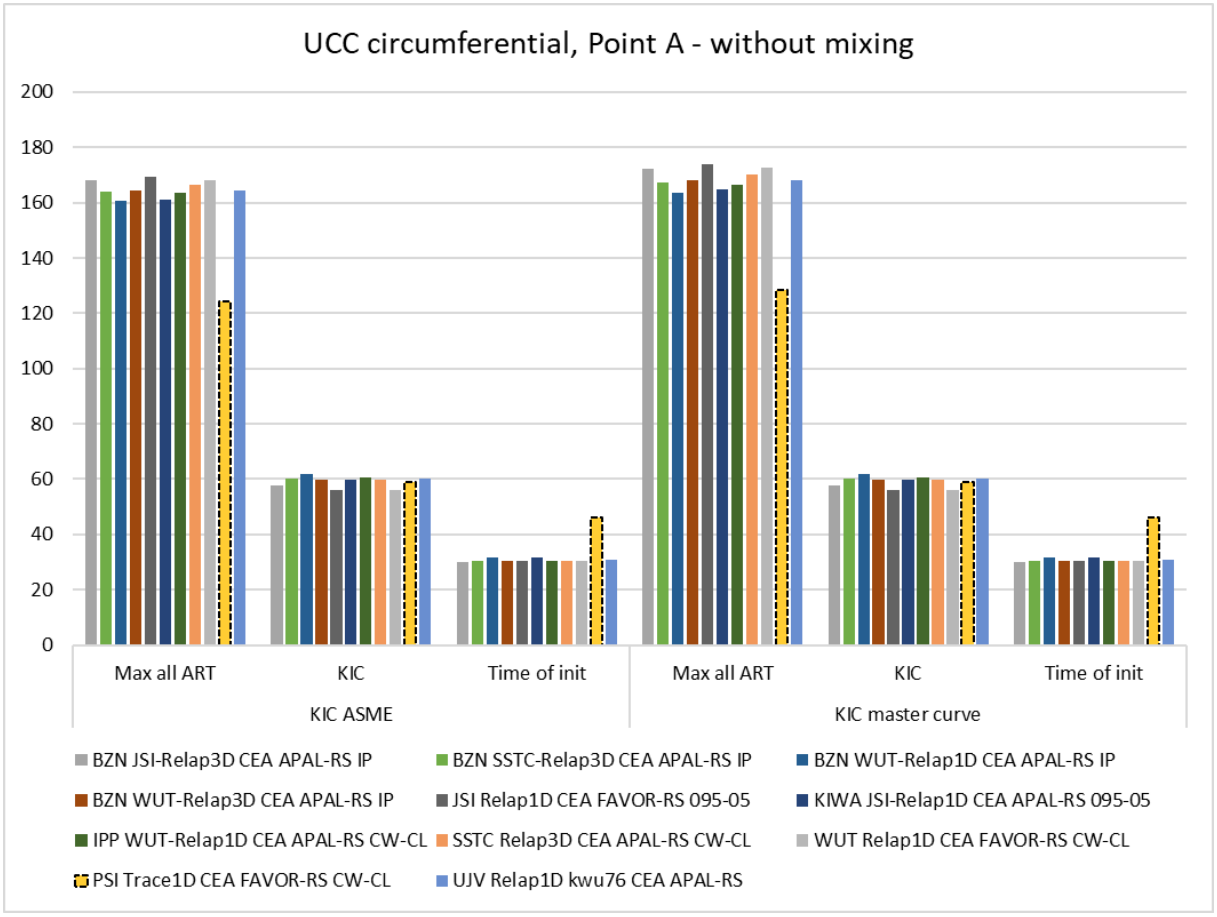

Figure 4.70: Maximum allowable ART (°C) WPS-max approach lower bound – UCC circumferential Point A without TH mixing

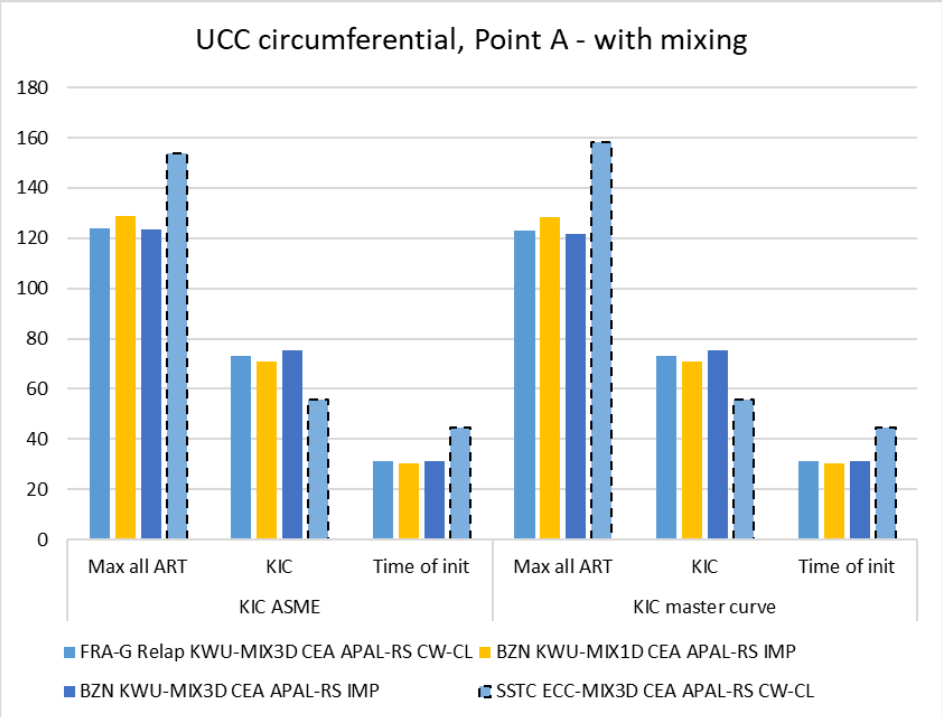

Figure 4.71: Maximum allowable ART (°C) WPS-max approach lower bound – UCC circumferential Point A with TH mixing

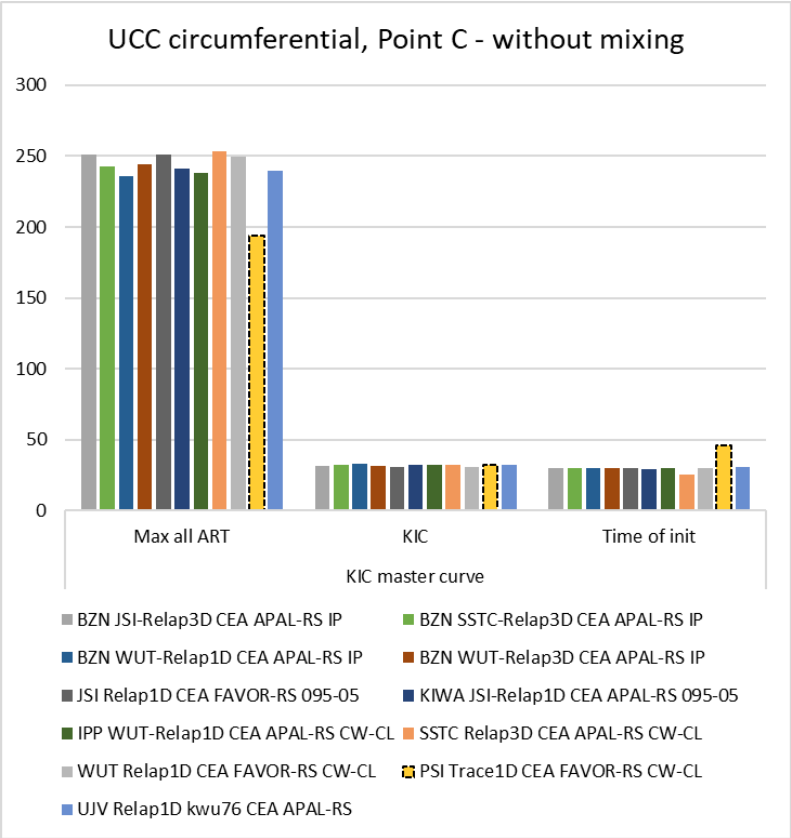

Figure 4.72: Maximum allowable ART (°C) WPS-max approach lower bound – UCC circumferential Point C without TH mixing (no limit for ASME approach)

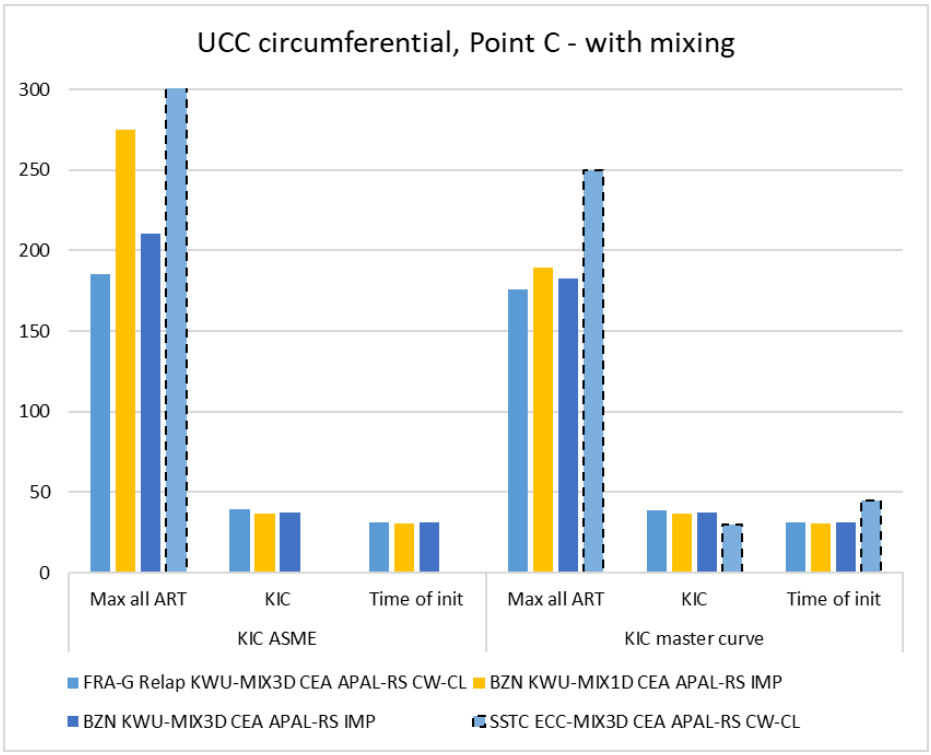

Figure 4.73: Maximum allowable ART (°C) WPS-max approach lower bound – UCC circumferential Point C with TH mixing

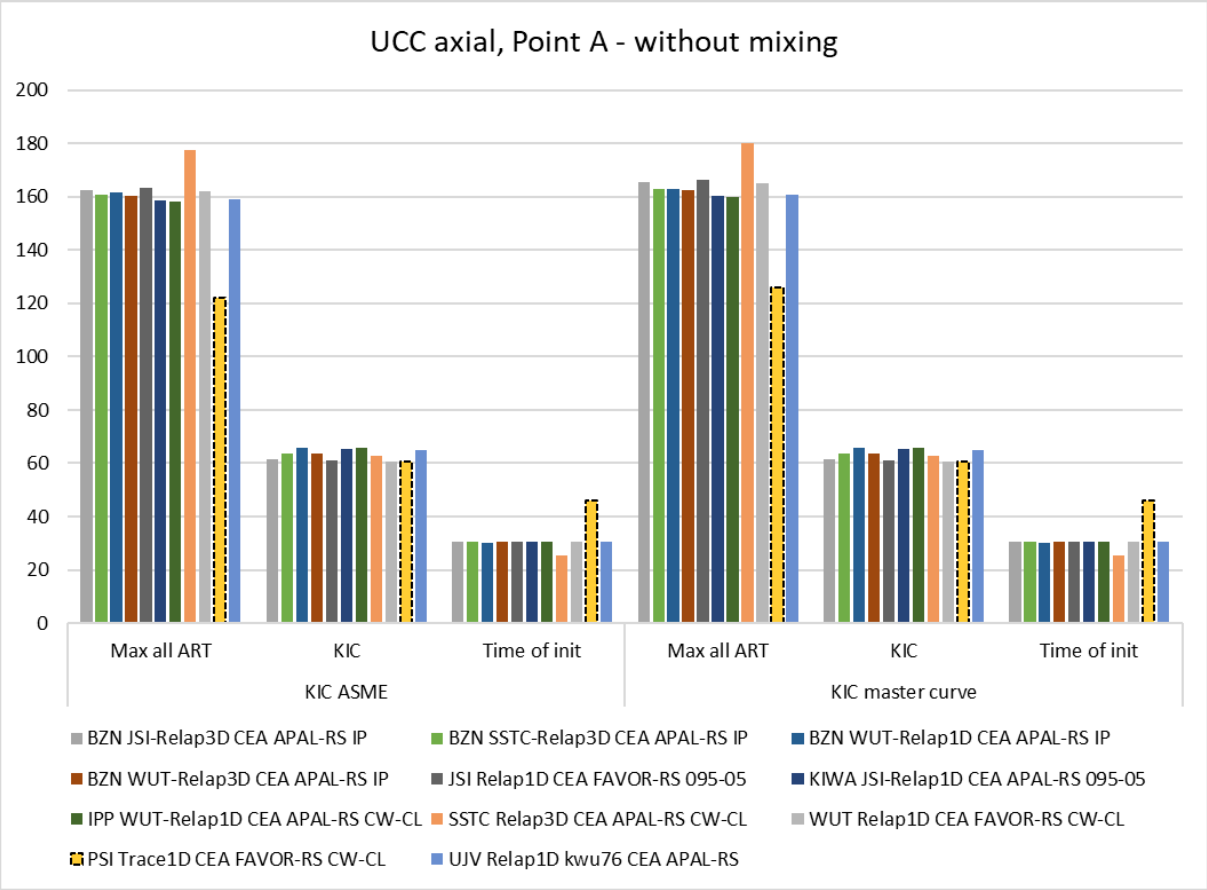

Figure 4.74: Maximum allowable ART (°C) WPS-max approach lower bound – UCC axial Point A without TH mixing

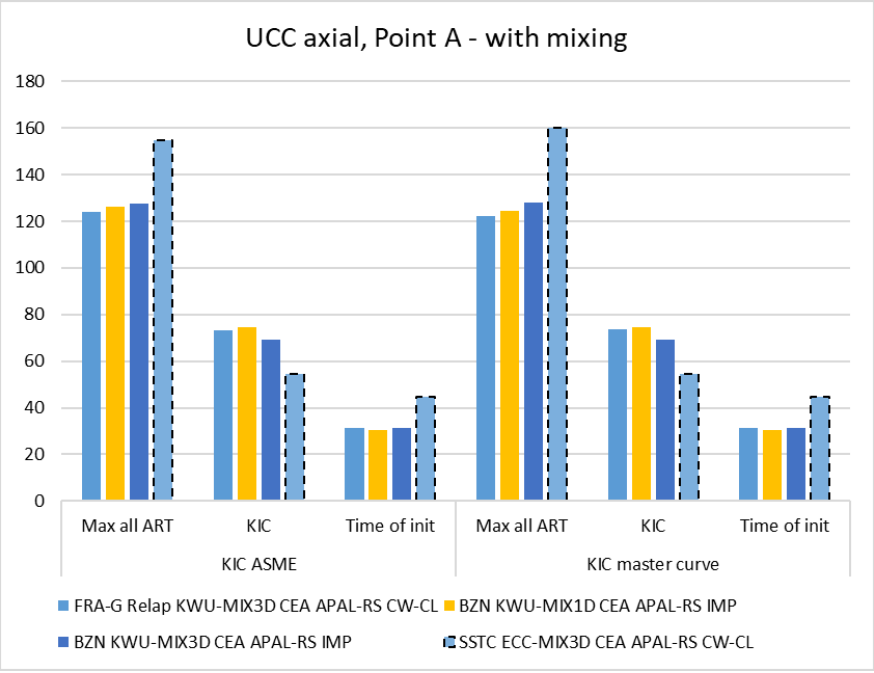

Figure 4.75: Maximum allowable ART (°C) WPS-max approach lower bound – UCC axial Point A with TH mixing

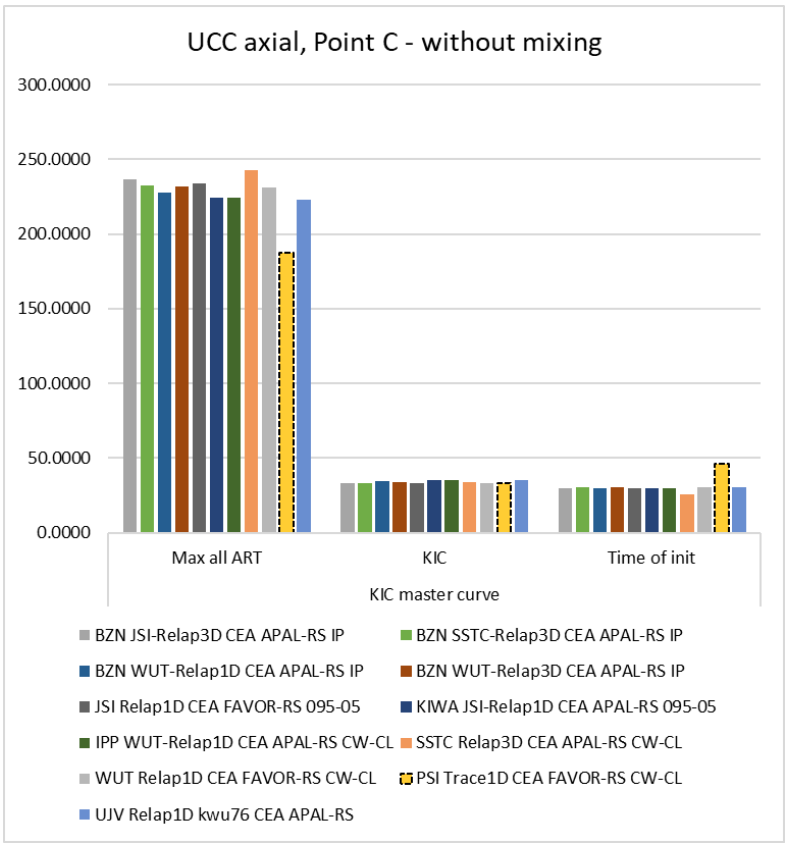

Figure 4.76: Maximum allowable ART (°C) WPS-max approach lower bound – UCC axial Point C without TH mixing (no limit for ASME approach)

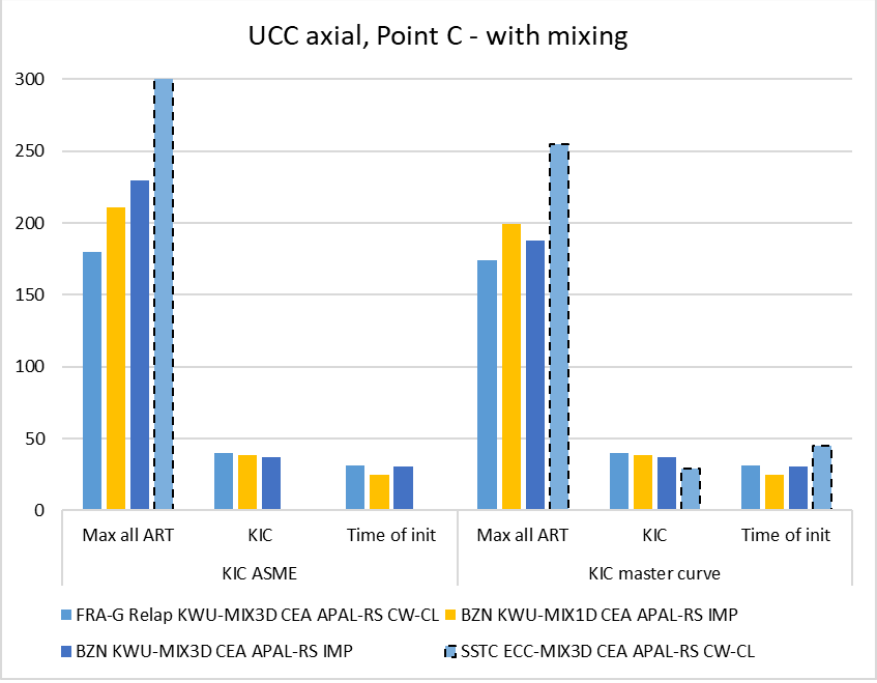

Figure 4.77: Maximum allowable ART (°C) WPS-max approach lower bound – UCC axial Point C with TH mixing

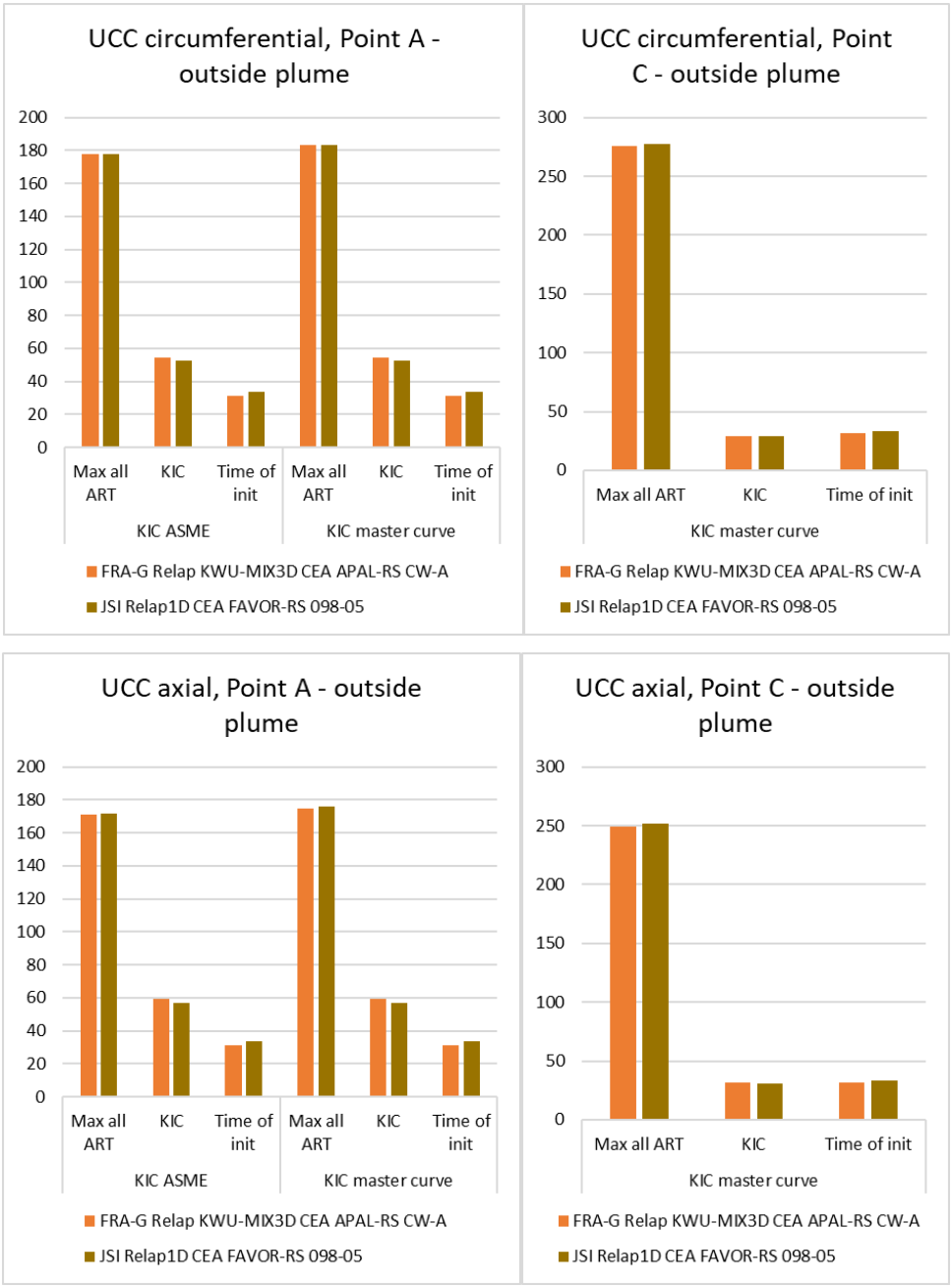

Figure 4.78: Maximum allowable ART (°C) WPS-max approach lower bound – UCC outside plume location

4.3.2.3 Embedded crack

The results for the embedded crack (Figure 4.79 and Figure 4.80), all calculated with FAVOR, show again high results for ECC-MIX and Relap and lower results for Trace.

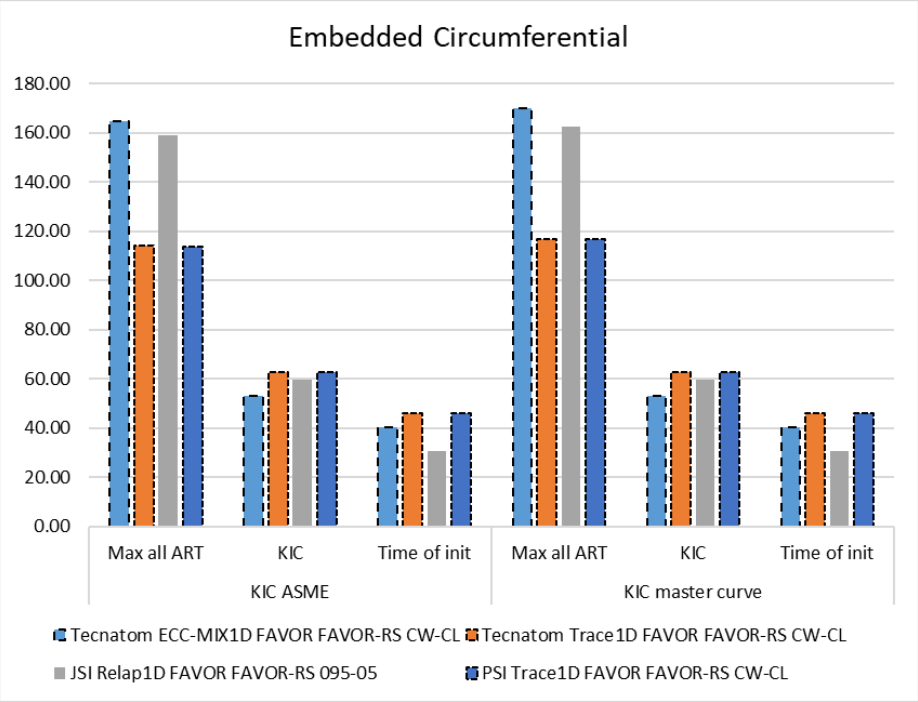

Figure 4.79: Maximum allowable ART (°C) WPS-max approach lower bound – Embedded crack circumferential

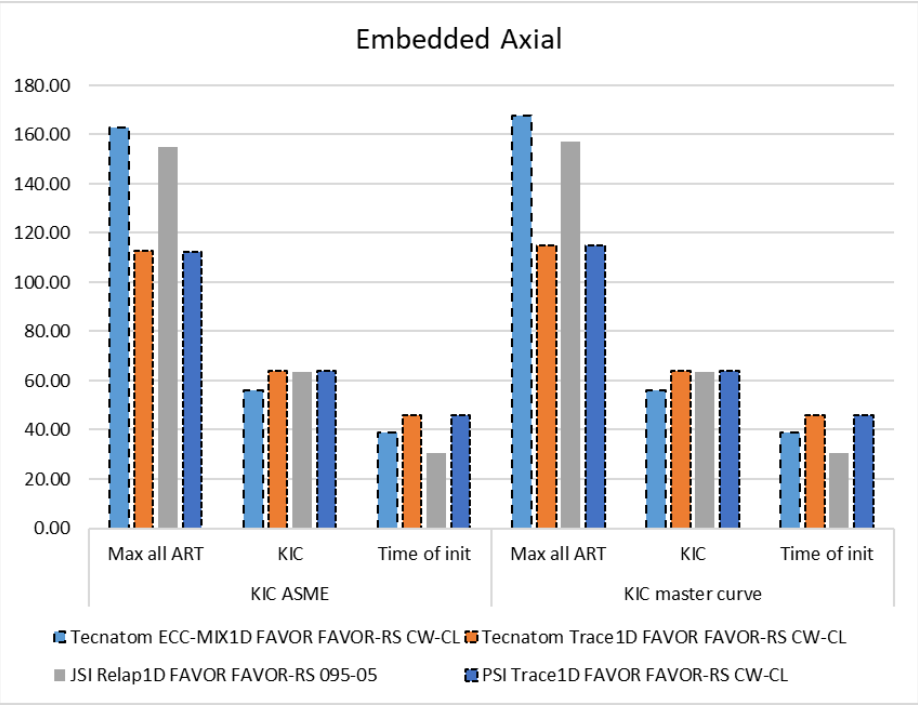

Figure 4.80: Maximum allowable ART (°C) WPS-max approach lower bound – Embedded crack axial

4.3.3 Sophisticated WPS approaches

In this chapter the results for max. all. ART using several sophisticated WPS approaches (lower bound) are presented. In addition, sophisticated WPS approaches were also applied taking into account ASME and master curve mean curves. These results are given in [3].

For details regarding the WPS approaches see Deliverable 1.2 [6].

4.3.3.1 TCC

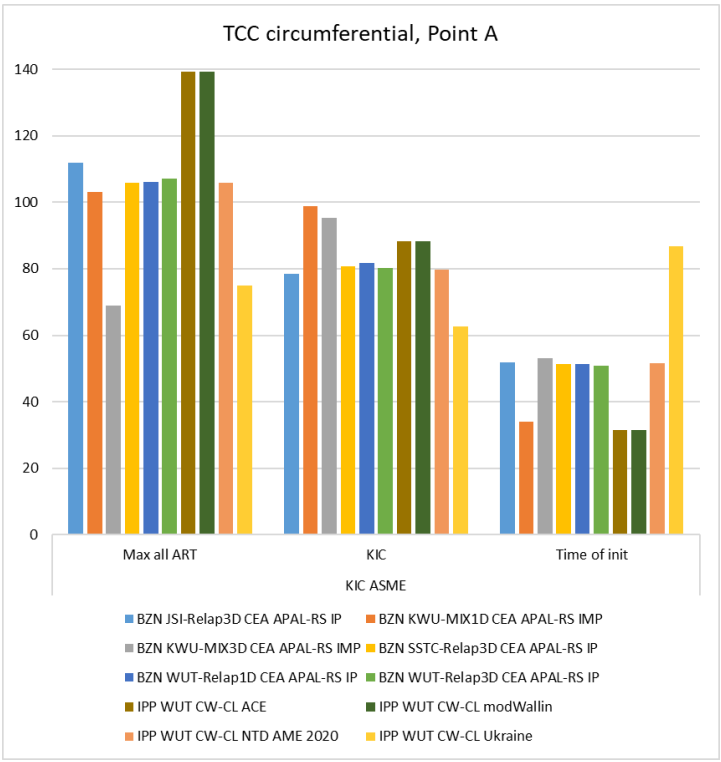

Figure 4.81: Maximum allowable ART (°C) sophisticated WPS approaches ASME lower bound – TCC circumferential Point A

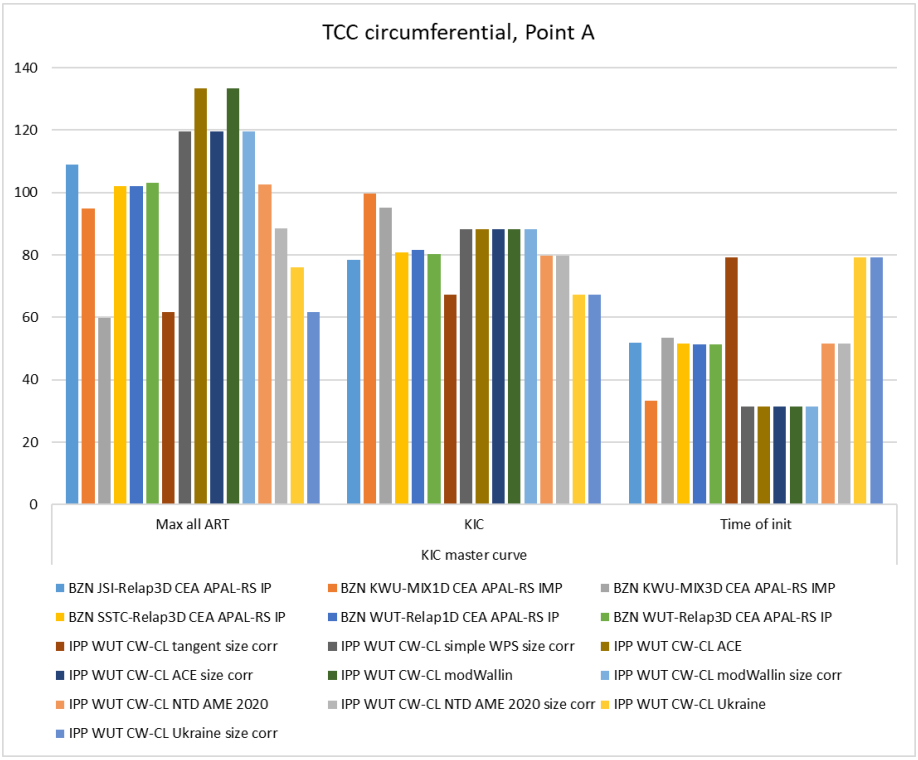

Figure 4.82: Maximum allowable ART (°C) sophisticated WPS approaches master curve lower bound – TCC circumferential Point A

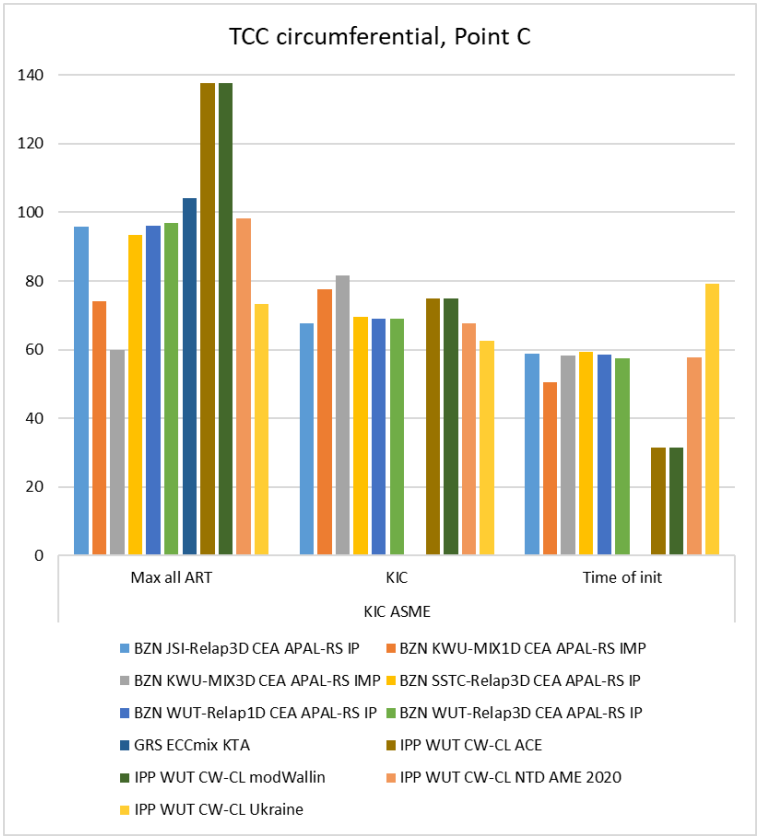

Figure 4.83: Maximum allowable ART (°C) sophisticated WPS approaches ASME lower bound – TCC circumferential Point C

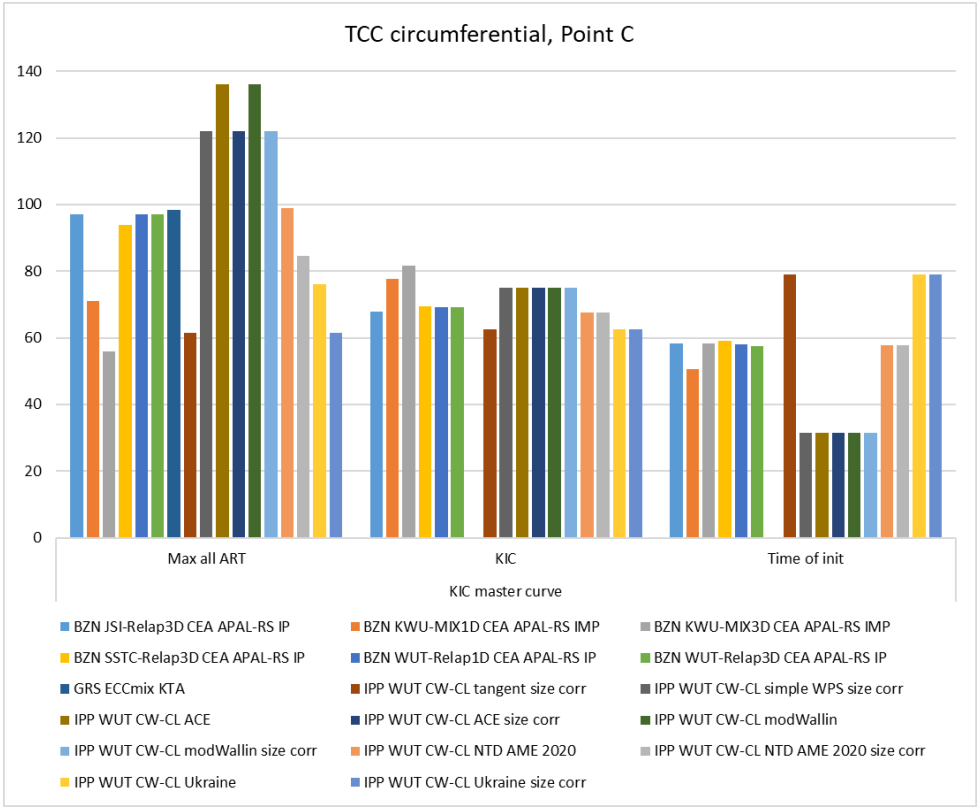

Figure 4.84: Maximum allowable ART (°C) sophisticated WPS approaches master curve lower bound – TCC circumferential Point C

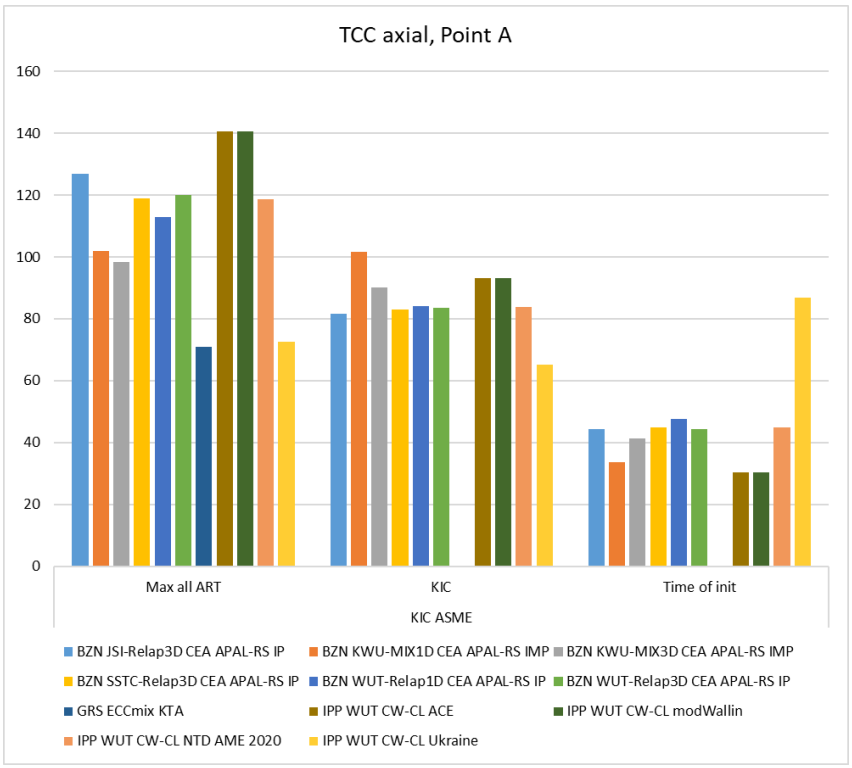

Figure 4.85: Maximum allowable ART (°C) sophisticated WPS approaches ASME lower bound – TCC axial Point A

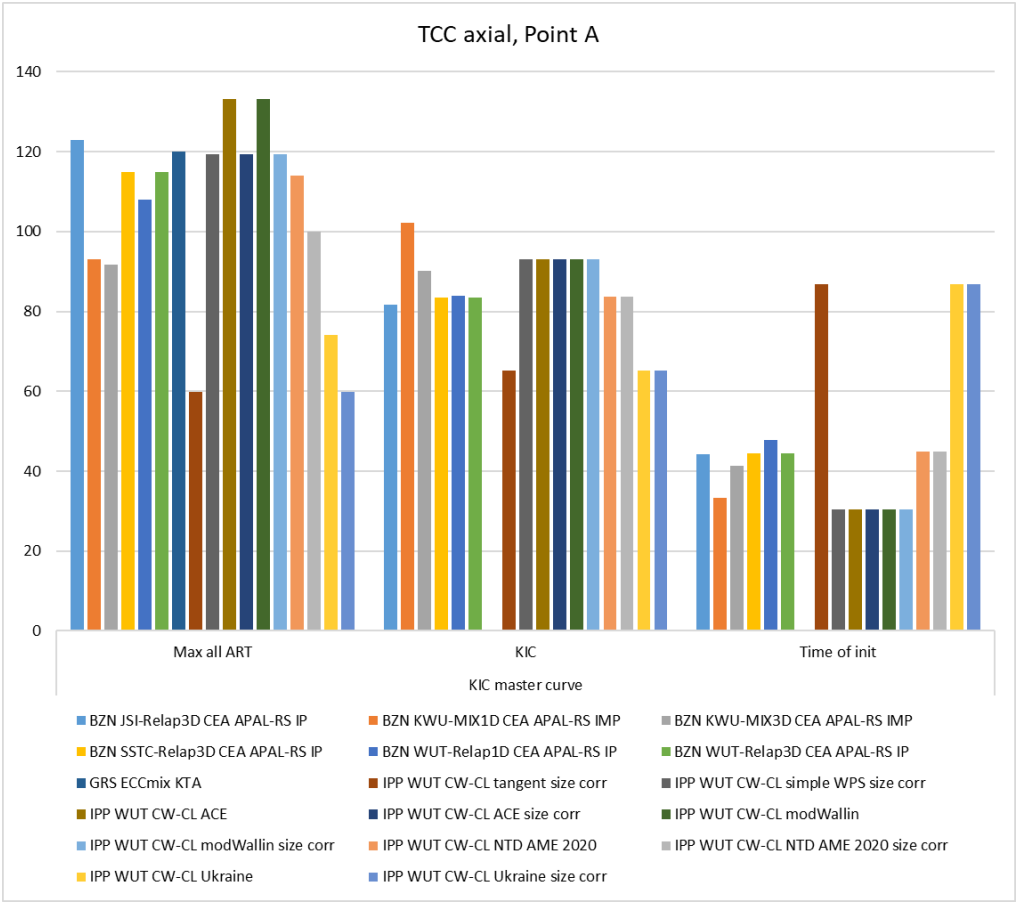

Figure 4.86: Maximum allowable ART (°C) sophisticated WPS approaches master curve lower bound – TCC axial Point A

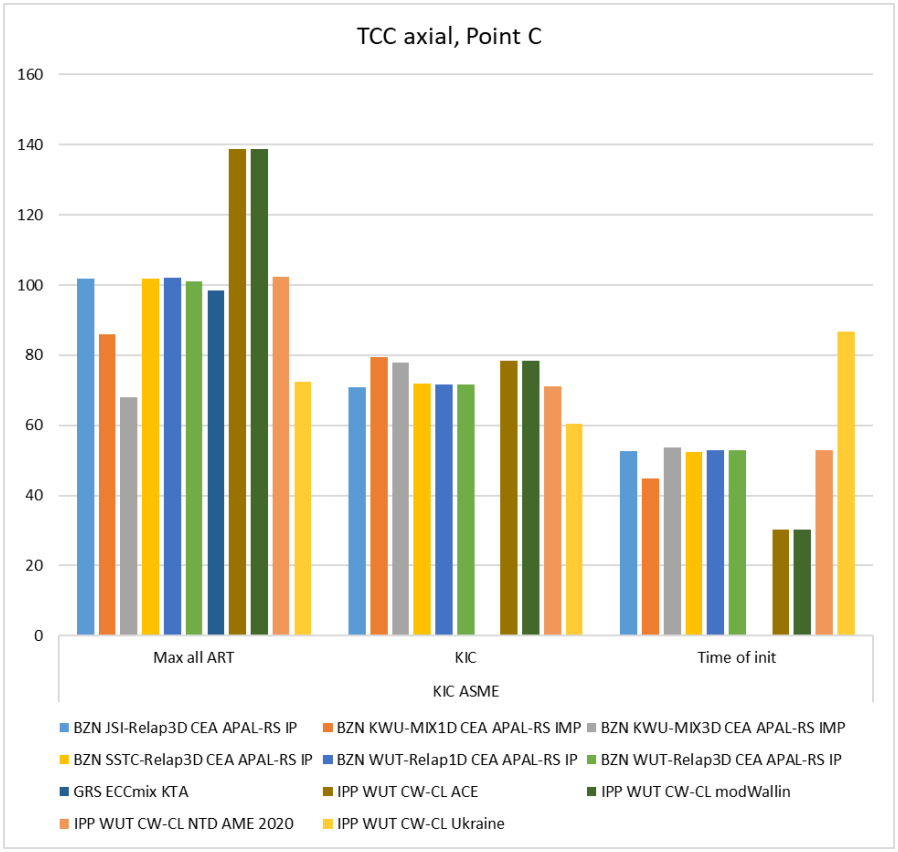

Figure 4.87: Maximum allowable ART (°C) sophisticated WPS approaches ASME lower bound – TCC axial Point C

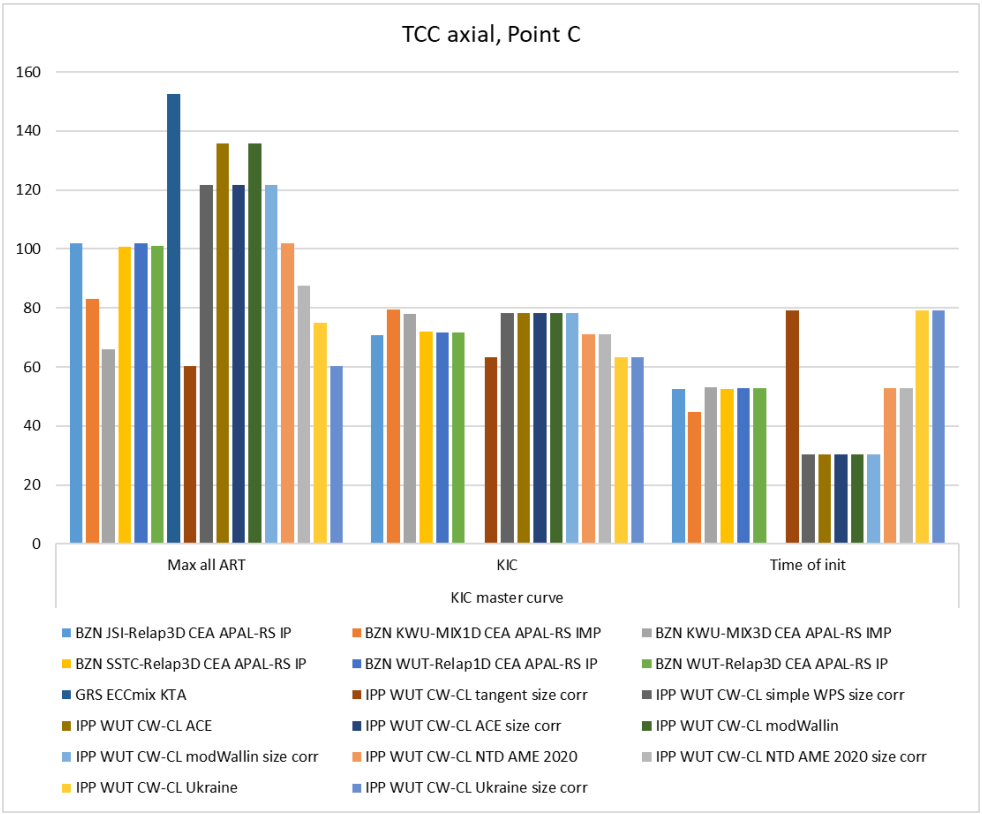

Figure 4.88: Maximum allowable ART (°C) sophisticated WPS approaches master curve lower bound – TCC axial Point C

4.3.3.2 UCC

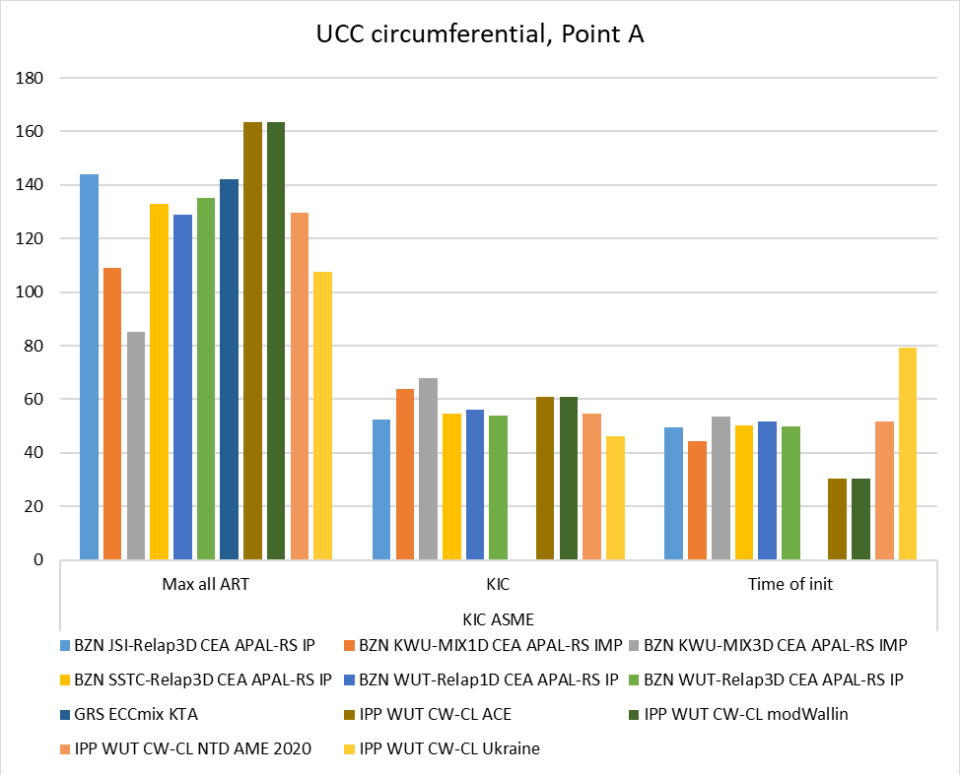

Figure 4.89: Maximum allowable ART (°C) sophisticated WPS approaches ASME lower bound – UCC circumferential Point A

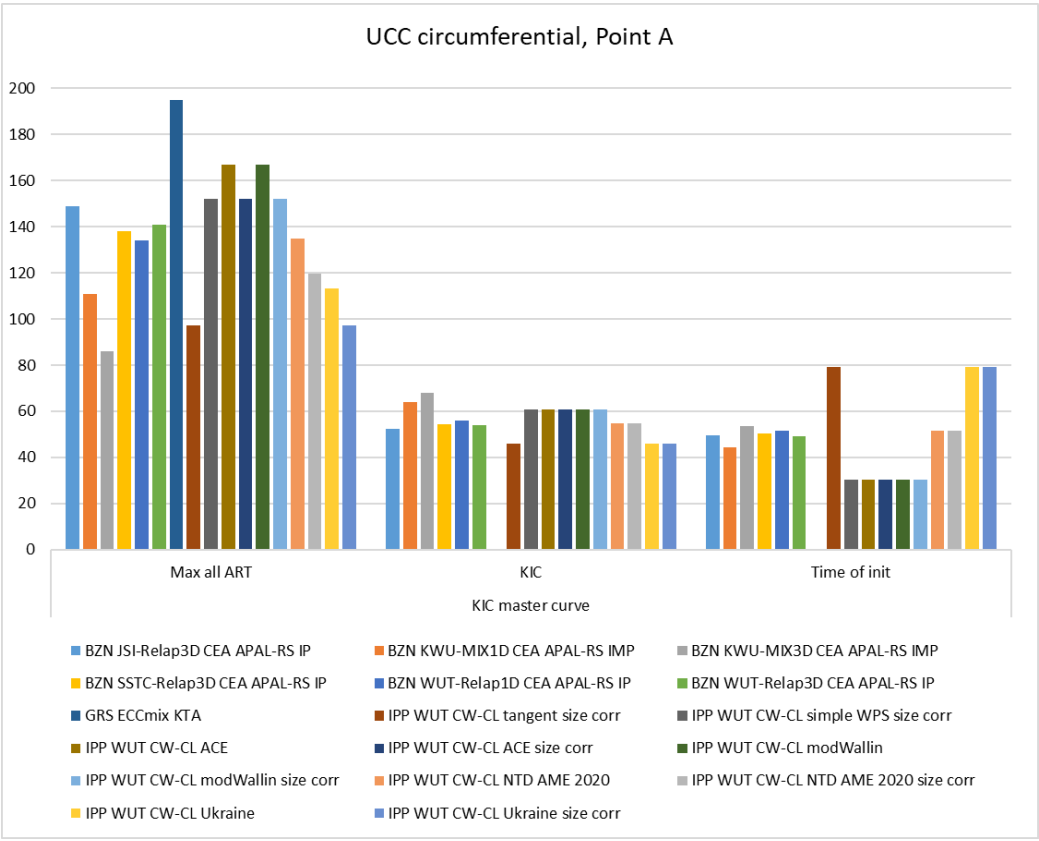

Figure 4.90: Maximum allowable ART (°C) sophisticated WPS approaches master curve lower bound – UCC circumferential Point A

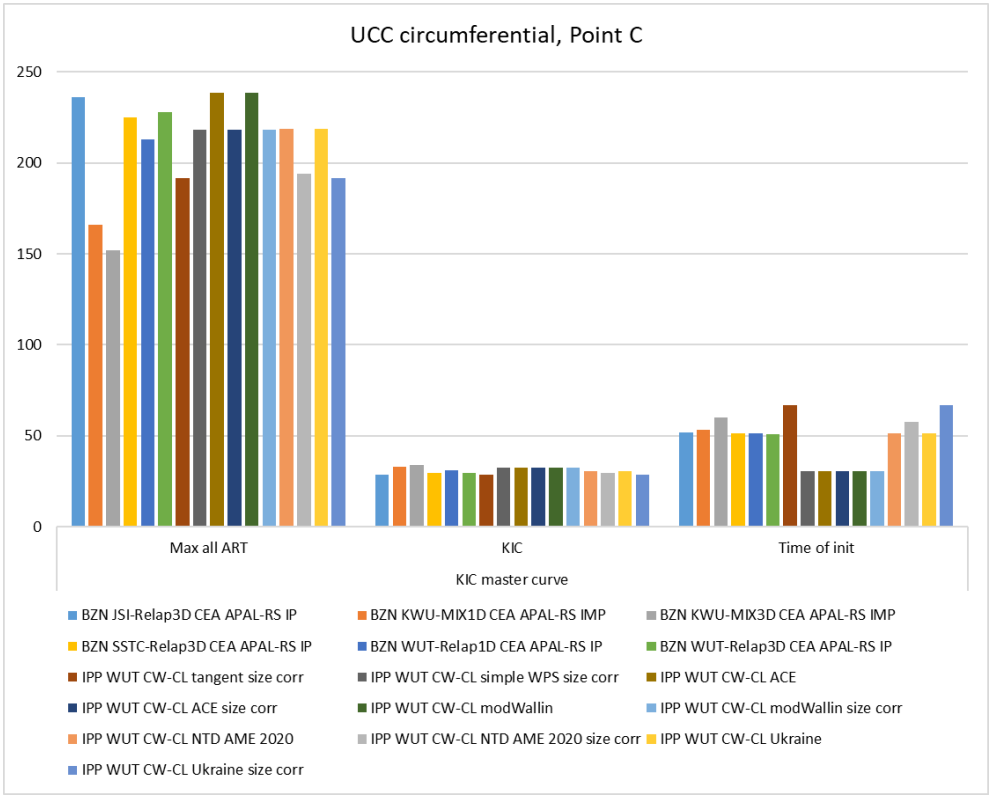

Figure 4.91: Maximum allowable ART (°C) sophisticated WPS approaches master curve lower bound – UCC circumferential Point C

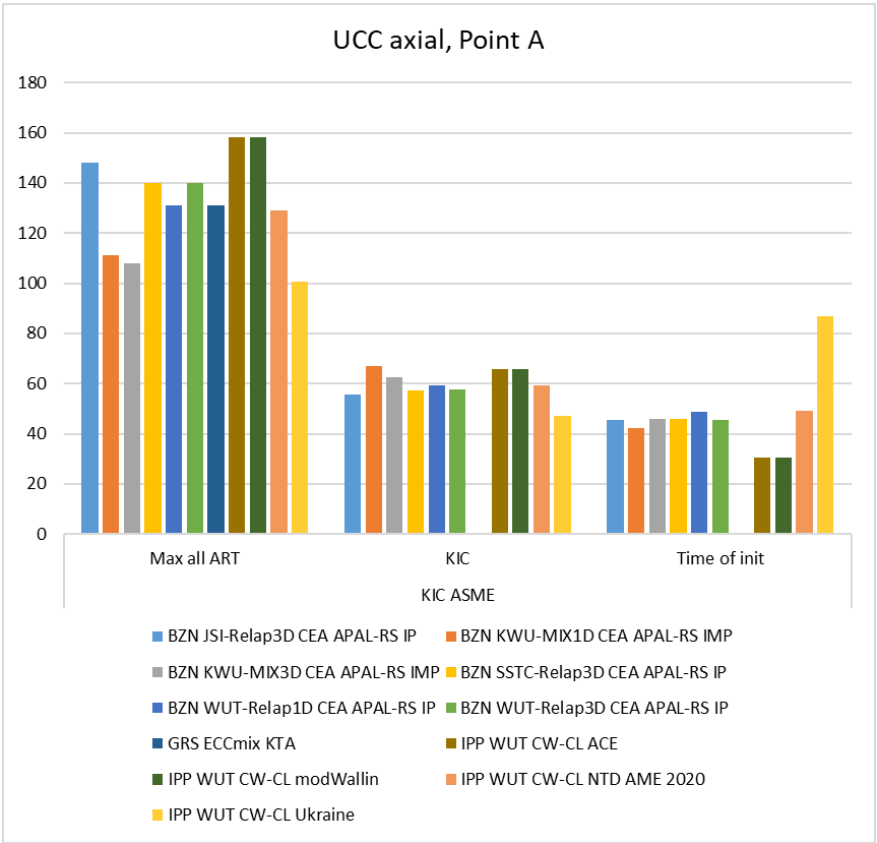

Figure 4.92: Maximum allowable ART (°C) sophisticated WPS approaches ASME lower bound – UCC axial Point A

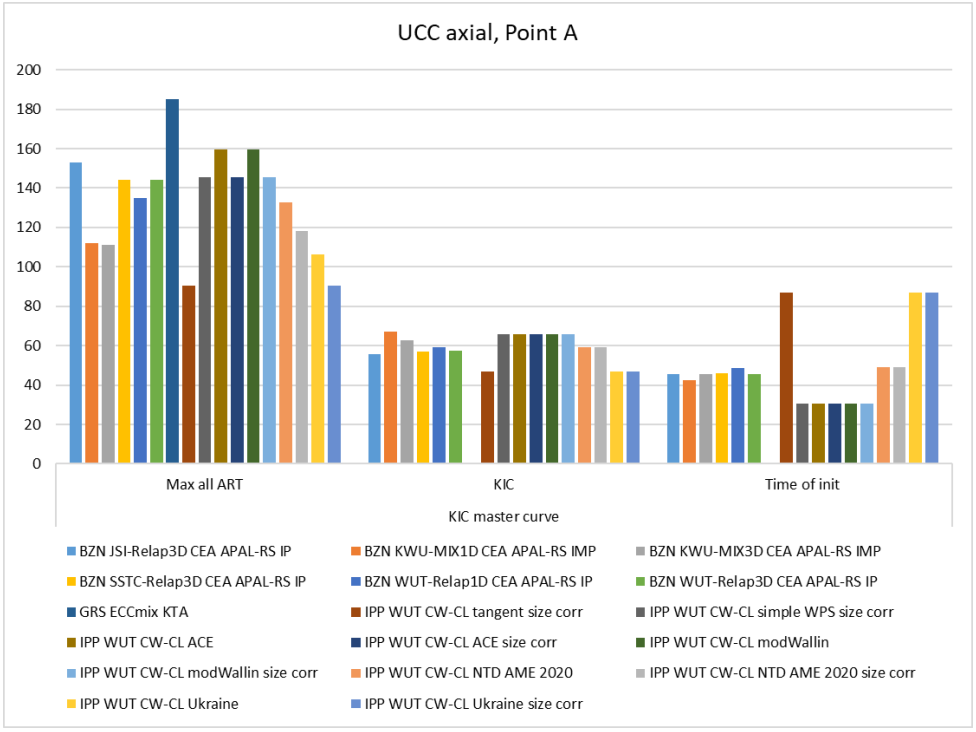

Figure 4.93: Maximum allowable ART (°C) sophisticated WPS approaches master curve lower bound – UCC axial Point A

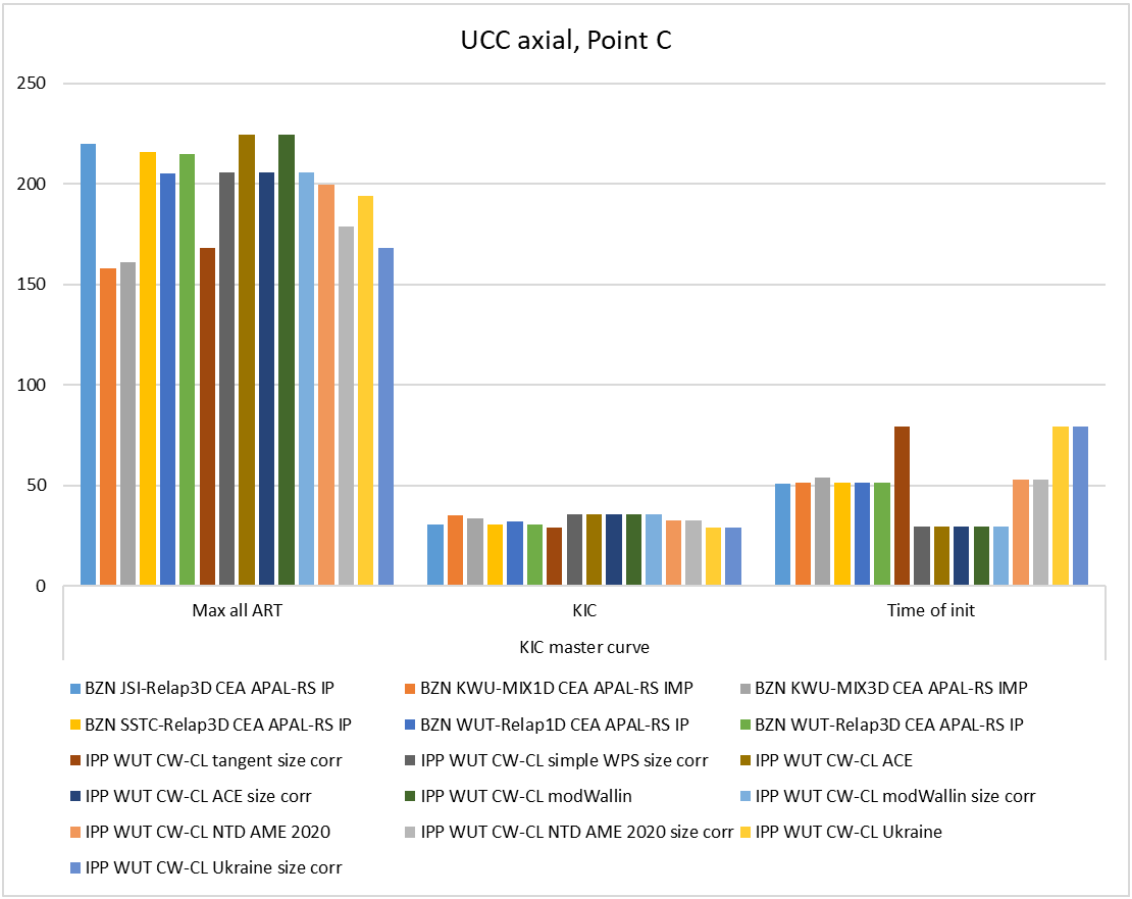

Figure 4.94: Maximum allowable ART (°C) sophisticated WPS approaches master curve lower bound – UCC axial Point C

4.3.4 FW Locations

4.3.4.1 Tangent approach

In this chapter the results at flange weld (FW) location for the tangent approach with the lower bound ASME and master curve concepts are shown, see Figure 4.95 to Figure 4.102. For the FW location there are only results for the lower bound curves. The results match the K_I results from chapter 4.2.1 well when looking at the K_I value at the time of initiation.

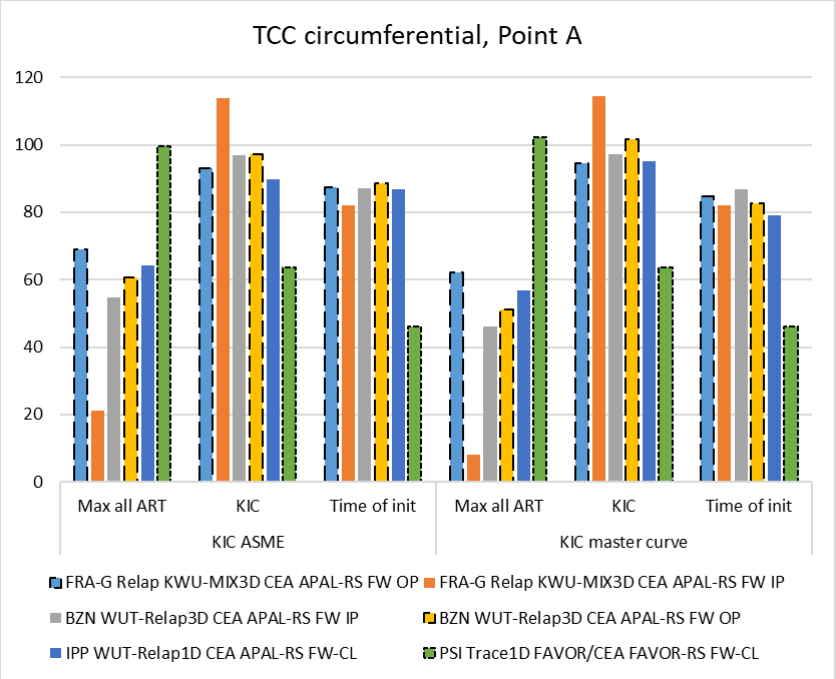

Figure 4.95: Maximum allowable ART (°C) tangent approach lower bound – TCC circumferential Point A

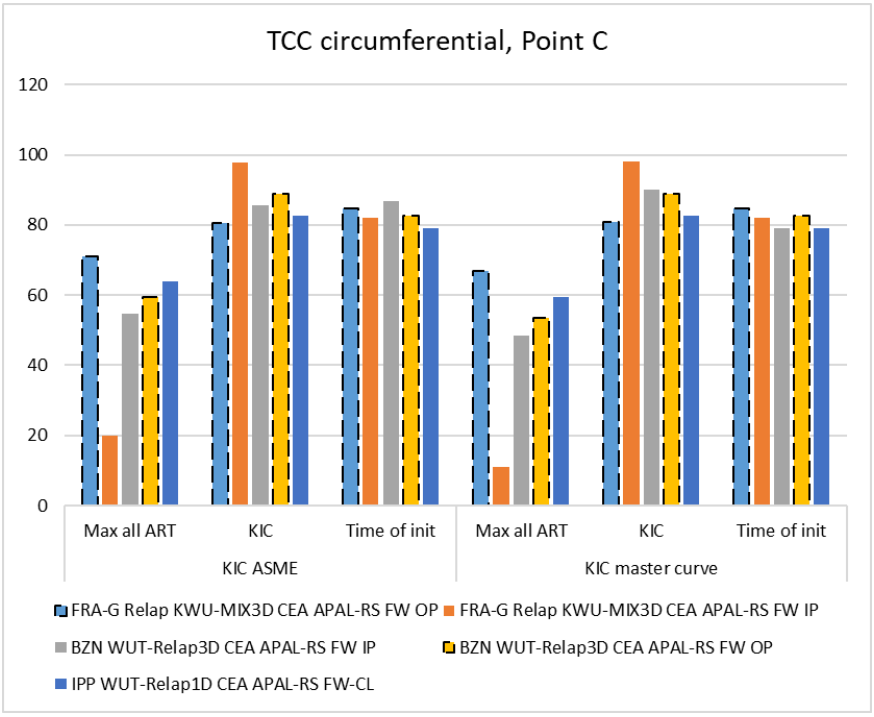

Figure 4.96: Maximum allowable ART (°C) tangent approach lower bound – TCC circumferential Point C

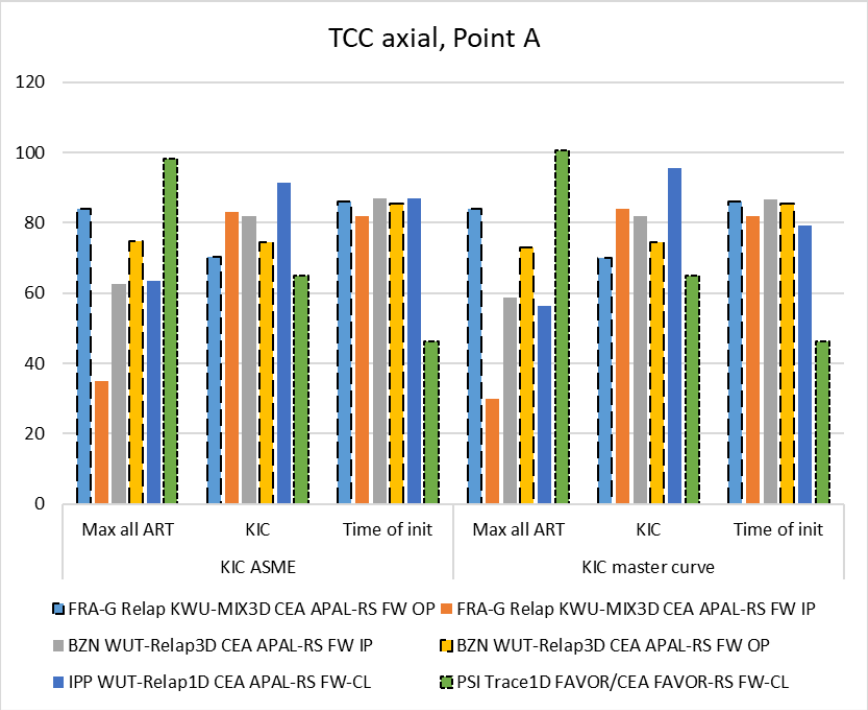

Figure 4.97: Maximum allowable ART (°C) tangent approach lower bound – TCC axial Point A

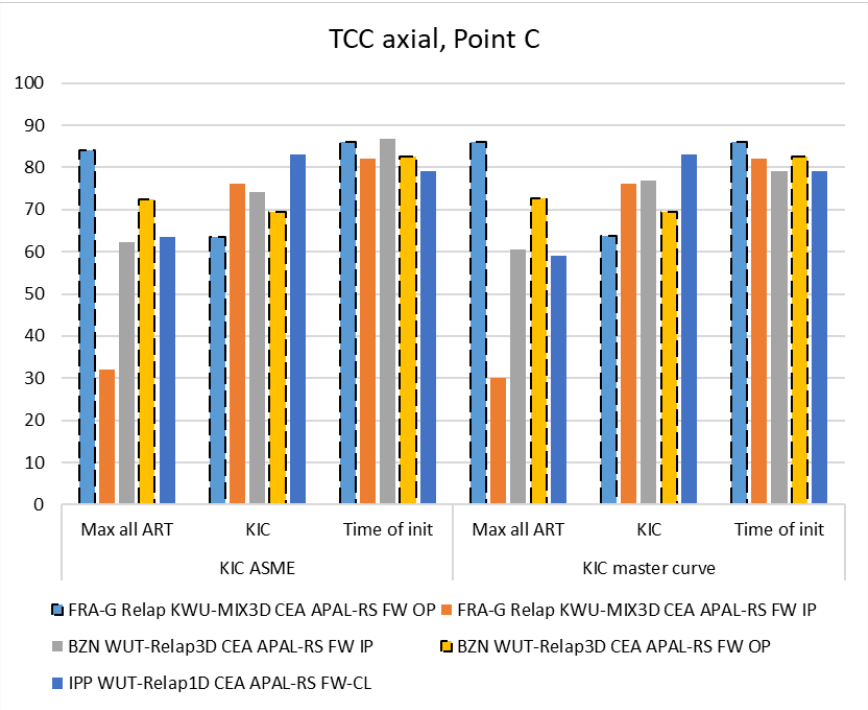

Figure 4.98: Maximum allowable ART (°C) tangent approach lower bound – TCC axial Point C

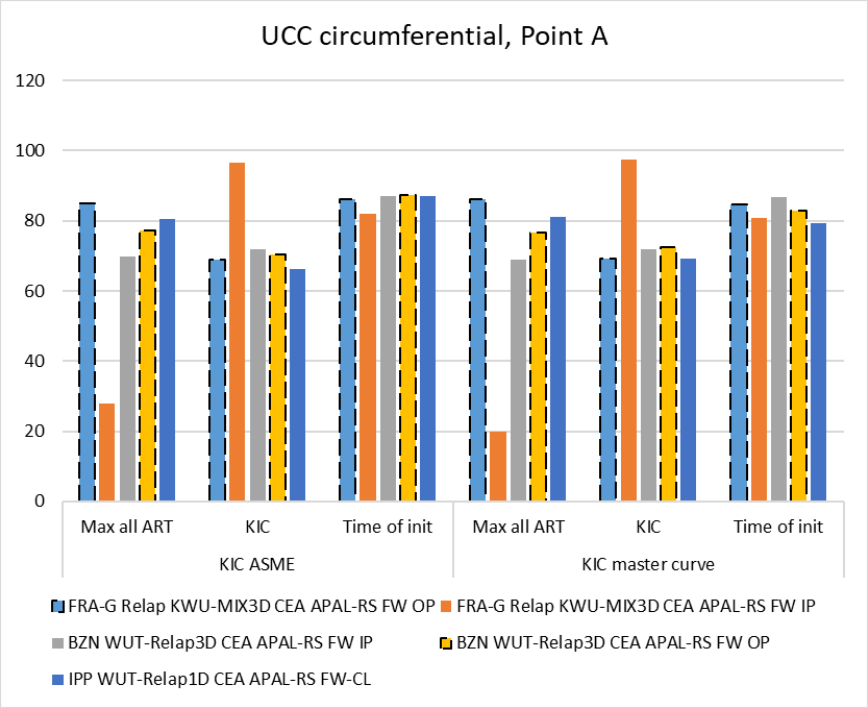

Figure 4.99: Maximum allowable ART (°C) tangent approach lower bound – UCC circumferential Point A

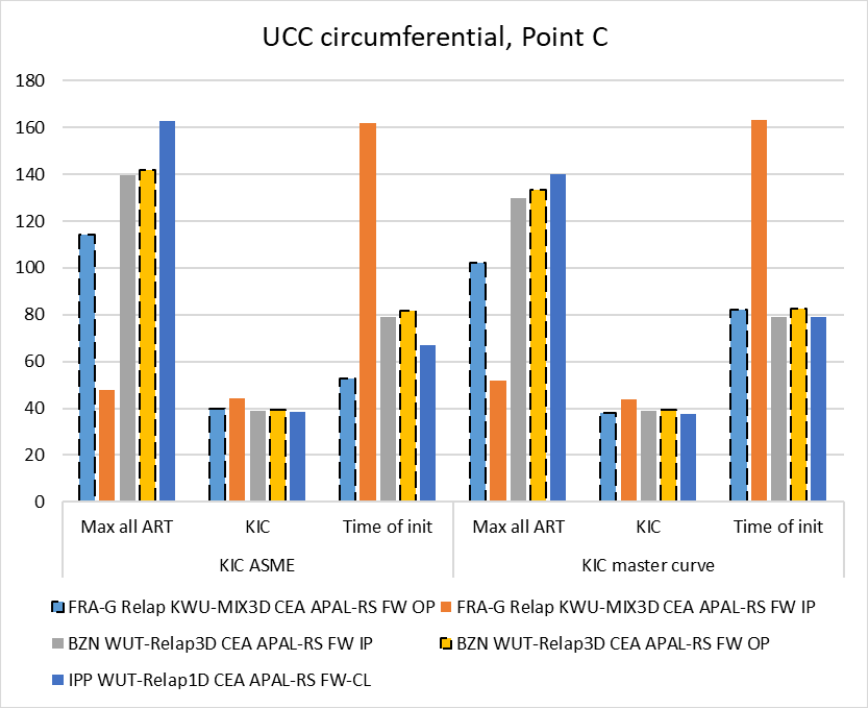

Figure 4.100: Maximum allowable ART (°C) tangent approach lower bound – UCC circumferential Point C

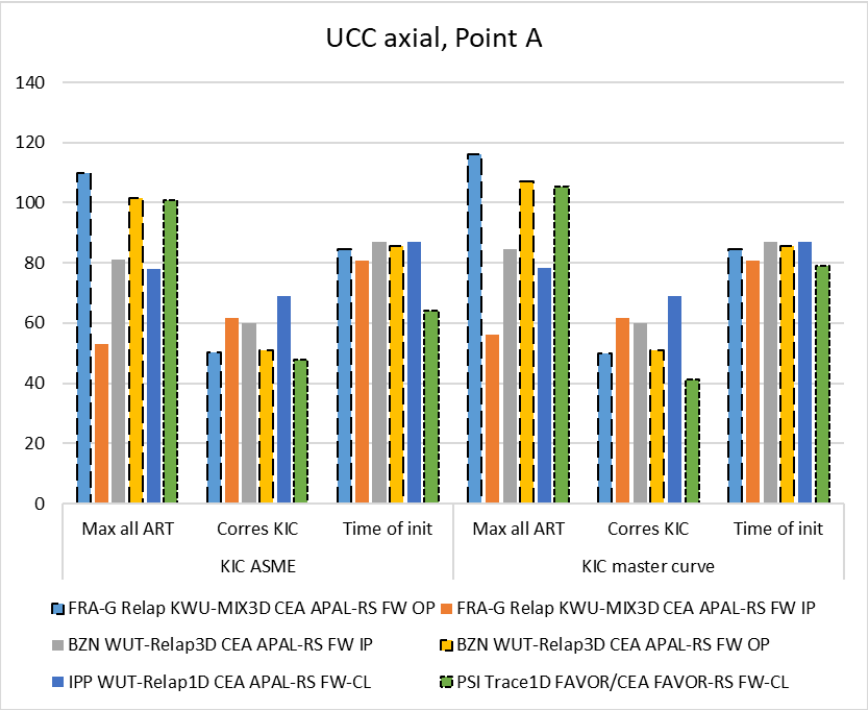

Figure 4.101: Maximum allowable ART (°C) tangent approach lower bound – UCC axial Point A

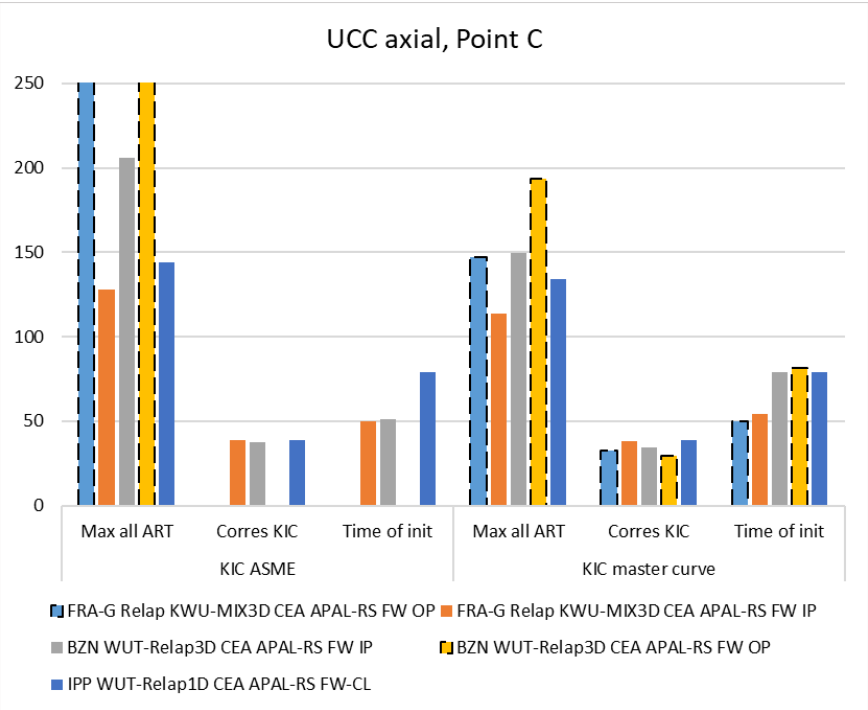

Figure 4.102: Maximum allowable ART (°C) tangent approach lower bound – UCC axial Point C

4.3.4.2 Simple WPS approach

In this chapter the results at the FW location for the simple WPS-max approach with the lower bound ASME and master curve approach results are shown, see Figure 4.103 to Figure 4.110. For the FW location there are only results for the lower bound curves. The results match the K_I results from chapter 4.2.1 well when looking at the K_I value at the time of initiation.

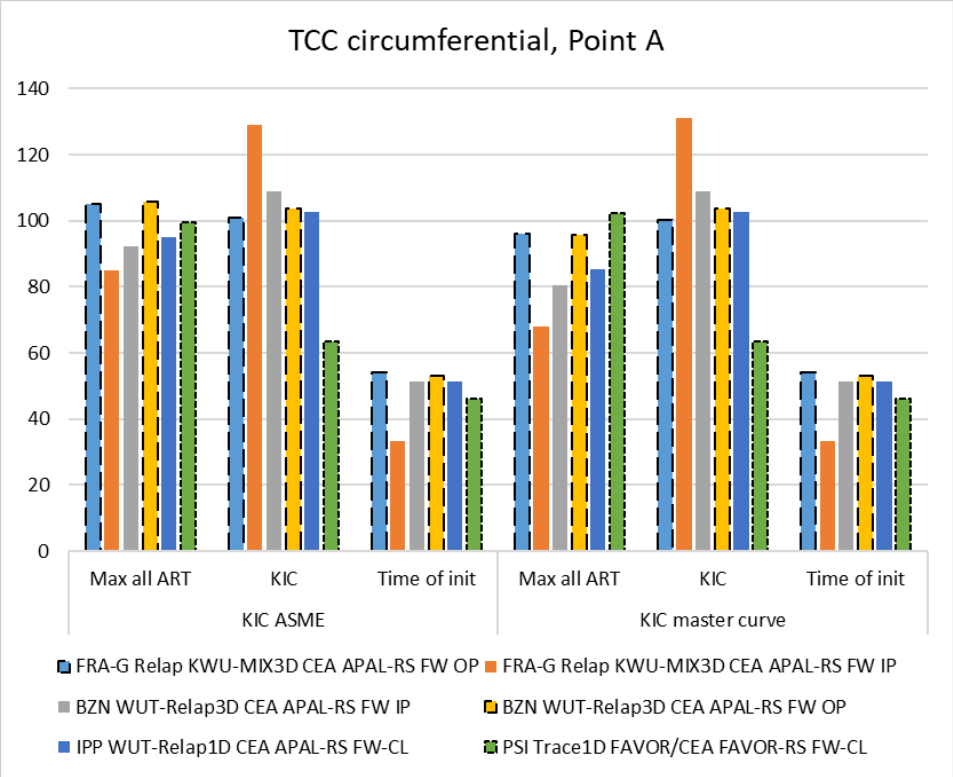

Figure 4.103: Maximum allowable ART (°C) WPS-max approach lower bound – TCC circumferential Point A

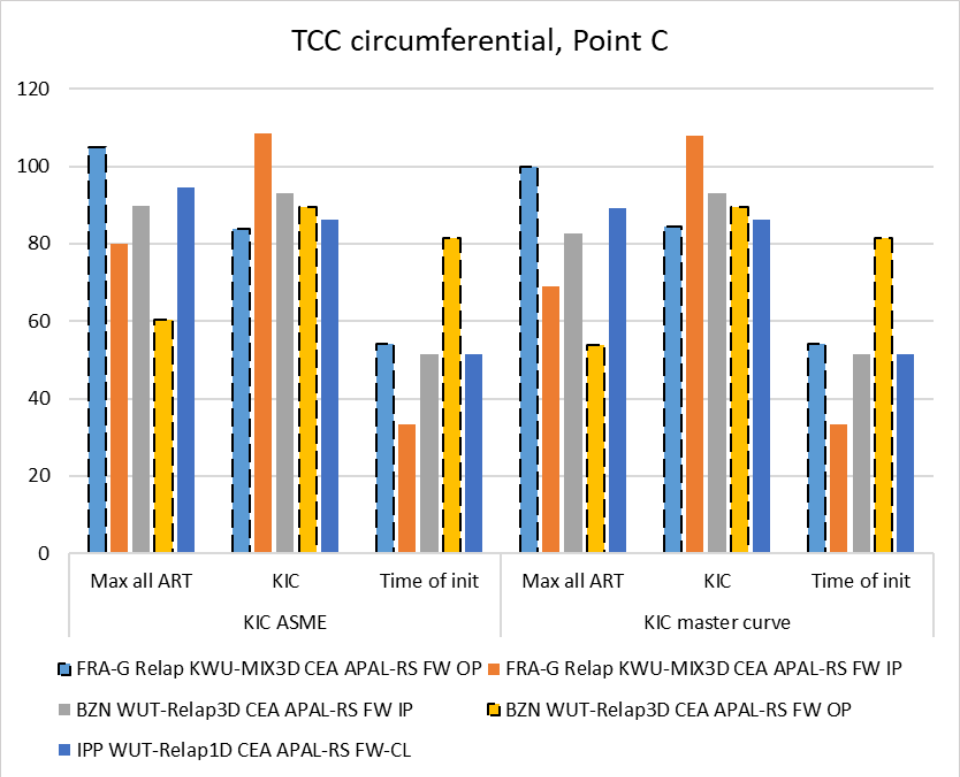

Figure 4.104: Maximum allowable ART (°C) WPS-max approach lower bound – TCC circumferential Point C

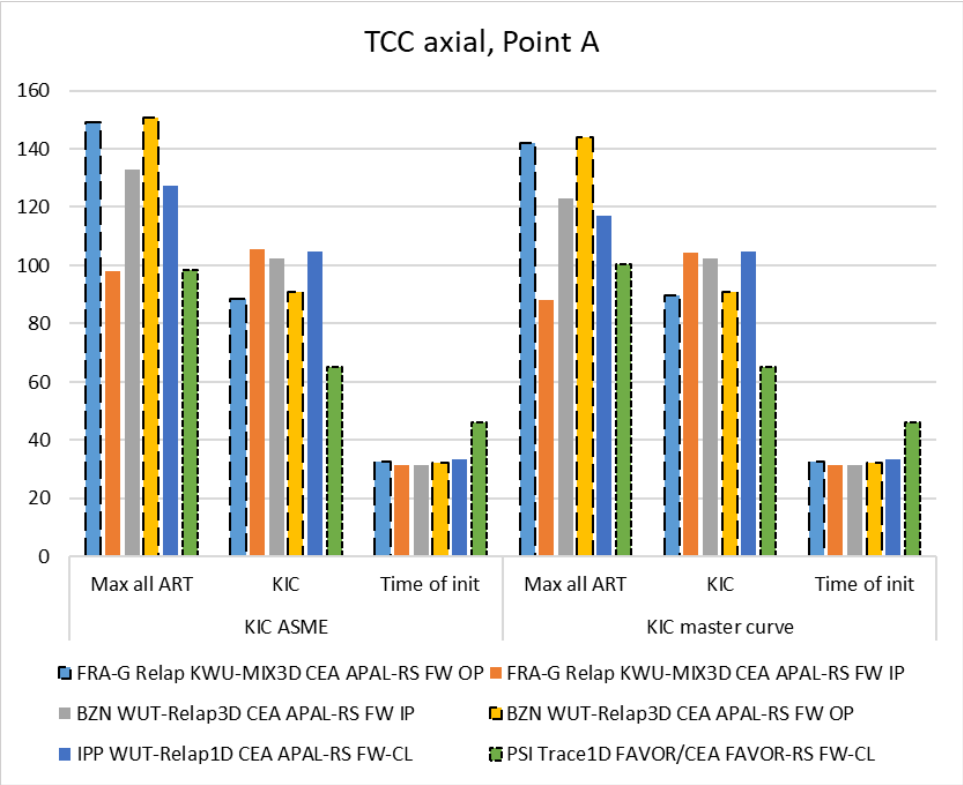

Figure 4.105: Maximum allowable ART (°C) WPS-max approach lower bound – TCC axial Point A

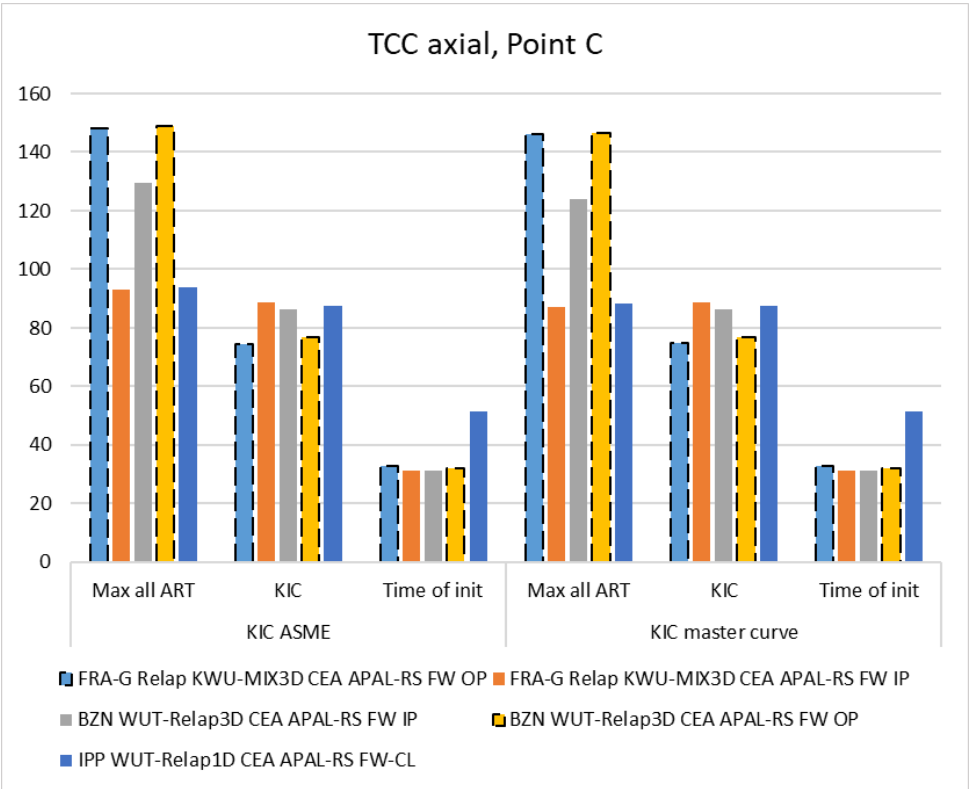

Figure 4.106: Maximum allowable ART (°C) WPS-max approach lower bound – TCC axial Point C

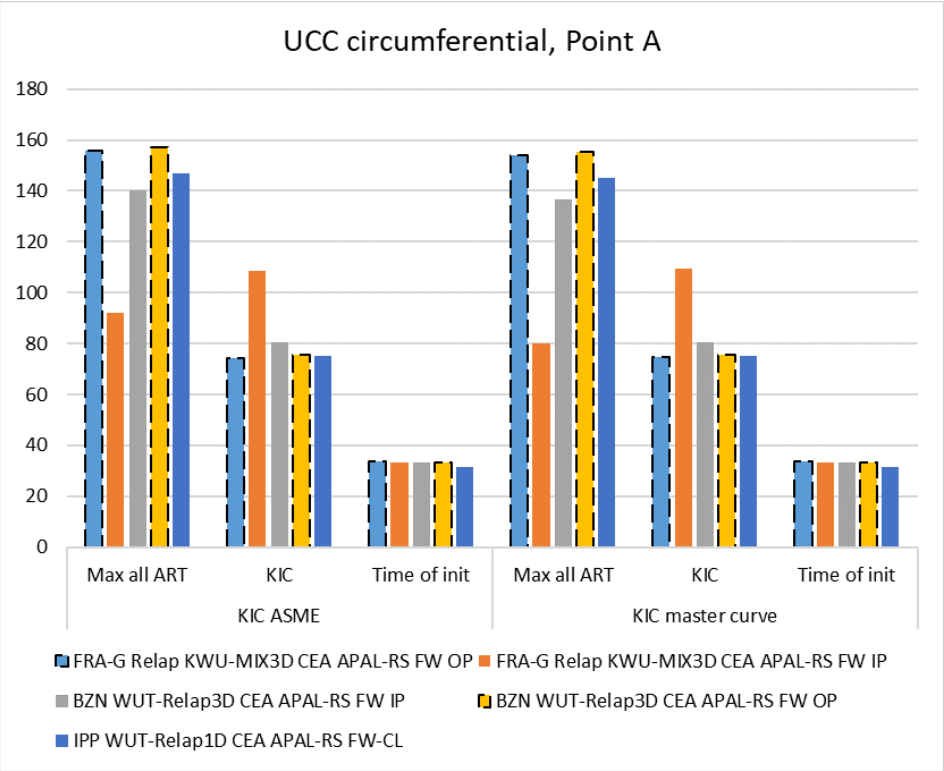

Figure 4.107: Maximum allowable ART (°C) WPS-max approach lower bound – UCC circumferential Point A

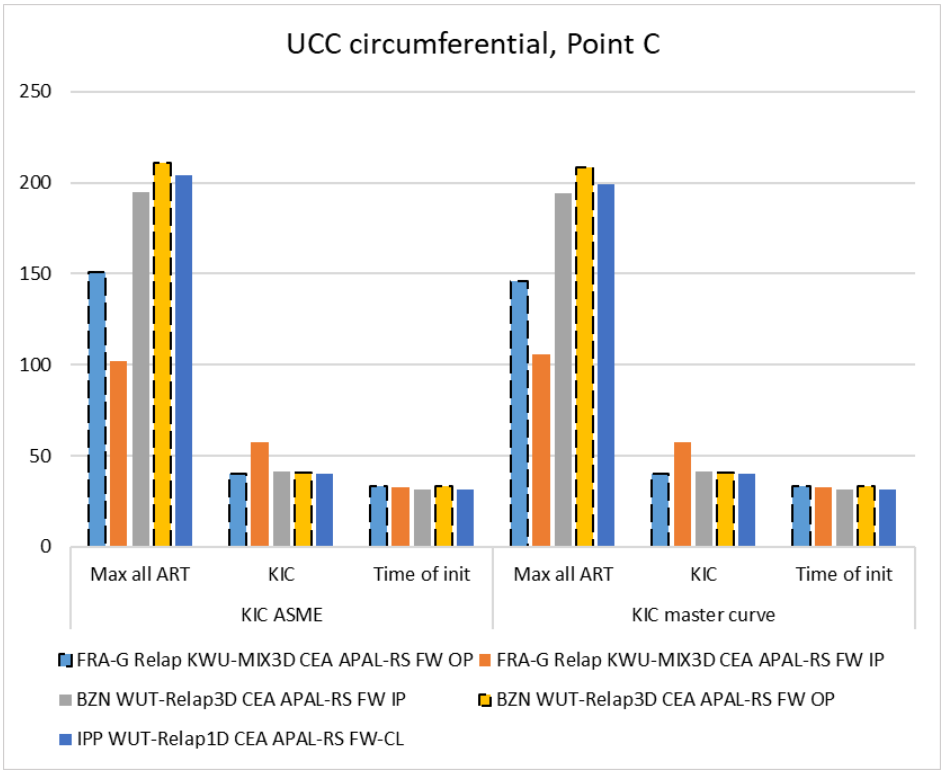

Figure 4.108: Maximum allowable ART (°C) WPS-max approach lower bound – UCC circumferential Point C

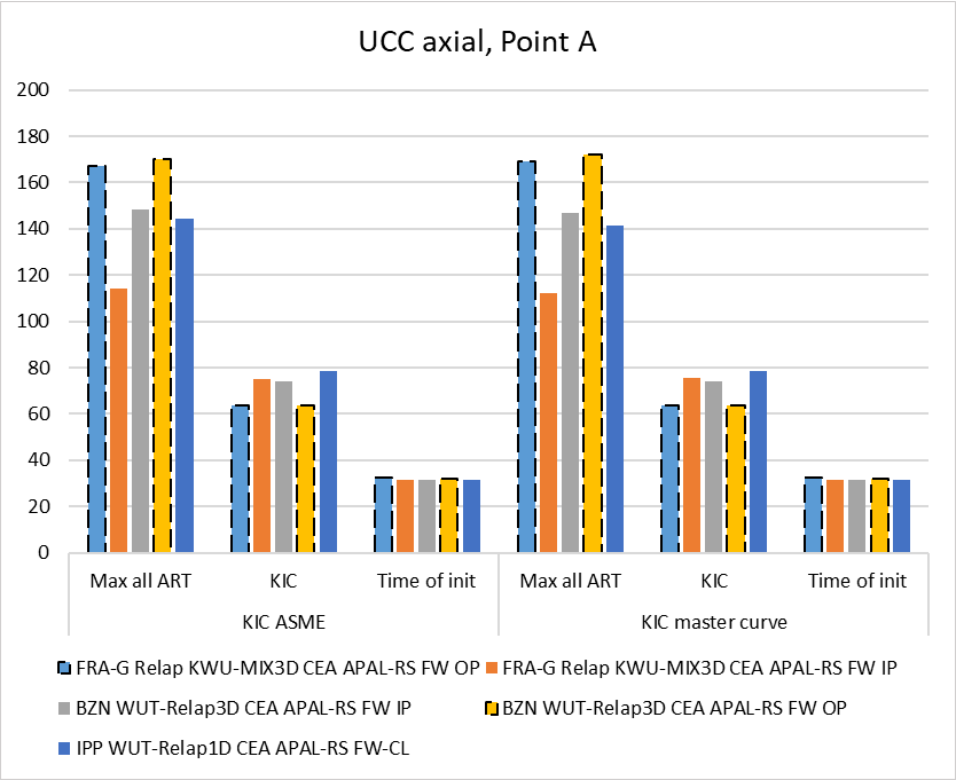

Figure 4.109: Maximum allowable ART (°C) WPS-max approach lower bound – UCC axial Point A

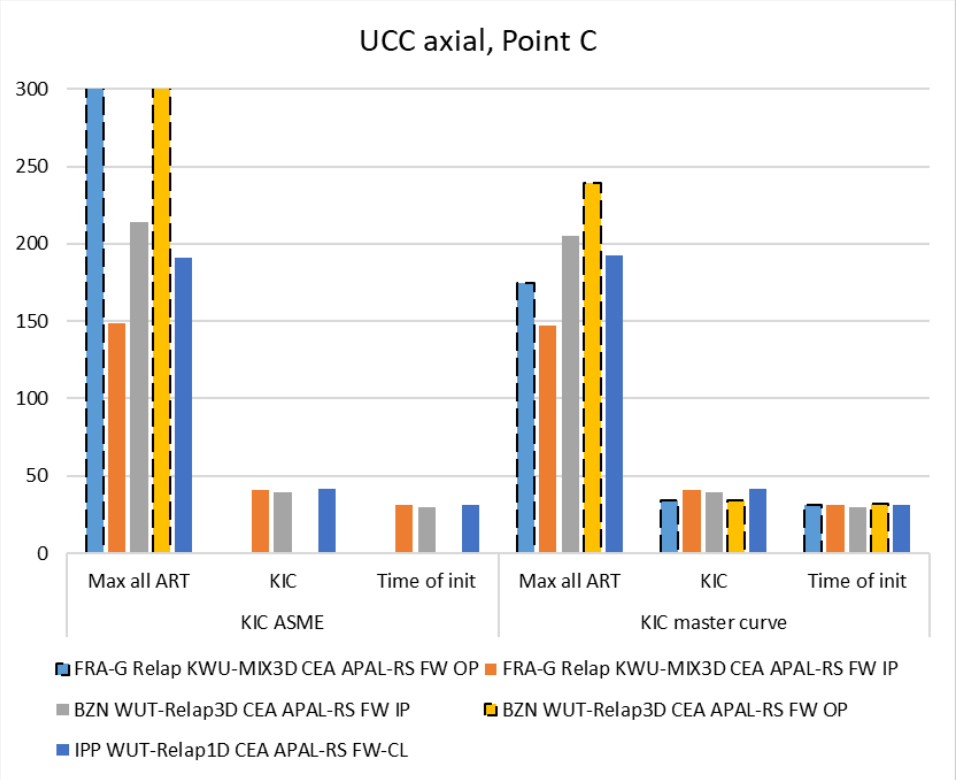

Figure 4.110: Maximum allowable ART (°C) WPS-max approach lower bound – UCC axial Point C

4.3.4.3 Sophisticated WPS approaches

In this chapter the results at the FW-CL location for max. allow. ART using several sophisticated WPS approaches (lower bound) are presented, see Figure 4.111 for TCC and Figure 4.112 for UCC. In this chapter only the master curve results are shown since there were only few results submitted for the ASME approach. For details regarding the WPS approaches see Deliverable 1.2 [7].

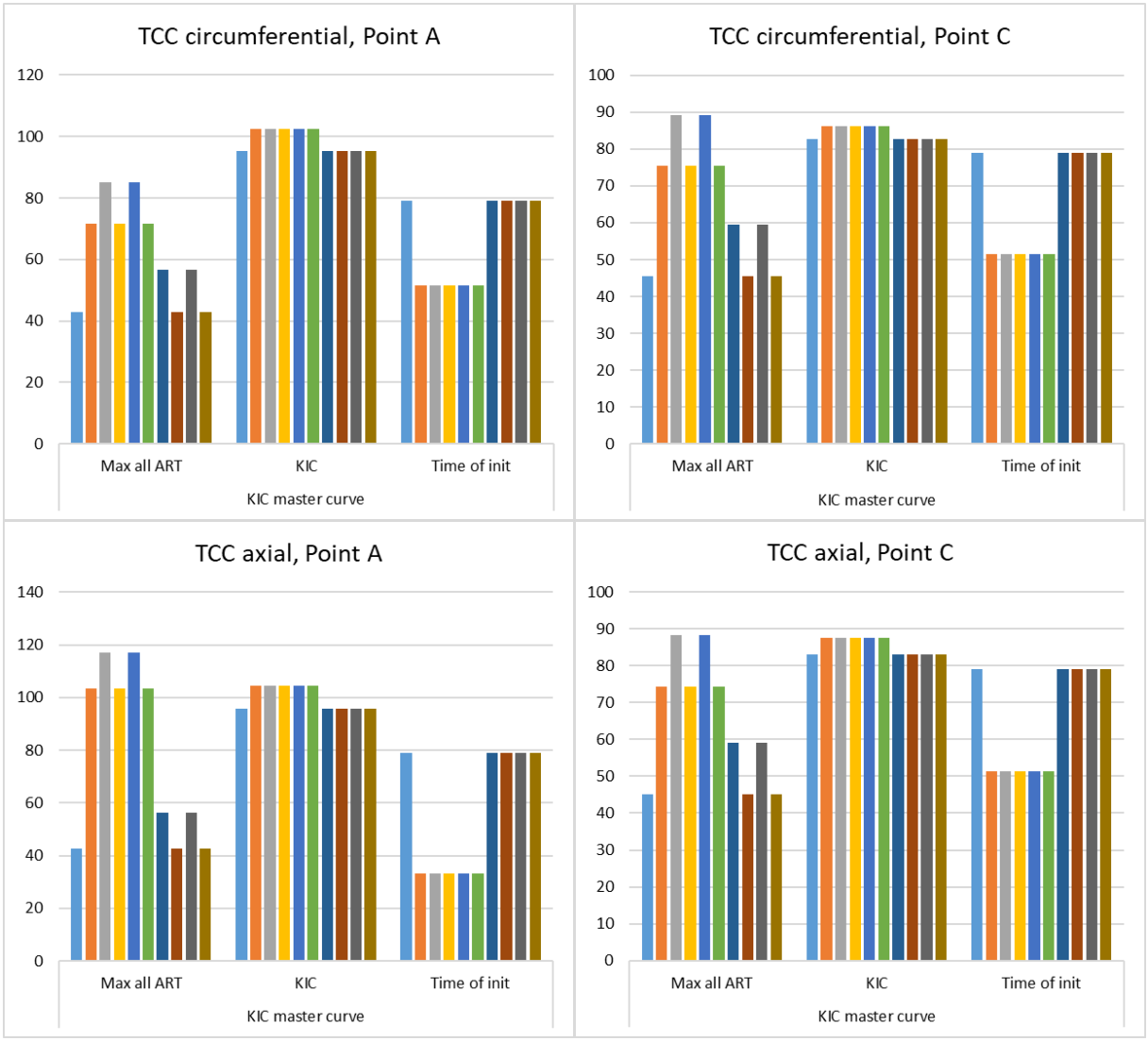

Figure 4.111: Maximum allowable ART (°C) sophisticated WPS approaches master curve lower bound – TCC

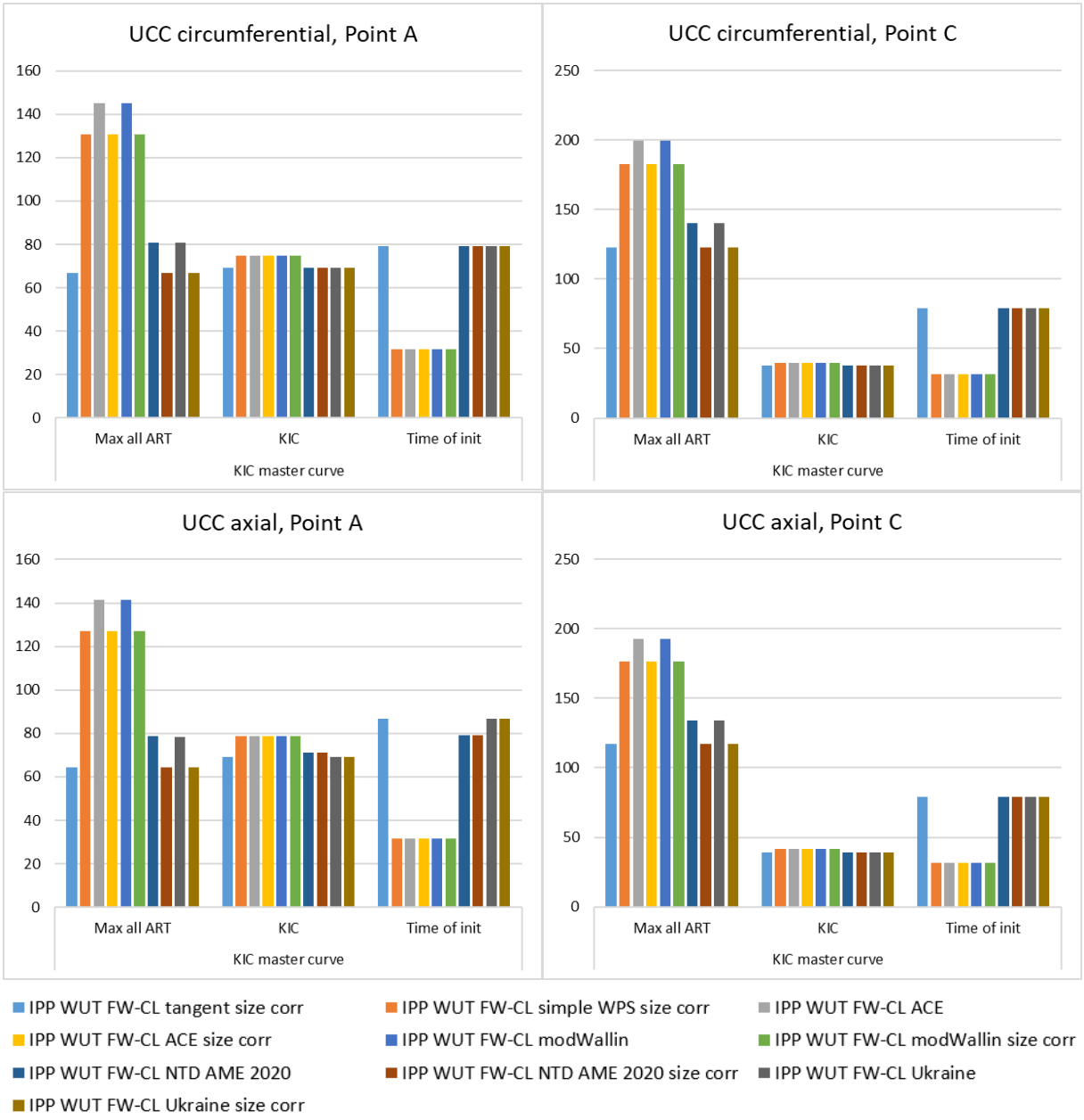

Figure 4.112: Maximum allowable ART (°C) sophisticated WPS approaches master curve lower bound – UCC

4.3.5 Observations and recommendations

The results for the benchmark part 2.2 confirm the conclusions of part 2.1, i.e., that the choice of TH code, K_I formula and consideration of TH mixing can have a considerable influence on the max. all. ART results. This influence is highly dependent on the location, crack orientation, and transient considered. The consideration of TH mixing is confirmed to be less relevant in the locations outside of plume.

The results presented above confirm the conclusions that are also mentioned in deliverable 1.2 of the APAL project [7]. The tangent approach gives the smallest results for max. allow. ART, whereas the simple WPS-max gives higher results. The results for the sophisticated WPS approaches are either in agreement with the tangent or simple WPS-max approach; or lie in between for the investigated transient.

5 Safety margins related to LTO improvements and TH uncertainties

The LTO improvements having potentially an impact on PTS analysis results were identified in WP1, see [8], and the appropriate advanced TH analyses were performed within WP2 (Deliverable D2.1 [9]). Based on the results obtained from these analyses, nine LTO improvements (including three operator actions) were selected for further investigations within WP3 and WP4. The goal of task 3.4 is to establish benefit (margin) of the individual LTO improvements (including LTO improvements involving operator actions) with respect to the base case (i.e., without any LTO improvement). The margin is determined by comparison of results obtained in task 3.4 (analysis encompassing the LTO improvements) with the results obtained in task 3.3 (analysis of the base case). The margin was determined in terms of values of maximum allowable adjusted reference temperature (max. all. ART).

The impact of the uncertainties in TH data on results of PTS analysis (task 3.5) was evaluated via performing deterministic fracture-mechanics analyses for statistical TH data sets obtained from TH analysis using the Wilks' method. The used statistical TH analysis based on Wilks' method involves generation of 59 data sets of input TH parameters (or more in some cases) leading to 59 generated TH transients. The margins related to uncertainties in TH data were evaluated by comparison of max. all. ART values determined for the specific cases of the TH input data (base case, best-estimate case, conservative case) with a lower limit value of max. all. ART resulting from fracture-mechanics calculations based on Wilks TH data sets.

Task 3.4 aimed at deterministic assessment of safety margin related to LTO improvements. The following work was performed:

- Fracture-mechanics calculations to determine the stress intensity factors in specified points of the postulated cracks for the examined LTO improvements,
- Evaluation of max. all. ART (RT_{NDT}^{a} or T_0^{a}) for the examined LTO improvements using both tangent approach and WPS approach,
- Comparing values of max. all. ART for the examined LTO improvements with corresponding value of max. all. ART for the base case (results from D3.3 [3], see section 4.3),
- Evaluation of margins in RPV integrity that may be gained by implementation of the individual LTO improvements.

Task 3.5 aimed at deterministic margin assessment related to TH uncertainties. The following work was performed:

- Fracture-mechanics calculations to determine the stress intensity factors in specified points of postulated cracks for 59 (or more in some cases) transients obtained from Wilks' method, using data from structural calculations performed in task 4.1,
- Evaluation of max. all. ART (RT_{NDT}^{a} or T_0^{a}) for all sampled transients obtained from Wilks' method using both tangent approach and WPS approach,
- Comparing values of max. all. ART obtained for the specific cases of the TH input data (base case, best-estimate case, conservative case) with a lower limit value of max. all. ART resulting from fracture-mechanics calculations based on Wilks TH data sets,
- Comparison of values of max. all. ART reveals the margins related to uncertainties in TH data, since it shows the level of conservatism (in terms of max. all. ART) in specific cases of the TH input data (base case, best-estimate case, conservative case) compared to the lower limit value of max. all. ART resulting from Wilks' method.

5.1 Safety margins related to LTO improvements

Evaluation of safety margins related to LTO improvements (for APAL-ICAS T2 transient) is the subject of Task 3.4. This task was focused on comparison of results obtained from fracture-mechanics calculations performed for different LTO improvements with the results of calculations performed for the appropriate base cases (without LTO improvements). For the comparison, the base case (BC) results from Task 3.3 Part 2 were (in most cases) used[8].

The results of the Task 3.4 are presented in such a form that for each LTO the following comparatives figures and tables were constructed:

- K_I vs. T curves (where T means temperature) were compared between the partners, whereby graphs based on TH mixing codes (both with and without RS in SA) are displayed separately from the graphs obtained based on TH system codes. In addition to this, graphs based on the TH system codes were further divided into two groups, which were also displayed separately – with and without RS in SA. This form of presentation of the results was selected to increase the clarity of the figures.
- Values of max. all. ART for LTO, BC and LTO margin were compared between the partners (bar plots). In these plots, LTO margin means the following difference denoted as Delta max. all. ART:

  LTO margin = Delta max. all. ART = max. all. ART for LTO – max. all. ART for BC

- The comparison was performed separately for each crack configuration (axial/circumferential, point A/point C) and for each approach (tangent/WPS-max).

The bar plots, tables and detailed K_I vs. T plots are presented only in D3.4 [4]. Here, the values of LTO margins calculated by all partners are presented in [5] in the form of scatter plots. The K_I vs. T plots are demonstrated here in [5] for all LTO improvements together with their corresponding base case calculations by the results of WUT.

All the results presented here in Chapter 5.1 are for the core weld in plume/in merging plume location. Other locations are discussed in Chapter 3.6.1 of [4].

5.1.1 Short description of LTO improvements

TH analyses of various variants of LTO improvements were performed in Task 2.1, and based on these results, LTO improvements were selected for further examination within Tasks 3.1 and 3.4, see Table 5.1. LTO improvements No. 1 – 5 and 7 are plant improvements, while LTO improvements No. 6, 8 and 9 are operator actions. All LTO improvements No. 1 – 9 were analysed within Task 3.4.

Table 5.1: List of LTO improvements selected for analyses in D3.1

LTO improvement / Operator action	Simulated change
1. Heating of water in the HPSI tanks	Heated from 15 °C to 45 °C
2. Heating of water in the ACCs	Heated from 20 °C to 50 °C
3. Heating of water in the LPSI tanks	Heated from 15 °C to 45 °C
4. Decreasing the HPI head	Decreased down to 75%

[8] KIWA used in Task 3.4 for analyses of LTO 4, 5, and 6 a base case different from that one of Task 3.3. In particular, for LTO 4 and LTO 6, KIWA used the base case for the specific TH data from SSTC and WUT, respectively. For LTO 5, KIWA used TH data based on the best-estimate case instead of base case, as mentioned in other parts of this deliverable D3.4.

5. Decreasing the HPI capacity	Decreased down to 75 %
6. Reduction of HPSI flow (operator action)	Reduced at 1800 s to one pump
7. Decreasing of ACC pressure	Decreased from 26 bar to 20 bar
8. Change of cool down rate (operator action)	Changed from 100 K/h to 200 K/h
9. Isolation of ACCs (operator action)	ACC isolated at 500 s

An overview of TH system and mixing codes used for TH analyses of the LTO improvements No. 1 – 9 (as performed in D2.1) is included in Table 5.2.

Table 5.2: System and mixing TH codes that were used in Task 2.1 (D2.1) to analyse the LTO improvements No. 1 - 9

LTO improvement / Operator action	System code/partner	Mix code/partner
1. Heating of water in the HPSI tanks	RELAP5/UJV, WUT, FRA-G TRACE/PSI	KWU-MIX/FRA-G
2. Heating of water in the ACCs	RELAP5/WUT, FRA-G TRACE/PSI ATHLET/GRS	ECC-MIX/GRS KWU-MIX/FRA-G
3. Heating of water in the LPSI tanks	RELAP5/WUT, FRA-G TRACE/PSI ATHLET/GRS	ECC-MIX/GRS KWU-MIX/FRA-G
4. Decreasing the HPI head	RELAP5/SSTC TRACE/PSI ATHLET/GRS	ECC-MIX/GRS
5. Decreasing the HPI capacity	RELAP5/KIWA, SSTC TRACE/PSI	
6. Reduction of HPSI flow (operator action)	RELAP5/WUT, FRA-G	KWU-MIX/FRA-G
7. Decreasing of ACC pressure	RELAP5/JSI, WUT TRACE/PSI	
8. Change of cool down rate (operator action)	RELAP5/WUT, FRA-G	KWU-MIX/FRA-G
9. Isolation of ACCs (operator action)	RELAP5/FRA-G, WUT	KWU-MIX/FRA-G

5.1.2 Summary evaluation of LTOs for TCC

In this Section, we attach two types of graphs in which additional comparisons of results are performed.

In the first type of graphs, comparison of K_I vs. T curves for 1 partner for all LTOs analysed by that partner is presented. There were two partners performing calculations for all LTOs, namely WUT and UJV, and for this purpose the results of WUT were selected. To make the figures showing the comparison sufficiently clear, we divided the appropriate set of K_I vs. T curves into three figures: In the first one (Figure 5.1), the K_I vs. T curves corresponding to the most influential LTOs (LTOs 1, 6 and 8) are displayed, incl. their appropriate BC. In the second figure (Figure 5.2), the K_I vs. T curves corresponding to several of the least influential LTOs (LTOs 2, 3, 7 and 9) are displayed, incl. the corresponding BC. Finally, in the third figure (Figure 5.3), the K_I vs. T curves corresponding to the remaining least influential LTOs (LTOs 4 and 5) are displayed, incl. the corresponding BC. Additionally, a K_I vs. T curve based on KWU-MIX for LTO 9 and the corresponding BC curve were added into the second figure, since for LTO 9 WUT performed two calculations, one based on Relap-SSTC and the second one based on KWU-MIX.

The following comments may be given regarding the Figure 5.1 – Figure 5.3: Figure 5.1 confirms significant effect of LTOs 1, 6 and 8 on max. all. ART for tangent approach. Figure 5.2 elucidates why there is a very small effect of LTOs 2, 3, 7 and 9 on max all. ART for tangent approach and not too large effect (both positive and negative) for WPS-max approach. Concerning LTO 4 and 5, it is seen from Figure 5.3 that LTO 4 has negligibly small (positive) effect on max. all. ART for tangent approach, which is in accordance with WUT results and a large negative effect on max. all. ART for WPS-max approach. For LTO 5, Figure 5.3 shows that there is a small positive effect of LTO 5 on max. all ART for tangent approach, and a large negative effect for WPS-max approach. From point of view of TH analysis, LTO 4 and LTO 5 have a common feature that there is a later HPI injection and decreased rate of cooling in the RPV in the early stages of the transient (up to about 2000 s), but in period from 2000 to 3000 s, a significant increase of the rate of cooling occurs (after the ACCs start injecting), in consequence of which there are large negative margins for WPS-max approach.

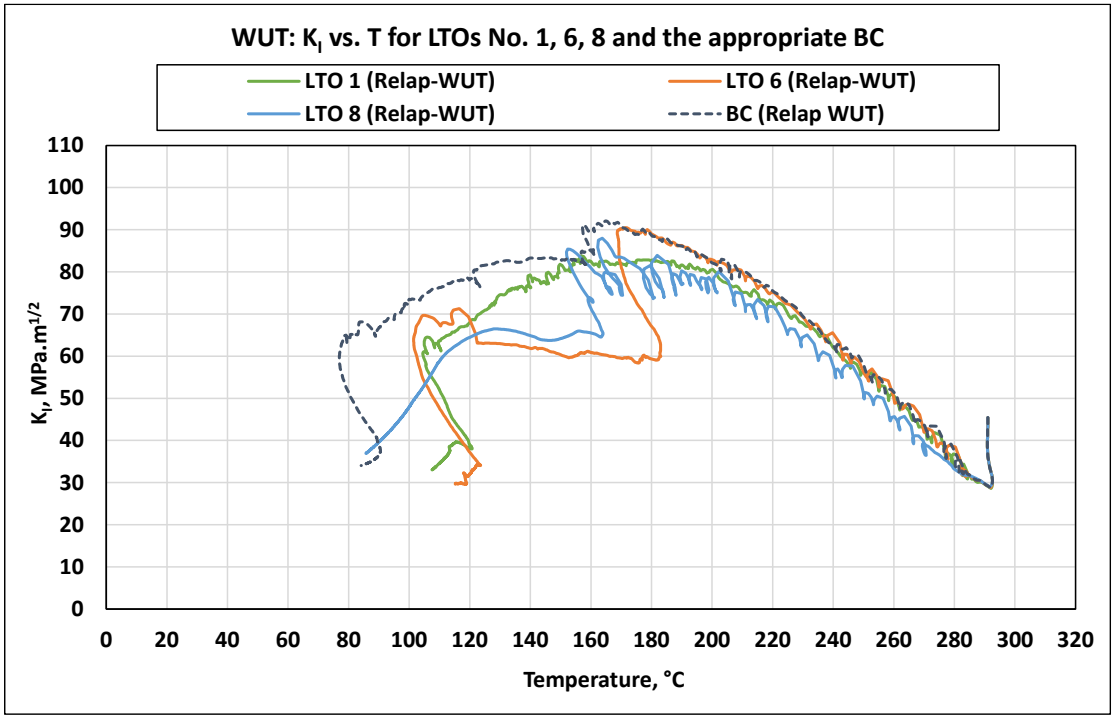

Figure 5.1: K_I vs. T curves for 1 partner (WUT) for 3 most influential LTOs (No. 1, 6, 8) and BC (all based on Relap-WUT). For TCC, axial, point A.

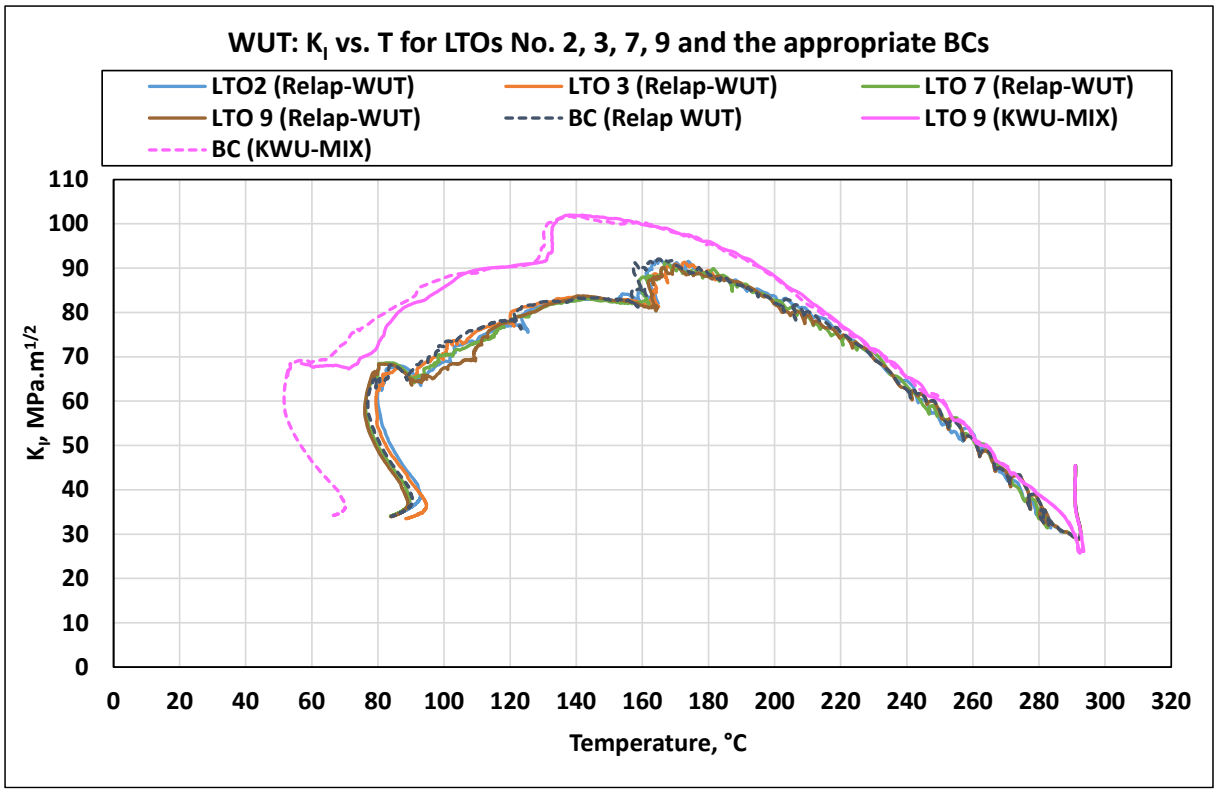

Figure 5.2: K_I vs. T curves for 1 partner (WUT) for 4 (of in total 6) least influential LTOs (No. 2, 3, 7, 9) and BC based on Relap-WUT. Graph for LTO 9 based on KWU-MIX is added, together with BC. For TCC, axial, point A.

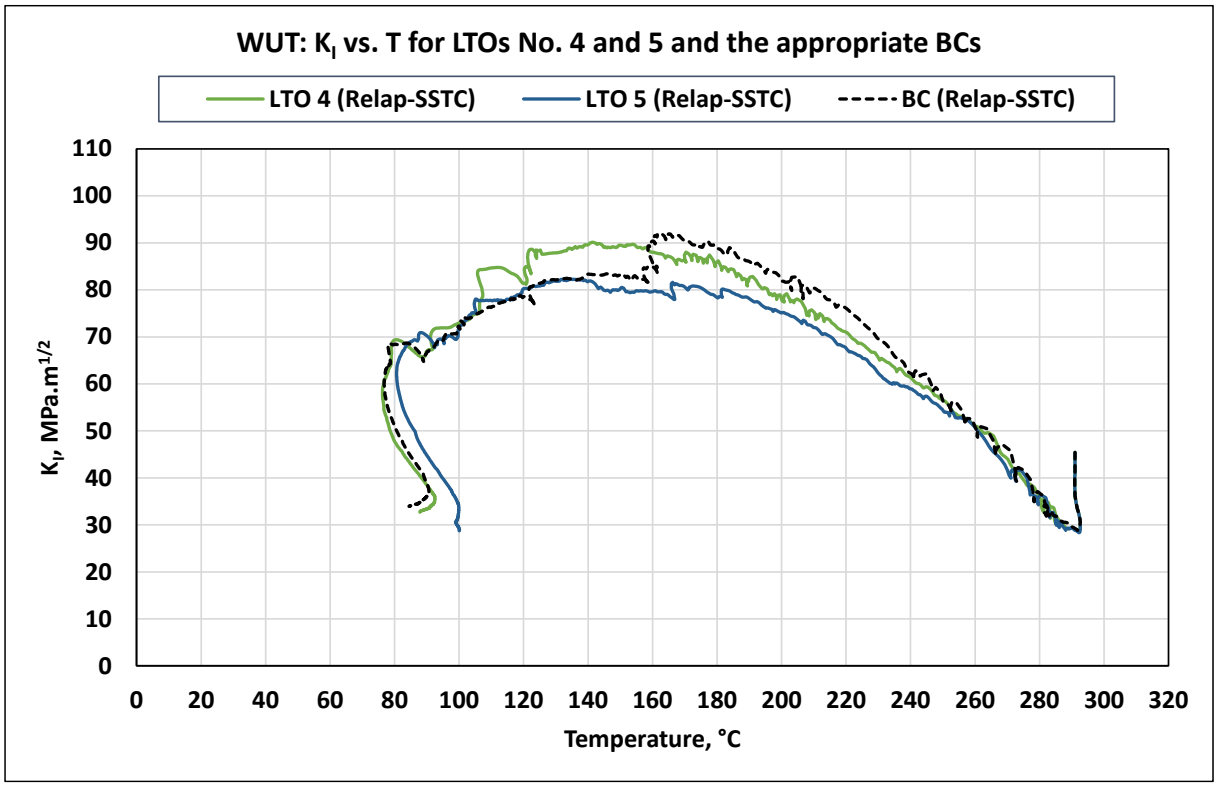

Figure 5.3: K_I vs. T curves for 1 partner (WUT) for 2 remaining least influential LTOs (No. 4, 5) and BC (all curves based on Relap-SSTC). For TCC, axial, point A.

Second type of graphs are graphs summarizing the LTO margins for all LTOs together, based on results of different partners using input TH data from different TH codes. These graphs were constructed for each of the configurations (axial/circumferential, Point A/Point C) and approaches (tangent/WPS-max), and they are seen in Figure 5.4 – Figure 5.11. From these figures several conclusions may be drawn.

All figures related to tangent approach have qualitatively similar character:

- The largest margin (most beneficial effect on max. all. ART) have LTO 1 (Heating of water in the HPSI tanks), LTO 6 (Reduction of HPSI flow – operator action) and LTO 8 (Change of cool down rate – operator action).
- The least effect (in average zero effect, or even small negative effect) have all other LTOs, i.e., LTOs No. 2, 3, 4, 5, 7, 9.
- There is no significant qualitative difference between figures related to different crack orientations (axial/circumferential) and points on the crack front (A/C).

All figures related to WPS-max approach also have some common qualitative features:

- The scatter of LTO margins for individual LTOs is relatively large (significantly larger than in case of tangent approach).
- Based on Figure 5.7, Figure 5.9, and Figure 5.11, it is not possible to determine any LTO that would have a significant positive LTO margin (i.e., clear beneficial effect on max. all. ART). Only Figure 5.5 (axial, point A) suggests that there could be a positive effect of LTO 1 on max. all. ART for WPS-max approach. Concerning LTO 4 and LTO 5, they often exhibit negative margins (aggravating effect on max. all. ART) for WPS-max approach.
- There is no significant qualitative difference between figures related to different crack orientations (axial/circumferential) and points on the crack front (A/C).
- The large scatter in the data for individual LTOs witnesses in favour of the fact that the WPS-max approach is very sensitive to the shape of KI vs. T curve (namely to the position of the global maximum of KI), which in turn is very sensitive to both the TH code used and the transient parameters selected, and also very sensitive to the point for which the K_I vs. T curve is constructed (point A or point C). Consequently, the max. all. ART calculated based on WPS-max approach is not a stable quantity with respect to various aspects associated with both TH analysis and structural and/or fracture-mechanics analysis. For these reasons, the WPS-max approach cannot be recommended for application in PTS analysis, if a standard evaluation for one transient (with input TH parameters selected based on expert judgement) is performed. Nevertheless, WPS-max approach may be applicable in combination with analysis of the full Wilks data set. In particular, WPS-max approach is not very suitable for assessment of the benefits of LTO improvements.

Note. The conclusion about the fact that WPS-max approach is not suitable (recommendable) for application in PTS analysis does not concern other WPS approaches. Other (national) WPS approaches are much more stable with respect to the above-mentioned aspects of TH analysis and/or structural and fracture-mechanics analyses, which is due, for example, to the fact that they consider 90% of maximum of KI vs. T curve as a criterion for determination of max. all. ART.

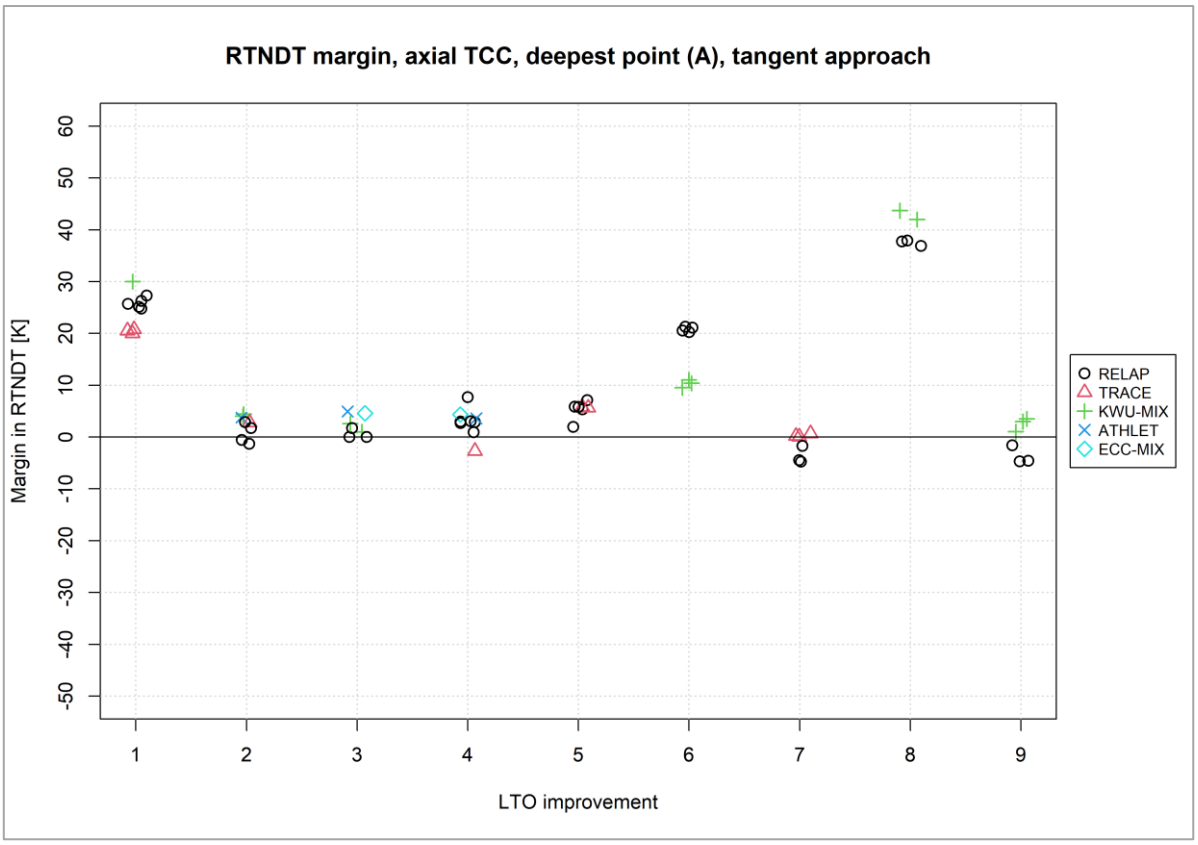

Figure 5.4: Comparison of LTO margins for all LTOs, tangent approach. For TCC, axial, point A.

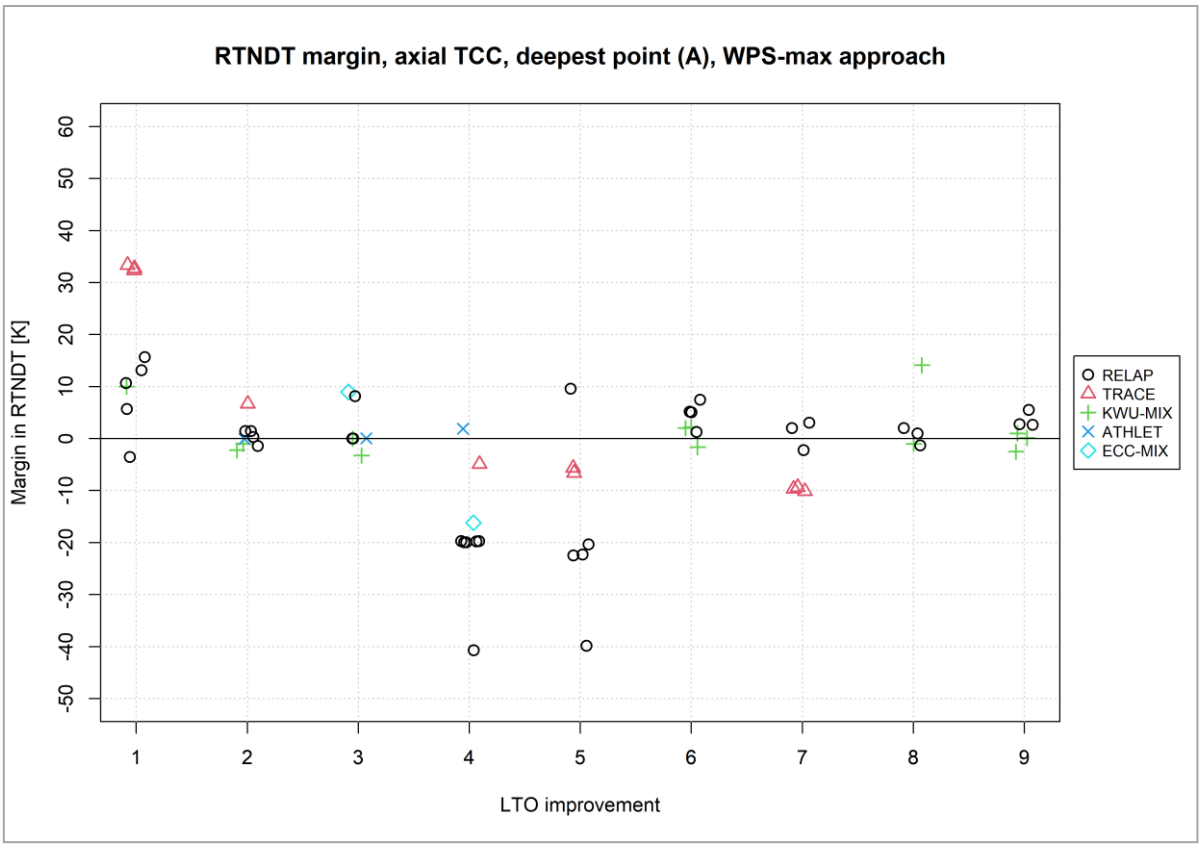

Figure 5.5: Comparison of LTO margins for all LTOs, WPS-max approach. For TCC, axial, point A.

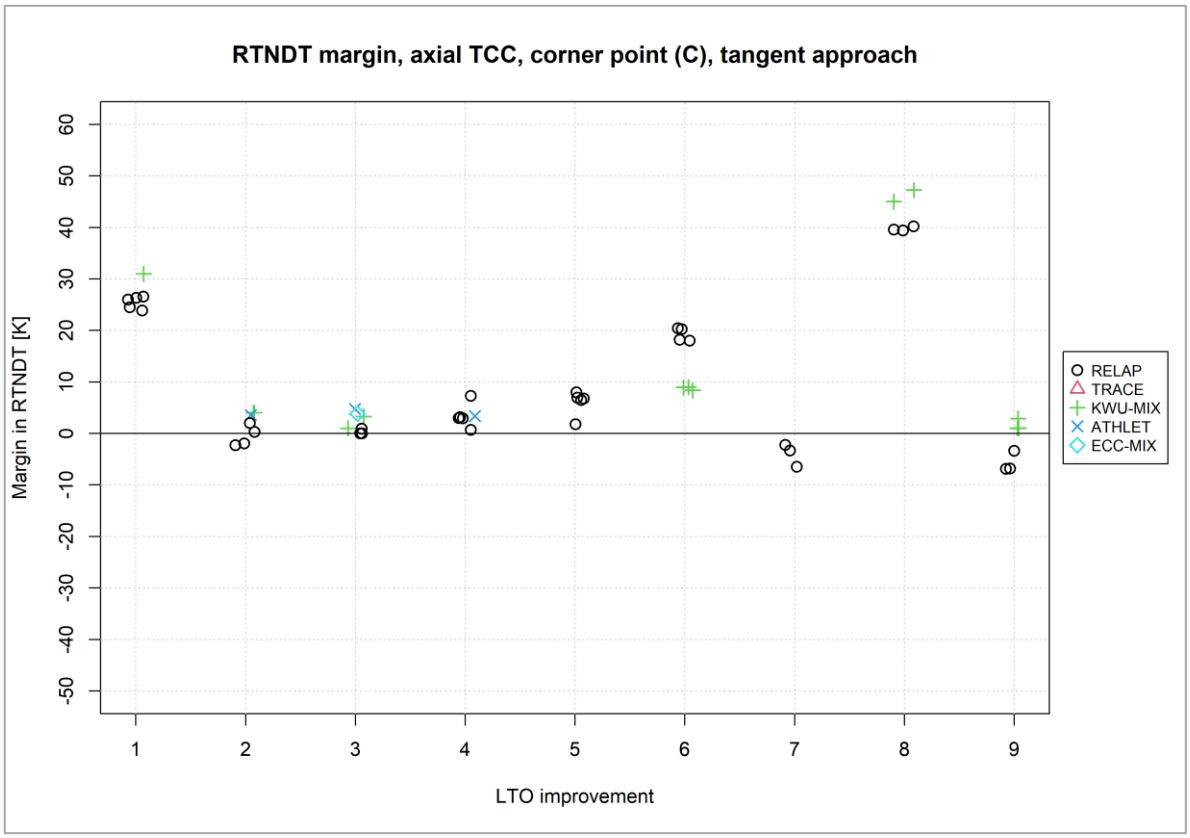

Figure 5.6: Comparison of LTO margins for all LTOs, tangent approach. For TCC, axial, point C.

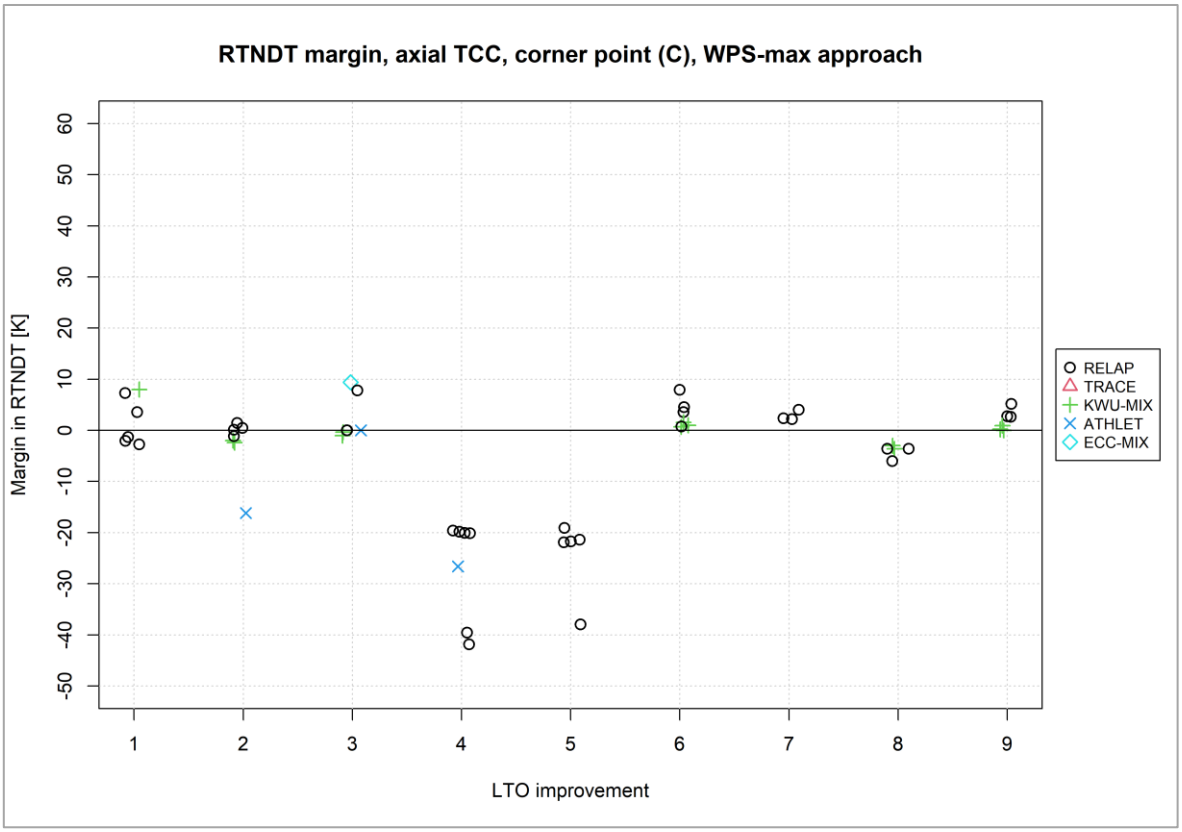

Figure 5.7: Comparison of LTO margins for all LTOs, WPS-max approach. For TCC, axial, point C.

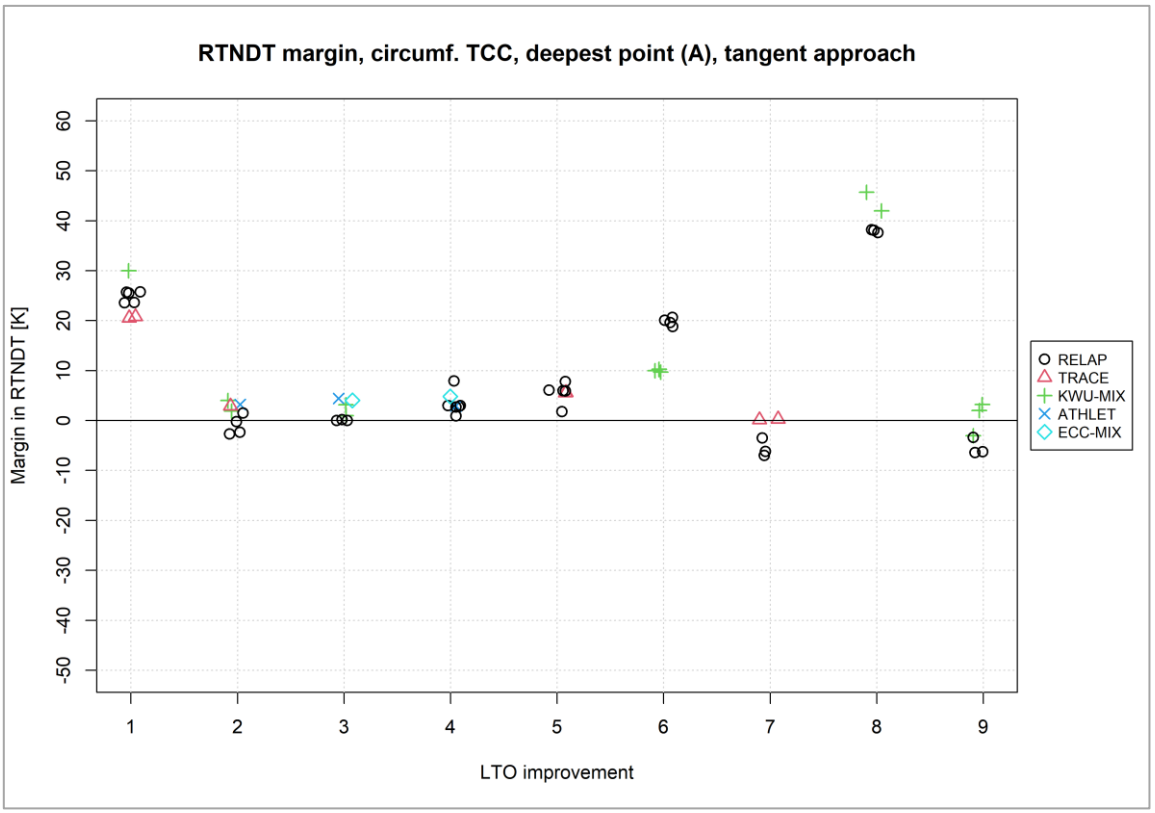

Figure 5.8: Comparison of LTO margins for all LTOs, tangent approach. For TCC, circumferential, point A.

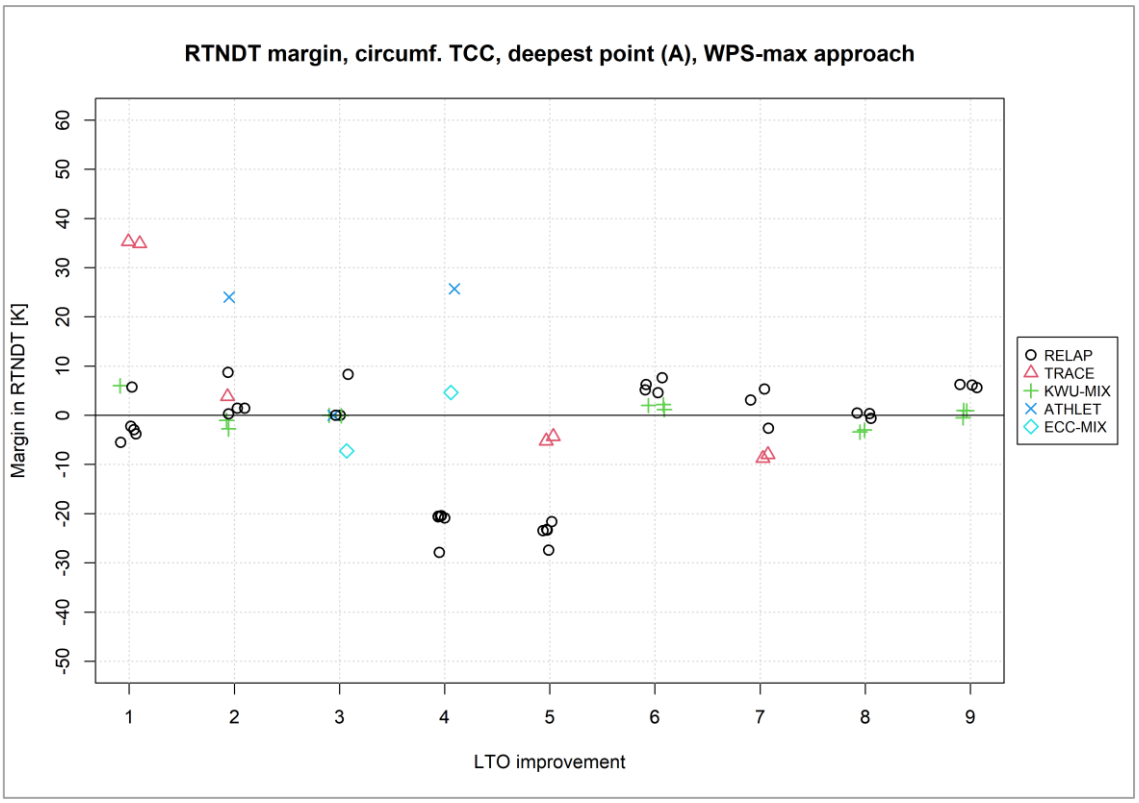

Figure 5.9: Comparison of LTO margins for all LTOs, WPS-max approach. For TCC, circumferential, point A.

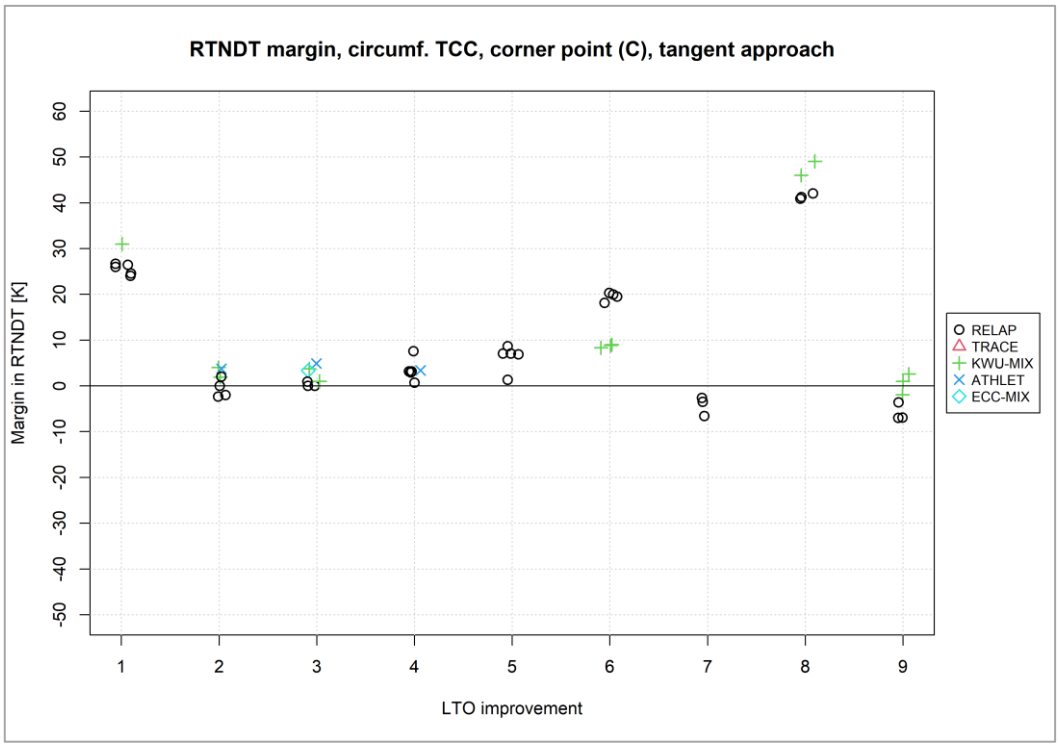

Figure 5.10: Comparison of LTO margins for all LTOs, tangent approach. For TCC, circumferential, point C.

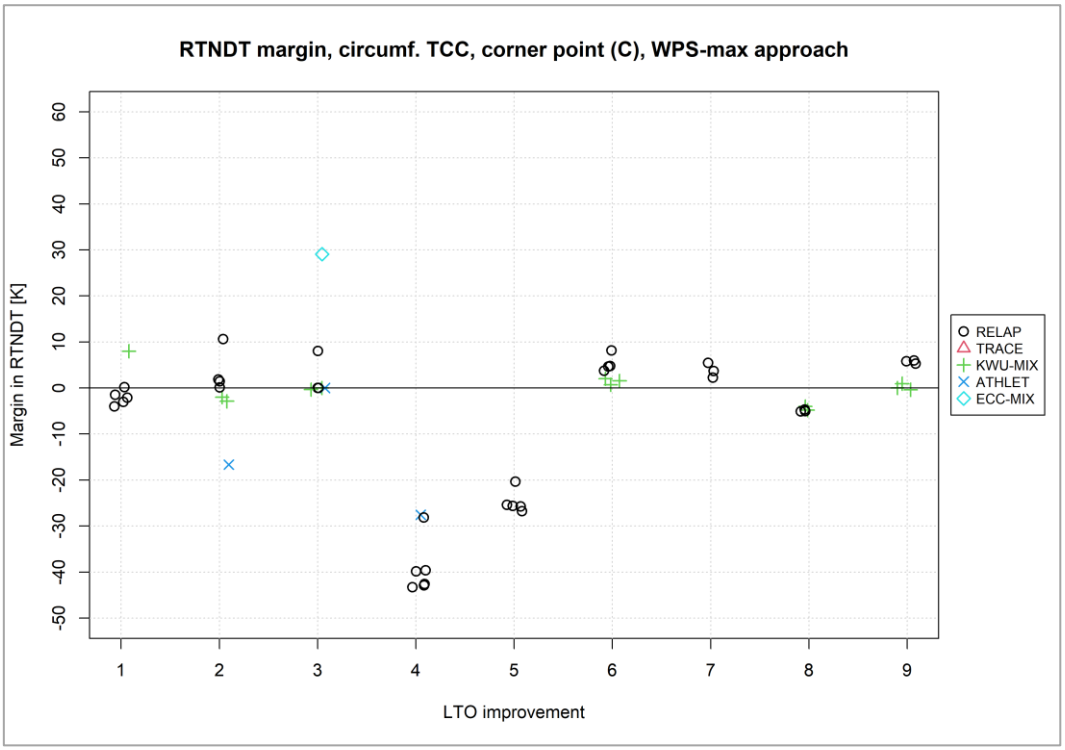

Figure 5.11: Comparison of LTO margins for all LTOs, WPS-max approach. For TCC, circumferential, point C

5.1.3 Summary evaluation of LTOs for UCC

In this Section, we attach graphs summarizing the LTO margins for UCC for all LTOs together, based on results of different partners using input TH data from different TH codes; these graphs are seen in Figure 5.12 – Figure 5.15. In these figures, the results for point A of both axial and circumferential crack and for both tangent and WPS-max approach are presented (for point C, mostly undefined margins[9] were obtained).

For tangent approach, it is seen from Figure 5.12 and Figure 5.14 that the most influential LTO improvements are LTO No. 1, 5, 6 and 8.

For WPS-max approach, it is seen from Figure 5.13 and Figure 5.15 that the margins have significantly larger scatter for each LTO improvement than in case of tangent approach, and, besides this, that the only LTO improvement that seems to have a moderately significant (positive) effect on max. all. ART is LTO improvement No. 1.

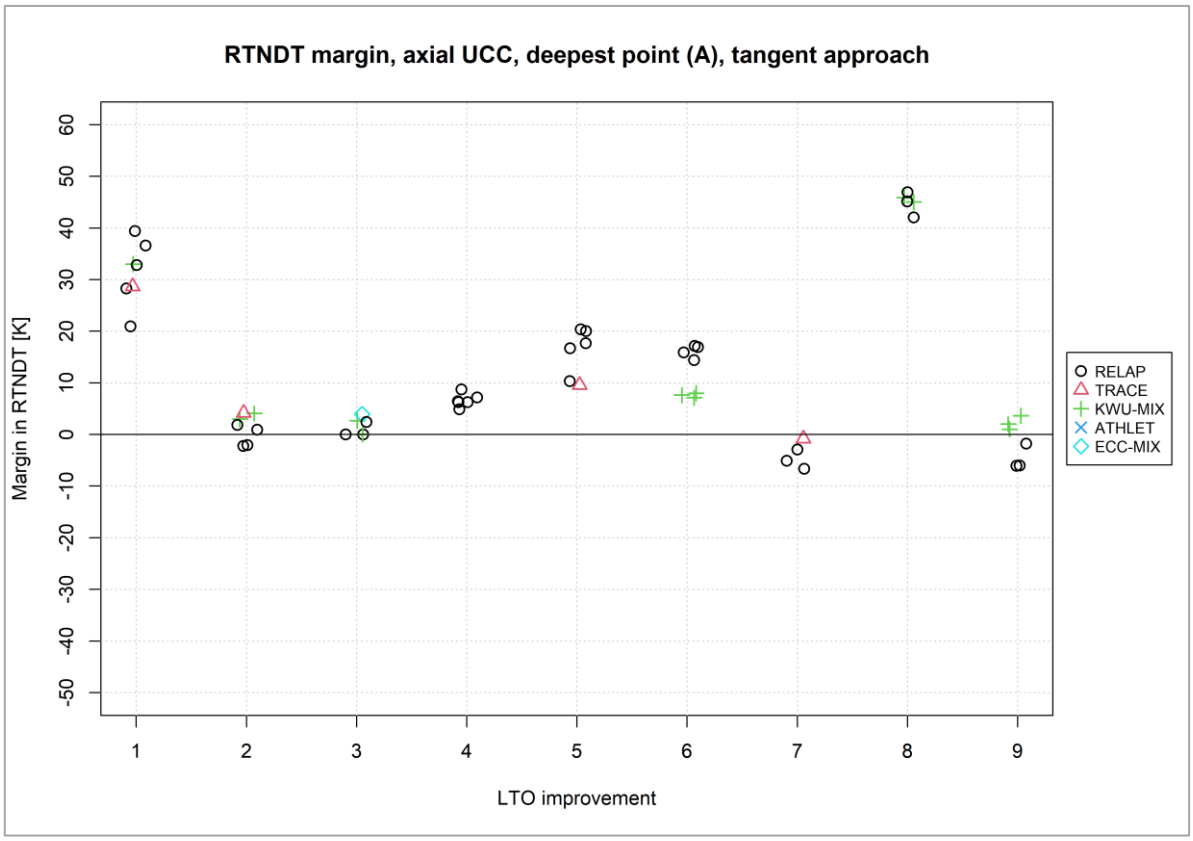

Figure 5.12: Comparison of LTO margins for all LTOs, tangent approach. For UCC, axial, point A.

[9] It means, that either for the base case, or for the LTO improvements the max. all. ART is unlimited (infinite) due to very small values of KI.

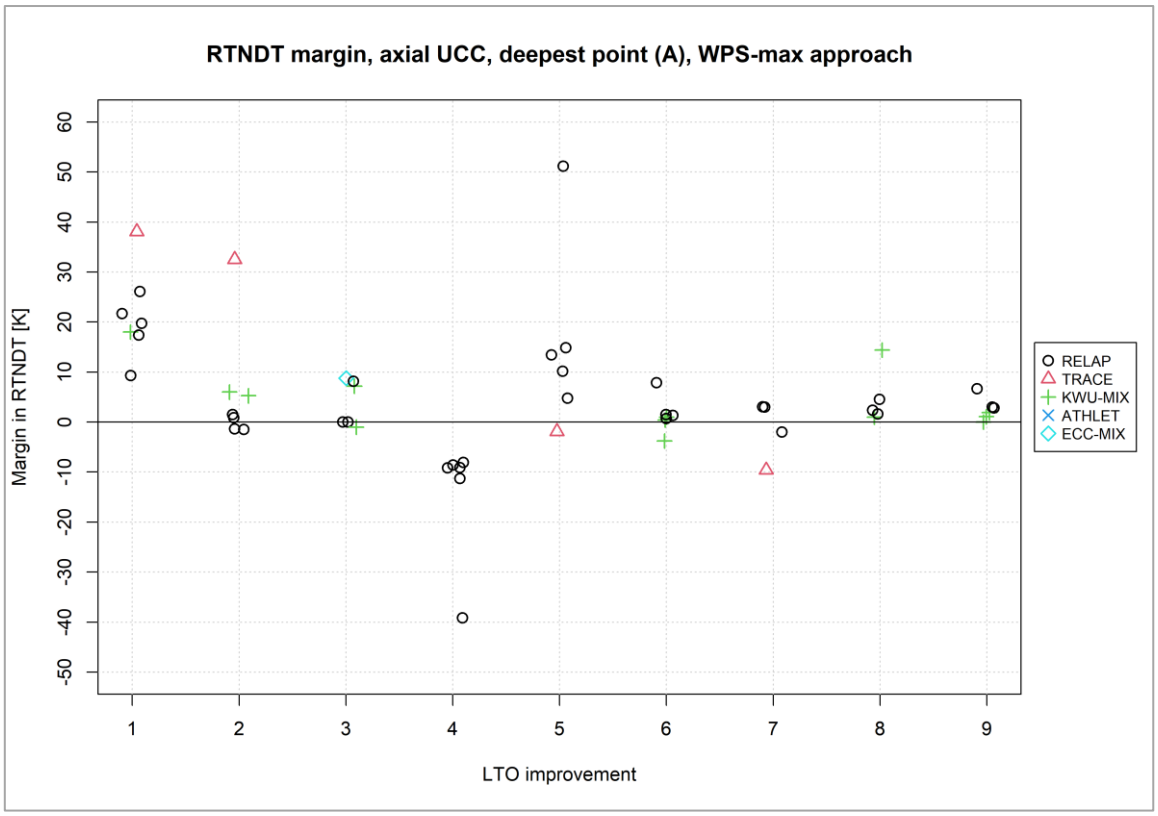

Figure 5.13: Comparison of LTO margins (benefits) for all LTOs considering WPS-max approach. For UCC, axial, point A.

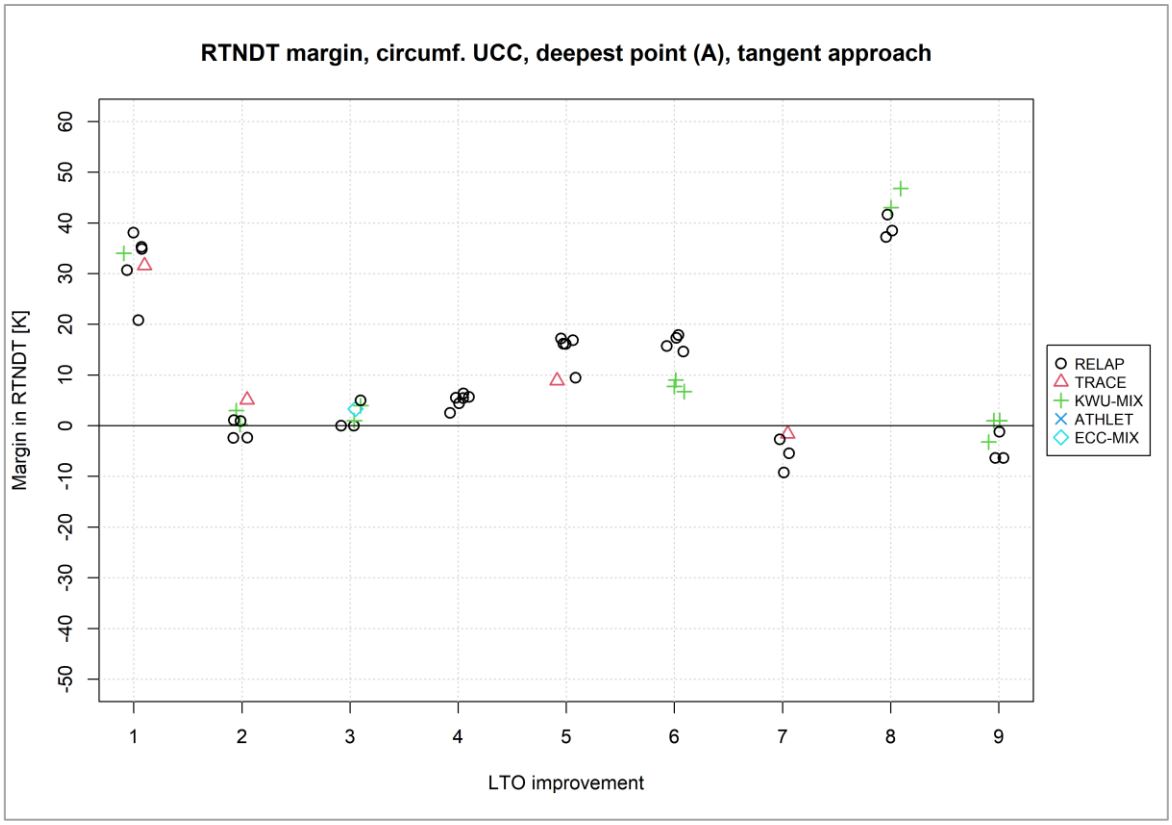

Figure 5.14: Comparison of LTO margins for all LTOs, tangent approach. For UCC, circumferential, point A.

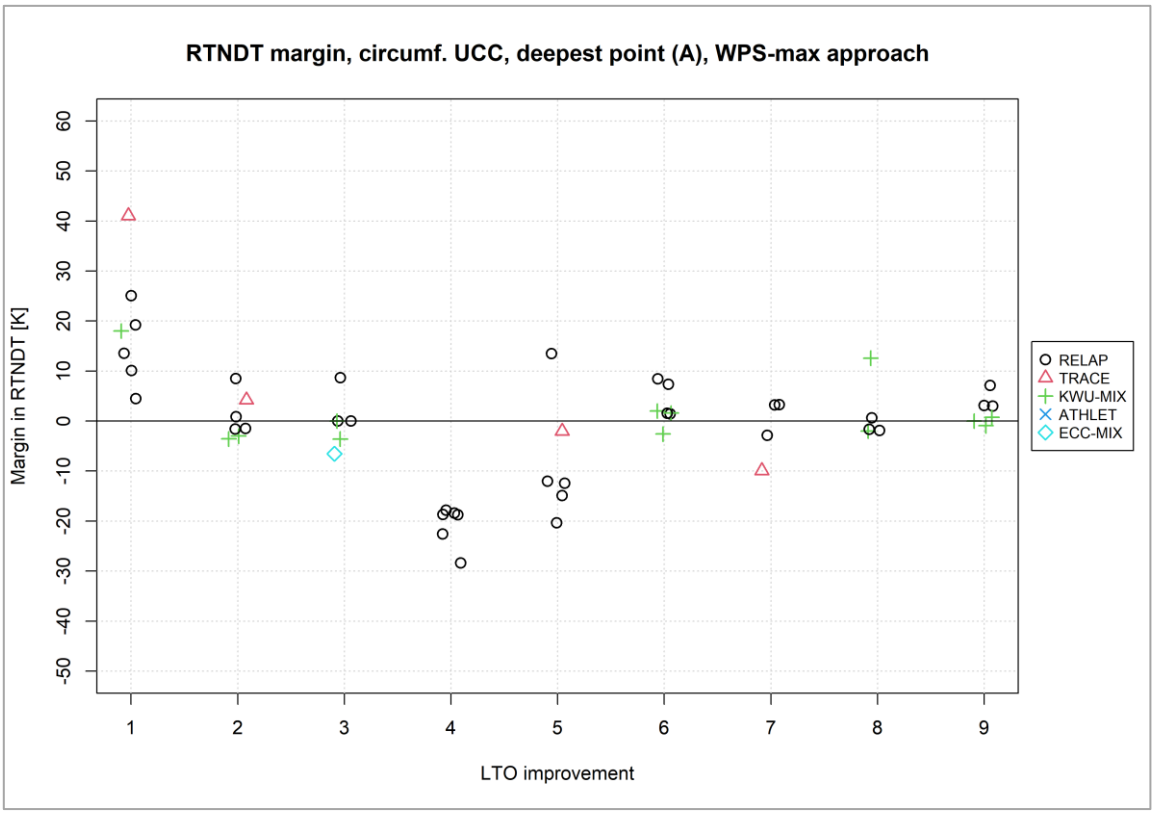

Figure 5.15: Comparison of LTO margins for all LTOs, WPS-max approach. For UCC, circumferential, point A.

5.1.4 Summary of evaluation of LTOs for embedded crack

The results for EC are summarized in the following Figure 5.16 – Figure 5.19. From these figures, it is seen that LTO 1 and 8 are beneficial based on max. all. ART values calculated using tangent approach. The embedded cracks were not assessed for LTO 3, 6 and 9.

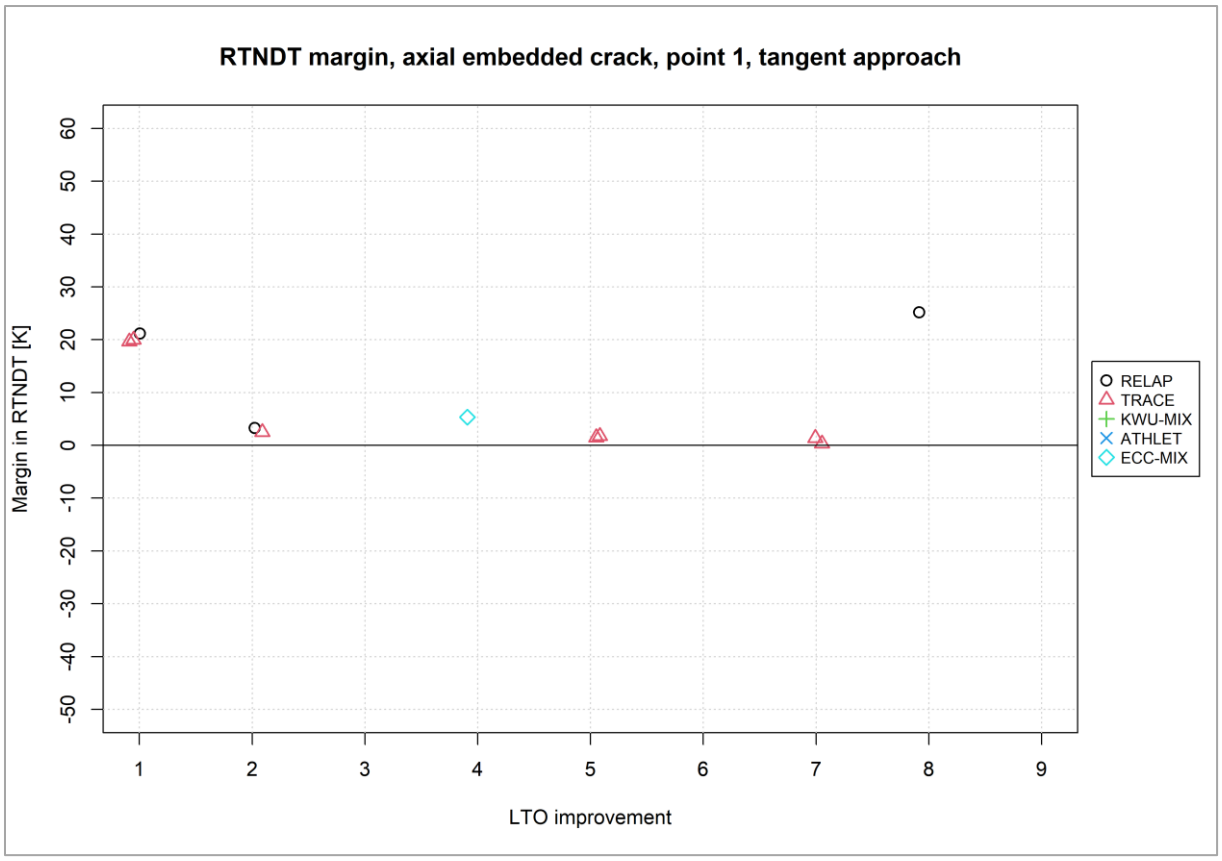

Figure 5.16: Comparison of LTO margins for all LTOs, tangent approach. For EC, axial, point 1.

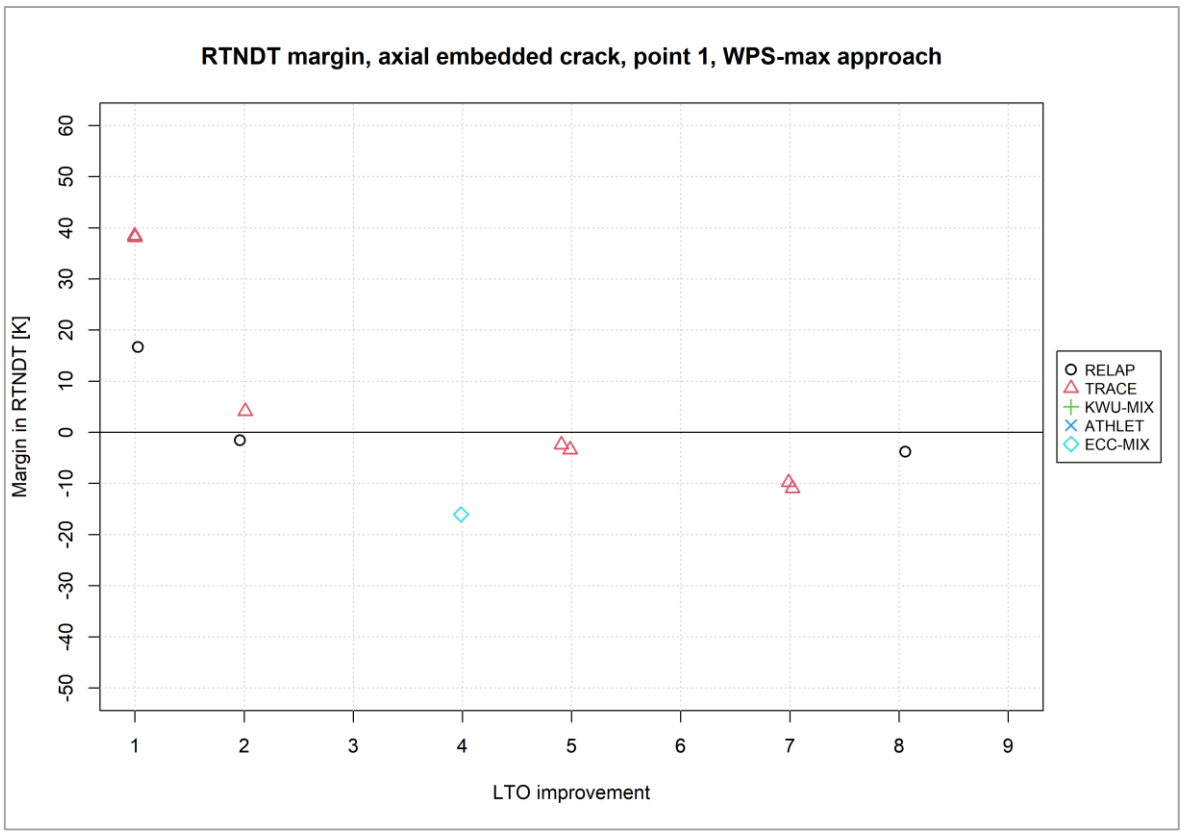

Figure 5.17: Comparison of LTO margins for all LTOs, WPS-max approach. For EC, axial, point 1.

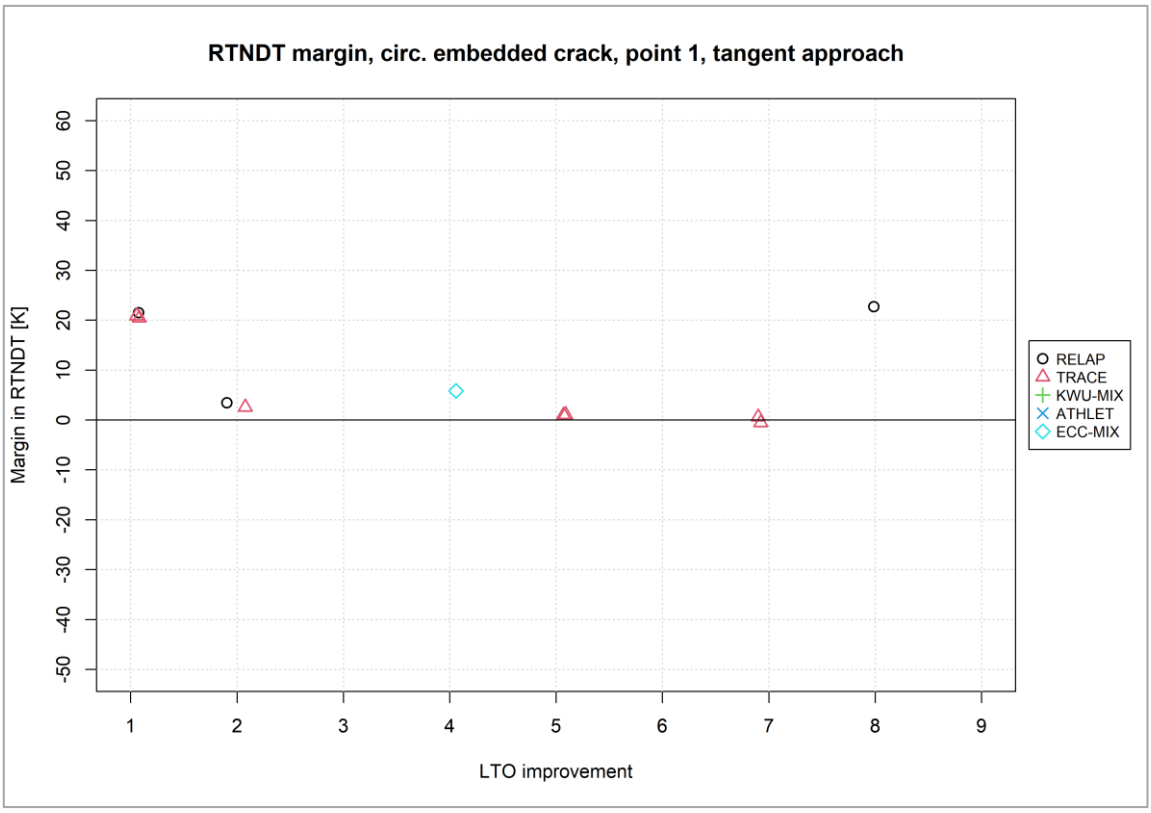

Figure 5.18: Comparison of LTO margins for all LTOs, tangent approach. For EC, circumferential, point 1.

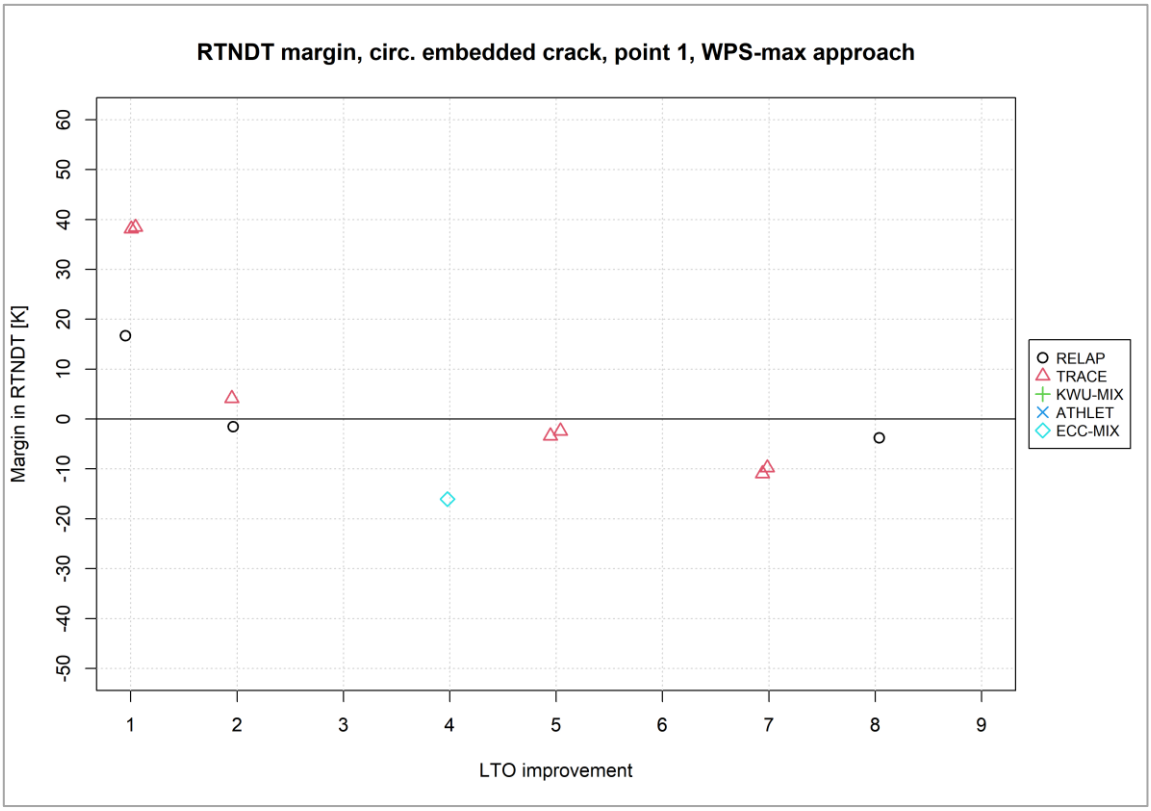

Figure 5.19: Comparison of LTO margins for all LTOs, WPS-max approach. For EC, circumferential, point 1.

5.2 Safety margins related to TH uncertainties

5.2.1 Comparison of temperature vs. time curves (based on Wilks data sets)

Six different RELAP Wilks data sets were constructed in WP 2 and used in Task 3.5: Relap-UJV (59 and 93 transients), Relap-JSI (59 and 130 transients), Relap-KIWA (59 transients), and Relap-SSTC (59 transients). The Wilks TH data sets generated by the same partner are statistically independent (each data set contains uniquely sampled TH transients), but they are generated from the same underlying statistical distributions of the input TH parameters. To see any potential differences between the datasets, the first 59 transients from four Wilks TH data sets produced by different partners were compared: Relap-UJV-93 (structural calculations by BZN), Relap-SSTC-59 (structural calculations by IPP), Relap-JSI-130 (structural calculations by JSI) and Relap-KIWA-59 (structural calculations by KIWA). The comparisons are shown by pairs (to make the figures clear) in the Figure 5.20 - Figure 5.25, where wall temperatures at the point A are plotted against time. The comparisons show that all four datasets have mutually different underlying statistical distributions. The reason for this difference was not clarified.

Figure 5.26 shows a comparison of the first 59 transients from the following three Wilks TH data sets: Relap-UJV-93, TRACE-PSI-59 and ATHLET-GRS-59. Thus, the figure illustrates the differences between the results from three different system TH codes. The differences are quite large, but they can be explained by the fact that the transients come from calculations with different TH codes. Especially possible differences in code specific input data sets, assumed distribution functions and boundary conditions as well as thermohydraulic model assumptions can cause these differences.

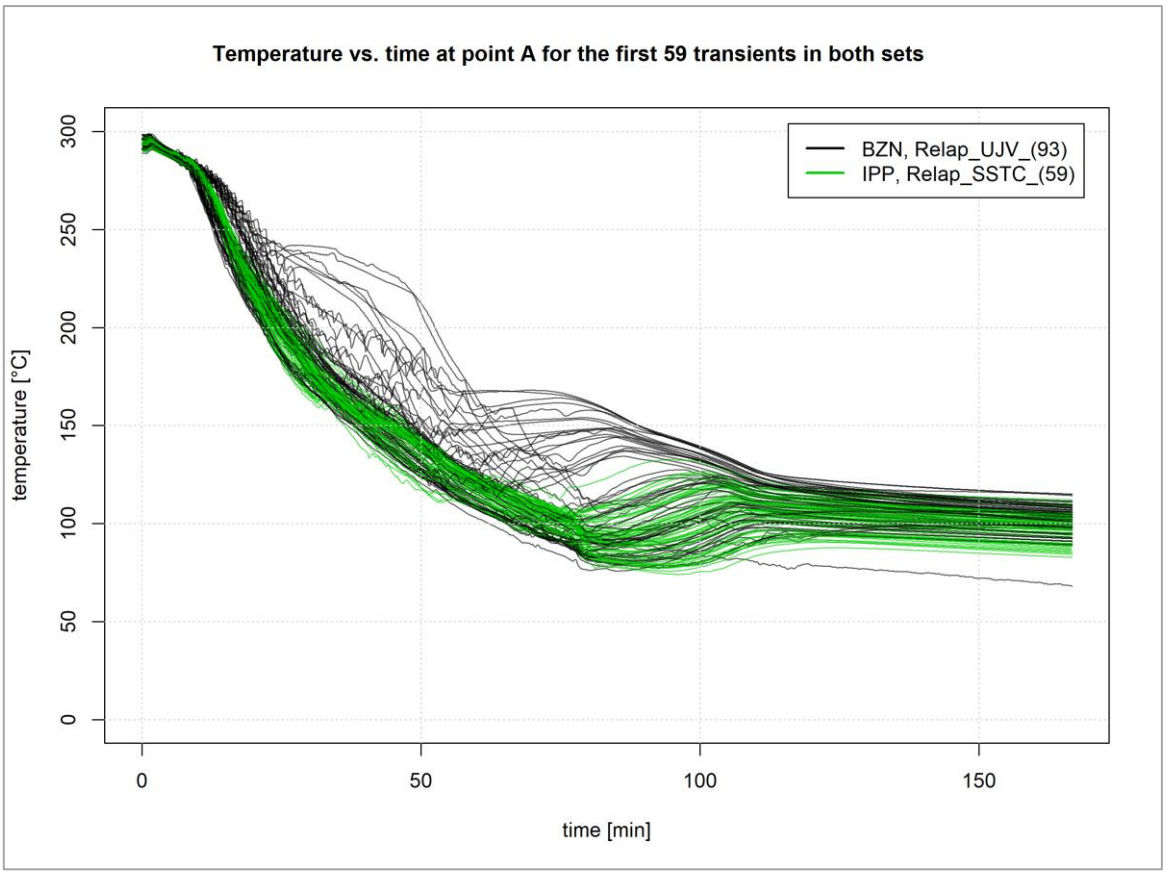

Figure 5.20: Comparison of temperature vs. time curves (results of heat transfer calculation) for Wilks set of transients obtained by BZN and IPP at the deepest point (pt. A) of TCC and UCC.

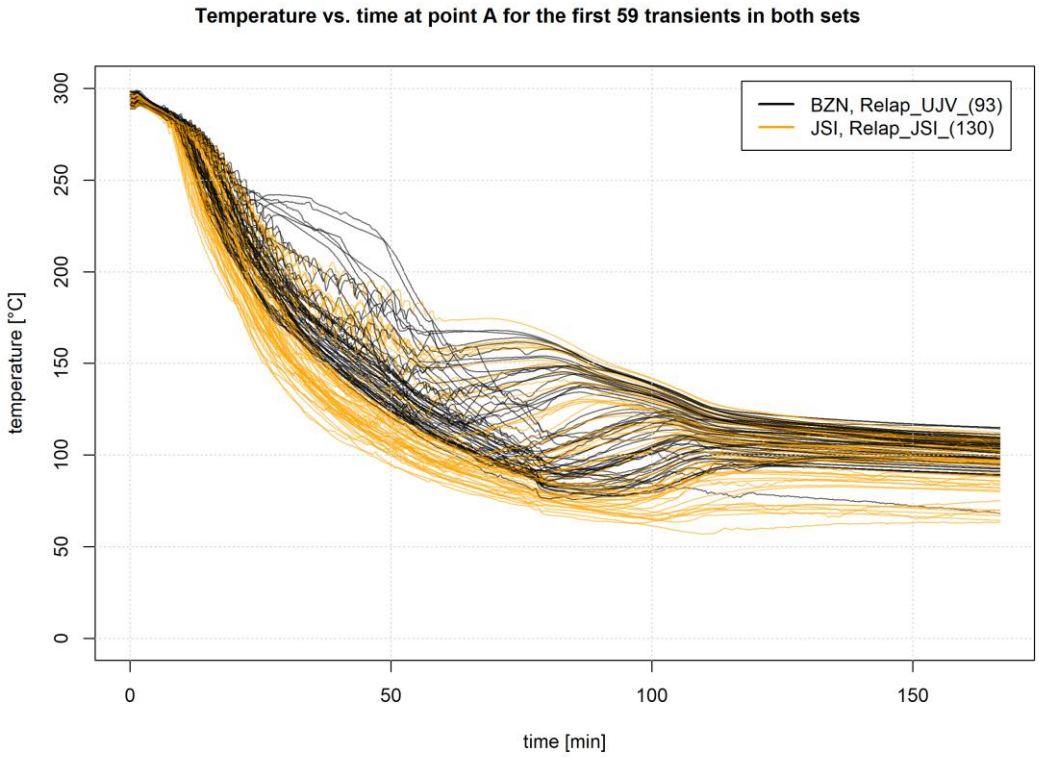

Figure 5.21: Comparison of temperature vs. time curves (results of heat transfer calculation) for Wilks set of transients obtained by BZN and JSI. For the deepest point (pt. A) of TCC and UCC.

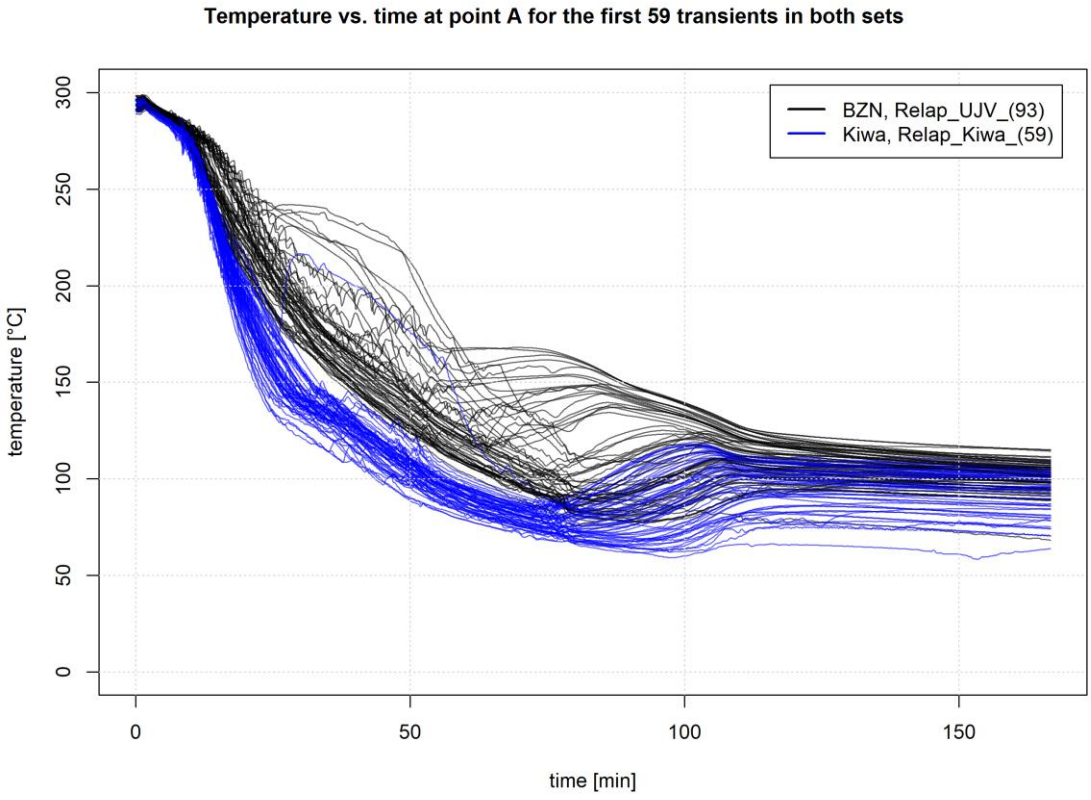

Figure 5.22: Comparison of temperature vs. time curves (results of heat transfer calculation) for Wilks set of transients obtained by BZN and KIWA. For the deepest point (pt. A) of TCC and UCC.

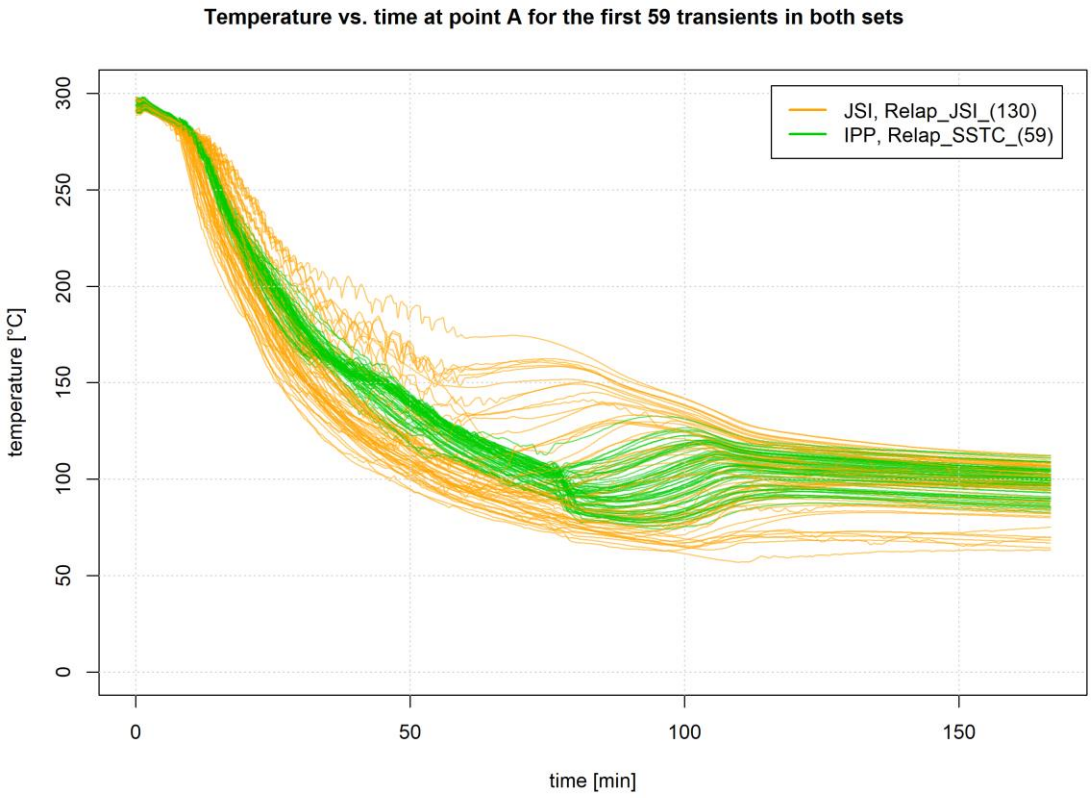

Figure 5.23: Comparison of temperature vs. time curves (results of heat transfer calculation) for Wilks set of transients obtained by JSI and IPP. For the deepest point (pt. A) of TCC and UCC.

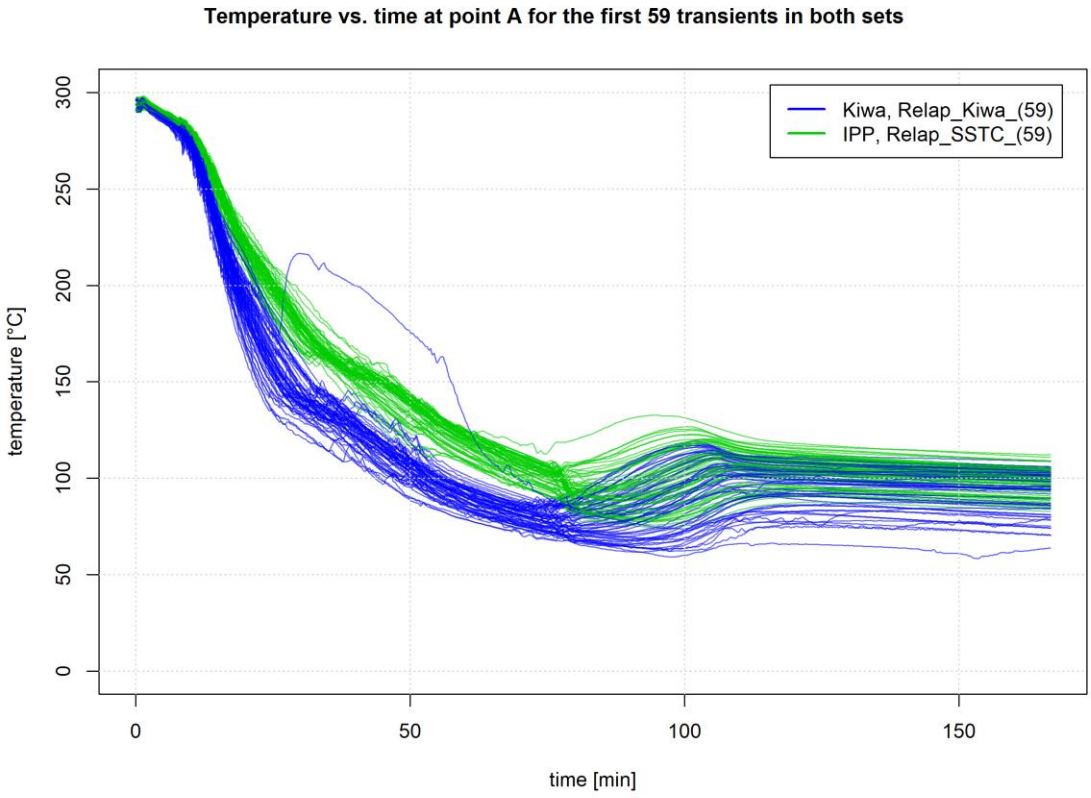

Figure 5.24: Comparison of temperature vs. time curves (results of heat transfer calculation) for Wilks set of transients obtained by KIWA and IPP. For the deepest point (pt. A) of TCC and UCC.

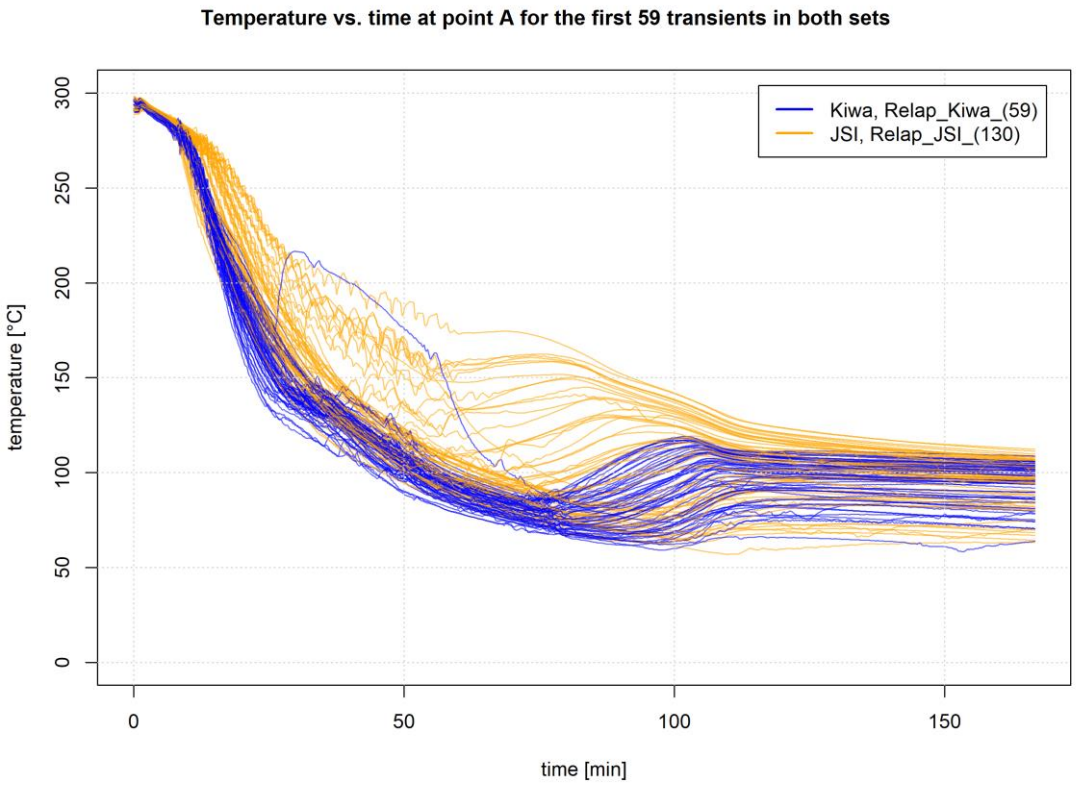

Figure 5.25: Comparison of temperature vs. time curves (results of heat transfer calculation) for Wilks set of transients obtained by KIWA and JSI. For the deepest point (pt. A) of TCC and UCC.

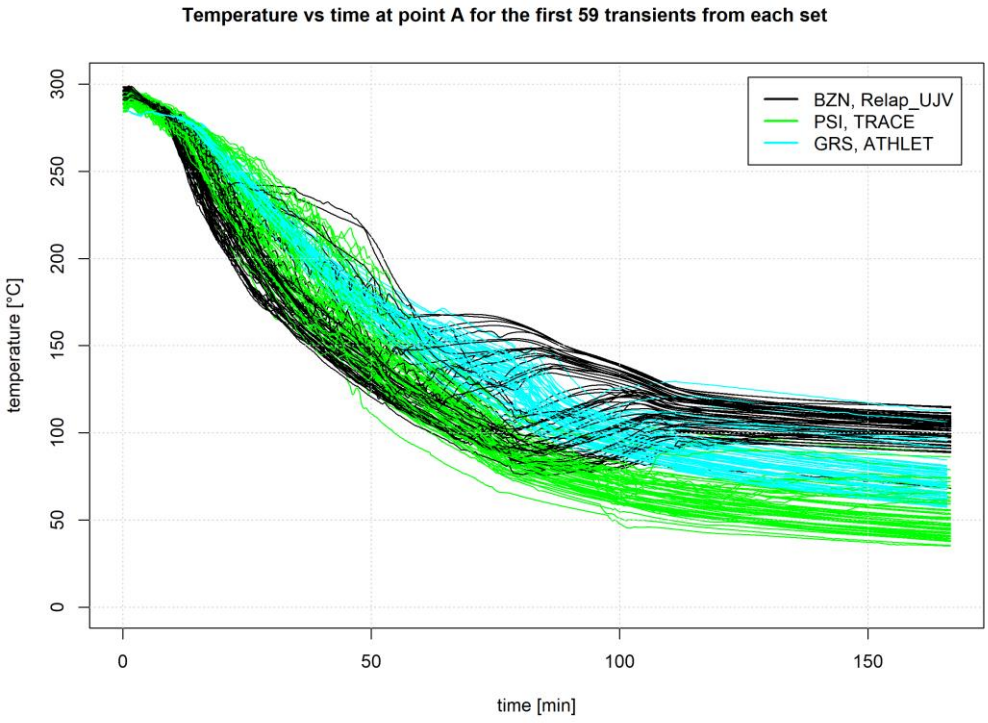

Figure 5.26: Comparison of temperature vs. time curves from TRACE, ATHLET and Relap-UJV. Temperature vs. time curves from SA calculations by BZN (first 59 transients from Relap-UJV-93), PSI (TRACE-PSI-59) and GRS (ATHLET-GRS-59). For the deepest point (pt. A) of TCC and UCC.

5.2.2 Comparison of empirical CDFs (based on Wilks data sets)

Empirical cumulative distribution functions (CDFs) of max. all. RT_{NDT} were constructed for all Wilks sets analysed by the partners. The empirical CDFs represent the statistical distribution of the max. all. RT_{NDT} values due to uncertainties in TH input parameters. As such, they represent the impact of the TH uncertainties on the results of the deterministic RPV integrity assessment. They also make it possible to compare mutually the results of different partners as well as results obtained for different Wilks sets (by the same or different partner).

The graphs of empirical CDFs are shown in the Figure 5.27 to Figure 5.34 for the different assessments (TCC or UCC; axial or circumferential; Point A; tangent or WPS-max approach). Values of max. all. RT_{NDT} larger than 250 °C are not shown in the graphs and may be considered as infinite (corresponding to no limitation on the RPV lifetime for the relevant calculation variant). In the graphs, it is possible to directly compare mutually the median values of max. all. RT_{NDT} which correspond to the value of 0.5 of the cumulative probability. The lowest values in the Wilks sets are also clearly seen, but their probability level depends on the number of the values in the corresponding Wilks set (59, 93 or 130). They represent the best estimate of the quantiles 1/59 = 1,79%; 1/93 = 1,11% and 1/130 = 0,77% of max. all. RT_{NDT}, respectively. As stated before, the smallest value from the Wilks set containing 59 values (or 2nd smallest value from 93, respectively) also corresponds to the 95%/95% lower tolerance limit of max. all. RT_{NDT} (i.e., to the lower estimate of the 5% quantile of max. all. RT_{NDT} estimated with 95% confidence).

Graphs of empirical CDFs for point C are similar. They are presented in [4].

The following groups of similar results with the same underlying statistical distributions of the TH input parameters (and TH transients) may be considered:

- FRA-G (KWU-MIX-93)
- PSI (TRACE-PSI-130), PSI (TRACE-PSI-93), TEC (TRACE-PSI-59)
- GRS (ATHLET-59)
- UJV (Relap-UJV-93), BZN (Relap-UJV-93), UJV (Relap-UJV-59)
- IPP (Relap-SSTC-59), SSTC (Relap-SSTC-59)
- KIWA (Relap-KIWA-59)
- JSI (Relap-JSI-130), WUT (Relap-JSI-130), WUT (Relap-JSI-59)

In this list, the partners performing the SA and FM calculations are indicated and their input Wilks TH data sets are stated in the parentheses.

The Figure 5.27 shows empirical CDFs for the deepest point (pt. A) of axial TCC for all calculation variants (all partners and all Wilks TH datasets). The groups of results with the same underlying statistical distribution of the TH input parameters are distinguished by different colours.

The results of PSI and TEC for the TRACE-PSI-59 Wilks set should be very similar, because they are based on the same set of TH transients and differ only in the SA and FM calculations. The same should be true for the following pairs of calculations: IPP and SSTC calculations for the Relap-SSTC-59 data set, JSI and WUT calculations for the Relap-JSI-130 data set, and UJV and BZN calculations for the Relap-UJV-93 data set. This was confirmed for all calculations with the exception of IPP and SSTC calculations for the Relap-SSTC-59 TH dataset. In this case, some differences in the results were observed between IPP and SSTC. These differences may be attributed to the structural and/or fracture-mechanics analysis.

On the other hand, the results of UJV based on Relap-UJV-93 were expected to differ somewhat from the results of UJV based on Relap-UJV-59 dataset, because the Relap-UJV-93 and Relap-UJV-59 datasets correspond to different finite samples drawn from the same underlying distribution of the TH transients (and TH input parameters). The same holds for the following pairs of calculations:

- PSI (TRACE-PSI-130) and PSI (TRACE-PSI-93)
- PSI (TRACE-PSI-130) and TEC (TRACE-PSI-59)
- JSI (Relap-JSI-130) and WUT (Relap-JSI-59)

From the Figure 5.27, it is seen that the minimum and median values of max. all. RT_{NDT} are lowest for FRA-G and highest for GRS. This can be partially explained by the fact that the FRA-G calculations include TH mixing and the GRS calculations are the only ones that do not take residual stresses into account. Further sources of the scatter are the differences in thermohydraulic results (see **Figure 5.26**).

For the deepest point of UCC, the resulting values of max. all. RT_{NDT} obtained by GRS are much larger than those obtained by other partners. For the corner point (pt. C) of UCC, some partners calculated all max. all. RT_{NDT} values larger than 250 °C or even infinite.

The embedded crack was assessed only by PSI and JSI using TRACE and RELAP, respectively. The results are presented in [4].

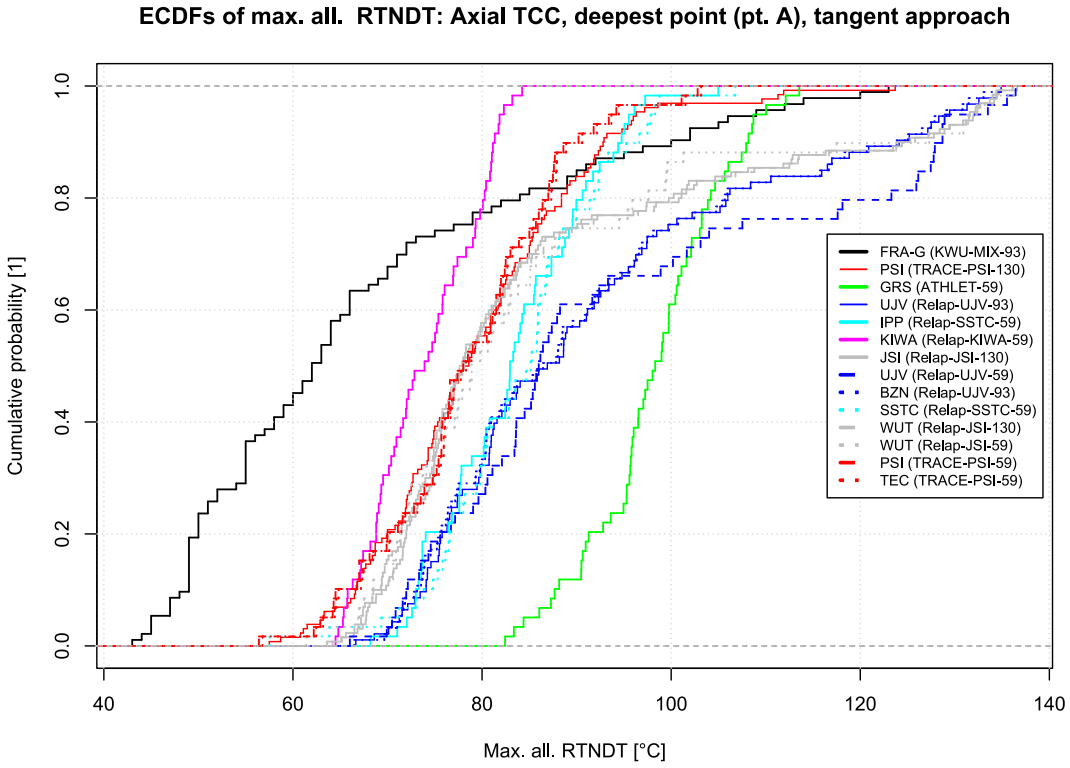

Figure 5.27: Comparison of empirical CDFs of max. all. RT_{NDT}, as calculated by individual partners. For deepest point (pt. A) of axial TCC, tangent approach.

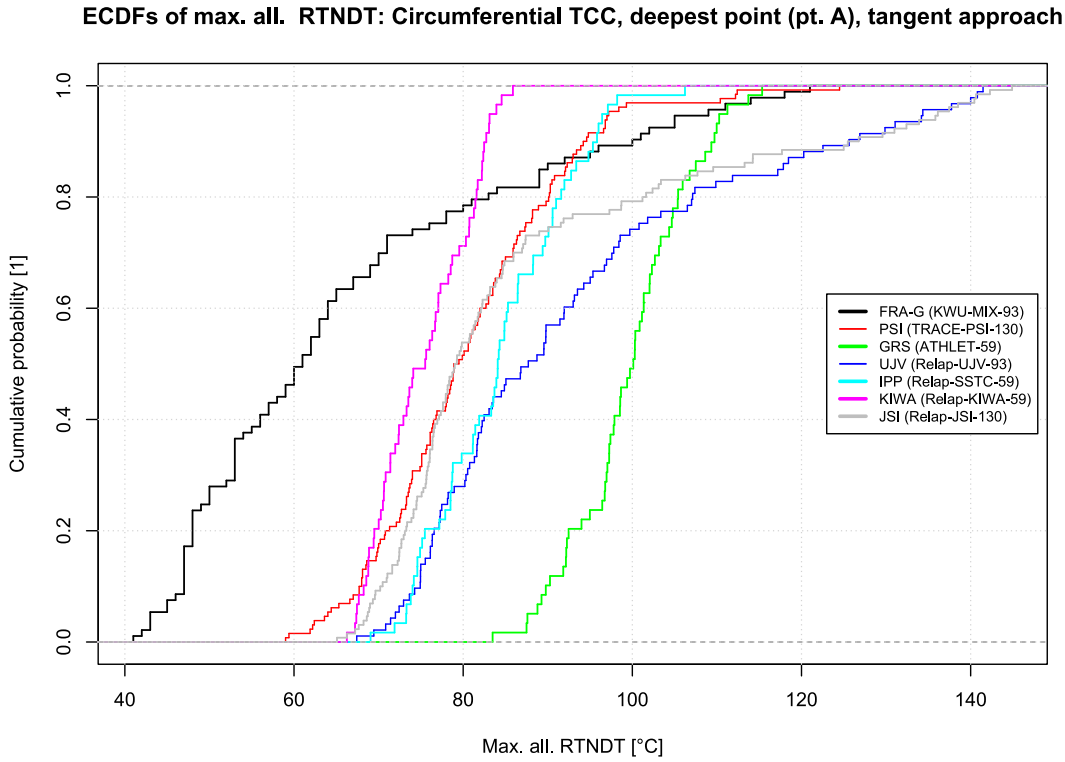

Figure 5.28: Comparison of empirical CDFs of max. all. RT_{NDT} obtained by individual partners, with "similar" results removed for clarity. For deepest point (pt. A) of circumf. TCC, tangent approach

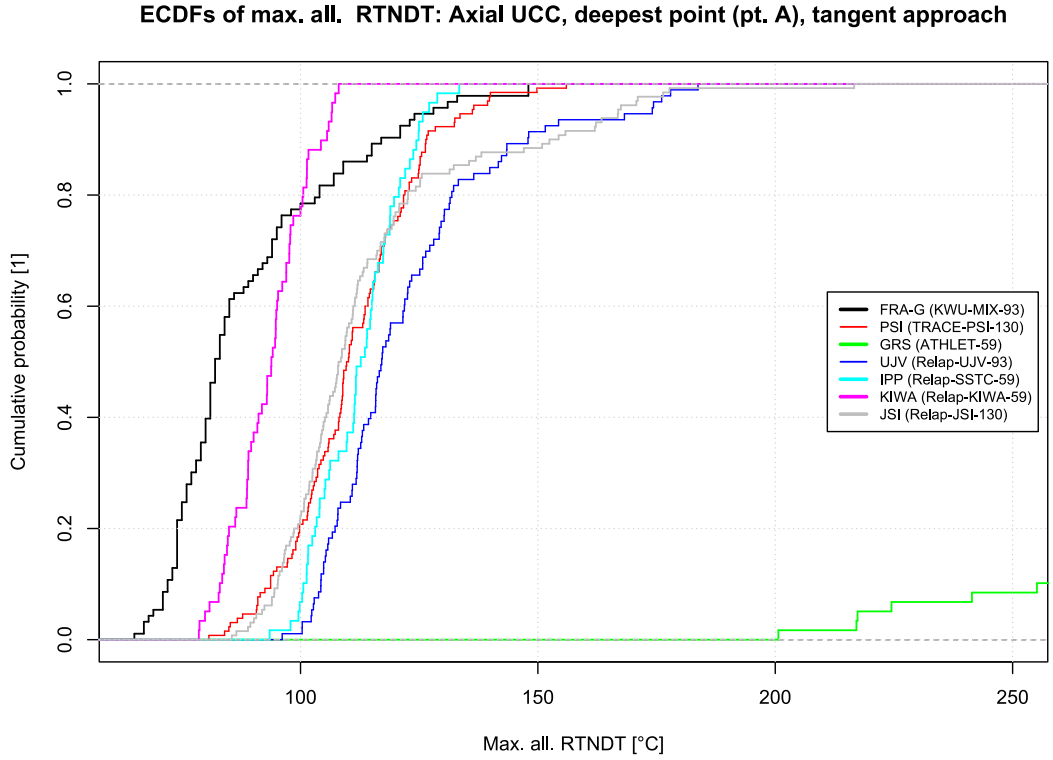

Figure 5.29: Comparison of empirical CDFs of max. all. RT_{NDT} obtained by individual partners, with "similar" results removed for clarity. For deepest point (pt. A) of axial UCC, tangent approach

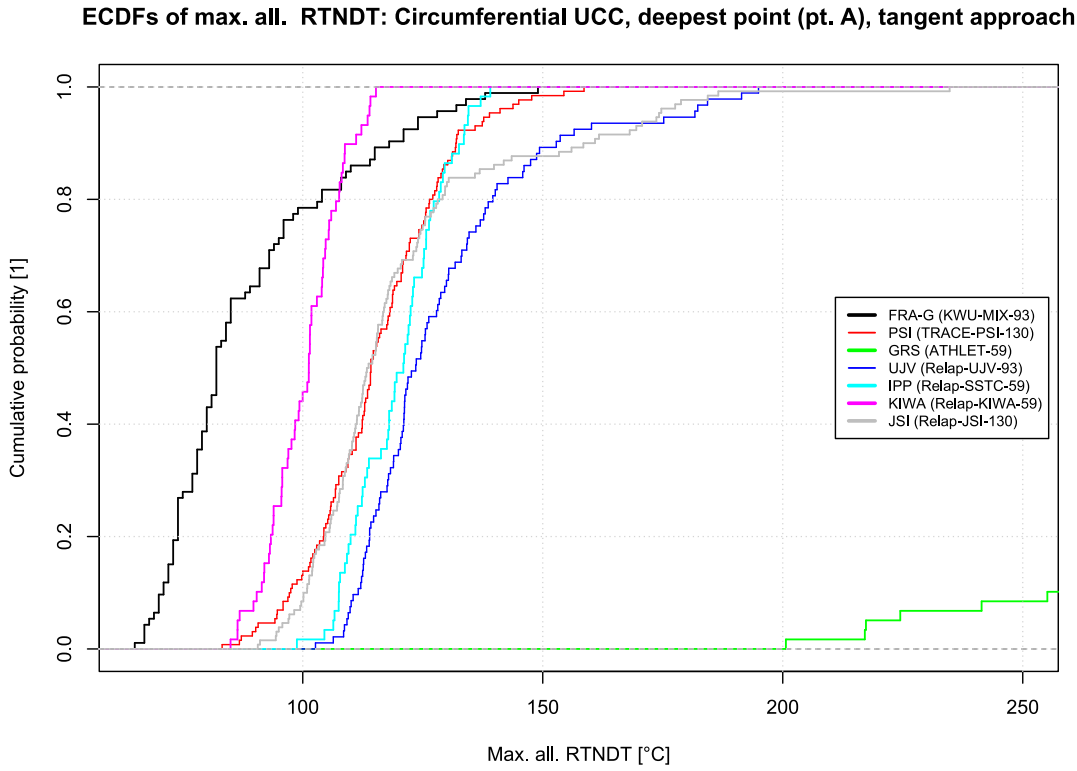

Figure 5.30: Comparison of empirical CDFs of max. all. RT_{NDT} obtained by individual partners, with "similar" results removed for clarity. For deepest point (pt. A) of circumf. UCC, tangent approach

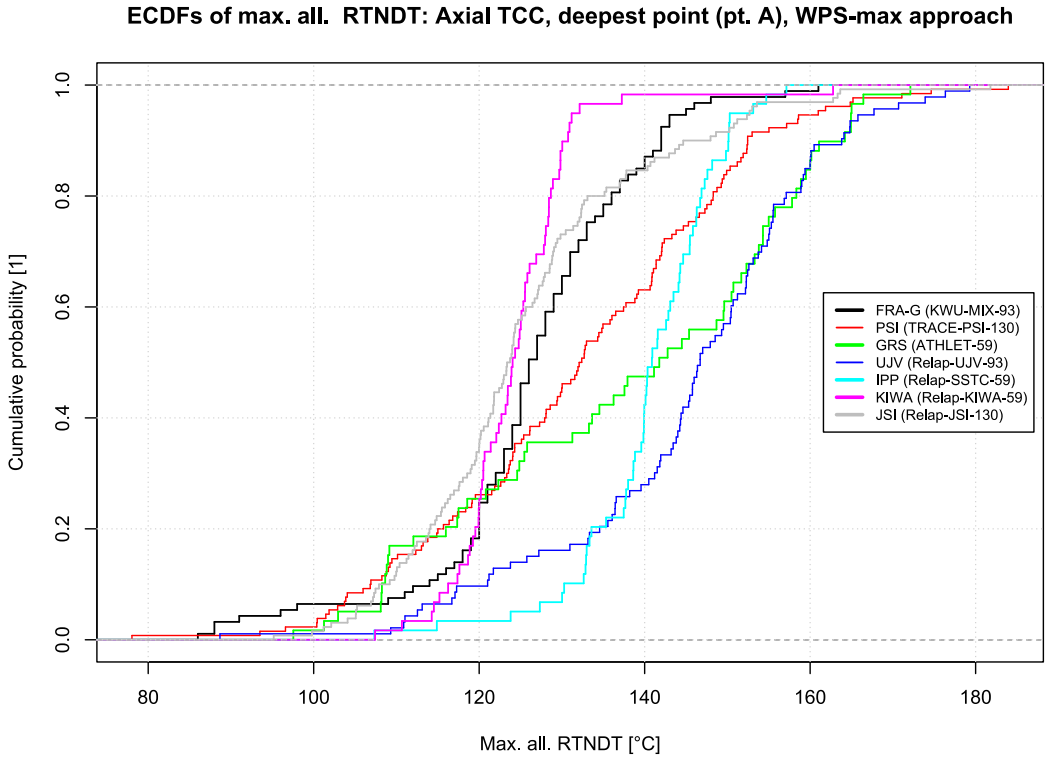

Figure 5.31: Comparison of empirical CDFs of max. all. RT_{NDT} obtained by individual partners, with "similar" results removed for clarity. For deepest point (pt. A) of axial TCC, WPS-max approach.

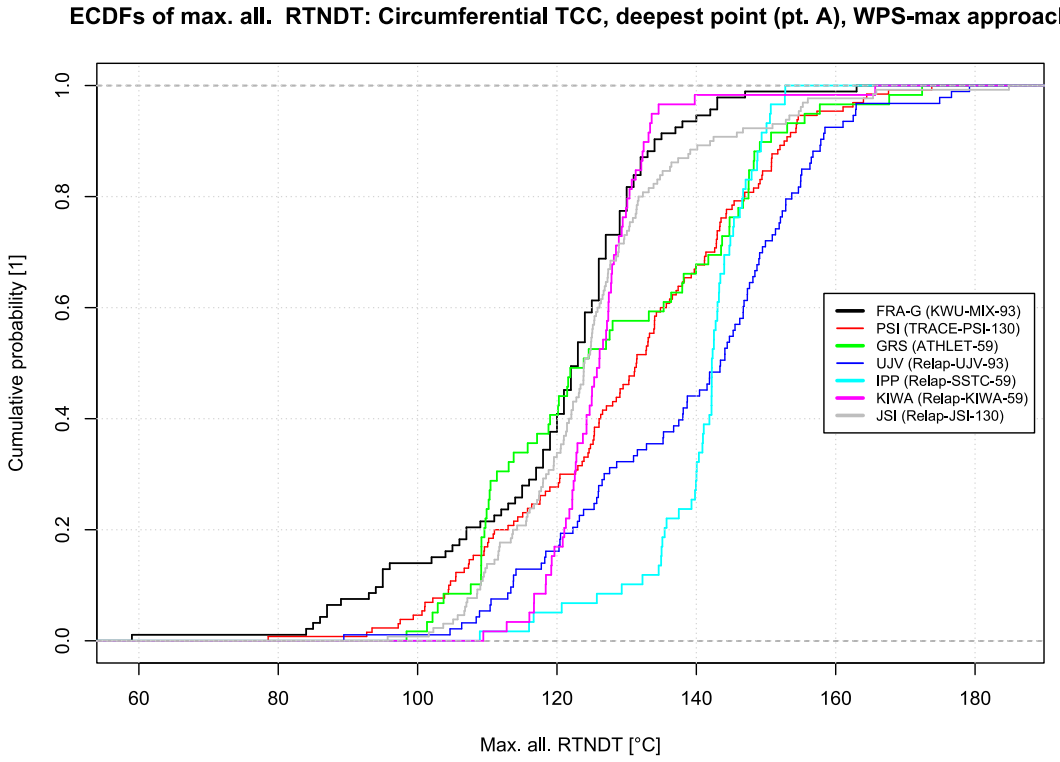

Figure 5.32: Comparison of empirical CDFs of max. all. RT_{NDT} obtained by individual partners, with "similar" results removed for clarity. For deepest point (pt. A) of circumf. TCC, WPS-max approach

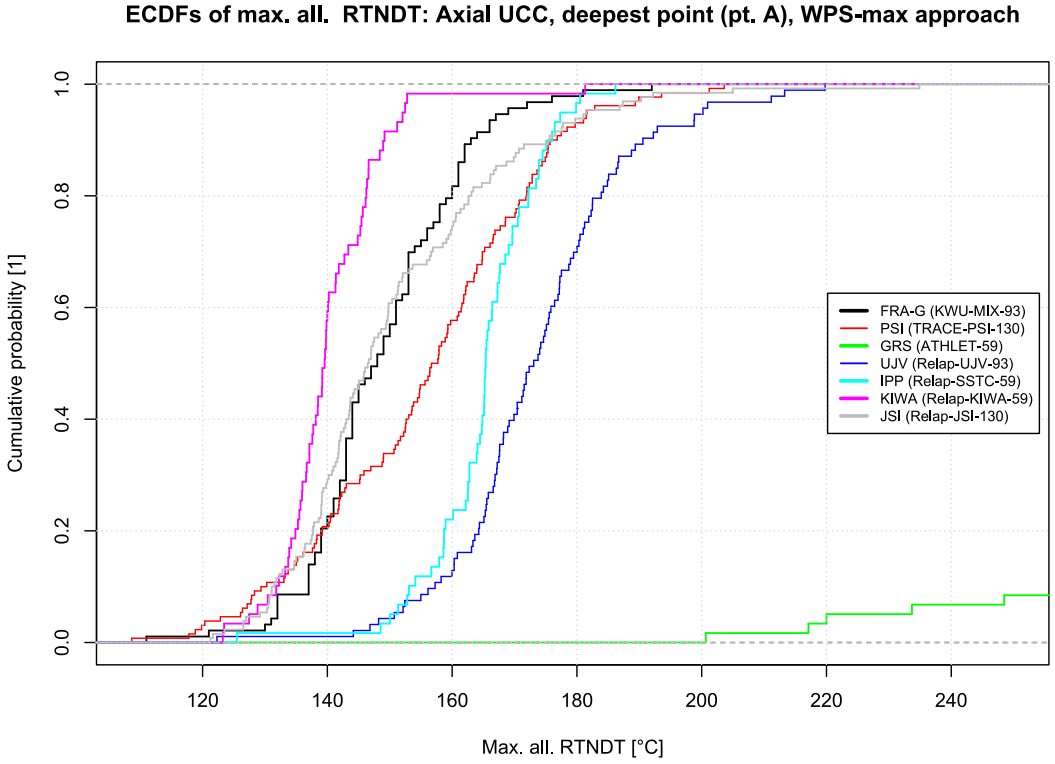

Figure 5.33: Comparison of empirical CDFs of max. all. RT_{NDT} obtained by individual partners, with "similar" results removed for clarity. For deepest point (pt. A) of axial UCC, WPS-max approach

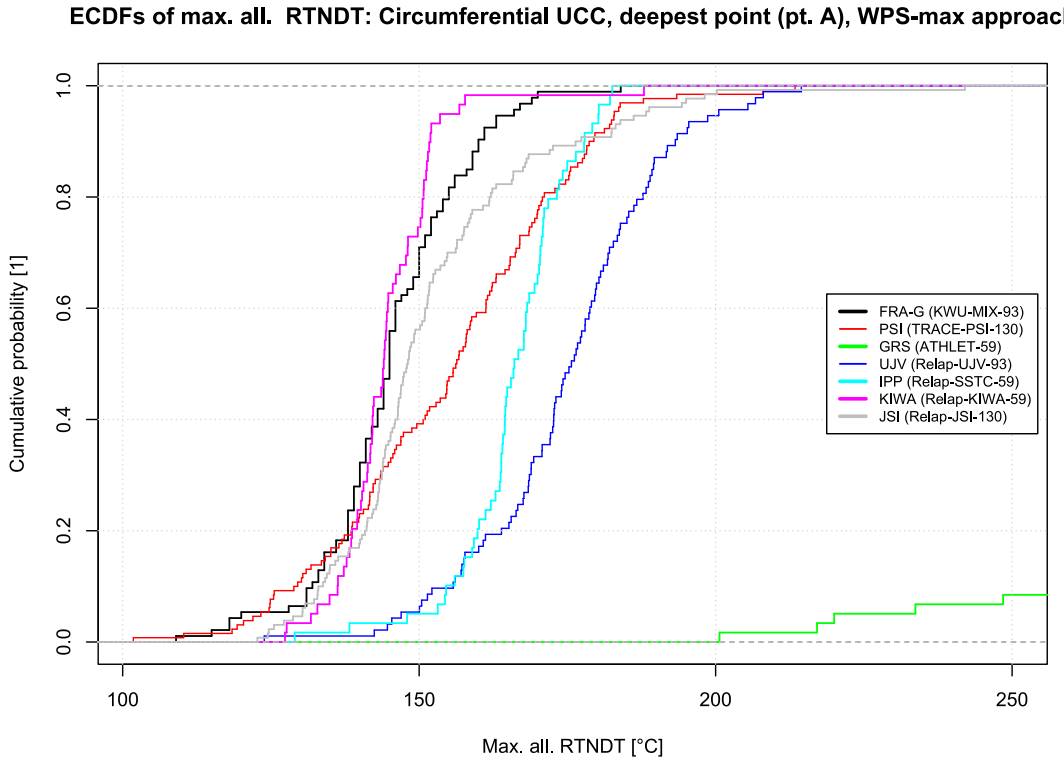

Figure 5.34: Comparison of empirical CDFs of max. all. RT_{NDT} obtained by individual partners, with "similar" results removed for clarity. For deepest point (pt. A) of circumf. UCC, WPS-max approach

5.2.3 Comparison of 95%/95% lower limit values of max. all. RT_{NDT} (based on Wilks data sets) and selected margins

It is seen from Figure 5.27 to Figure 5.34 that for TCC, there is a relatively good accordance in 95%/95% lower limit values between the partners using RELAP[10] for axial/circumferential crack, point A/C, tangent approach, while the 95%/95% lower limit values obtained based on FRA-G KWU-MIX TH analyses, resp. GRS ATHLET TH analyses, are lower, resp. higher than those based on RELAP. Concerning calculation by GRS, the higher values of 95%/95% lower limit may be partly due to the fact that GRS did not include RS in their SA. Concerning calculation by FRA-G, the lower values of 95%/95% lower limit are due to the fact that FRA-G considered effect of cold plume.

For WPS-max approach, there is larger scatter in 95%/95% lower limit values between the individual partners than for the tangent approach. Further, from a detailed examination of the results that is presented in [4], it is seen that values of the 95%/95% lower limit values for point C are in most cases somewhat lower than those for point A for TCC.

It is also worth noting that although the distributions of the fracture-mechanics calculation results (K_I vs. T curves) calculated based on RELAP are different for different partners, the appropriate 95%/95% lower limit values of max. all. RT_{NDT} are quite close each to other, with the only exception of SSTC, see the footnote No. 10.

[10] The only exception is calculation by SSTC, where slightly lower 95%/95% lower limit values were obtained than those obtained by the other partners using RELAP, and especially than those obtained by the IPP partner whose results were based on precisely the same results of TH calculations.

As for the results based on TRACE, the TEC_59 and PSI_59 results are based on the same Wilks data set, and therefore they differ only by SA and fracture-mechanics calculations; consequently, their results are practically the same (as expected). Analogously, JSI_130 and WUT_130 are based on the same Wilks TH data sets, and their results also are practically the same.

UJV_59 and UJV_93 results are based on different number of samples but have the same statistical distribution of TH parameters. No substantial differences were seen in results between these two calculations, with the exception of WPS-max approach for TCC, where some difference is seen.

For UCC, it is seen from detailed results presented in [4], that the 95%/95% lower limit values in point C are in most cases higher than those in point A and in many cases they are infinite. This corresponds to the fact that the under-clad crack does not tend to initiate in point C.

Comparison of the 95%/95% lower limit values with median values from the Wilks set and values of max. all. RT_{NDT} for the base case (BC) and best estimate case (BE) is seen in Table 5.3 for the deepest point of axial TCC. For other crack configurations, this information can be found in Annex 7 of [4].

The conservative case transient (CC) was analysed only by UJV and JSI. CC is a transient with all TH parameters set to their conservative values (according to the opinion of TH experts) within the intervals of their uncertainties. BZN evaluated this transient using the TH data from UJV. Comparison of the conservative case with the base case and with results from the Wilks sets for the deepest point of axial TCC in seen in Table 5.4. For other crack configurations, this information can be found in Annex 7.2 of [4].

Table 5.3: Overview of 95%/95% lower limit and median values of max. all. RT_{NDT}, and values of max. all. RT_{NDT} for the base case and best estimate case, as obtained by different partners. For TCC, axial, point A.

Partner and number of TH data sets	TH code	Tangent approach				WPS-max approach			
		Wilks 95%/95% [°C]	Wilks set median [°C]	BC [°C]	BE [°C]	Wilks 95%/95% [°C]	Wilks set median [°C]	BC [°C]	BE [°C]
FRA_G_93	KWU-MIX	44,0	62,0	38,0	49,0	88,0	126,0	105,0	130,0
GRS_59	ATHLET	82,4	98,3	90,6	NA	97,5	141,8	149,1	NA
UJV_59	Relap	66,0	86,0	70,9	83,7	79,9	146,9	151,0	150,1
UJV_93	Relap	68,6	86,9	70,9	83,7	109,3	146,7	151,0	150,1
BZN_93	Relap-UJV	69,7	86,4	70,7	83,3	104,8	146,6	150,4	149,8
SSTC_59	Relap	57,5	85,2	64,4	83,5	96,1	141,3	131,8	134,8
IPP_59	Relap-SSTC	68,2	83,0	68,7	80,8	107,3	140,9	137,3	133,6
Kiwa_59	Relap	64,5	73,9	71,9	73,7	107,4	124,0	136,9	124,1
JSI_130	Relap	66,4	78,1	73,8	75,4	101,2	123,6	137,6	125,3
WUT_59	Relap-JSI	61,4	78,9	72,9	75,3	97,1	123,5	141,7	124,4
WUT_130	Relap-JSI	65,6	77,8	72,9	75,0	101,8	123,2	141,7	124,9
PSI_59	TRACE	56,4	78,0	73,7	84,5	82,9	136,0	108,8	141,0
PSI_130	TRACE	60,8	78,4	73,7	84,5	96,6	132,2	108,8	141,0
Tec_59	TRACE-PSI	56,8	78,3	74,2	84,8	74,8	137,9	109,3	141,3

Table 5.4: Comparison of the conservative case to the base case and to 95%/95% lower limit and median values of max. all. RT_{NDT} calculated from the Wilks sets. For TCC, axial, point A.

	TH code	Tangent approach	WPS-max approach

Partner and number of TH data sets		Wilks 95%/95% [°C]	Wilks set median [°C]	CC [°C]	BC [°C]	Wilks 95%/95% [°C]	Wilks set median [°C]	CC [°C]	BC [°C]
UJV_59	Relap	66,0	86,0	65,4	70,9	79,9	146,9	145,9	151,0
UJV_93	Relap	68,6	86,9	65,4	70,9	109,3	146,7	145,9	151,0
BZN_93	Relap-UJV	69,7	86,4	64,6	70,7	104,8	146,6	145,6	150,4
JSI_130	Relap	66,4	78,1	73,2	73,8	101,2	123,6	106,0	137,6

From the tables above and given in Annex 7.2 of [4] the following conclusions may be drawn:

Ad (BC – 95%/95%) margin, for TCC and UCC, tangent approach: FRA-G obtained always negative value of this margin ranging from -37 to -4 K, which means conservative value of max. all. RT_{NDT} for BC. The other partners obtained either positive values of this margin (with exception of several cases, when the margin was of small negative value, not lower than -1,7 K), or undefined[11], or infinite. Undefined or infinite values were obtained in majority of cases for point C of axial or circumferential orientation of UCC.

Ad (BE – 95%/95%) margin, for TCC and UCC, tangent approach: All partners obtained either positive values of this margin (which means that BE is less conservative than 95%/95%, as expected), or undefined, or infinite.

For WPS-max approach, for TCC and UCC: All partners obtained either positive, or undefined, or (positive) infinite values for (BC – 95%/95%) and (BE – 95%/95%) margins, with the only exception of FRA-G in case of point C of axial and circumferential UCC for (BC – 95%/95%) margin, where negative values of -18 K and -31 K were obtained, respectively. Obtaining significant positive or even (positive) infinite values of (BC – 95%/95%) and/or (BE – 95%/95%) margins means that the values of max. all. RT_{NDT} for BC and BE are significantly less conservative than the 95%/95% value obtained from Wilks' analysis. The values of these margins for partners other than FRA-G vary in range from 3,5 to 83,7 K for the (BC – 95%/95%) margin, and from 16,3 to 117,1 K for the (BE – 95%/95%) margin.

For EC, both tangent and WPS-max approach: All partners obtained positive values of (BC – 95%/95%) and (BE – 95%/95%) margins with one exception of PSI (PSI_59) in case of axial crack, point 1, where the (BC – 95%/95%) margin was of negative value (-6,4 K).

Undefined or infinite values of (BC – 95%/95%) and (BE – 95%/95%) margins were obtained (in absolute majority of cases) for point C of axial or circumferential orientation of UCC. This finding witnesses in favour of the fact that the under-clad crack does not tend to initiate at point C (point near the base-clad interface) when $K_{IC}^{5\%}ASME$ fracture criterion is used.

In summary, it may be stated for all examined types of the cracks (TCC, UCC and EC) that the best-estimate (BE) transient was always less (or equally) conservative than the corresponding 95%/95% transient for both tangent and WPS-max approach. In some cases, the max. all. RT_{NDT} value was infinite for both the best-estimate transient and the 95%/95% transient, constituting no risk to the RPV integrity. This is an expected result.

The base-case (BC) transient was often similarly conservative as the 95%/95% transient for the tangent approach. Significant exceptions are results from TRACE, JSI-Relap (especially for UCC) and Kiwa-Relap,

[11] Undefined value of (BC-95%/95%) margin is obtained, if the values of max. all. RT_{NDT} for BC and 95%/95% are both infinite. Similar for the (BE-95%/95%) and (CC-95%/95%) margins.

and ATHLET (only for UCC), where the base-case transients are non-conservative in comparison with the 95%/95% transient even for the tangent approach. However, for the WPS-max approach, the base-case transients were often non-conservative in comparison with the 95%/95% transient. This may be attributed to the fact that the base-case transient was, most likely, constructed to be conservative with respect to the tangent approach, not with respect to the WPS-max approach.

Values of (CC – 95%/95%) margin were determined by several partners (UJV, JSI and BZN). From Table 5.4 it is seen that for tangent approach, UJV and BZN obtained either negative values of this margin, or small positive values (not higher than 1,4 K), or negative infinite or undefined values (in case of point C of circumferential UCC), which means (in most cases) conservative values of max. all. RT_{NDT} for CC. JSI obtained small positive values of this margin for both TCC and UCC, i.e., moderately non-conservative values of max. all. RT_{NDT} for CC. For WPS-max approach, there is quite large scatter in values of this margin among the partners, whereby in many cases large positive margins were obtained (mainly for TCC). This implies quite large non-conservativeness of max. all. RT_{NDT} values of CC for WPS-max approach. This result is due to the fact that the TH input parameters for the conservative transient (CC) were selected conservatively according to the criteria relevant for the tangent approach, not for the WPS-max approach.

It may be stated in general that it is very difficult or even impossible to find a set of TH input parameters that would constitute a conservative transient according to the WPS-max approach, based only on engineering judgement and not on sensitivity studies or Wilks' analysis.

Thus, it may be recommended that the if the WPS approach is used, it must be used with great care and should be combined with Wilks analysis (or similar sensitivity analysis), since otherwise there is a risk of selecting a transient which would lead to a non-conservative value of max. all. RT_{NDT}.

A detailed examination of the tables given in Annex 7.2 of [4] shows some additional conclusions:

The consistency in results obtained (by each partner) between axial and circumferential crack was confirmed, for both TCC and UCC, and tangent and WPS-max approaches.

For points A and C of axial and circumferential orientations of TCC: For tangent approach, quite large portion of the partners obtained higher value for (BE-95%/95%) margin than for (BC-95%/95%) margin, which is an expected result, but for WPS-max approach, they obtained the opposite result (lower value for (BE-95%/95%) margin than for (BC-95%/95%) margin). This concerns mainly partners UJV_59, UJV_93, WUT_59, WUT_130, JSI_130, IPP_59, and KIWA_59.

For point A of axial and circumferential orientations of UCC: Values of (BE-95%/95%) and (BC-95%/95%) margins exhibit quite large scatter among the individual partners, both for tangent approach and WPS-max approach, but the results for axial and circumferential crack for each partner are consistent. For point C of axial and circumferential orientations of UCC, the (BE-95%/95%) and (BC-95%/95%) margins are often infinite or undefined.

Summary from the above presented results found for (BC-95%/95%) and (BE-95%/95%) margins: Comparing the values of (BC-95%/95%) and (BE-95%/95%) margins, we see that for tangent approach the expected relation between these margins is confirmed (value of (BE-95%/95%) margin is higher than value of (BC-95%/95%) margin), but for WPS-max approach this relation is often violated (opposite relation is valid). This finding is relevant mainly for TCC. For UCC, there is large scatter in values of these margins, as mentioned above.

The results obtained from evaluation of (median – 95%/95%) margin are summarized in tables 7.245 – 7.245 given in Annex 7.2 of [4].

Evaluation of (median – 95%/95%) margins may be useful for characterization of the impact of the TH uncertainties on PTS analysis. The results of evaluation of (median – 95%/95%) margins may be presented as follows:

For TCC: Values of (median – 95%/95%) margin vary in range from 9,3 to 32 K for tangent approach and from 16,1 to 70,5 K for WPS-max approach (no value is infinite).

For UCC: For point A, tangent approach, finite values of the (median – 95%/95%) margin vary in range from 15 to 31,5 K, but 2 values were found infinite (GRS, ATHLET, median value for both axial and circumferential crack). For point A, WPS-max approach, finite values of this margin vary in range from 16,3 to 58,3 K, but 2 values were found infinite (GRS, ATHLET, median value for both axial and circumferential crack). For point C, for both tangent and WPS-max approach, values of this margin are often infinite, since the value of median is infinite, or they are undefined, since both the 95%/95% value and the median value are infinite. Results obtained for point C are associated with the fact that the under-clad crack does not tend to initiate at point C.

5.2.4 Comparison of the behaviour of the tangent and WPS-max approach

To demonstrate the different behaviour of the tangent and WPS-max approach, the Relap-UJV-59 data set was selected together with the deepest point of axial TCC as an example.

The distribution of the max. all. RT_{NDT} values over the transients in the Wilks set for the tangent and WPS-max approach is shown in Figure 5.35 and Figure 5.36, respectively. Different colours of the K_I-T curves in these figures correspond to the different values of max. all. RT_{NDT} shown on the scale on the right-hand side of the figures.

The figures show the transient with the lowest max. all. RT_{NDT} value highlighted by a black bold line. This transient coincides with the 95%/95% transient, since the Wilks set contains 59 transients. The lower bound fracture toughness curve (K_{Ic} curve according to the ASME approach) that corresponds to the lowest value of max. all. RT_{NDT} in the Wilks set is also shown in the figures. It is indicated by a black dashed line. For the tangent approach, the K_{Ic} curve is tangent to the whole bunch of the K_I-T curves.

It is seen from the figures that the distribution of the max. all. RT_{NDT} values over the transients in the Wilks set differs substantially between the tangent approach and WPS-max approach. The transient with the lowest value of max. all. RT_{NDT} is also different for the tangent approach than for the WPS-max approach.

For the tangent approach, the worst transients in the Wilks set (indicated by black and red colours in Figure 5.35) are those that reach close to the K_{Ic} curve. A low final temperature and a high maximum SIF value are typical for most of these transients.

For the WPS-max approach, the worst transients (indicated by black and red colours in Figure 5.36) are those with relatively high global maximum of SIF that is located in the area of low temperatures. Their global maximum of SIF is found in the upper left part of the area covered by the K_I-T curves.

As was already stated above, the tangent approach is robust to small perturbations of the K_I-T curves. This means that a small perturbation in the K_I-T curve can lead only to a small change in the max. all. RT_{NDT} value. On the contrary, the WPS-max approach is unstable to small perturbations of the K_I-T curve. A very small perturbation of the K_I-T curve may significantly shift the position of the global maximum of SIF in the K_I-T diagram to a position of a different local maximum of SIF, which may lead to an abrupt, large change in the resulting max. all. RT_{NDT} value.

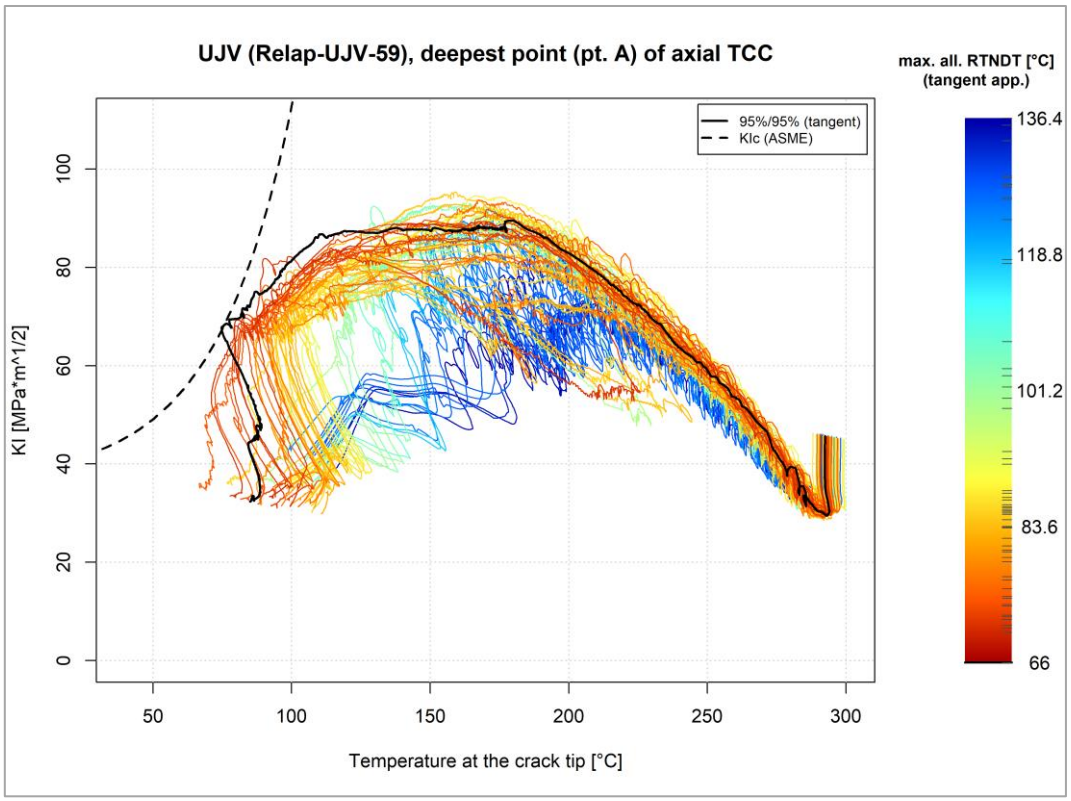

Figure 5.35: K_I vs. T curves resulting from UJV calculation for the Relap-UJV-59 dataset. The colours indicate values of max. all. RT_{NDT} according to the WPS-max approach. For pt. A of ax. TCC.

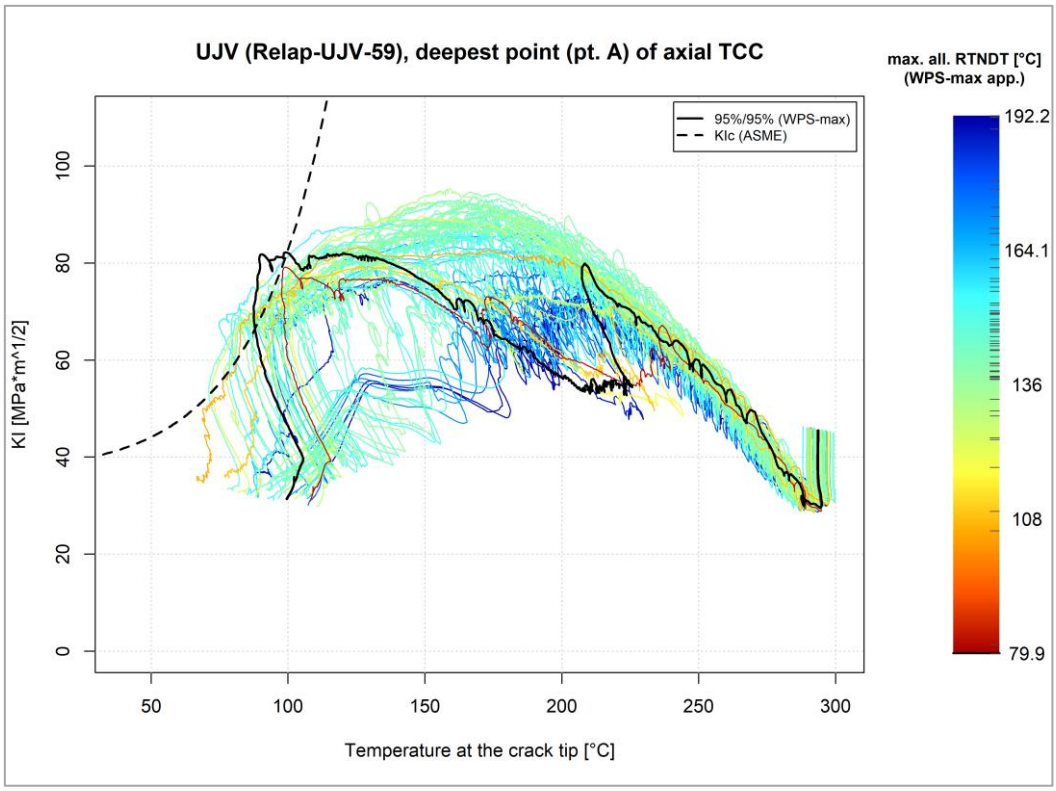

Figure 5.36: K_I vs. T curves resulting from UJV calculation for the Relap-UJV-59 dataset. The colours indicate values of max. all. RT_{NDT} according to the WPS-max approach. For pt. A of ax. TCC.

6 Conclusions

6.1 Conclusions from structural assessment

6.1.1 General Conclusions on structural assessment

The general conclusions on structural assessment are described in section 2.5.1 and can be summarized as follows:

- Use of TH data in case of 1D finite element simulations: 7 cases were chosen where the TH data were averaged or, in some cases, taken from an exact location, thus leading to 0D, 1D and 2D TH data. The agreement of resulting temperatures and stresses among partners was good. It was also concluded that the 2D TH data version (TH data from a given location e.g., at core weld under the cold plume) gives the most conservative results. Any averaging of TH data leads to non-conservative solution.
- In the case of the flange weld the effect of the geometry had to be checked as the position of this weld is close to the nozzle region with higher wall thickness. The results showed that in this case the 1D finite element simulations with 2D TH data do not deliver the correct results as compared to the 2D or 3D simulations, and they underestimate the stress fields.
- Several sensitivity cases were analysed:
    - The results of location investigations showed that the stress values depend highly on where the stress values are taken from. As expected, the out of plume position resulted in lower stress values, while the flange weld and nozzle corner positions generated higher stresses.
    - Beside the locations the thickness of the cladding, the mesh and the time step were also varied, which showed lower impact on the temperature and stress results.

6.1.2 Assessment of LTO improvements

The LTO improvements determined in WP2 were investigated with 1D and 3D finite element simulations. The structural assessment calculations were done for 9 LTO cases, 3 of them being operator actions (LTO6, LTO8 and LTO9).

Table 2.9 shows the evaluation of impact of LTO improvements on the temperature and stress field. It should be noted that the evaluation was made based on the results of the temperature and stress field at the crack tip location (16 mm from the wet surface). The results of the evaluation for the deterministic integrity assessment are presented here in chapter 6.3. It should be also noted that the evaluation of impact of LTO improvement is valid for the assessed PTS regime and can be different for different regimes.

Table 6.1: Evaluation of impact of LTO improvements on the temperature and stress fields

	LTO improvement	Temperature field	Stress field
LTO1	Heating of water in the HPIS tanks	Beneficial	Beneficial
LTO2	Heating of water in the ACCs	No impact	No impact
LTO3	Heating of water in the LPIS tanks	No impact	No impact
LTO4	Decreasing the HPSI head	Small impact	Small impact
LTO5	Decreasing the HPSI capacity	Beneficial	Beneficial
LTO6	Reduction of HPIS flow (operator action)	Unclear	Unclear
LTO7	Decreasing of ACC pressure	No or small impact	No or small impact
LTO8	Change of cooldown rate (operator action)	Unclear	Unclear
LTO9	Isolation of ACCs (operator action)	No impact	No impact

6.1.3 Structural Assessment for TH uncertainties

6.1.3.1 TH input data

TH input data for structural analyses was obtained from TH uncertainty analyses based on the Wilks method as described in Section 2.4.1. For the TH analyses, different TH codes were used such as RELAP5, ATHLET, TRACE and KWU-MIX (for mixing calculations) together with several tools for uncertainty evaluation, e.g. DAKOTA, SUSA, etc. TH uncertainty analyses were performed for 59, 93 and 130 Wilks data sets (transients).

The TH analysis results used as the TH input data for structural assessments are summarised for each partner in Table 2.8. A detailed review and comparison of the TH results from uncertainty analyses between different partners have been carried out in APAL Deliverable 2.3 [10]. However, it is worth to include a short summary of this comparison and point out some observed differences in the TH data as it has a direct bearing on some deviations in the calculated temperatures and stresses.

Figure 2.66 illustrates a comparison of fluid temperature as a function of time used by JSI, IPP and KIWA as the TH parameter used for the temperature and stress calculations. These partners have been chosen as they performed TH uncertainty analyses based on 59 Wilks data sets using RELAP5 in combination with the uncertainty evaluation software SUSA.

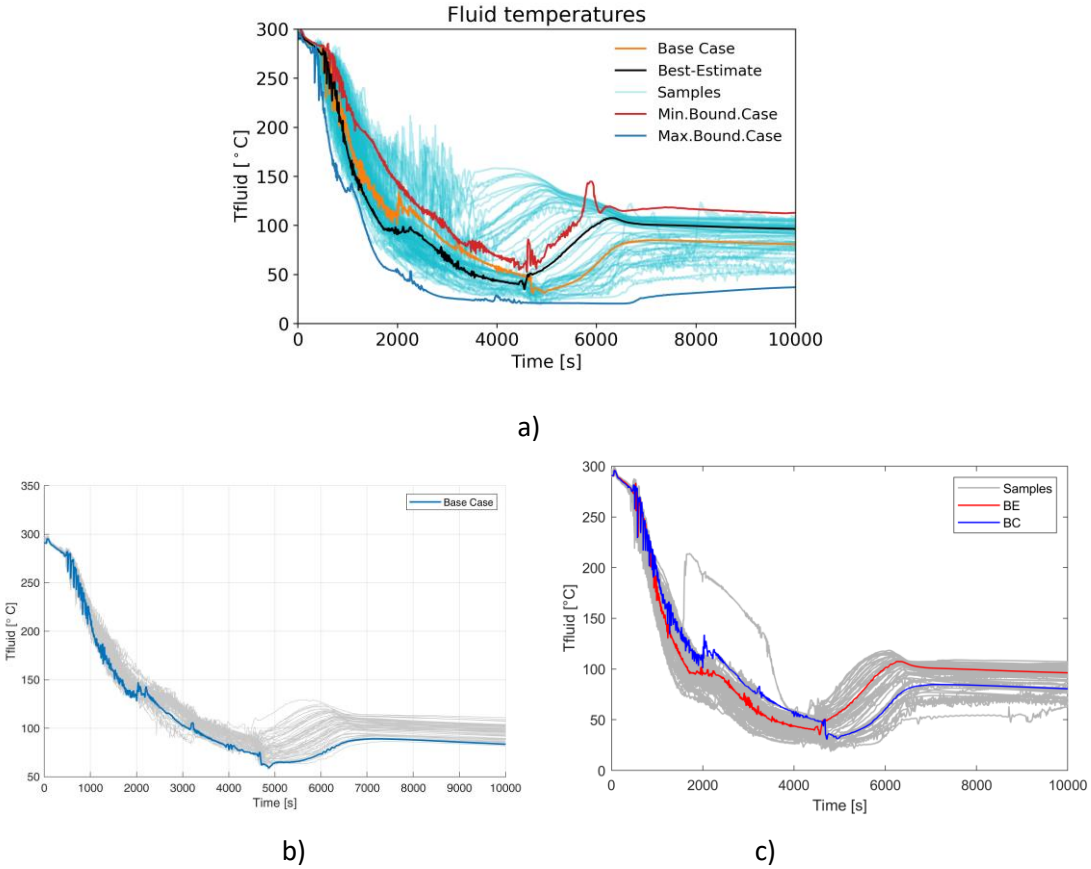

Figure 6.1: Comparison of fluid temperature as a function of time used for structural analyses by a) JSI, b) IPP and c) KIWA. Wilks 59 data samples.

Significant variations in Wilks results can be observed between JSI, IPP and KIWA. JSI results have much wider spread in the Wilks data samples in comparison to the IPP and KIWA data. One of the KIWA Wilks data samples demonstrates a clear deviation in the temperature trend when the fluid temperature increases in the time range between 1800 to 4000 s. Similar trend has also been observed in KIWA results from TH analyses for LTO improvements, namely LTO5 for high pressure injection flow (HPSI) reduction. KIWA performed the TH analyses by reducing HPSI flow from 100% down to 75% with 5%

increments. The characteristic rise of temperature, similar to the one in Figure 2.66, was observed in the results for HPSI reduction to 75%. For higher HPSI levels (80%-100%) the temperature rise in this time range was not observed or it was much lower and less pronounced.

The temperature rise for HPSI at 75% may be explained by the following considerations. By reducing the emergency coolant quantity (HPSI flow) pumped into the reactor primary system the void fraction (ratio of steam to total volume) increases substantially. The void fraction in volume 9101 for HPSI 75% at 1500-3000 s is much larger than that for HPSI 80% which would support this assumption (void fraction values in HPSI cases 100%-80% at around 1500-3000 sec do not change much actually). It means that there is substantially more gas phase in downcomer which causes deterioration of heat transfer at certain conditions. This in turn leads to higher temperature rise in downcomer as it was obtained in the calculations for 75%. There should be a threshold somewhere between 75% and 80% HPSI reduction levels when the emergency coolant inflow is so low that most of the coolant in the downcomer boils thereby deteriorating heat transfer.

Differences in fluid temperature can also be observed in the TH data for Wilks 93 data sets that have been calculated by FRA-G, UJV and WUT as shown in Figure 2.67.

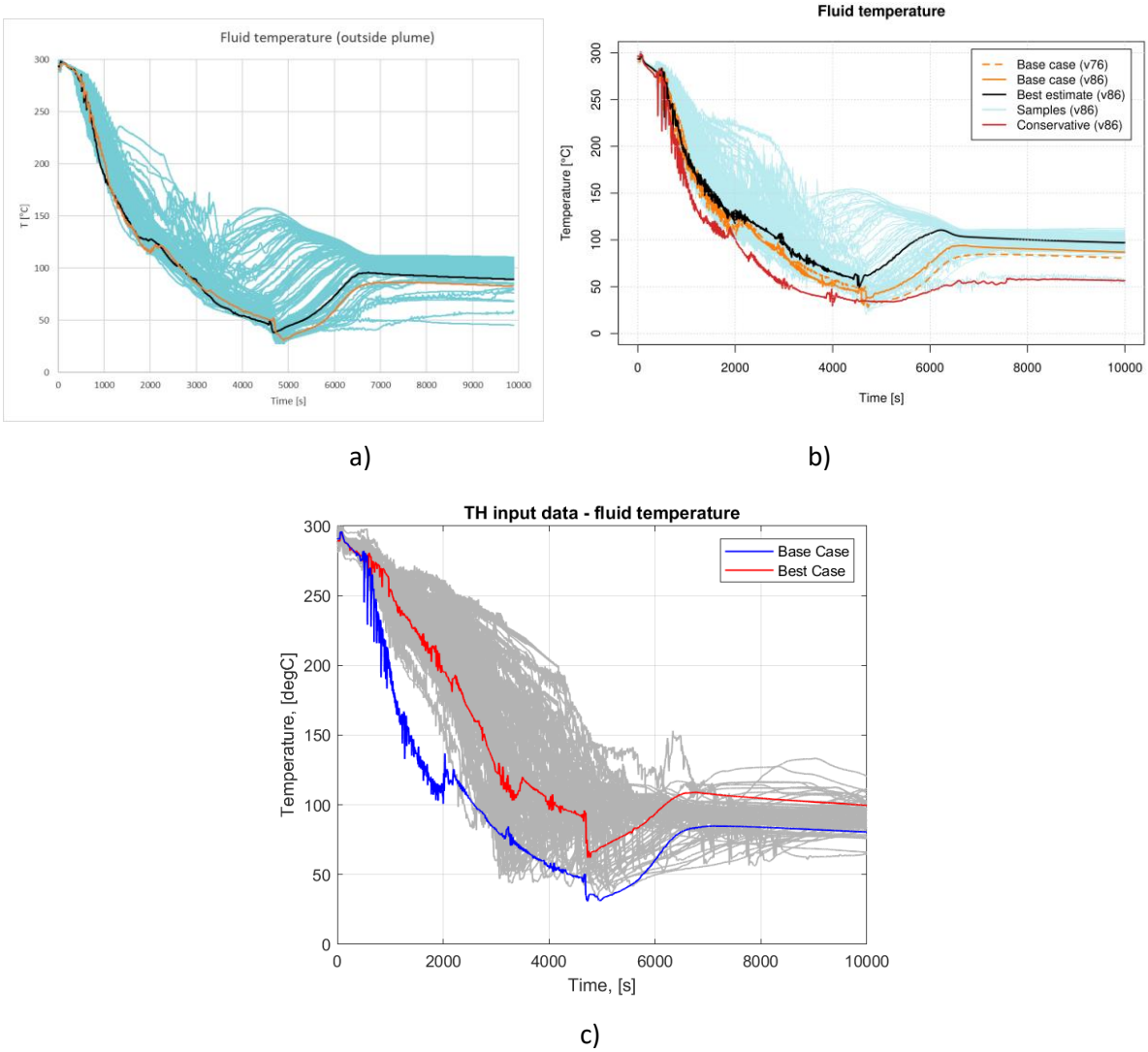

Figure 6.2: Comparison of fluid temperature as a function of time used for structural analyses by a) FRA-G, b) UJV and c) WUT. Wilks 93 data samples.

6.1.3.2 Structural results

It is somewhat cumbersome to make comparative plots containing results from all or several partners due to large amount of data curves. Therefore, only some qualitative comparisons and observed deviations in the structural results are provided herein.

Temperature at the RPV inner surface for the Best Estimate case analysed by PSI (TH code TRACE) exhibits a local peak with temperature increase at about 2600 s. This temperature peak results in local abrupt decrease in calculated stresses at the inner surface. Thus, hoop stresses exhibit a decrease by about 200 MPa as shown in Figure 2.68. Similar trends for the Best Estimate case can also be found in the results from TECNATOM who used the TH data from PSI for the structural analyses.

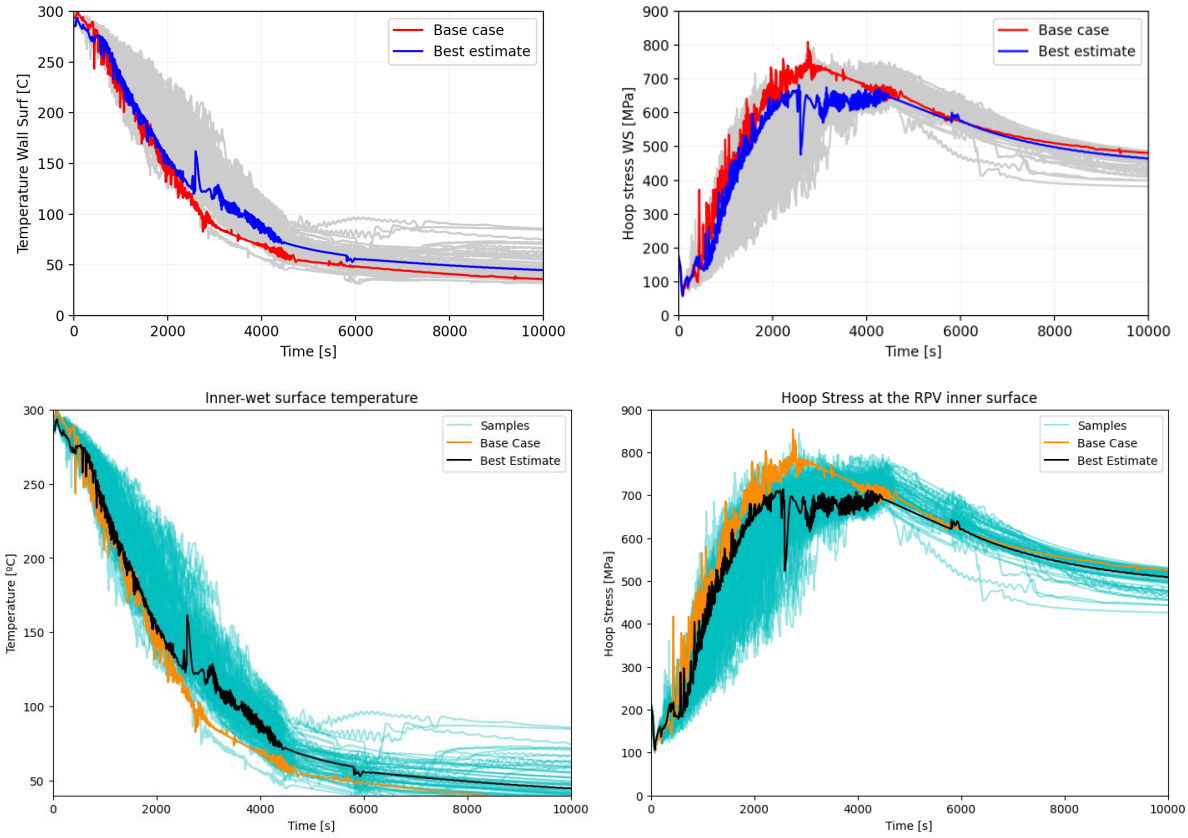

Figure 6.3: RPV inner-surface temperature and hoop stresses at the inner surface as a function of time. PSI (top) vs Tecnatom (bottom) results for Wilks 59 data samples.

In previous Section 5.1 it was described that one of the KIWA Wilks TH data samples demonstrated a clear deviation in the temperature trend when the fluid temperature increased in the time range between 1800 to 4000 s, see Figure 2.66(c). This deviation in the TH data affects also the structural results leading to decrease of calculated stresses in the given time range. An example of this behaviour is presented in Figure 2.69. The trend is observed in all plots from KIWA provided in Section 4.2.5. An explanation to this Wilks TH data sample behaviour is given in Section 3.6.8.

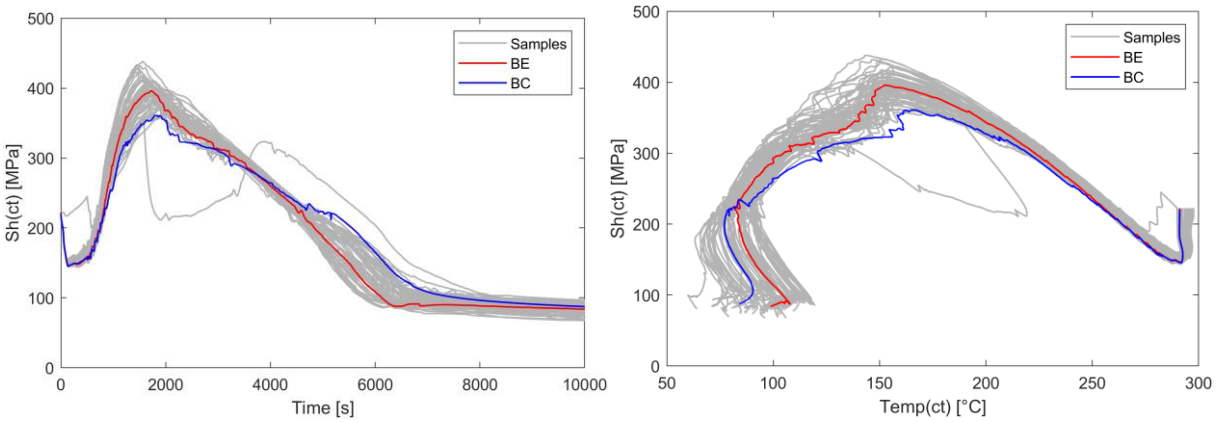

Figure 6.4: Hoop stresses at the crack tip location as a function of time and as a function of crack tip temperature. KIWA results for Wilks 59 data samples.

6.2 Conclusions from first benchmark performance

Within task 3.3 of the APAL project extensive calculations for the PTS analysis were performed by each partner. This includes SIF calculation, max. all. ART calculation, and crack arrest calculation. In this deliverable the results of each partner were compared and discussed.

Within part 1 of the benchmark a common understanding of the whole assessment could be established (see chapter 4.1) by producing results using all the same input data. This first assessment was helpful to identify critical steps within the defined benchmark. A summary of the insights concerning the SIF calculation (part 1.1) is given in chapter 4.1.5:

- Observed uncertainties/scatter of results
- "Oscillations" in the beginning of the transient
- Corrected plastic correction for SIF calculation for UCC
- Correct use of crack face pressure for SIF calculation for TCC

For the max. all. ART calculation (part 1.2) there were no issues to discuss between the partners.

Once the results of part 1 were harmonized between all partners, the influence of different locations, TH data, structural analysis, K_I solutions, and some other parameters was assessed in part 2 of the benchmark. The variation of these methods/data can have a considerable influence on the obtained K_I results (part 2.1). The observations and insights regarding these aspects are given in chapter 4.2.2:

- The FAVOR calculation of K_I leads to a lower K_I of up to 20 MPa√m compared to the CEA method. A part of that difference is probably caused by the required interpolation of crack depth/crack length ratios in FAVOR.
- The consideration of TH mixing is less relevant in the locations outside of plume. For the inside plume locations TH mixing can play an influential role, the difference is large for circumferential crack and not so large for the axial crack.

The corresponding results for max. allow. ART in general reflect the differences in K_I. However, the magnitude of the difference in K_I is highly dependent on the location, crack orientation, and transient considered. A summary of the part 2.2 observations and insights is given in chapter 4.3.5:

- The results for the benchmark part 2.2 confirm the conclusions of part 2.1, i.e., that the choice of TH code, K_I formula and consideration of TH mixing can have a considerable influence on the max. allow. ART results.
- The tangent approach gives the smallest results for max. allow. ART, whereas the simple WPS-max gives higher results. The results for the sophisticated WPS approaches are either in agreement with the tangent or simple WPS-max approach; or lie in between for the investigated transient.

6.3 Conclusions for chapter "Safety margins related to LTO improvements"

A SB LOCA PTS scenario with 50 cm^2 break in hot leg and with loss of offsite power was investigated for a 4-loop KWU-1300 PWR of German Konvoi design. A base case scenario and 9 LTO improvements were analysed in the former stages of the APAL project by different partners using system thermal TH codes RELAP, ATHLET (GRS) and TRACE (PSI). Mixing analyses were performed by FRA-G using the KWU MIX code and by GRS using ECC MIX. LTO improvements No. 1 – 5 and 7 are plant improvements, while LTO improvements No. 6, 8 and 9 are operator actions.

The main conclusions drawn are as follows:

Effect of LTO improvements on max. all. ART for tangent approach: For TCC, the LTO improvements No. 1, 6 and 8 were found as most influential, producing significant positive margins and generating thus benefits in max. all. ART. For UCC, the LTO improvements No. 1, 5, 6 and 8 were found as most influential, producing significant positive margins in max. all. ART. For EC, the LTO improvements No. 1 and 8 were found as beneficial, producing significant positive margins. The embedded cracks were not assessed for LTO 3, 6 and 9.

Effect of LTO improvements on max. all. ART for WPS-max approach: For all examined types of cracks (TCC, UCC, and EC) either a large scatter in values of LTO margin was observed, or the LTO margins are close to zero (positive or negative), or the margins have large negative values. Therefore, it may be concluded that no LTO improvement has significant positive (beneficial) effect on max. all. ART if WPS-max approach is applied.

The summary of all LTO improvements and their impact on max. all. RT_{NDT} is given in ***Table 6.2***. The impact was evaluated based on the scatter plots presented in Figure *5.4* – Figure *5.19*. It should be noted that the evaluation of impact of LTO improvement is valid for the assessed PTS regime (SB LOCA) and can be different for different regimes.

General conclusion drawn for UCC: The obtained K_I values are in general lower than those obtained for TCC. Further, for UCC, most of the margins for point C were obtained undefined or infinite; this result is consequence of the shape of the postulated underclad crack which is of low a/c ratio (a/c=1/3), and therefore the crack does not tend to initiate at point C.

Note concerning LTO improvements No. 4 and 5: For WPS-max approach, the LTO 4 and LTO 5 margins often reached large negative values, mainly for TCC and partly also for UCC. This is associated with the fact that the maxima of the K_I vs. T curves for both LTO 4 and LTO 5 are shifted to lower temperatures compared to the corresponding K_I vs. T curves for base cases. This in turn is consequence of the conditions in TH analyses for both transients, since both transients (LTO 4 and LTO 5) have a common feature that there is a later HPI injection and decreased rate of cooling in the RPV in the early stages of the transient (up to about 2000 s), but in period from 2000 to 3000 s, a significant increase of the rate of cooling occurs (after the ACCs start injecting). Thus, it can be summarized that LTO improvements No. 4 and 5 have no effect on max. all. ART for tangent approach, but for WPS-max approach they have (in most cases) a large negative effect.

General conclusion regarding WPS-max approach (for both TCC and UCC): The large scatter in margins found for some of the LTOs (mainly for LTO 1, LTO 3, LTO 4, LTO 5 and to a lesser extent also LTO 2) witnesses in favour of the fact that the WPS-max approach is very sensitive to the shape of K_I vs. T curve which in turn is very sensitive to both the TH code used and the transient parameters selected, and also very sensitive to the point for which the K_I vs. T curve is constructed (point A or point C). Consequently, the max. all. ART calculated based on WPS-max approach is not a stable quantity with respect to various aspects associated with both TH analysis and structural and fracture-mechanics analyses. Among other, WPS-max approach is also sensitive to the time step used in the structural and fracture-mechanics analyses. For these reasons, the WPS-max approach cannot be recommended for

application in PTS analysis, if a standard evaluation for one transient (with input TH parameters selected based on expert judgement) is performed. Nevertheless, WPS-max approach may be applicable in combination with analysis of the full Wilks data set.

Effect of LTO improvements on max. all. RT_{NDT} for "other locations": The results for other locations than core weld IP/IMP were not discussed in this report, but they are discussed in Chap. 3.6.1 of [4] in more detail. For TCC, for core weld OP, core weld IP, and flange weld IP locations, LTO 1 and LTO 8 have significant positive effect on values of max. all. RT_{NDT} (for tangent approach), while LTO 6 has only moderate positive effect on max. all. RT_{NDT} for these locations. For flange weld OP location, only LTO 1 and 8 have significant positive effect on max. all. RT_{NDT}. For nozzle IP location, only LTO 1 has significant positive effect on max. all. RT_{NDT}.

For UCC, the conclusions concerning LTO effect are qualitatively similar as those for TCC, with some exceptions of core weld OP or flange weld OP locations, where margins in point C are often undefined (i.e., values of max. all. RT_{NDT} are infinite for both LTO and BC). This corresponds to the fact that underclad crack postulated in these locations does not tend to initiate at point C.

Mutual comparison of individual "other locations" from point of view of max. all. RT_{NDT} values: Nozzle IP location is typically not a critical location, although its max. all. RT_{NDT} values are the lowest ones, since RPV nozzles are only marginally irradiated components, and therefore their (material) RT_{NDT} values are typically significantly lower than that the RT_{NDT} values of the core weld. However, in PTS evaluations, it is recommended to assess all locations examined in the report [4] (core weld, flange weld and nozzle) regarding their resistance against fast (brittle) fracture.

Effect of LTO improvements evaluated based on $\mathbf{K_{IC}^{mean}}$ASME curve: Evaluation based on $\mathrm{K_{IC}^{mean}}$ASME curve showed (see Chap. 3.6.2.1 of [4]) that of the examined LTO 1, 4, 5, and 7, only LTO 1 has significant positive effect on max. all. RT_{NDT}. This is the same conclusion as for evaluation based on $\mathrm{K_{IC}^{5\%}}$ASME curve, performed for LTO 1, 4, 5 and 7, and this conclusion is valid both for tangent and WPS-max approaches. Values of max. all. RT_{NDT} calculated based on $\mathrm{K_{IC}^{mean}}$ASME curve are significantly higher than those calculated based on $\mathrm{K_{IC}^{5\%}}$ASME curve. For both tangent and WPS-max approach, the margin values obtained based on $\mathrm{K_{IC}^{mean}}$ASME curve do not differ substantially from those obtained based on $\mathrm{K_{IC}^{5\%}}$ASME curve. For WPS-max approach, LTO 4 and 7 have a non-negligible negative effect on max. all. RT_{NDT}; this statement is valid both for evaluation based on $\mathrm{K_{IC}^{mean}}$ASME curve and that one based on $\mathrm{K_{IC}^{5\%}}$ASME curve.

Effect of LTO improvements evaluated based on $K_{IC}^{5\%}MC$ curve: Fracture-mechanics assessment of the LTO margin based on $K_{IC}^{5\%}MC$ curve was performed (see Chap. 3.6.2.2 of [4]) without size correction. This led to max. all. T_0 values of similar magnitude as the corresponding max. all. RT_{NDT} values (in most cases). Only in the case of the corner point (point C) of UCC, the max. all. T_0 values were generally lower than their corresponding max. all. RT_{NDT} values. This is caused by a different level of the lower shelf fracture toughness between the lower bound curve equation in ASME approach and that one in T_0 Master Curve approach.

When examining the effects of different LTO improvements on max all. ART, some additional conclusions were drawn.

Table 6.2: Evaluation of impact of LTO improvements based on results presented in Chapter 5.1, core weld location (IP, IMP)

	LTO improvement	Simulated change	Tangent approach	WPS-max approach
LTO1	Heating of water in the HPSI tanks	Heated from 15 °C to 45 °C	Beneficial	Large scatter (beneficial for EC)

LTO2	Heating of water in the ACCs	Heated from 20 °C to 50 °C	No impact	Large scatter
LTO3	Heating of water in the LPSI tanks	Heated from 15 °C to 45 °C	No impact	No impact
LTO4	Decreasing the HPI head	Decreased down to 75%	No impact	Detrimental, large scatter
LTO5	Decreasing the HPI capacity	Decreased down to 75 %	No impact (beneficial for UCC)	Detrimental, large scatter
LTO6	Reduction of HPSI flow (operator action)	Reduced at 1800 s to one pump	Beneficial	No impact
LTO7	Decreasing of ACC pressure	Decreased from 26 bar to 20 bar	No impact	No impact
LTO8	Change of cool down rate (operator action)	Changed from 100 K/h to 200 K/h	Beneficial	No impact
LTO9	Isolation of ACCs (operator action)	ACC isolated at 500 s	No impact	No impact

These additional conclusions are summarized under the following points:

Ad results based on KWU-MIX, for both TCC and UCC: K_I values calculated based on KWU-MIX are in general higher than those generated based on TH system codes. The reason for this is a more pronounced cold plume effect in TH results from KWU-MIX than in the TH results from system TH codes (e.g., RELAP), in particular, lower temperature in the cold plume, higher difference in temperature between the cold plume and ambient and lower final temperature in the results from KWU-MIX. The more pronounced cold plume effect in mixing calculations is in general caused by modelling of TH phenomena in the mixing codes that are not modelled or not properly modelled in the system TH codes, especially the thermal stratification in the cold leg and merging of the cold plumes.

As a consequence of the higher K_I values and lower temperatures at the postulated crack position, the values of max. all. ART obtained using KWU-MIX are lower than those obtained using system TH codes (RELAP or TRACE). Nevertheless, in most cases, this fact has no or small effect on values of LTO margin.

Ad results based on ECC-MIX, for TCC: K_I values generated based on ECC-MIX are significantly lower than those based on KWU-MIX (even when the same RS profile and SIF formulae are considered in both calculations), in consequence of which values of max. all. ART based on ECC-MIX are significantly higher than those based on KWU-MIX, but this fact has only small impact on LTO margin values for tangent approach.

Ad results based on RELAP, for TCC: There is a very good mutual accordance in K_I vs. T curves between the partners using RELAP TH code. Whether APAL RS or FAVOR RS are used in the SA does not play a significant role in determination of K_I values.

Ad results based on RELAP, for UCC: There is also a very good mutual accordance in K_I vs. T curves between the partners using RELAP TH code, but in dependence on type of RS used in SA: The very good accordance is reached only if the same type of RS is used in SA (either APAL RS or FAVOR RS). Using APAL RS in SA leads to higher K_I values than using FAVOR RS in SA (the difference is not large but is clearly seen).

Ad results based on TRACE, for both TCC and UCC: K_I values generated based on TRACE are lower (mainly for the beginning and middle parts of the transient, but not for the late phase of the transient) than those generated based on RELAP. This is due to the fact that K_I values were calculated using formulae from FAVOR, which give incorrect (too low) K_I values for TCC of the given dimensions. This fact usually had no effect on values of LTO margins for tangent approach, while for WPS-max approach the impact may be larger.

Ad effect of performing 3d calculation vs. 1d calculation: For TCC, the effect of performing 3d calculation vs. 1d calculation on K_I values is small, especially for calculations based on system TH codes. For inputs from mixing TH calculations (KWU-MIX), the results from 3d structural calculations include the cold plume effect (different temperatures in the cold plumes and ambient are modelled in 3D SA, whereas the temperatures from the cold plume are imposed on the whole wet surface in 1D SA), which may potentially be significant for some TH transients. However, this effect was rather small for the analysed SB LOCA scenario (1D SA and 3D SA provide similar but not the same results for the KWU-MIX input data). For UCC, the difference in K_I values between 3d and 1d structural calculations is also not large.

Ad effect of RS: For TCC, the difference in K_I values due to APAL and FAVOR RS profiles is small. For UCC, the difference is larger than in the case of TCC, and due to the non-linearity caused by the plastic correction, the effect of RS on K_I values may slightly depend on time and on the analysed transient.

The calculations based on ATHLET and some 3d calculations were performed without residual stress due to weld, only residual stresses due to stress-free temperature were included. In these calculations, the SIF values are smaller and the max. all. ART values are higher than in the corresponding calculations involving RS. (The APAL RS produces SIF of about 8,7 MPaVm at the deepest point of axial TCC and 4,2 MPaVm at the corner point of axial TCC.) In general, the effect of RS on the resulting margins values was, however, small.

Open issues: Evaluation of the effect of LTO improvements on max. all. T_0 was performed without size correction by most partners, based on recommendation presented in D3.2 [2]. It is a question how the results of evaluation of this effect would change if the size correction were performed.

Outliers: For tangent approach, practically no outliers in LTO margins were found and, moreover, the scatter in values of LTO margin is low. For WPS-max approach, the scatter in values of LTO margin is significantly higher than that one for tangent approach, which is associated with the unstable character of WPS-max approach that is very sensitive to the shape of K_I vs. temperature curve. The scatter found for WPS-max approach is especially large for LTO 4 and LTO 5, and in some cases also for LTO 1 and LTO 2 (results based on TRACE), but in all these cases this result may be explained by the specific shape of K_I vs. temperature curve for these LTOs, where there are fluctuations in these curves near the points of their maxima. Thus, it may be summarized that in fact there are no real outliers in values of LTO margins even for WPS-max approach.

Known discrepancies:

It is known that UJV used incorrect (obsolete) version of TH inputs for LTO 3. The impact of this error on max. all. RT_{NDT} and margin values was, however, small.

Some TH transients for the LTO improvements were produced only up to 5000 s instead of 10000 s by some partners. This might potentially have some impact on the resulting max. all. RT_{NDT} and margin values. This impact is, however, supposed to be small (insignificant).

6.4 Conclusions for chapter “Safety margins related to TH uncertainties”

SB LOCA with 50 cm^2 break in HL with loss of offsite power was investigated for a 4-loop KWU-1300 PWR of German Konvoi design.

The SB LOCA scenario was analysed in the former stages of the APAL project by several partners using system thermal hydraulic codes RELAP, ATHLET and TRACE. Mixing analyses were performed by FRA-G using the KWU-MIX code and by GRS using ECC-MIX (as a submodule of ATHLET).

Statistical data sets of TH transients were generated by several partners using several TH codes, with randomly sampled input TH parameters. These data sets were used in Task 3.5 to calculate a conservative lower limit value of the max. all. RT_{NDT} that covers 95% of the population of TH transients with 95% confidence (denoted as 95%/95% lower limit value) following the principles of the Wilks' non-parametric statistical method. Moreover, other important thermal-hydraulic transients were generated by the partners: base case, best-estimate and conservative TH transients. The conservative transient was analysed only by UJV, JSI and BZN as a non-mandatory task.

For the given TH transients, structural calculations using 1D FEM were performed in Tasks 3.1 and 4.1 for the core weld in plume (or in merging plumes for KWU-MIX) location. Subsequently, within Task 3.5, the fracture-mechanics analyses were performed, the values of max. all. RT_{NDT} were calculated and the 95%/95% lower limit values of max. all. RT_{NDT} were determined. Moreover, they were compared to the max. all. RT_{NDT} values for the corresponding deterministic base case, best-estimate, and conservative transients.

The following conclusions were drawn from comparison of 95%/95% lower limit values of max. all. RT_{NDT} with max. all. RT_{NDT} values for BC, BE and CC:

In summary, it may be stated for all types of cracks (TCC, UCC and EC) that the best-estimate (BE) transient was always less (or equally) conservative than the corresponding 95%/95% transient for both tangent and WPS-max approach. This is an expected result.

The base case (BC) transient was often similarly conservative as the 95%/95% transient for the tangent approach. Significant exceptions are results from TRACE, JSI-Relap, Kiwa-Relap, and ATHLET (only for UCC), where the base-case transients are non-conservative in comparison with the 95%/95% transient even for the tangent approach. However, for the WPS-max approach, the base-case transients were often non-conservative in comparison with the 95%/95% transient. This may be attributed to the fact that the base-case transient was, most likely, constructed to be conservative with respect to the tangent approach, not with respect to the WPS-max approach.

The conservative case (CC) transient was analysed only by UJV, JSI and BZN. This transient is similarly or more conservative than the corresponding 95%/95% transient for the tangent approach. However, it may be largely non-conservative (in comparison with the corresponding 95%/95% transient) with respect to the WPS-max approach. This result is due to the fact that the TH input parameters for the conservative transients were selected conservatively according to the criteria relevant for the tangent approach, not for the WPS-max approach.

General conclusion concerning WPS-max approach: It follows from evaluation of (BC-95%/95%) and (CC-95%/95%) margins that there is a large scatter in values of these margins for WPS-max approach. In most cases, the 95%/95% transient is much more conservative than the BC and CC transients for the WPS-max approach. It may be stated that it is in general very difficult or even impossible to find a set of TH input parameters based only on the engineering judgement that would constitute a transient conservative according to the WPS-max approach. Several sensitivity calculations of max. all. ART may be needed to find an adequate set of conservative TH input parameters. Thus, it may be recommended that the if the WPS approach is used, it must be used with great care and should be combined with Wilks' analysis. If Wilks' analysis (or other similar sensitivity analysis) is not used, there is a risk of selecting a transient which would lead to a non-conservative value of max. all. RT_{NDT}.

Open issues: As open issue may be considered the fact that there are quite large differences in results of TH calculations performed by RELAP, which leads to different distributions of both the K_I vs. temperature curves and values of max. all. RT_{NDT}. Nevertheless, the 95%/95% lower limit values are similar. The reasons for this fact have not been clarified.

Outliers: As outliers may be considered values of max. all. RT_{NDT} obtained by GRS from the Wilks' method (among other, 95%/95% lower limit values) for under-clad cracks, deepest point of the crack front (point A), for both tangent and WPS-max approaches, as well as for the conservative WPS approach. This result may possibly be associated with using an approximate estimation scheme for the plastic correction in the fracture model for UCC in PROST (version 2023).

7 References

[1] Bernadett Pusztai-Spisák, et. al.
"Stress and temperature distributions for benchmark performance"
APAL Deliverable No. 3.1, 31.05.2024

[2] Sébastien Blasset, et. al.
"Benchmark definition"
APAL Deliverable No. 3.2, 02.09.2022

[3] Katharina Angermeier, et. al.
"First Benchmark Performance"
APAL Deliverable No. 3.3, 19.12.2023

[4] Miroslav Pošta, et. al.
"Safety margin related to LTO improvements and TH uncertainties"
APAL Deliverable No. 3.4, 28.06.2024

[5] Andrey Shipsha, et. al.
"WP4 Public Summary report"
APAL Deliverable No. 4.7, 06.09.2024

[6] Pistora Vladislav, et. al.
"State-of-the-art for weld residual stress"
APAL Deliverable No. 1.1, 31.03.2021

[7] Cueto-Felgueros, et. al.
"State-of-the-art for warm pre-stress"
APAL Deliverable No. 1.2, 19.04.2021

[8] Cueto-Felgueros, et. al.
"Public summary report of WP1"
APAL Deliverbale No. 1.6, 20.12.2021

[9] Puustinen Markku, et. al.
"Results of TH Analysis for Selected LTO Improvements"
APAL Deliverable No. 2.1, 19.04.2022

[10] Kral Pavel, et. al.
"Results of TH Analysis Related to TH Uncertainties"
APAL Deliverable No. 2.3, 15.12.2022

[11] Kral Pavel, et. al.
"Public Summary Report of WP2"
APAL Deliverable No. 2.4, 31.03.2023

[12] M.Niffenegger, K.Reichlin "The proper use of thermal expansion coefficient in finite element calculation" Laboratory of nuclear material Paul Scherrer Institute
Nuclear Engineering and Design 243 (2012) 356– 359

[13] Case N-830-1 "Direct Use of Fracture Toughness for Flaw Evaluations of Pressure Boundary Materials in Class 1 Ferritic Steel Components" Section XI, Division 1, Draft 2021

[14] DEFI-PROSAFE D6.9.1 "Approach adopted for safety margin evaluation based on probabilistic" V4/270816

[15] P.T. Williams, T.L. Dickson, B.R. Bass, and H.B. Klasky, Fracture Analysis of Vessels – Oak Ridge, FAVOR, v16.1, Computer Code: Theory and Implementation of Algorithms, Methods, and Correlations, ORNL/LTR-2016/309 (Adams Access No. ML16273A033), Oak Ridge National Laboratory, Oak Ridge, TN (USA), September 2016.

[16] T.L. Dickson, P.T. Williams, B.R. Bass, and H.B. Klasky, *Fracture Analysis of Vessels – Oak Ridge – FAVOR, v16.1, Computer Code: User's Guide,* ORNL/TM-2016/310, Oak Ridge National Laboratory, Oak Ridge, TN (USA), August 2016

[17] Marie S., Chapuliot S., "Improvement of the calculation of the stress intensity factors for underclad and through-clad defects in a reactor pressure vessel subjected to a pressurised thermal shock" International Journal of Pressure Vessels and Piping 85 / 517-531, 2008

[18] Marie S, Ménager Y, Chapuliot S. Stress intensity factors for underclad and through clad defects in a reactor pressured vessel submitted to a pressurized thermal shock. Int J Press Vessels Piping 2005;82:746–60

[19] S. Marie, M. Nédelec., "A new plastic correction for the stress intensity factor of an under-clad defect in a PWR vessel subjected to a pressurised thermal shock."International Journal of Pressure Vessels and Piping, Elsevier, 2007, 84 (3), pp.159-170. ff10.1016/j.ijpvp.2006.09.019ff. ffcea-02355784f https://hal-cea.archives-ouvertes.fr/cea-02355784/document

[20] Pressurized Thermal Shock in Nuclear Power Plants: Good Practices for Assessment, IAEA TECDOC No. 1627

[21] Dillström P.: PROSIR – Final Report, Report No.: 2016-500778, Inspecta Research Report, 2016

[22] E.Keim, G.Bartholomé "Analysis of Crack Growth of a Crack in the HDR-Nozzle Loaded by Thermal Shocks" SMIRT8 – 1985

[23] Safety Standards of the Nuclear Safety Standards Commission (KTA) "Components of the Reactor Coolant Pressure Boundary of Light Water Reactors Part 2: Design and Analysis" KTA 3201.2 (2017-11)

[24] Genshichiro Katsumata, Valéry Lacroix, Yinsheng Li "Effect of interaction of embedded crack and free surface on remaining fatigue life" 2016, AIMS Materials Science, 3(4): 1748-1758. DOI: 10.3934/matersci.2016.4.1748

[25] S.Chapuliot "Stress intensity factor calculation in sharp and beveled edge nozzle corners" InternationalJournalofPressureVesselsandPiping141(2016)11-18

[26] CAPAL (FAVOR version adapted for APAL project): https://indico.psi.ch/event/15518/

8 Annexes

8.1 Stress and temperature plots from 3D FE with input from RELAP in combination with mixing code (KWU-MIX) – base case transient

The analyses of the temperature fields in the RPV wall which are precursors of the stress analyses are based on the input data coming from KWU-MIX analyses. Temperatures of the fluid layer which is in contact with the RPV wall and related heat transfer coefficients are applied as time and location dependent properties on the inner surface of the RPV. The outer surface of the RPV is assumed to be adiabatic.

In the structural analysis the loads defined on the FE model of the RPV incorporate the internal pressure of the coolant as well as pressure related internal forces caused by components connected to the RPV which are not explicitly modelled in the FE model, namely the main coolant lines. These forces are modelled by applying tensile stresses to the nozzles cross sections. The sealing surface of the RPV is fixed in axial direction; all nodes on the symmetry plane are constrained in x-direction. In order to prevent the movement of the FE model in y-direction one node on the symmetry plane is also constrained in y-direction.

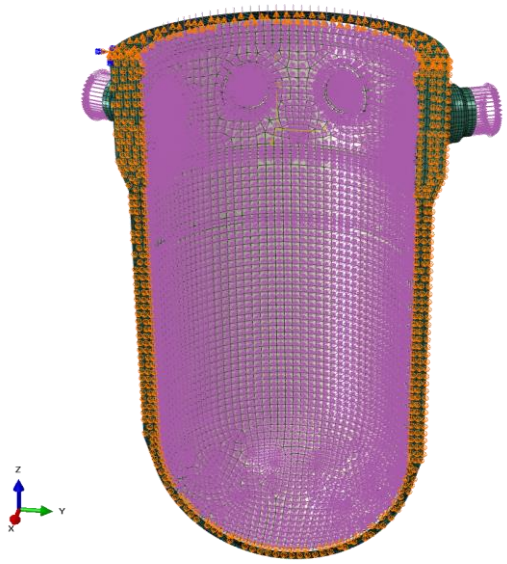

Figure 8.1: Boundary conditions (orange) and mechanical loads (pink) applied

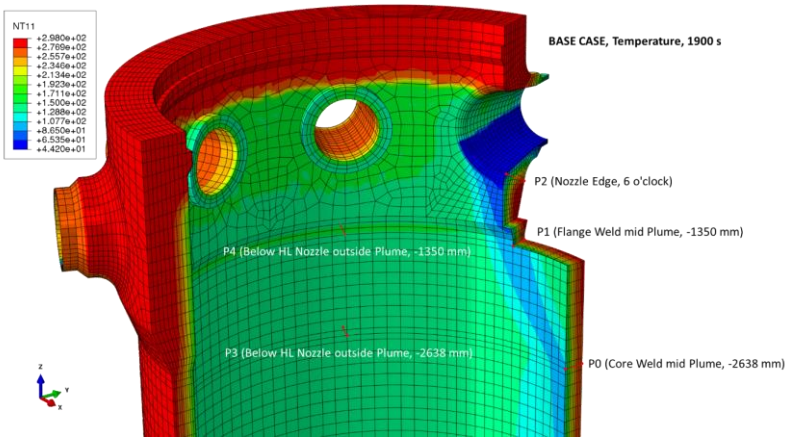

Figure 8.2: Paths evaluated by FRA-G, Temperature field for Base Case at 1900 s

8.1.1 Stress and temperature fields for base case transient at core weld position P0

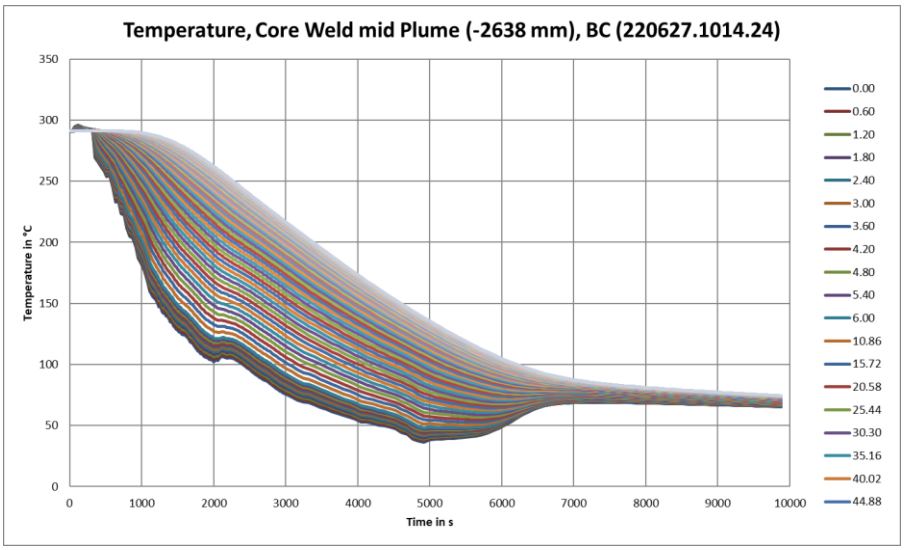

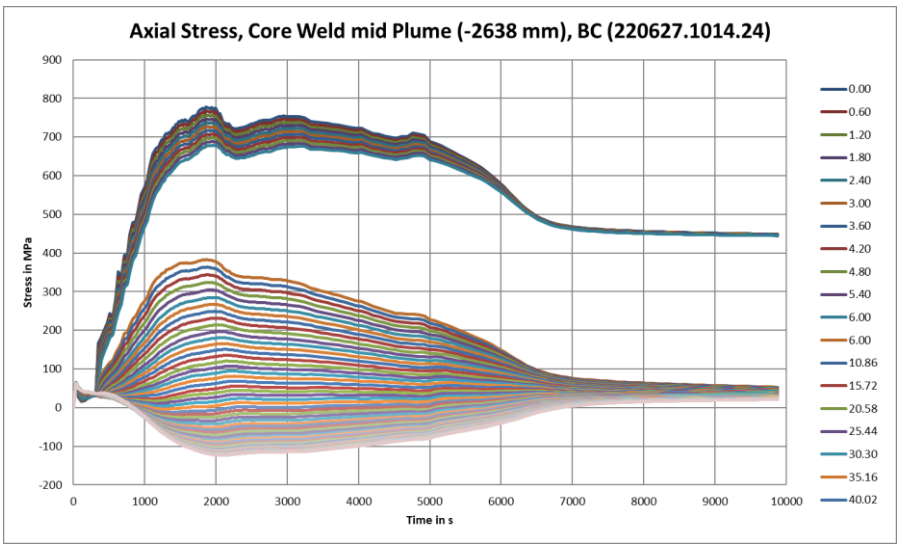

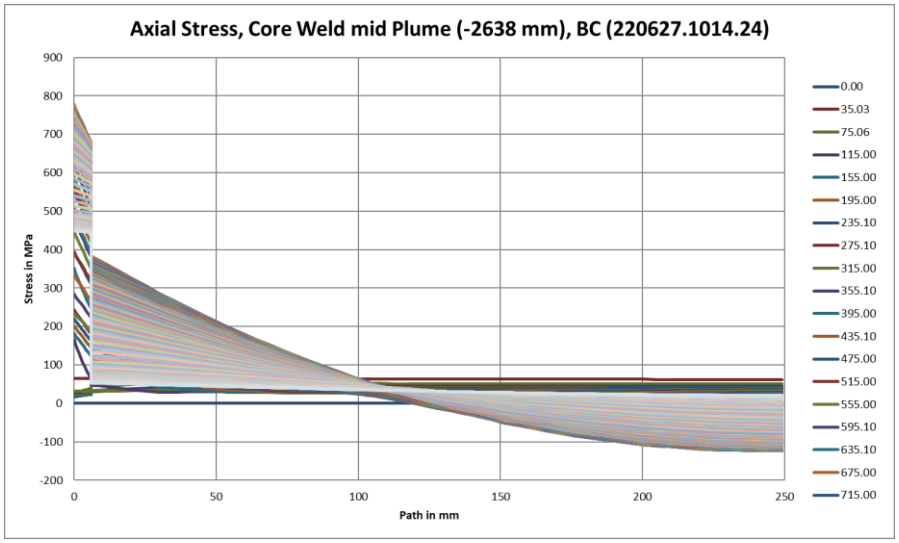

8.1.2 Stress and temperature fields for base case transient at flange weld position P1

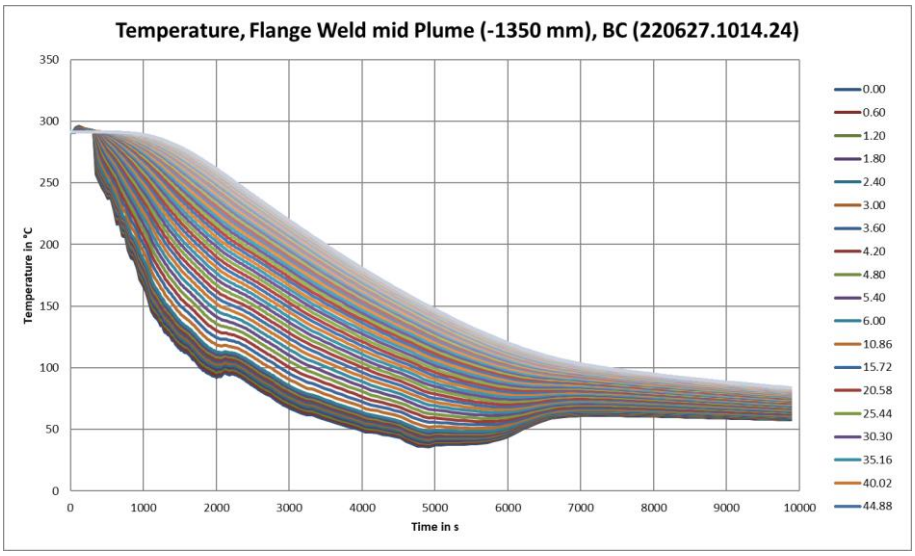

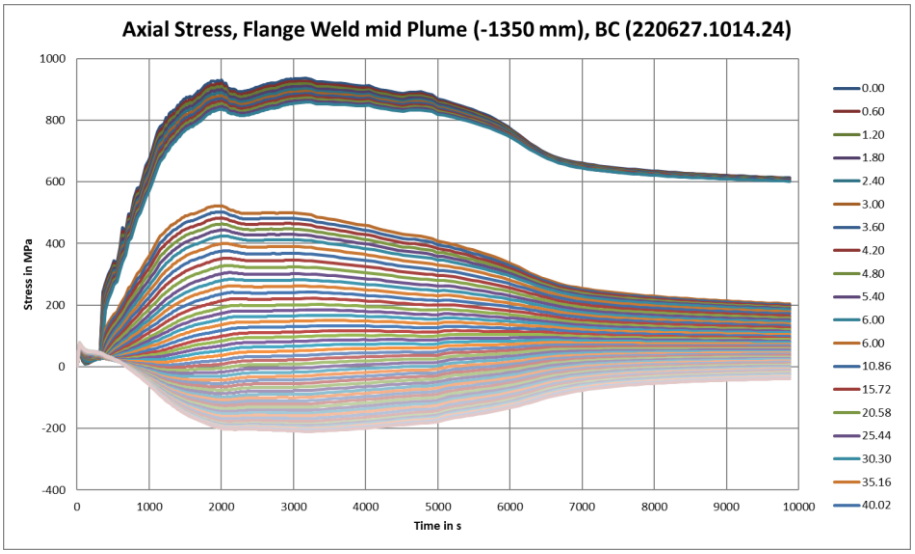

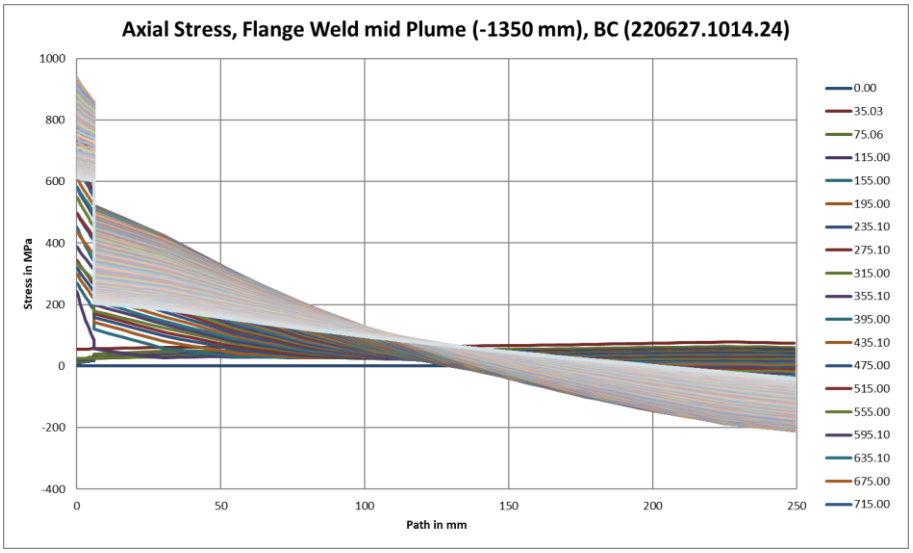

8.1.3 Stress and temperature fields for base case transient at core weld position – outside plume P3

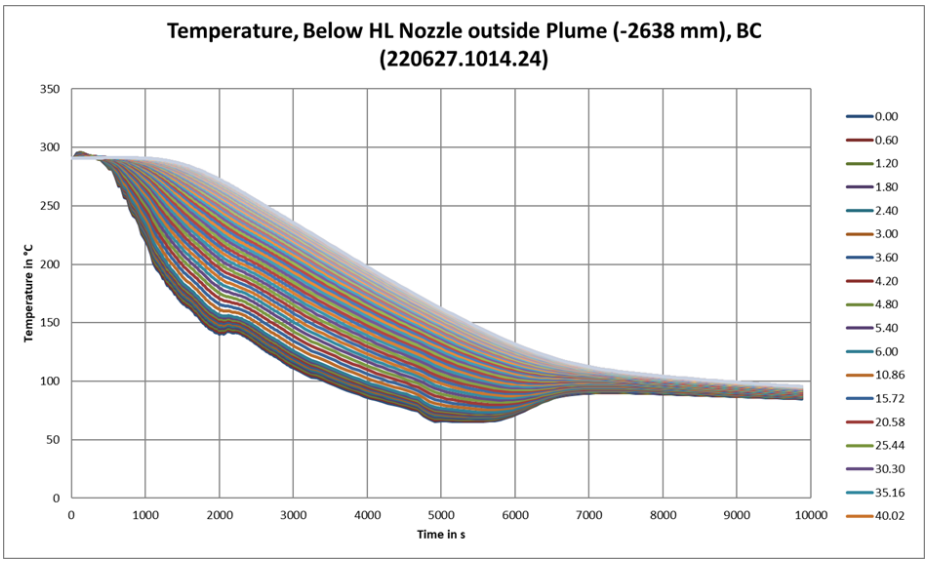

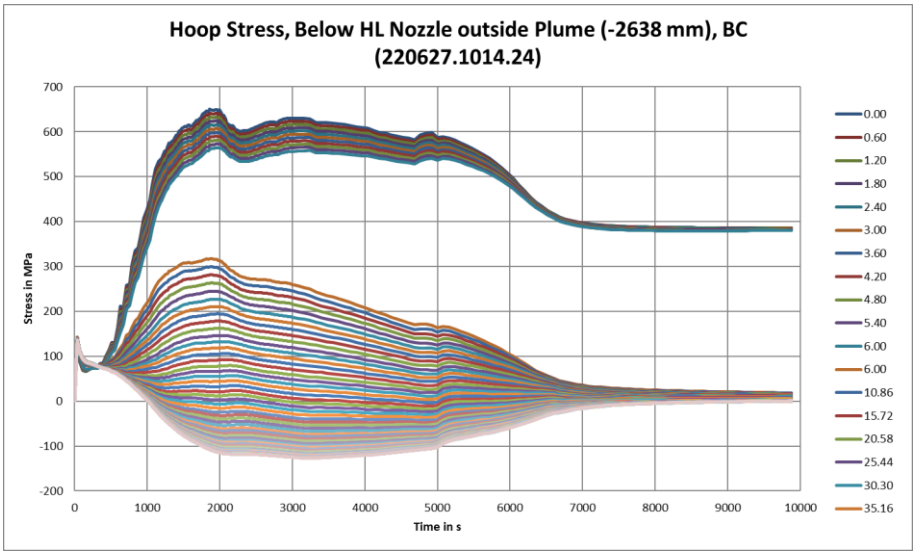

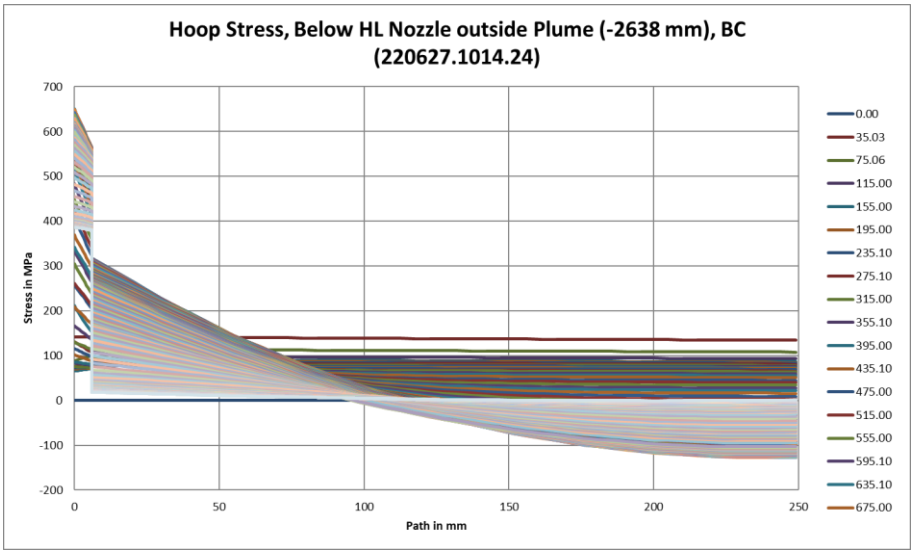

8.1.4 Stress and temperature fields for base case transient at nozzle corner P2

